

MIMO Antennas in Radar Applications

Guest Editors: Wen-Qin Wang, Mathini Sellathurai,
Frankie Kit Wing Chan, Wei Xu, and Shengqi Zhu





MIMO Antennas in Radar Applications

International Journal of Antennas and Propagation

MIMO Antennas in Radar Applications

Guest Editors: Wen-Qin Wang, Mathini Sellathurai,
Frankie Kit Wing Chan, Wei Xu, and Shengqi Zhu



Copyright © 2015 Hindawi Publishing Corporation. All rights reserved.

This is a special issue published in “International Journal of Antennas and Propagation.” All articles are open access articles distributed under the Creative Commons Attribution License, which permits unrestricted use, distribution, and reproduction in any medium, provided the original work is properly cited.

Editorial Board

Ana Alejos, Spain
Mohammad Ali, USA
Jaume Anguera, Spain
Ercument Arvas, USA
Alexei Ashikhmin, USA
Herve Aubert, France
Paolo Baccarelli, Italy
Xiulong Bao, Ireland
Toni Björninen, Finland
Djuradj S. Budimir, UK
Paolo Burghignoli, Italy
Shah N. Burokur, France
Giuseppe Castaldi, Italy
Felipe Cátedra, Spain
Chih-Hua Chang, Taiwan
Deb Chatterjee, USA
Shih Yuan Chen, Taiwan
Yu Jian Cheng, China
Renato Cicchetti, Italy
Lorenzo Crocco, Italy
Claudio Curcio, Italy
Francesco D'Agostino, Italy
Maria E. De Cos, Spain
Tayeb A. Denidni, Canada
Giuseppe Di Massa, Italy
Michele D'Urso, Italy
Francisco Falcone, Spain
Quanyuan Feng, China
Miguel Ferrando Bataller, Spain
Flaminio Ferrara, Italy
Vincenzo Galdi, Italy
Feifei Gao, China

Junping Geng, China
Claudio Gennarelli, Italy
Rocco Guerriero, Italy
Kerim Guney, Turkey
Song Guo, Japan
Qian He, China
Mohamed Himdi, France
Heng-Tung Hsu, Taiwan
Jun Hu, China
Yi Huang, UK
Tamer S. Ibrahim, USA
M. T. Islam, Malaysia
Weixiang Jiang, China
M. R. Kamarudin, Malaysia
Nemai Karmakar, Australia
Kyeong Jin Kim, USA
Ahmed A. Kishk, Canada
Slawomir Koziel, Iceland
Luis Landesa, Spain
Ding-Bing Lin, Taiwan
Angelo Liseno, Italy
Giampiero Lovat, Italy
Lorenzo Luini, Italy
Jose M. M. G. Pardo, Spain
Atsushi Mase, Japan
Diego Masotti, Italy
Giuseppe Mazzearella, Italy
C. Mecklenbräuker, Austria
Massimo Migliozi, Italy
Mark Mirotznik, USA
Ahmed T. Mobashsher, Australia
Ananda S. Mohan, Australia

Marco Mussetta, Italy
N. Nasimuddin, Singapore
Miguel Navarro-Cia, UK
Mourad Nedil, Canada
Pavel Nikitin, USA
Symeon Nikolaou, Cyprus
Giacomo Oliveri, Italy
Athanasios Panagopoulos, Greece
Ikmo Park, Korea
Matteo Pastorino, Italy
Mugen Peng, China
Massimiliano Pieraccini, Italy
Xianming Qing, Singapore
Ahmad Safaai-Jazi, USA
Safieddin Safavi-Naeini, Canada
Magdalena Salazar-Palma, Spain
Stefano Selleri, Italy
John J. Shynk, USA
Prabhakar Singh, India
Raffaele Solimene, Italy
Seong-Youp Suh, USA
Sheng Sun, Hong Kong
Larbi Talbi, Canada
Luciano Tarricone, Italy
Parveen Wahid, USA
Yuanxun Ethan Wang, USA
Wen-Qin Wang, China
Shiwen Yang, China
Yuan Yao, China
Jingjing Zhang, Denmark

Contents

MIMO Antennas in Radar Applications, Wen-Qin Wang, Mathini Sellathurai, Frankie Kit Wing Chan, Wei Xu, and Shengqi Zhu
Volume 2015, Article ID 696790, 2 pages

Joint Multichannel Motion Compensation Method for MIMO SAR 3D Imaging, Ze-min Yang, Meng-dao Xing, Guang-cai Sun, and Zheng Bao
Volume 2015, Article ID 852520, 7 pages

Joint Two-Dimensional Ambiguity Resolving Based on Space-Time Filtering for MIMO-SAR, Ping-ping Huang, Hua-sheng Li, Sheng Zhang, and Guang-Cai Sun
Volume 2014, Article ID 452141, 8 pages

Joint Direction-of-Departure and Direction-of-Arrival Estimation in a UWB MIMO Radar Detecting Targets with Fluctuating Radar Cross Sections, Idnin Pasya, Naohiko Iwakiri, and Takehiko Kobayashi
Volume 2014, Article ID 847815, 15 pages

LPI Optimization Framework for Target Tracking in Radar Network Architectures Using Information-Theoretic Criteria, Chenguang Shi, Fei Wang, Mathini Sellathurai, and Jianjiang Zhou
Volume 2014, Article ID 654561, 10 pages

Computationally Efficient DOA Tracking Algorithm in Monostatic MIMO Radar with Automatic Association, Huaxin Yu, Xiaofei Zhang, Xueqiang Chen, and Hailang Wu
Volume 2014, Article ID 501478, 10 pages

Transmit Waveform Optimization for Spatial-Frequency Diversity MIMO Radar in the Presence of Clutter, Yonghao Tang, Xiaofeng Ma, Weixing Sheng, and Yubing Han
Volume 2014, Article ID 510569, 9 pages

An Efficient Signal Reconstruction Algorithm for Stepped Frequency MIMO-SAR in the Spotlight and Sliding Spotlight Modes, Jiajia Zhang, Guangcai Sun, Mengdao Xing, Zheng Bao, and Fang Zhou
Volume 2014, Article ID 329340, 8 pages

The PARAFAC-MUSIC Algorithm for DOA Estimation with Doppler Frequency in a MIMO Radar System, Nan Wang, Wenguang Wang, Fan Zhang, and Yunneng Yuan
Volume 2014, Article ID 684591, 5 pages

Transmit Beampattern Synthesis with Constant Beamwidth and Sidelobe Control for Wideband MIMO Radar, Pengcheng Gong and Zhenhai Shao
Volume 2014, Article ID 376279, 6 pages

Channel Phase Error Compensation for MIMO-SAR, Lei Zhang, Yunkai Deng, and Robert Wang
Volume 2014, Article ID 798673, 7 pages

Multiband Microwave Imaging Analysis of Ionosphere and Troposphere Refraction for Spaceborne SAR, Fan Zhang, Guojun Li, Wei Li, and Wei Hu
Volume 2014, Article ID 913056, 9 pages

Sparse Recovery for Bistatic MIMO Radar Imaging in the Presence of Array Gain Uncertainties, Jun Li, Shengqi Zhu, Xixi Chen, Li Lv, Guisheng Liao, and Menglei Yi
Volume 2014, Article ID 807960, 6 pages



3D Imaging Algorithm for Down-Looking MIMO Array SAR Based on Bayesian Compressive Sensing,

Xiaozhen Ren, Lina Chen, and Jing Yang

Volume 2014, Article ID 612326, 9 pages

“Three Crossings” Compensations of the High Speed Moving MIMO Radar, Cheng Luo and Zishu He

Volume 2014, Article ID 761084, 7 pages

Low Complexity Direction and Doppler Frequency Estimation for Bistatic MIMO Radar in Spatial Colored Noise, Lingyun Xu, Guangbin Zhang, Xiaofei Zhang, and Zongze Xu

Volume 2014, Article ID 358563, 8 pages

Correction of Channel Imbalance for MIMO SAR Using Stepped-Frequency Chirps, Xiulian Luo,

Yunkai Deng, Robert Wang, Lei Guo, and Mingjiang Wang

Volume 2014, Article ID 161294, 8 pages

Special MISO-SAR and MIMO-SAR Modes for Bidirectional Imaging, Hai Jiang, Hongjun Song,

Lei Guo, and Wei Wang

Volume 2014, Article ID 320384, 10 pages

Editorial

MIMO Antennas in Radar Applications

**Wen-Qin Wang,¹ Mathini Sellathurai,² Frankie Kit Wing Chan,³
Wei Xu,⁴ and Shengqi Zhu⁵**

¹*School of Communication and Information Engineering, University of Electronic Science and Technology of China, Chengdu 611731, China*

²*School of Engineering & Physical Sciences, Heriot-Watt University, Edinburgh EH14 4AS, UK*

³*Department of Electronic Engineering, City University of Hong Kong, Hong Kong*

⁴*Institute of Electronics, Chinese Academy of Sciences, Beijing 100190, China*

⁵*National Key Laboratory of Radar Signal Processing, Xidian University, Xi'an 710071, China*

Correspondence should be addressed to Wen-Qin Wang; wqwang@uestc.edu.cn

Received 11 August 2014; Accepted 11 August 2014

Copyright © 2015 Wen-Qin Wang et al. This is an open access article distributed under the Creative Commons Attribution License, which permits unrestricted use, distribution, and reproduction in any medium, provided the original work is properly cited.

Conventional single-antenna radar is inherently limited in meeting the rising demands of future applications. Innovative radar technologies are thus needed to be developed. Multiple-input multiple-output (MIMO) radar allows for simultaneous transmission and reception by multiple antennas or channels. In particular, MIMO radar offers potential to gather additional information to overcome the restrictions of single-antenna radars in target radar cross section scintillation, low system gain, and poor identify capability. The multiple antennas can be placed either in a monostatic platform or in distributed platforms. This system flexibility offers opportunities to develop new radar technologies and applications. Although MIMO antennas in radar target detection and estimation applications have received much attention in recent years (see [1] and the references therein), there still are many open questions, especially in applying MIMO antennas to radar imaging applications (see [2] and the references therein).

The purpose of this special issue is to bring together MIMO antenna signal processing and application related investigations, stimulating the continuing efforts to understand MIMO radar, develop new MIMO radar imaging technologies, and evaluate their applications. From the manifold submissions, we have selected interesting papers. These papers concern different MIMO antennas and their applications in target detection, tracking, beam pattern synthesis, radar imaging, and sparse recovery. To help interested readers with a quick reference to the main themes of these papers, we briefly introduce them as follows.

Target localization in radar has been intensively studied in literature; however, the localization resolution is limited by the signal bandwidth, and usage of multiple stations is required to avoid ghost targets. On the contrary, it is possible for MIMO radar to jointly estimate the direction-of-departure (DOD) and direction-of-arrival (DOA) by applying array processing at both of the transmitting and receiving arrays. I. Pasya et al. present a joint DOD and DOA estimation in a MIMO radar utilizing ultra wideband signals for detecting targets with fluctuating radar cross sections. H. Yu et al. propose a low-complexity DOA estimation and tracking algorithm for monostatic MIMO radar. Doppler shift is also an important issue in MIMO radar, but it is often ignored in existing literatures. N. Wang et al. utilize the parallel factor (PARAFAC) algorithm to estimate the Doppler frequency and then exploit the multiple signal classification (MUSIC) to estimate the DOA. L. Xu et al. present a DOA and Doppler frequency joint estimator for bistatic MIMO radar in spatial colored noise.

Different from monostatic MIMO radar, distributed MIMO radar may provide significant performance improvement for target detection and localization. However, optimal power allocation is a challenge in distributed MIMO radar network. C. Shi et al. propose an interesting low probability of intercept (LPI) optimization framework for target tracking in distributed MIMO radar network. The authors use two information theoretic criteria, namely, Bhattacharyya distance and J -divergence, as the metrics for target detection performance.

Waveform diversity design for MIMO radar has received much attention [3]. A promising research direction is joint optimization of transmitted waveforms and receiving filters with clutter suppression. Y. Tang et al. propose a transmit waveform optimization for spatial frequency diversity MIMO radar in the presence of clutter. Besides effective clutter suppression, the proposed method also can suppress target scintillation. Furthermore, P. Gong and Z. Shaopropose a transmit beam pattern synthesis with constant beamwidth and sidelobe control for wideband MIMO radar by optimal designing of the power spectral density matrix.

This special issue focuses on MIMO radar imaging related topics, especially MIMO synthetic aperture radar (SAR) which places multiple antennas in moving platforms and employs synthetic aperture technique for two-dimensional (2D) or three-dimensional (3D) imaging. The multiple antennas in a MIMO SAR can be arranged either in elevation direction (cross-track), in azimuth direction (along-track), or in both dimensions [4]. Good operation flexibility and reconfigurability can thus be obtained by exploiting the equivalent phase centers, but optimizing the array configuration requires further investigations [5]. H. Jiang et al. investigate several special multiple-input single-output (MISO) and MIMO SAR modes for bidirectional imaging.

J. Zhang et al. present an efficient algorithm to reconstruct the signal of MIMO SAR using stepped frequency waveforms in spotlight and sliding spotlight modes. The authors introduce a Doppler ambiguity resolving algorithm based on subaperture division and an improved frequency-domain bandwidth synthesis method. P. Huang et al. and Z. Yang et al. present joint 2D ambiguity resolving for MIMO SAR and joint multichannel motion compensation for MIMO SAR 3D imaging, respectively. Since compressive sensing technique plays an important role in sparse array design [6], two papers exploiting compressive sensing technique for MIMO radar imaging are included in this special issue. J. Li et al. propose a sparse recovery for bistatic MIMO radar imaging in presence of array gain uncertainties, where the imaging is performed by compressive sensing with a consideration of both the transmitting and receiving array gain uncertainties. X. Ren et al. present a new strategy based on Bayesian compressive sensing theory for down-looking MIMO SAR imaging. The authors transform the cross-track imaging process into a problem of sparse signal reconstruction from noise measurements.

Another important MIMO radar topic is system implementation. The first hardware constraint is channel imbalance. Existing solutions can be classified as two categories: internal calibration and external calibration. X. Luo et al. propose an external calibration, where the channel imbalance errors are estimated from the peak of a corner reflector or a strong point target in the scenario. The second hardware constraint is motion compensation. Such problem is discussed by C. Luo and Z. He. Additionally, spaceborne MIMO SAR may be degraded by ionosphere effects. F. Zhang et al. analyze the impacts of ionosphere and troposphere refraction on spaceborne multiband SAR imaging. The authors conclude that the refraction effects should be compensated in low-frequency band.

All papers appearing in this special issue have been subject to a strict peer-reviewing process. Through this special issue, we have provided a medium of dissemination for valuable ideas and conclusions on MIMO antennas in radar applications. At the same time, we hope that more innovations can be stimulated for future advances on this exciting subject.

Acknowledgment

We would like to thank all authors for their highly professional contributions and the reviewers for their valuable ideas, time, and suggestions.

Wen-Qin Wang
Mathini Sellathurai
Frankie Kit Wing Chan
Wei Xu
Shengqi Zhu

References

- [1] J. Li and P. Stoica, *MIMO Radar Signal Processing*, John Wiley & Sons, New York, NY, USA, 2009.
- [2] W.-Q. Wang, *Multi-Antenna Synthetic Aperture Radar*, CRC Press, New York, NY, USA, 2013.
- [3] B. Friedlander, "On the role of waveform diversity in MIMO radar," in *Proceedings of the 45th Asilomar Conference on Signals, Systems and Computers (ASILOMAR '11)*, pp. 1501–1505, Pacific Grove, Calif, USA, November 2011.
- [4] W.-Q. Wang, "MIMO SAR imaging: potential and challenges," *IEEE Aerospace and Electronic Systems Magazine*, vol. 28, no. 8, pp. 18–23, 2013.
- [5] G. Krieger, "MIMO-SAR: opportunities and pitfalls," *IEEE Transactions on Geoscience and Remote Sensing*, vol. 52, no. 5, pp. 2628–2645, 2013.
- [6] L. Carin, D. Liu, and B. Guo, "Coherence, compressive sensing, and random sensor arrays," *IEEE Antennas and Propagation Magazine*, vol. 53, no. 4, pp. 28–39, 2011.

Research Article

Joint Multichannel Motion Compensation Method for MIMO SAR 3D Imaging

Ze-min Yang, Meng-dao Xing, Guang-cai Sun, and Zheng Bao

Key Laboratory for Radar Signal Processing, Xidian University, Xi'an 710071, China

Correspondence should be addressed to Guang-cai Sun; rsandsgc@126.com

Received 26 January 2014; Revised 28 April 2014; Accepted 5 June 2014

Academic Editor: Wen-Qin Wang

Copyright © 2015 Ze-min Yang et al. This is an open access article distributed under the Creative Commons Attribution License, which permits unrestricted use, distribution, and reproduction in any medium, provided the original work is properly cited.

The multiple-input-multiple-output (MIMO) synthetic aperture radar (SAR) system with a linear antenna array can obtain 3D resolution. In practice, it suffers from both the translational motion errors and the rotational motion errors. Conventional single-channel motion compensation methods could be used to compensate the motion errors channel by channel. However, this method might not be accurate enough for all the channels. What is more, the single-channel compensation may break the coherence among channels, which would cause defocusing and false targets. In this paper, both the translational motion errors and the rotational motion errors are discussed, and a joint multichannel motion compensation method is proposed for MIMO SAR 3D imaging. It is demonstrated through simulations that the proposed method exceeds the conventional methods in accuracy. And the final MIMO SAR 3D imaging simulation confirms the validity of the proposed algorithm.

1. Introduction

Conventional single-channel synthetic aperture radar (SAR) uses wideband signal and synthetic apertures to obtain high range resolution and high azimuth resolution, respectively. But it could not resolve along height due to the lack of baseline in the elevation direction. The imaging results are the projection from the scene in 3D to the range-azimuth plane. To resolve along height, the multiple-input-multiple-output (MIMO) SAR system [1–3] uses multichannel to form the baseline in the third dimension. Technically, the MIMO SAR system could place its sensor in many different layouts. Two possible geometries of MIMO SAR are along-track array (for the reduction of azimuth-ambiguities, moving target indication, superresolution, etc.) and across-track array (for the reduction of elevation-ambiguities, interferometry, 3D imaging, etc.) [4].

The MIMO SAR system has two main advantages: (1) the degrees of freedom can be greatly increased by the concept of virtual array provided by the multiple antennas [3]; (2) the MIMO SAR system can provide plenty of transmitting elements and receiving elements to satisfy the cross-track sampling [5]. Due to the second advantage, it can significantly

improve the resolution of the third dimension. Thus it is widely used for 3D imaging. Profiting from the unique advantages, airborne MIMO SAR 3D imaging technique has become a field of intensive research in recent years. However, studies about the MIMO SAR are mostly concentrated on antenna arrangements [4, 6], waveform designs [7, 8], and imaging algorithms [4, 9]. The motion compensation (MOCO) has not been paid much attention. To deal with the motion errors, the most preferable way is using a high-precision navigation system. However, in many cases, due to the limit of accuracy of such systems, motion errors are unlikely to be compensated correctly. Thus MOCO methods based on raw data are widely used. Conventional MOCO methods [10–12] or autofocus methods [13, 14] only deal with the translational motion errors of the carrier aircraft. This is reasonable in single-channel SAR imaging because the sensor is normally placed at the centroid of the plane. The rotational motion errors only alter the beam direction and could be compensated through beam control. Nevertheless, for the MIMO SAR system, the rotational motion errors could no longer be ignored because they affect the relative positions of the sensors. Conventionally the motion errors are estimated and compensated separately for each channel. We refer to

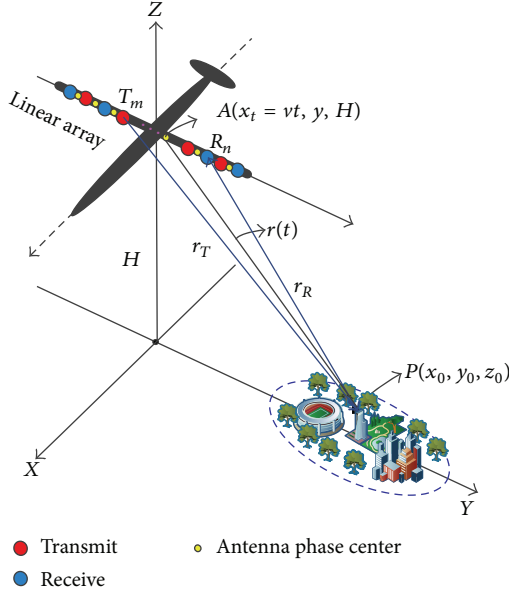


FIGURE 1: The ideal geometry of MIMO SAR 3D imaging.

this method as single-channel MOCO (SC-MOCO) method. This method may break the coherence among channels which would cause defocusing and false targets. In this paper, making use of the linear features of the MIMO system, a joint multichannel MOCO (JMC-MOCO) method is proposed for MIMO SAR 3D imaging. This new method can estimate and compensate both the translational motion errors and the rotational motion errors. Thus it is of high value for the MIMO SAR 3D imaging.

The paper is organized as follows. In Section 2, we first discuss the ideal geometry of MIMO SAR 3D imaging. Then both the translational motion errors and the rotational motion errors are analyzed in Section 3. In Section 4, the JMC-MOCO method for the MIMO SAR 3D imaging is introduced in detail. Simulations in Section 5 confirm that the proposed method is of higher accuracy than that of the conventional single-channel method.

2. Signal Mode and Imaging Geometry of MIMO SAR

The MIMO SAR utilizes an across-track array to gain the third dimension resolution. The transmitter and receiver antennas are usually distributed nonuniformly along the linear across-track array. Assume a MIMO SAR platform flies at the altitude of H along the X -axis with velocity v . The MIMO array with M transmit elements and N receive elements is linearly laid out along the Y -axis. Signal sorting would be operated after the collecting of data, and MN valuable signals can be saved for the imaging process during each pulse. The ideal geometry of MIMO SAR 3D imaging is indicated in Figure 1.

Ignoring two-way antenna characteristics and propagation attenuation, after demodulation and range compression, the echo signal transmitted by the m th transmitter T_m

reflected by a generic point target $P(x_0, y_0, z_0)$ and received by the n th receiver R_n is given by

$$e(\tau, t) = \rho \cdot s\left(\tau - \frac{2r(t)}{c}\right) \exp\left(-j4\pi \frac{r(t)}{\lambda}\right), \quad (1)$$

where $s(\tau)$ is the transmitted signal, τ is the fast time, t is the slow time, ρ is the reflectivity of P , c is the time speed, and λ is the wavelength; $r(t) = (r_T + r_R)/2$ [15] denotes the range from the antenna phase center (APC) $A(x_t = vt, y, H)$ of T_m and R_n to P ; r_T and r_R are the range from T_m and R_n to P , respectively. Then

$$r(t) = \sqrt{(vt - x_0)^2 + (y - y_0)^2 + (H - z_0)^2}, \quad (2)$$

where y is the across-track position of the APC.

As described in [16, 17], the image is formed in three steps, namely, the compression in the range direction, the focusing in the azimuth direction using the SAR principle, and the beam forming operation to focus the data in the across-track direction.

3. Imaging Geometry of MIMO SAR with Motion Errors

In practice, due to the presence of atmospheric turbulence that produces sensor track deviations from an ideal straight track, motion errors need to be accurately compensated. There have been numerous good methods dealing with the translational motion errors but ignoring the rotational motion errors [10–12]. These methods are adequate for single-channel SAR, because the sensor is usually placed at the centroid of the carrier aircraft and the rotational motion errors can be compensated through beam control. However, for MIMO SAR system, the rotational motion errors would change the baseline position and decrease the quality of the final image eventually.

Before the introduction of our method, we first discuss the core element that causes the defocusing of SAR images, that is, the range migration error.

As shown in Figure 2, a blue dashed arrow identifies the offset from the ideal position of the carrier plane to its true position. Then the translational motion error is $\Delta \mathbf{r} = [\Delta x_t, \Delta y_t, \Delta z_t]$. The subscript t means time-variant. In Figure 3, the rotational motion error of the carrier aircraft is characterized by three angles $[\theta_t, \varphi_t, \phi_t]$ with θ_t denoting the pitch angle, φ_t denoting the roll angle, and ϕ_t denoting the yaw angle. Among them, θ_t does not affect the array position. The rotation matrixes of φ_t and ϕ_t can be written as $\mathbf{T}_\varphi = \begin{bmatrix} 1 & 0 & 0 \\ 0 & \cos \varphi_t & -\sin \varphi_t \\ 0 & \sin \varphi_t & \cos \varphi_t \end{bmatrix}$ and $\mathbf{T}_\phi = \begin{bmatrix} \cos \phi_t & -\sin \phi_t & 0 \\ \sin \phi_t & \cos \phi_t & 0 \\ 0 & 0 & 1 \end{bmatrix}$, respectively. Then, the real position of the APC can be denoted as

$$\begin{aligned} \mathbf{A} &= [x_t, 0, H]^T + \mathbf{T}_\varphi \mathbf{T}_\phi [0, y, 0]^T + \Delta \mathbf{r}^T \\ &= [x_t - y \sin \phi_t + \Delta x_t, y \cos \phi_t \cos \varphi_t + \Delta y_t, \\ &\quad H + y \cos \phi_t \sin \varphi_t + \Delta z_t]^T. \end{aligned} \quad (3)$$

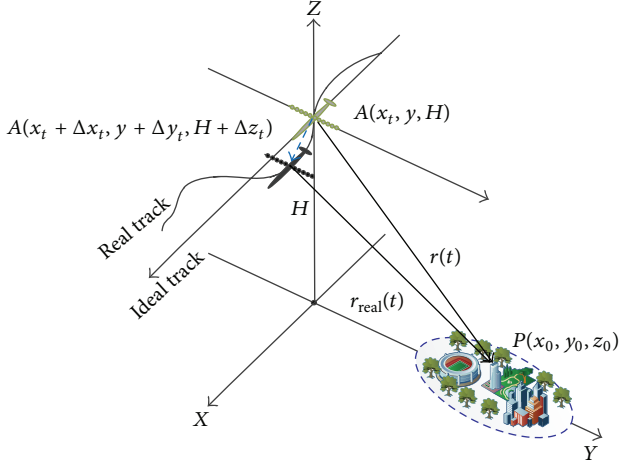


FIGURE 2: The geometry of MIMO SAR 3D imaging with translational motion errors.

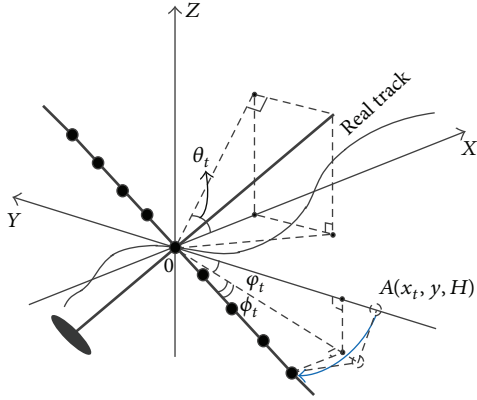


FIGURE 3: The geometry of MIMO SAR 3D imaging with rotational motion errors.

The slant range from A to the point target P can now be written as

$$\begin{aligned} r_{\text{real}}(t) &= \left((x_t - y \sin \phi_t + \Delta x_t - x_0)^2 \right. \\ &\quad + (y \cos \phi_t \cos \varphi_t + \Delta y_t - y_0)^2 \\ &\quad + (H + y \cos \phi_t \sin \varphi_t + \Delta z_t - z_0)^2 \Big)^{1/2} \\ &= \sqrt{r(t)^2 + r_e^2}, \end{aligned} \quad (4)$$

where

$$\begin{aligned} r_e &= \left(2(x_t + \Delta x_t - x_0)(-y \sin \phi_t) + \Delta x_t^2 \right. \\ &\quad + 2\Delta x_t(x_t - x_0) + 2(-\Delta y_t y_0 - \Delta z_t z_0) \\ &\quad + 2y(y_0(1 - \cos \phi_t \cos \varphi_t) - z_0 \cos \phi_t \sin \varphi_t \\ &\quad \left. + \Delta y_t \cos \phi_t \cos \varphi_t + \Delta z_t \cos \phi_t \sin \varphi_t) \right)^{1/2} \end{aligned} \quad (5)$$

is the range error caused by the translational and rotational motion errors and needs to be compensated. In the next

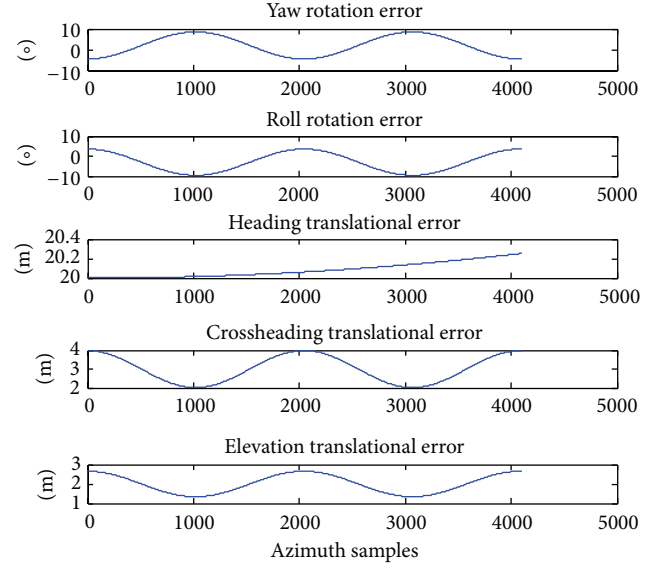


FIGURE 4: The simulated rotational motion errors and the translational motion errors.

section, the JMC-MOCO method is discussed in detail to estimate and compensate the range error.

4. Joint Multichannel MOCO Method for MIMO SAR 3D Imaging

To compensate the motion errors, the conventional method is used to estimate and compensate the motion errors for each channel. However, the inevitable estimating errors of each channel may cause the incoherence among channels which would cause defocusing and false targets. Combining the linear properties of the across-track array, in this section we present a new method which can compensate both the translational motion errors and the rotational motion errors and preserve the coherence among different channels at the same time.

To avoid the incoherence after motion error compensation, the motion error estimating and compensating need to be jointed among channels. From (4) and (5) we can see that, due to the rotational motion errors, the range error differs along the linear across-track array. To clearly uncover the relationship between the range error and the array, we expand (4) according to Taylor expansion as follows:

$$r_{\text{real}}(t) \approx r_0 + \frac{(x_t - x_0)^2}{2r_0} + \alpha_t + \beta_t \cdot y + \frac{y^2}{2r_0}, \quad (6)$$

where $r_0 = \sqrt{y_0^2 + (H - z_0)^2}$ is the ideal zero-Doppler range from the center APC to the point target, $(x_t - x_0)^2/2r_0$ is the ideal range migration, and

$$\begin{aligned} \alpha_t &= \frac{\Delta x_t(x_t - x_0)}{r_0} - \Delta y_t \frac{y_0}{r_0} + \Delta z_t \frac{H - z_0}{r_0} \\ &\quad + \frac{\Delta x_t^2 + \Delta y_t^2 + \Delta z_t^2}{2r_0}, \end{aligned}$$

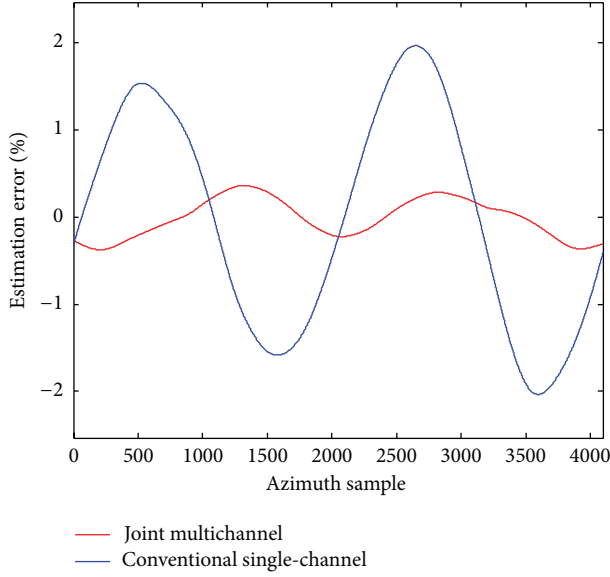


FIGURE 5: Comparison of the center APC Doppler rate estimation accuracy between the proposed method and the conventional method.

$$\beta_t = -\frac{x_t - x_0}{r_0} \sin \phi_t - \frac{y_0}{r_0} \cos \phi_t \cos \varphi_t + \frac{H - z_0}{r_0} \cos \phi_t \sin \varphi_t. \quad (7)$$

$y^2/2R_B$ is typically small and can be neglected. Then the range error $\alpha_t + \beta_t \cdot y$ is linear along the across-track array. Moreover, α_t is only related to the translational motion errors, and β_t is only related to the rotational motion errors.

The range error alters the Doppler rate and finally defocuses the image. Hence, to estimate the motion error, let us first analyze the true Doppler rates. As expressed in (1), after range compression, the phase history of P is

$$\Phi(t) = -\frac{4\pi r_{\text{real}}(t)}{\lambda}. \quad (8)$$

Substitute (6) into (8) and derive (8) twice, and the Doppler rate can be denoted as

$$\gamma = \gamma_0 + A(t) + B(t)y, \quad (9)$$

where

$$\gamma_0 = -\frac{2v^2}{(\lambda R_B)} \quad (10)$$

is the ideal Doppler rate,

$$\begin{aligned} A(t) &= \left(-2 \left[\Delta a_{xt} (x_t - x_0 + \Delta x_t) + 2\Delta v_{xt} v + \Delta v_{xt}^2 \right. \right. \\ &\quad \left. \left. - \Delta a_{yt} y_0 + \Delta a_{zt} (H - z_0) \right] \right) (\lambda r_0)^{-1}, \\ B(t) &= \frac{2}{\lambda r_0} \left[2v\omega_{\phi t} \cos \phi_t + a_{\phi t} (x_t - x_0) \cos \phi_t \right. \\ &\quad \left. - \omega_{\phi t}^2 (x_t - x_0) \sin \phi_t \right] \\ &\quad + \frac{2y_0}{\lambda r_0} \left[-a_{\phi t} \sin \phi_t \cos \varphi_t - a_{\varphi t} \cos \phi_t \sin \varphi_t \right. \\ &\quad \left. + 2\omega_{\phi t} \omega_{\varphi t} \sin \phi_t \sin \varphi_t \right. \\ &\quad \left. - (\omega_{\phi t}^2 + \omega_{\varphi t}^2) \cos \phi_t \cos \varphi_t \right] \\ &\quad + \frac{2(H - z_0)}{\lambda r_0} \left[a_{\phi t} \sin \phi_t \sin \varphi_t - a_{\varphi t} \cos \phi_t \cos \varphi_t \right. \\ &\quad \left. + 2\omega_{\phi t} \omega_{\varphi t} \sin \phi_t \cos \varphi_t \right. \\ &\quad \left. + (\omega_{\phi t}^2 + \omega_{\varphi t}^2) \cos \phi_t \sin \varphi_t \right]. \end{aligned} \quad (11)$$

In (11), Δv_{xt} is the speed error of the plane. Δa_{xt} , Δa_{yt} , and Δa_{zt} denote the translational acceleration in the track direction, the across-track direction, and the elevation direction, respectively. $\omega_{\phi t}$ and $\omega_{\varphi t}$ denote the angular velocity of the yaw angle and the roll angle. a_{ϕ} and a_{φ} are the corresponding angular acceleration.

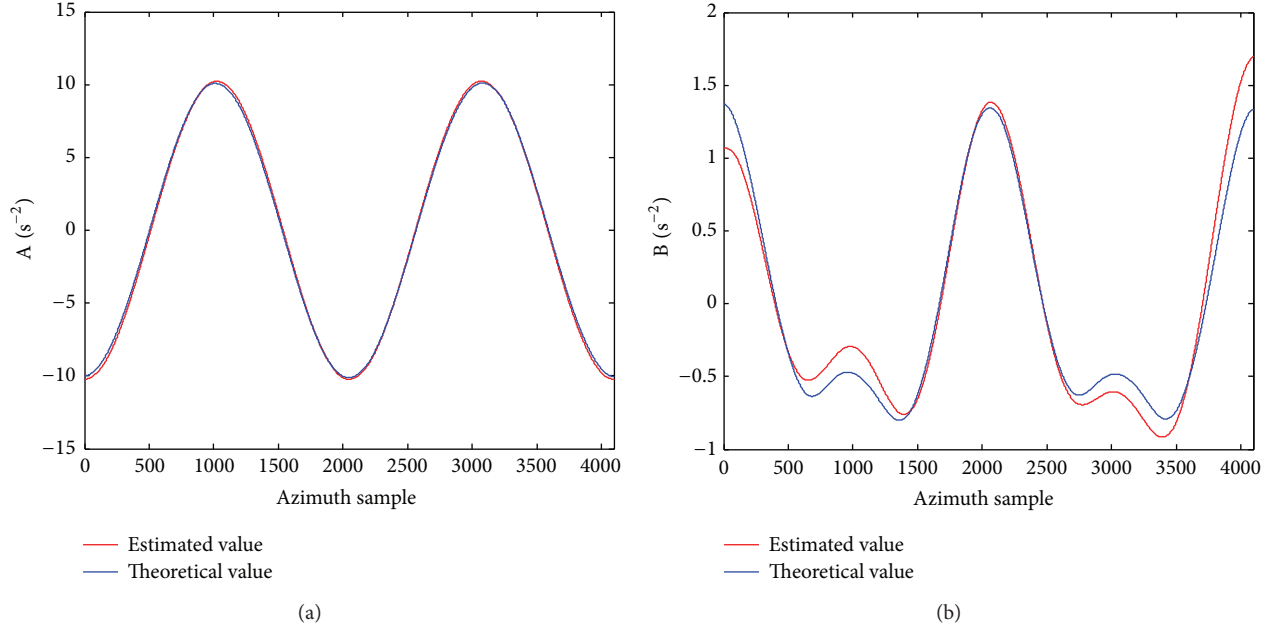
From (9) we can see that the true Doppler rate γ contains three parts: the ideal Doppler rate γ_0 and two error terms. Similar to the case of range, $A(t)$ is only related to the translational motion errors, and $B(t)$ is only related to the rotational motion errors. That means, due to the rotational motion errors, the true Doppler rate scales linearly with the across-track position of the APC. The SC-MOCO method does not estimate the linear property of the motion errors; consequently it breaks the coherence among channels after motion compensation. This linear feature is used in the following to design a new motion compensation method that compensates both the translational motion errors and the rotational motion errors.

Suppose there are K channels. Using the map drift (MD) method [18, 19] to estimate the Doppler rate of each channel, we have the Doppler rate array

$$\hat{\gamma} = [\hat{\gamma}_1, \hat{\gamma}_2, \dots, \hat{\gamma}_K, \gamma_K]^T, \quad (12)$$

where $\hat{\gamma}_k$ denotes the Doppler rate of the k th channel. In order to estimate the two unknown parameters A and B in (9), a cost function is designed as follows:

$$J(A, B) = \sum_{k=1}^K (\hat{\gamma}_k - \gamma_0 - A - B\gamma_k)^2, \quad (13)$$

FIGURE 6: Comparison between the estimated value and the theoretical value of (a) A and (b) B .

where y_k is the position of the k th channel. The aim is to find (A, B) that minimizes J , that is, the stagnation point. Let the partial derivatives of J be equal to 0; we have

$$\begin{aligned} \frac{\partial J}{\partial A} &= -2 \sum_{k=1}^K \hat{y}_k + 2K\gamma_0 + 2KA + 2B \sum_{k=1}^K y_k = 0, \\ \frac{\partial J}{\partial B} &= -2 \sum_{k=1}^K (\hat{y}_k y_k) + 2\gamma_0 \sum_{k=1}^K y_k \\ &\quad + 2A \sum_{k=1}^K y_k + 2B \sum_{k=1}^K y_k^2 = 0. \end{aligned} \quad (14)$$

By solving (14), A and B can be written as

$$\begin{aligned} A &= \frac{\sum_{k=1}^K \hat{y}_k \times \sum_{k=1}^K y_k^2 - \sum_{k=1}^K (\hat{y}_k y_k) \times \sum_{k=1}^K y_k}{N \sum_{k=1}^K y_k^2 - \left(\sum_{k=1}^K y_k \right)^2} - \gamma_0, \\ B &= \frac{K \sum_{k=1}^K (\hat{y}_k y_k) - \sum_{k=1}^K \hat{y}_k \times \sum_{k=1}^K y_k}{K \sum_{k=1}^K y_k^2 - \left(\sum_{k=1}^K y_k \right)^2}. \end{aligned} \quad (15)$$

This method combines all the estimating results of each channel to obtain the linear coefficient and then derives each Doppler rate. Comparing to the conventional SC-MOCO method, this method has three advantages: (1) the estimating accuracy is dramatically improved; (2) the influence from occasional bad estimating values can be suppressed; and (3) the multichannels maintain coherence after motion estimation. This will be demonstrated in Section 5 through simulations.

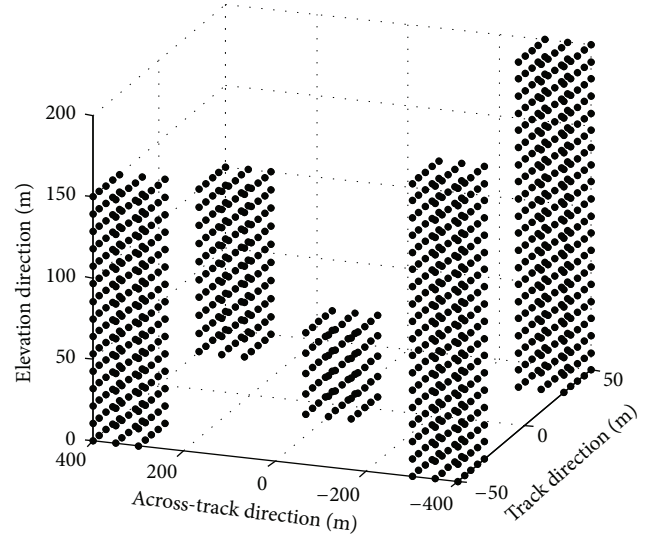


FIGURE 7: Point targets layout.

5. Simulations

5.1. Motion Error Estimation Comparison between the Proposed Method and the Conventional Method. In order to prove that the proposed method is of higher precision than the conventional method, a MIMO SAR system with a linear MIMO array is simulated. The key simulation parameters are listed in Table 1. The linear MIMO array contains 32 APCs. Nine points are set in a line along the track direction with spacing of 2 m. Common translational motion errors and rotational motion errors shown in Figure 4 are imported

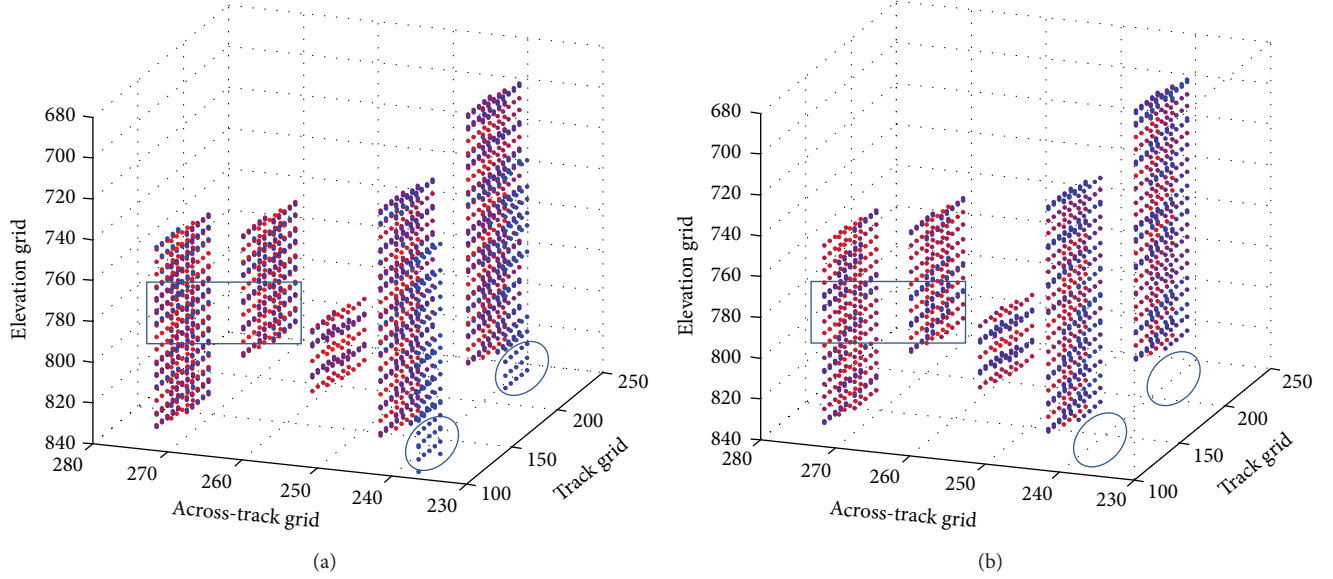


FIGURE 8: The imaging results with (a) the SC-MOCO method and (b) the proposed JMC-MOCO method.

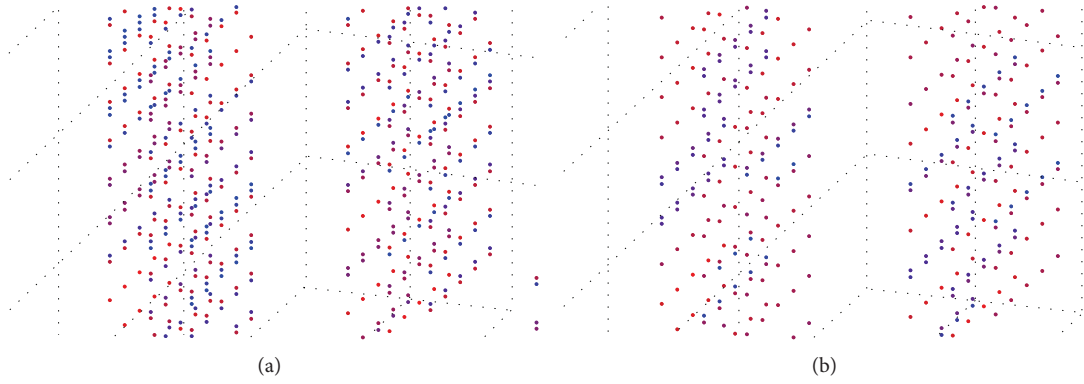


FIGURE 9: The magnified imaging results with (a) the SC-MOCO method and (b) the proposed JMC-MOCO method.

TABLE 1: Simulation parameters.

Wavelength	0.0313 m
Bandwidth	150 MHz
Pulse duration	2 μ s
PRF	180 Hz
Antenna width	2 m
Flying height	6 km
Flying speed	150 m/s
Incidence angle	60°
Baseline length	8 m

into the simulation. As shown in Figure 4, the yaw angle and the roll angle vary in a range of $\pm 10^\circ$. The translational motion errors in the across-track direction and the elevation direction are within ± 4 m. All the motion errors mentioned above vary frequently. The translational motion error in the track direction is, nonetheless, quite different due to the enormous inertia of the plane. It is hardly time-varying but

accumulative. Hence, the added translational motion error in the track direction is around 20 m and changes slowly.

After range compression and migration correction, the echo data are processed separately by the proposed JMC-MOCO method and the conventional SC-MOCO method.

For the center APC, the Doppler rate estimation errors (defined as Estimation error = ((Estimated value - Real value)/Real value) \times 100%) of these two methods are shown in Figure 6. As can be seen from Figure 5, the Doppler rate estimation errors of the proposed method are small and less undulate, which means that the proposed method has significant improvement in estimation accuracy. Figure 6 shows the estimation results and the real value of the Doppler rate coefficients A and B . Figures 5 and 6 prove that the proposed method is of high accuracy.

5.2. MIMO SAR 3D Imaging Simulation. Now we apply our method to simulated MIMO SAR 3D imaging and compare the imaging results with the conventional method. In the simulation, a complex 3D model containing 5 tall “buildings”

is constructed with 1020 points. The structure of the model is illustrated in Figure 7. The simulated linear MIMO array contains 512 equivalent APCs with spacing of $\lambda/2$, where λ is the wavelength. The motion errors in Figure 4 are imported into the simulation. The parameters in Table 1 are adopted.

After MOCO with the conventional method and the proposed JMC-MOCO method, the 3D imaging results are shown in Figures 8(a) and 8(b), respectively. Only the points whose energy is stronger than -10 dB of the strongest points are pointed in Figure 8 in different colors according to their energy. As we can see, the 5 “buildings” in Figure 8(b) are finely focused, while, in Figure 8(a), there are some unexpected false points, as marked in circles. This is because the respective estimation and compensation of each channel break the incoherence. This problem is well fixed in the proposed JMC-MOCO method. The subscene marked in a box in Figure 8 is magnified in Figure 9 for better comparison. As can be seen, the 3D model is better focused with the proposed method. Hence, the proposed MOCO method can significantly improve the imaging quality.

6. Conclusions

This paper proposed a JMC-MOCO method to estimate and compensate both the translational motion errors and the rotational motion errors for the MIMO SAR 3D imaging. Instead of estimating and compensating motion errors channel by channel, the proposed MOCO method utilizes the linear properties of the linear MIMO array, combining all the channel data to improve the accuracy of motion error estimation. It is demonstrated through 3D scenario imaging simulation that this new method can significantly improve the image quality.

Conflict of Interests

The authors declare that there is no conflict of interests regarding the publication of this paper.

References

- [1] X. Zhuge and A. G. Yarovoy, “A sparse aperture MIMO-SAR-based UWB imaging system for concealed weapon detection,” *IEEE Transactions on Geoscience and Remote Sensing*, vol. 49, no. 1, pp. 509–518, 2011.
- [2] Y. Yang and R. S. Blum, “MIMO radar waveform design based on mutual information and minimum mean-square error estimation,” *IEEE Transactions on Aerospace and Electronic Systems*, vol. 43, no. 1, pp. 330–343, 2007.
- [3] W. Q. Wang, “Virtual antenna array analysis for MIMO synthetic aperture radars,” *International Journal of Antennas and Propagation*, vol. 2012, Article ID 587276, 10 pages, 2012.
- [4] J. H. G. Ender and J. Klare, “System architectures and algorithms for radar imaging by MIMO-SAR,” in *Proceedings of the IEEE Radar Conference (RADAR '09)*, pp. 1–6, Pasadena, Calif, USA, May 2009.
- [5] W. Wang, “MIMO SAR imaging: Potential and challenges,” *IEEE Aerospace and Electronic Systems Magazine*, vol. 28, no. 8, pp. 18–23, 2013.
- [6] X. Wencheng, Z. Xiaoling, and S. Jun, “MIMO antenna array design for airborne down-looking 3D imaging SAR,” in *Proceedings of the 2nd International Conference on Signal Processing Systems (ICSPS '10)*, pp. V2452–V2456, Dalian, China, July 2010.
- [7] W. Wang, “Space-time coding MIMO-OFDM SAR for high-resolution imaging,” *IEEE Transactions on Geoscience and Remote Sensing*, vol. 49, no. 8, pp. 3094–3104, 2011.
- [8] G. Krieger, M. Younis, S. Huber et al., “MIMO-SAR and the orthogonality confusion,” in *Proceeding of the 32nd IEEE International Geoscience and Remote Sensing Symposium (IGARSS '12)*, pp. 1533–1536, Munich, Germany, July 2012.
- [9] Z. B. Wu, Y. T. Zhu, and Y. Su, “Spectral domain filling and 3D SAR imaging of airborne MIMO array,” in *Proceedings of the IEEE Region 10 Conference (TENCON '13)*, pp. 1–4, Xi'an, China, October 2013.
- [10] A. Moreira and Y. Huang, “Airborne SAR processing of highly squinted data using a chirp scaling approach with integrated motion compensation,” *IEEE Transactions on Geoscience and Remote Sensing*, vol. 32, no. 5, pp. 1029–1040, 1994.
- [11] P. Prats, K. A. C. De Macedo, A. Reigber, R. Scheiber, and J. J. Mallorqui, “Comparison of topography- and aperture-dependent motion compensation algorithms for airborne SAR,” *IEEE Geoscience and Remote Sensing Letters*, vol. 4, no. 3, pp. 349–353, 2007.
- [12] J. C. Kirk Jr., “Motion compensation for synthetic aperture radar,” *IEEE Transactions on Aerospace and Electronic Systems*, no. 3, pp. 338–348, 1975.
- [13] W. Ye and T. S. Yeo, “Weighted least-squares estimation of phase errors for SAR/ISAR autofocus,” *IEEE Transactions on Geoscience and Remote Sensing*, vol. 37, no. 5, pp. 2487–2494, 1999.
- [14] G. A. Bendor and T. W. Gedra, “Single-pass fine-resolution SAR autofocus,” in *Proceedings of the IEEE National Aerospace and Electronics Conference (NAECON '83)*, pp. 482–488, Dayton, Ohio, USA, May 1983.
- [15] X. M. Peng, Y. P. Wang, W. X. Tan, W. Hong, and Y. Wu, “Downward looking 3D SAR based on uniform virtual phase centre restricted symmetrical distributed thinned array,” in *Proceedings of the 6th International Conference on Radar (RADAR '11)*, pp. 380–383, Chengdu, China, October 2011.
- [16] J. Klare, “A new airborne radar for 3D imaging—simulation study of ARTINO,” in *Proceedings of the 6th European Conference on Synthetic Aperture Radar (EUSAR '06)*, Dresden, Germany, May 2006.
- [17] J. Klare, A. Brenner, and J. Ender, “A new airborne radar for 3D imaging—image formation using the ARTINO principle,” in *Proceedings of the 6th European Conference on Synthetic Aperture Radar (EUSAR '06)*, Dresden, Germany, May 2006.
- [18] C. E. Mancill and J. M. Swiger, “A map drift autofocus technique for correcting higher order SAR phase errors,” in *Proceedings of the 27th Annual Tri-Service Radar Symposium Record*, pp. 523–525, 1981.
- [19] P. Samczynski and K. S. Kulpa, “Coherent mapdrift technique,” *IEEE Transactions on Geoscience and Remote Sensing*, vol. 48, no. 3, pp. 1505–1517, 2010.

Research Article

Joint Two-Dimensional Ambiguity Resolving Based on Space-Time Filtering for MIMO-SAR

Ping-ping Huang,¹ Hua-sheng Li,¹ Sheng Zhang,² and Guang-Cai Sun²

¹ College of Information Engineering, Inner Mongolia University of Technology, Hohhot 010051, China

² The National Key Laboratory of Radar Signal Processing, Xidian University, Xi'an 710071, China

Correspondence should be addressed to Ping-ping Huang; cimhwangpp@163.com

Received 16 March 2014; Revised 17 June 2014; Accepted 1 July 2014; Published 12 August 2014

Academic Editor: Shengqi Zhu

Copyright © 2014 Ping-ping Huang et al. This is an open access article distributed under the Creative Commons Attribution License, which permits unrestricted use, distribution, and reproduction in any medium, provided the original work is properly cited.

In order to resolve the range and azimuth ambiguity in MIMO-SAR imaging, this paper proposed a joint two-dimensional ambiguity resolving method based on space-time filtering, which according to the ambiguity in different subscene is relative to different nearest echo range, and different azimuth time is relative to different instantaneous incidence angle, to make two-dimensional space-time steering vector for resolving ambiguity of the echo, which also can finish the imaging processing at the same time. Simulation results validate the proposed processing approach for the MIMO-SAR system.

1. Introduction

Multiple-input and multiple-output spaceborne synthetic aperture radar (MIMO-SAR), as a high resolution and wide swath microwave remote sense system [1–5], is proved to be an extremely useful surveillance tool for moving target indication, wide swath imaging, and three-dimensional imaging.

ScanSAR also can obtain wide unambiguous swath coverage at the cost of a degraded azimuth resolution [6]. Multichannel line arrays can be arranged by range or azimuth [7], for the range multichannel can obtain wide swath coverage, utilizing digital beamforming to resolve range ambiguity, but there is still blind zone [8, 9]. With the emergence of techniques such as displaced phase center [10] and multiple aperture reconstruction [11, 12], a number of displaced azimuth subapertures are used to receive echoes in one pulse repetition interval (PRI), thereby increasing the effective azimuth sampling rate without changing the pulse repetition frequency (PRF). In this way, one can lower the requirement on PRF to achieve wider swath imaging without impairing azimuth resolution; in other words, one can broaden the Doppler spectrum to obtain finer azimuth resolution without reducing the swath coverage.

To obtain wide swath coverage and high resolution, one can utilize two-dimensional array to transmit and receive

SAR signals and then resolve the range and azimuth ambiguity [13]. However, this method makes range point target downlooking angle as range steer vector in approximate treatment and does not consider the changing of the downlooking angle with the azimuth time.

In this paper, a joint two-dimensional ambiguity resolving method for MIMO-SAR is proposed, which uses deferent targets relative to deferent range as steer vector which is independent of the downlooking angle. Firstly, the azimuth ambiguity is resolved. Then, the range ambiguity resolving and azimuth match filtering are performed instantaneously to get target image, which makes the imaging algorithms simpler.

This paper is organized as follows. Section 2 reviews the signal model of MIMO-SAR. The two-dimensional ambiguity resolving algorithm is analyzed in Section 3. Section 4 gives the simulations and validates the proposed processing approach for the MIMO-SAR system. Finally, Section 5 concludes this paper.

2. MIMO-SAR System Mode and Signal Model

Figure 1 presents the geometry of a multichannel SAR. It supposed that the whole antenna aperture was divided into

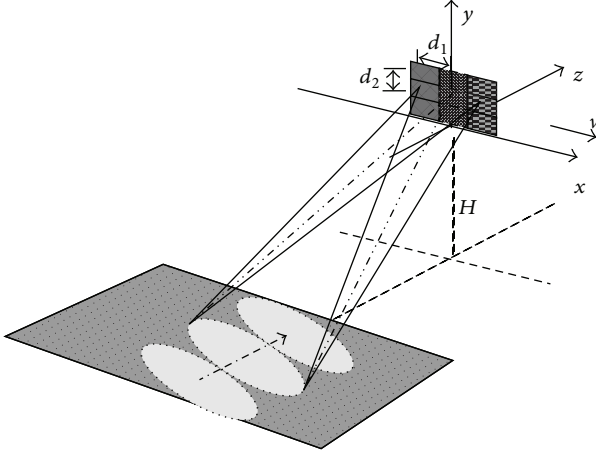


FIGURE 1: MIMO-SAR model.

$P \times Q$ subapertures, where P is the number of azimuth subapertures and its length is d_1 . Q is the number of azimuth subapertures and its height is d_2 . We denoted the p th column and the q th row as $X_p = X_0 + (p-1)d_1$, $p = 1, \dots, P$, with X_0 the azimuth beginning coordinate (X_p, Y_q, Z), and $Y_q = Y_0 + (q-1)d_2$, $q = 1, \dots, Q$, with Y_0 the range beginning coordinate.

Use the subcaptures on the same column range dimension transmit signals at the same time; through adjusting phase weighting to control the wave beam, the center of transmit wave beam is $Y'_q = (Y_q + Y_{q_0})/2$, $Y_{q_0} = Y_0 + d_2(Q-1)/2$, and the whole antenna receives the echo signal. According to the principle of equivalent phase center, this mode can be known as each equivalent phase center transmitting and receiving itself. The equivalent phase centers located at (X'_p, Y'_p, Z) , where $X'_p = (X_0 + X_p)/2$ and $Y'_p = (Y_q + Y_{q_0})/2$. The deferent range subapertures light the deferent subswaths from far to nearby adjusting phase weightings. The ellipses in Figure 1 are the subswaths.

Assume that, during the L th pulse period, the first range dimension subapertures transmit signal in the same time and make the wave beam light the L th subswath through controlling phase weighting. The transmitting signal can be expressed as follows:

$$s(t_k) = \frac{\sin(\pi Q d_2 (\sin \theta_l - \sin \theta) / 2\lambda)}{\sin(\pi d_2 (\sin \theta_l - \sin \theta) / 2\lambda)} \times \text{rect}\left(\frac{(t_k - \Delta T)}{T_{p_l}}\right) \times \exp\left(j2\pi f_c (t - \Delta T_l) + j\pi\gamma(t_k - \Delta T_l)^2\right), \quad (1)$$

where θ_l is the downlooking angle of the center line of l th subswath, f_c is the carrier frequency, $\lambda = c/f_c$ is the wavelength, $\Delta T_l = T_{p_1} + \dots + T_{p_{l-1}}$ is the delay time of the l th subpulse, $t = t_k + mT_r$ is the whole time, t_k is the fast time, m is a integer, T_r is pulse repetition interval, and γ is the chirp rate.

The baseband signal received by the p th row and the q th column subaperture was

$$s_{pq}(t_k, t_m) = \sum_{l=1}^L A(\theta_l) \text{rect}\left(\frac{(t_k - \Delta T_l - 2R_{pq,l}(t_m)/c)}{T_{p_l}}\right) \times \text{rect}\left(\frac{(X'_p + x - x_l)}{L_a}\right) \times \exp\left(j2\pi f_c \left(-\Delta T_l - \frac{2R_{pq,l}(t_m)}{c}\right)\right) \times \exp\left(j\pi\gamma \left(t_k - \Delta T_l - \frac{2R_{pq,l}(t_m)}{c}\right)^2\right), \quad (2)$$

where $A(\theta_l) = \sin(\pi Q d_2 (\sin \theta_l - \sin \theta) / 2\lambda) / \sin(\pi d_2 (\sin \theta_l - \sin \theta) / 2\lambda)$, $t_m = kT_r$ is slow time, k is a integer, and the value scope of l is from 1 to L , corresponding to the swath from far to near. $x = vt_m$, v is the flat velocity, and L_a is the length of synthetic aperture. $R_{pq,l}(t_m) = \sqrt{(X'_p + vt_m - x_l)^2 + (Y'_p - y_l)^2 + H^2}$ is the instantaneous slant range, (x_l, y_l, z_l) is the coordinates of one scatter point in the L th scene, and $H = Z_0 - z_l$. Assume that scene is plane, $z_l = 0$.

Performing the range match filtering to (2), we can gain

$$s_{pq}(t_k, t_m) \approx \sum_{l=1}^L A'(\theta_l) \sin c\left(t_k - \Delta T_l - \frac{2R_l(t_m)}{c}\right) \times \text{rect}\left(\frac{X'_p + x - x_l}{L_a}\right) \exp\left(-j\frac{4\pi}{\lambda} R_{pq,l}(t_m)\right), \quad (3)$$

where $A'(\theta_l) = A(\theta_l) \exp(-j2\pi f_c \Delta T_l)$, $R_l(t_m) = \sqrt{(X_0 + vt_m - x_l)^2 + (Y_0 - y_l)^2 + H^2}$ is the instantaneous distance from the scatter point on the l th subswath to (X_0, Y_0, Z_0) .

As we know, the MIMO-SAR can be considered as a space signal sampling which should satisfy the sampling equation as follows:

$$d \leq \frac{\lambda}{2}, \quad (4)$$

where d denotes the position change of antenna element and λ denotes the wavelength of the signal.

So the time delay should be

$$T_d = \frac{d}{c} \leq \frac{\lambda}{2c} = \frac{1}{2f_c}, \quad (5)$$

where f_c denotes the carrier frequency.

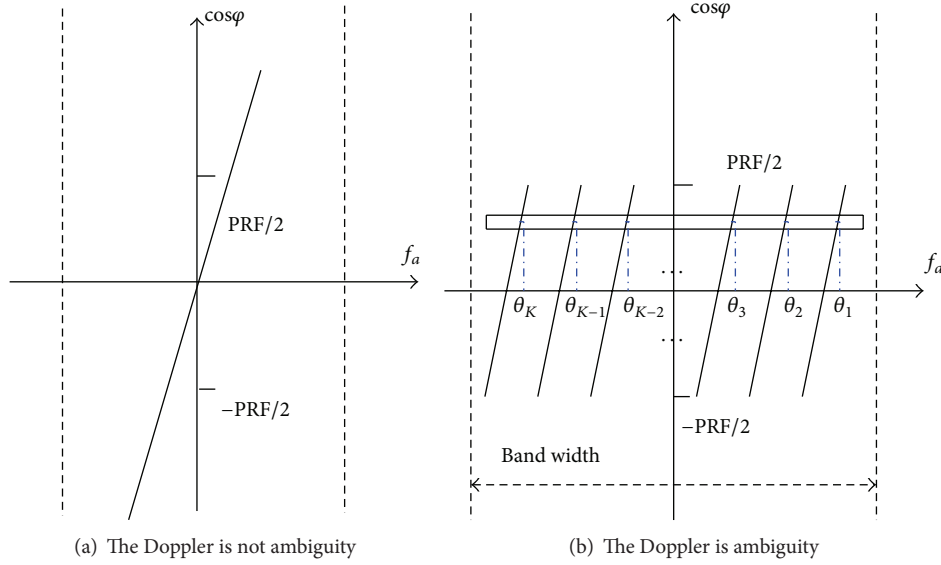


FIGURE 2: The relationship between cosine of cone angle and Doppler.

And the time resolution can be calculated by

$$T_r = \frac{1}{2B}, \quad (6)$$

where B denotes the bandwidth.

In a narrow band system f_c is much larger than B , so we can get T_d much smaller than T_r , which means that the time delay made by the position change of antenna element is very small compared with the time resolution.

The time delay made by the position change of antenna element can be ignored, which is reasonable because the distance between the elements is very small.

This system uses low PRF to get wide swath, but the low PRF can cause azimuth Doppler ambiguity; Figure 2 illuminates this.

After azimuth fast Fourier transforms (FFT), we can gain the Doppler ambiguity signal $s_{pq}(t_k, f_a)$:

$$\begin{aligned} s_{pq}(t_k, f_a) = & \sum_{l=1}^L \sum_{k=1}^K A'(\theta_l) \sin c \left(t_k - \Delta T_l - \frac{2R_l(f_a)}{c} \right) \\ & \times \text{rect} \left(\frac{f_a R_{B1}}{\sqrt{f_{am}^2 - f_a^2}} \right) \exp \left(-j \frac{2\pi f_a x_l}{v} \right) \\ & \times \exp \left(-j \frac{2\pi R_{Bq}}{v} \sqrt{f_{am}^2 - f_a^2} \right) \\ & \times \exp \left(j \frac{4\pi X'_p \cos \varphi_k(f_a)}{\lambda} \right), \end{aligned} \quad (7)$$

where $f_a \in (-\text{PRF}/2, \text{PRF}/2)$, $R_{Bq} = \sqrt{(Y_q - y_1)^2 + H^2}$ is the vertical distance from scatter point (x_1, y_1, z_1) to flight track,

$R_{pq,1}(f_a)$ is the instantaneous distance of scatter point, φ_k is the angle of instantaneous slant distance and flight track, and $\cos \varphi_k(f_a) = f_a / f_{am}$, $f_{am} = 2v/\lambda$.

When $R_1 = cT_{p1}/2 + R_2 = \dots = c(T_{p1} + \dots + T_{pL-1})/2 + R_L$ is satisfied, L different scatter points on L subswaths can make aliasing and then cause range ambiguity. But the different scatter points are corresponding to different downlooking angles, as shown in Figure 3.

According to the forgoing analysis, if the scatter instantaneous slant distance satisfies the preceding equation, (7) can be shown as

$$\begin{aligned} s_{pq}(t_k, f_a) = & \sum_{l=1}^L \sum_{k=1}^K A'(\theta_l) \sin c \left(t_k - \frac{2R_l}{c} \right) \\ & \times \text{rect} \left(\frac{f_a R_{B1}}{\sqrt{f_{am}^2 - f_a^2}} \right) \exp \left(-j \frac{2\pi f_a x_l}{v} \right) \\ & \times \exp \left(-j \frac{2\pi R_{Bq}}{v} \sqrt{f_{am}^2 - f_a^2} \right) \\ & \times \exp \left(-j \frac{4\pi X'_p \cos \varphi_k(f_a)}{\lambda} \right), \end{aligned} \quad (8)$$

where $\exp(-j(2\pi R_{Bq}/v)\sqrt{f_{am}^2 - f_a^2})$ and $\exp(j(4\pi X'_p \cos \varphi_k(f_a)/\lambda))$ are caused by the position of azimuth and range subapertures, and they are the steer vector for resolving ambiguity. One can know that there is the azimuth frequency in the range steer vector, so one needs to resolve the azimuth ambiguity firstly and then resolve the range ambiguity.

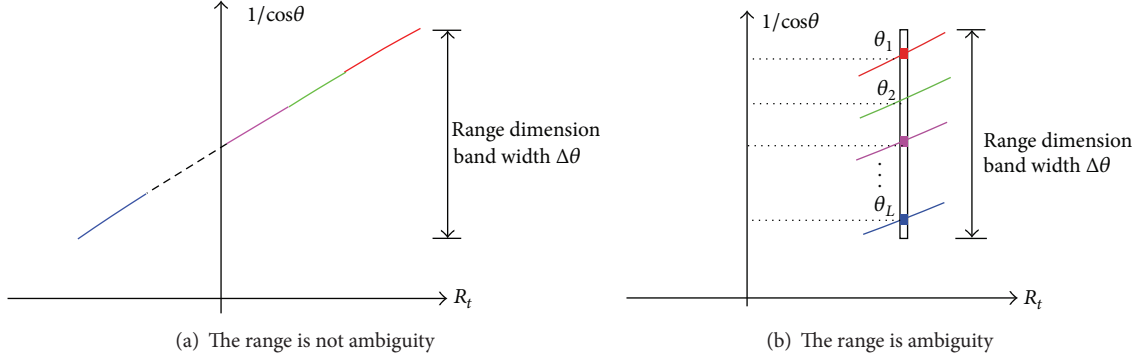


FIGURE 3: The relationship between downlooking angle and instantaneous slant distance.

3. Two-Dimensional Ambiguity Resolving

3.1. Resolving Azimuth Ambiguity. Because (8) is range and Doppler ambiguity signal, we express the matrix vector $\mathbf{z}_a(\varphi_k)$ as

$$\mathbf{z}_a(\varphi_k) = \left[\exp\left(\frac{j4\pi X'_1 \cos \varphi_k}{\lambda}\right), \dots, \exp\left(\frac{j4\pi X'_P \cos \varphi_k}{\lambda}\right) \right]^T. \quad (9)$$

In this paper, we use joint 2-dimensional method to resolve ambiguity based on static weighting vector. It is assumed that the vector matrix is $\mathbf{W}_{P \times K}$ and the n th column weighting vector is shown as

$$\mathbf{W}_n = [w_{1,n}, \dots, w_{P,n}, \dots, w_{P,n}]^T. \quad (10)$$

It means that the corresponding downlooking angle and azimuth angle position is 1 and other ambiguities are zero. Consider

$$\mathbf{W}_n^H \mathbf{z}_a = \mathbf{H}_n, \quad (11)$$

where $()^H$ expresses matrix conjugate transpose operator and $\mathbf{H}_n = [h_{1n}, \dots, h_{Kn}]^T$, $n = 1, \dots, K$, when $k = n$, $h_{kn} = 1$. Consider

$$\mathbf{W}_n = (\mathbf{H}_n \mathbf{z}_a^+)^H, \quad (12)$$

where $()^+$ denotes the pseudoinverse operation, $\mathbf{z}_a^+ = \text{pinv}(\mathbf{z}_a)$. Consider

$$\begin{aligned} \mathbf{S} &= [s_{11}, \dots, s_{P1}, s_{12}, \dots, s_{P2}, \dots, s_{1Q}, \dots, s_{PQ}]^T \\ &= \text{sinc}\left(t_k - \frac{2R_1}{c}\right) \text{rect}\left(\frac{f_a R_{B1}}{\sqrt{f_{am}^2 - f_a^2}}\right) \exp\left(-j \frac{2\pi f_a x_l}{v}\right) \\ &\quad \times \exp\left(-j \frac{2\pi R_{Bq} \sqrt{f_{am}^2 - f_a^2}}{v}\right) \mathbf{z}_a. \end{aligned} \quad (13)$$

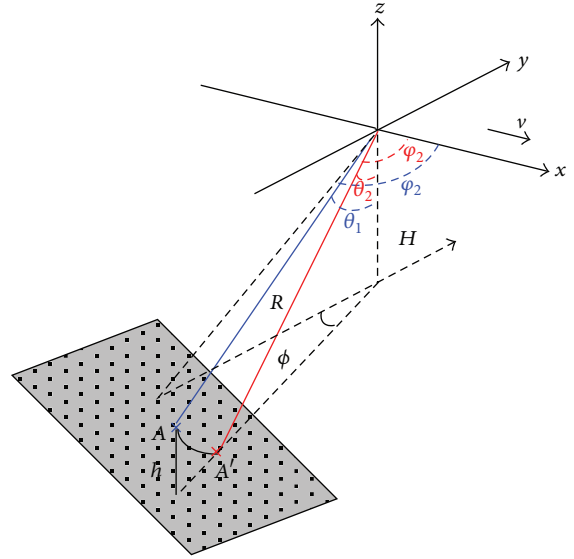
Using the weighting vector to resolve ambiguity, the following is gained:

$$\begin{aligned} \mathbf{S}' &= \mathbf{W}_n^H \mathbf{S} = \text{sinc}\left(t_k - \frac{2R_1}{c}\right) \\ &\quad \times \text{rect}\left(\frac{f_a R_{B1}}{\sqrt{f_{am}^2 - f_a^2}}\right) \exp\left(-j \frac{2\pi f_a x_l}{v}\right) \\ &\quad \times \exp\left(-j \frac{2\pi R_{Bq} \sqrt{f_{am}^2 - f_a^2}}{v}\right) \mathbf{W}_n^H \mathbf{z}_a \\ &= \text{sinc}\left(t_k - \frac{2R_1}{c}\right) \text{rect}\left(\frac{f_a R_{B1}}{\sqrt{f_{am}^2 - f_a^2}}\right) \\ &\quad \times \exp\left(-j \frac{2\pi f_a x_l}{v}\right) \\ &\quad \times \exp\left(-j \frac{2\pi R_{Bq} \sqrt{f_{am}^2 - f_a^2}}{v}\right) \mathbf{H}_n. \end{aligned} \quad (14)$$

After this, the resolving azimuth ambiguity operation is finished.

According to array signal theory, the Doppler ambiguity time K must satisfy the following formula: $K \leq P$. To the member of azimuth subaperture P , it can make one restriction direction at most and the other $P - 1$ is zero, so only P time's ambiguity can be resolved on azimuth Doppler dimension. With the same principle, only Q time ambiguity can be resolved on azimuth Doppler dimension.

After resolving the azimuth ambiguity, the signal is combined according to the Doppler spectrum. The range resolving ambiguity is followed.

$$\mathbf{z}_a(R_l) = \left[\exp\left(-j \frac{2\pi R_{B1} \sqrt{f_{am}^2 - f_a^2}}{\nu}\right), \dots, \exp\left(-j \frac{2\pi R_{BQ} \sqrt{f_{am}^2 - f_a^2}}{\nu}\right) \right]^T. \quad (15)$$
$$\mathbf{W}_m = [w_{1,m}, \dots, w_{q,m}, \dots, w_{Q,m}]^T. \quad (16)$$
$$\mathbf{W}_m^H \mathbf{z}_b = \mathbf{H}_m, \quad (17)$$
$$\mathbf{W}_m = (\mathbf{H}_m \mathbf{z}_b^+)^H, \quad (18)$$
$$\begin{aligned} \mathbf{S}' &= [s_1, \dots, s_Q]^T \\ &= \text{sinc}\left(t_k - \frac{2R_1}{c}\right) \text{rect}\left(\frac{f_a R_{B1}}{\sqrt{f_{am}^2 - f_a^2}}\right) \exp\left(-j \frac{2\pi f_a x_l}{v}\right) \\ &\quad \times \exp\left(-j \frac{2\pi R_{Bq} \sqrt{f_{am}^2 - f_a^2}}{v}\right) z_b. \end{aligned} \quad (19)$$

$$\begin{aligned} \mathbf{S}'' &= \mathbf{W}_m^H \mathbf{S}' = \text{sinc}\left(t_k - \frac{2R_1}{c}\right) \\ &\quad \times \text{rect}\left(\frac{f_a R_{Bq}}{\sqrt{f_{am}^2 - f_a^2}}\right) \exp\left(-j \frac{2\pi f_a x_l}{v}\right) \\ &\quad \times \exp\left(-j \frac{2\pi R_{Bq} \sqrt{f_{am}^2 - f_a^2}}{v}\right) \mathbf{W}_m^H \mathbf{z}_b \\ &= \text{sinc}\left(t_k - \frac{2R_1}{c}\right) \text{rect}\left(\frac{f_a R_{Bq}}{\sqrt{f_{am}^2 - f_a^2}}\right) \\ &\quad \times \exp\left(-j \frac{2\pi f_a x_l}{v}\right). \end{aligned} \quad (20)$$

3.3. Impact of Terrain Height Variance. Forenamed static weighting vector is based on the assumption that the terrain is flat. Here we can analyze the impact of terrain height variance on the weighting vector.

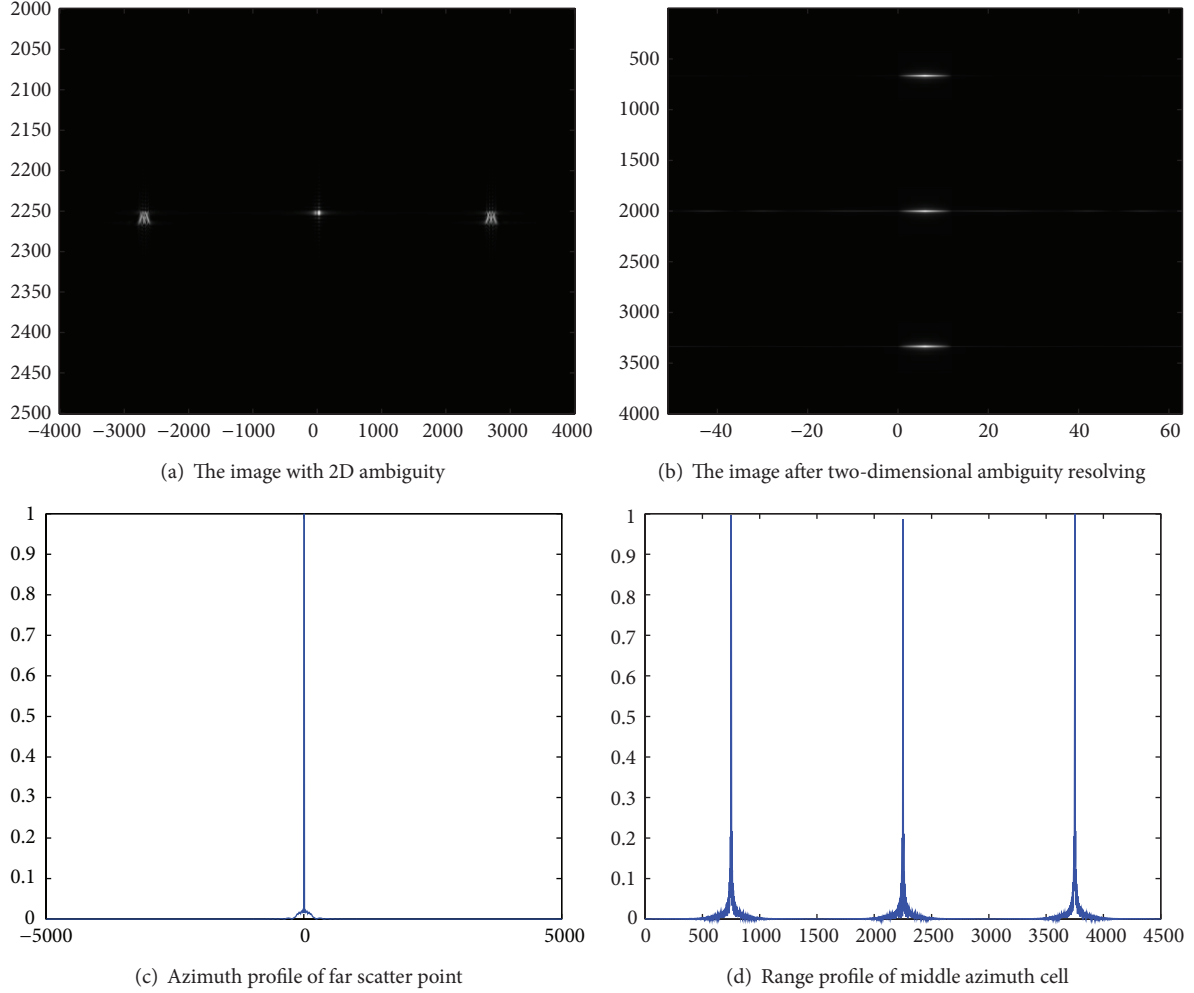


FIGURE 5: The image of joint two-dimensional processing.

As shown in Figure 4, there is a point A with the downlooking angle θ_1 and azimuth angle φ_1 ; we assume there is another point A' with a height difference h between A , so the phase difference of the weighting vector pointing to A and A' is

$$\Delta\Phi = \frac{2\pi d_1 (\cos \varphi_1 - \cos \varphi_2)}{\lambda} - \frac{2\pi d_2 (\sin \theta_1 - \sin \theta_2)}{\lambda}, \quad (21)$$

where θ_2, φ_2 are the downlooking angle and azimuth angle in the position of A' . From the geometry configuration of Figure 4, we can get that $\cos \varphi_1 = \sin \theta_1 \sin \phi$ and $\cos \varphi_2 = \sin \theta_2 \sin \phi$, so the phase difference can be written as

$$\begin{aligned} \Delta\Phi &= \frac{2\pi (\sin \theta_1 - \sin \theta_2) (d_1 \sin \phi - d_2)}{\lambda} \\ &= \frac{2\pi (d_1 \sin \phi - d_2) \left(\sqrt{R^2 - (H-h)^2} - \sqrt{R^2 - H^2} \right)}{\lambda R}. \end{aligned} \quad (22)$$

TABLE 1: Phase difference in the terrain with different height.

Height h (m)	Phase difference $\Delta\Phi$ (rad)	Remained clutter (dB)	Performance
352	$-\pi/32$	-20.2	Effective
940	$-\pi/12$	-11.7	Worse
1408	$-\pi/8$	-8.2	Much worse
3735	$-\pi/3$	0	Ineffective

The clutter which remained caused by the phase difference is

$$20 \log_{10} [1 - \exp(j\Delta\Phi)]. \quad (23)$$

With the simulating parameter of $H = 700$ km, $R = 880$ km, $\lambda = 0.03$ m, $d_1 = 1$ m, and $d_2 = 0.8$ m, we get that the simulation result of the clutter which remained varied with the height difference shown in Table 1.

From Table 1 we can see that if the change of terrain height is below 1 km, our proposed method can still be effective.

TABLE 2: Simulation parameters.

Parameters	Value
Height of satellite H (km)	700
Satellite velocity v (m/s)	7200
Carrier frequency f_c (GHz)	2
System PRF (Hz)	1200
Stepped-frequency signal band width B (MHz)	100
Transmitted pulse width T_Δ (μ s)	30
Azimuth subaperture length d_1 (m)	4
Elevation subaperture height d_2 (m)	0.8
Coordinates of the three scatter points (m)	(0, 42783.1, 0) (0, 36703.5, 0) (0, 39831.0, 0)

4. Simulation Experiment

To validate the proposed approach, a simulation experiment on point targets is carried out. The main system parameters are listed in Table 2. In this simulation, the whole antenna aperture was divided into 3×3 subapertures.

It is supposed that these scatter points have the same backscattering coefficient. Through calculation one can get $R_1 = cT_\Delta/2 + R_2 = cT_\Delta + R_3$, so the three scatter points are range-ambiguous with each other. The Doppler band width is $B_a = 2v/D = 3600$ Hz and the azimuth sample frequency is 1200 Hz, which makes the azimuth Doppler spectrum ambiguous with three times. Figure 5(a) shows the image of an original single channel. The azimuth and the range both have ambiguity. Range ambiguity makes three scatter points with different range positions mixed together, so only one point can be seen in Figure 5(a); because the system Doppler ambiguity three times, three focused points can be seen along azimuth. Both sides were ambiguity points and their energy was smaller than the center point obviously. Through the joint two-dimensional ambiguity resolving method proposed in this paper, the unambiguity image can be obtained as shown in Figure 5(b). After two-dimensional ambiguity resolving, the scatter points were located in their real positions. Figure 5(c) is azimuth profile of the far scatter point. In the figure, the standard sinc function was obtained after the azimuth pulse compressed, which shows the unambiguous Doppler spectrum was recovered by the joint two-dimensional processing. Figure 5(d) is range profile of the three range points. From the figure, one can note that the range ambiguity is also resolved.

5. Conclusion

In this paper, a novel joint two-dimensional ambiguity resolving method based on space-time filtering was proposed, which can resolve the range and azimuth ambiguity of MIMO-SAR for high-resolution and wide swath imaging. This method does not use any approximate operation, which can finish resolving ambiguity and two dimensions focused instantaneously. Imaging results of the simulated point target validate the proposed approach. Because this method does

not depend on SAR system work mode, it has certain general use.

Conflict of Interests

The authors declare that there is no conflict of interests regarding the publication of this paper.

Acknowledgments

This work was supported by the National Natural Science Foundation of China under Grant 61201433 and supported by Program for Young Talents of Science and Technology in Universities of Inner Mongolia Autonomous Region (NJYT-14-B09).

References

- [1] G. Krieger, N. Gebert, M. Younis, and A. Moreira, "Advanced synthetic aperture radar based on digital beamforming and waveform diversity," in *Proceedings of the IEEE Radar Conference (RADAR '08)*, pp. 767–772, Rome, Italy, May 2008.
- [2] A. Ossowska, J. H. Kim, and W. Wiesbeck, "Modeling of nonidealities in receiver front-end for a simulation of multistatic SAR system," in *Proceedings of the 4th European Radar Conference (EURAD '07)*, pp. 13–16, Munich, Germany, October 2007.
- [3] G. Krieger, N. Gebert, and A. Moreira, "Multidimensional waveform encoding: a new digital beamforming technique for synthetic aperture radar remote sensing," *IEEE Transactions on Geoscience and Remote Sensing*, vol. 46, no. 1, pp. 31–46, 2008.
- [4] W. Q. Wang, "Space-time coding MIMO-OFDM SAR for high-resolution imaging," *IEEE Transactions on Geoscience and Remote Sensing*, vol. 49, no. 8, pp. 3094–3104, 2011.
- [5] W. Wang, "Mitigating range ambiguities in high PRF SAR with OFDM waveform diversity," *IEEE Geoscience and Remote Sensing Letters*, vol. 10, no. 1, pp. 101–105, 2013.
- [6] P. Huang and W. Xu, "A new spaceborne burst synthetic aperture radar imaging mode for wide swath coverage," *Remote Sensing*, vol. 6, no. 1, pp. 801–814, 2014.
- [7] P. Huang, S. Li, and W. Xu, "Investigation on full-aperture on multichannel azimuth data processing in TOPS," *IEEE Geoscience and Remote Sensing Letters*, vol. 4, no. 11, pp. 728–732, 2014.
- [8] G. D. Callaghan and I. D. Longstaff, "Wide-swath space-borne SAR and range ambiguity," in *Proceedings of the IEEE Radar Conference*, pp. 248–252, Edinburgh, Scotland, October 1997.
- [9] G. D. Callaghan and I. D. Longstaff, "Wide-swath space-borne SAR using a quad-element array," *IEE Proceedings: Radar, Sonar and Navigation*, vol. 146, no. 3, pp. 159–165, 1999.
- [10] G. Krieger, N. Gebert, and A. Moreira, "Unambiguous SAR signal reconstruction from nonuniform displaced phase center sampling," *IEEE Geoscience and Remote Sensing Letters*, vol. 1, no. 4, pp. 260–264, 2004.
- [11] G. Krieger, N. Gebert, and A. Moreira, "SAR signal reconstruction from non-uniform displaced phase centre sampling," in *Proceedings of the IEEE International Geoscience and Remote Sensing Symposium Proceedings: Science for Society: Exploring and Managing a Changing Planet (IGARSS '04)*, vol. 3, pp. 1763–1766, Anchorage, AK, USA, September 2004.

- [12] N. Gebert, G. Krieger, and A. Moreira, "SAR signal reconstruction from non-uniform displaced phase centre sampling in the presence of perturbations," in *Proceedings of the IEEE International Geoscience and Remote Sensing Symposium (IGARSS '05)*, pp. 1034–1037, Seoul, Korea, July 2005.
- [13] P. Huang, W. Xu, and W. Qi, "Two dimension digital beam-forming pre processing in multibeam Scansar," *Progress in Electromagnetics Research*, vol. 136, pp. 495–508, 2013.

Research Article

Joint Direction-of-Departure and Direction-of-Arrival Estimation in a UWB MIMO Radar Detecting Targets with Fluctuating Radar Cross Sections

Idnin Pasya,^{1,2} Naohiko Iwakiri,³ and Takehiko Kobayashi¹

¹ Wireless Systems Laboratory, Tokyo Denki University, 5 Senju-Asahi-Cho, Tokyo 120-8551, Japan

² Faculty of Electrical Engineering, Universiti Teknologi MARA, 40450 Shah Alam, Selangor, Malaysia

³ The University of Tokyo, 7-3-1 Hongo, Bunkyo-ku, Tokyo 113-0033, Japan

Correspondence should be addressed to Idnin Pasya; idninpasya@gmail.com

Received 28 February 2014; Revised 28 May 2014; Accepted 1 June 2014; Published 13 July 2014

Academic Editor: Mathini Sellathurai

Copyright © 2014 Idnin Pasya et al. This is an open access article distributed under the Creative Commons Attribution License, which permits unrestricted use, distribution, and reproduction in any medium, provided the original work is properly cited.

This paper presents a joint direction-of-departure (DOD) and direction-of-arrival (DOA) estimation in a multiple-input multiple-output (MIMO) radar utilizing ultra wideband (UWB) signals in detecting targets with fluctuating radar cross sections (RCS). The UWB MIMO radar utilized a combination of two-way MUSIC and majority decision based on angle histograms of estimated DODs and DOAs at each frequency of the UWB signal. The proposed angle estimation scheme was demonstrated to be effective in detecting targets with fluctuating RCS, compared to conventional spectra averaging method used in subband angle estimations. It was found that a wider bandwidth resulted in improved estimation performance. Numerical simulations along with experimental evaluations in a radio anechoic chamber are presented.

1. Introduction

The introduction of multiple-input multiple-output (MIMO) radar enables numerous improvements on the conventional single input single output radar system. The MIMO radar is typically defined as a radar system utilizing multiple transmitting and receiving antennas that are either widely distributed or colocated [1–4]. The former exploits independent path of transmit-receive pairs to increase the probability of detection [1, 2]. On the other hand, the latter uses orthogonality of transmitting signals to obtain an increased degree of freedom and parameter identifiability [3, 4], which are very useful in target localization applications.

Target localization in radar has been intensively studied in literatures since the early years of radar. In general, radar systems estimate the target position by means of trilateration or triangulation. Trilateration can be implemented by using a minimum of two stations; however, the localization resolution is limited by the signal bandwidth, and usage of multiple stations is required to avoid ambiguities (ghost

targets). On the contrary, triangulation is based on the angles of targets observed from the radar stations, and hence it does not suffer from the bandwidth constraint. In MIMO radar, it is possible to jointly estimate the direction-of-departure (DOD) and direction-of-arrival (DOA) by implementing array processing at both of the transmitting and receiving arrays, as depicted in Figure 1. This makes it suitable for triangulation-based localization.

Numerous works on DOD and DOA estimation have been reported [5–8]. Nevertheless, these studies were mainly based on narrowband signal assumption. Target localization using the narrowband signal, however, was unstable due to fluctuation of target's radar cross section (RCS). In order to counter this problem, MIMO radars using multiple subcarriers and orthogonal frequency division multiplexing (OFDM) waveforms were proposed [9, 10]. Those schemes, however, only discussed one-dimensional angle estimation of a single target and implementation of limited number of subbands. Utilization of wider signal bandwidth might be useful in localizing target with significantly small or severely

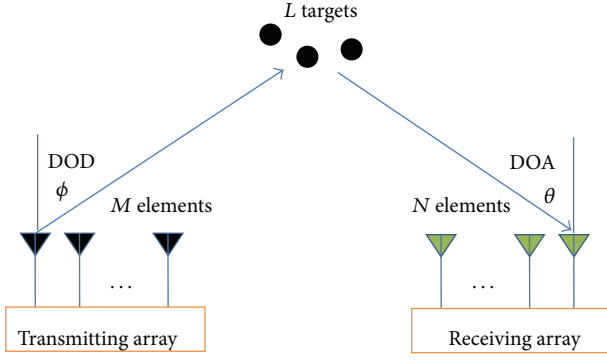


FIGURE 1: Overview of angle estimation in MIMO radar.

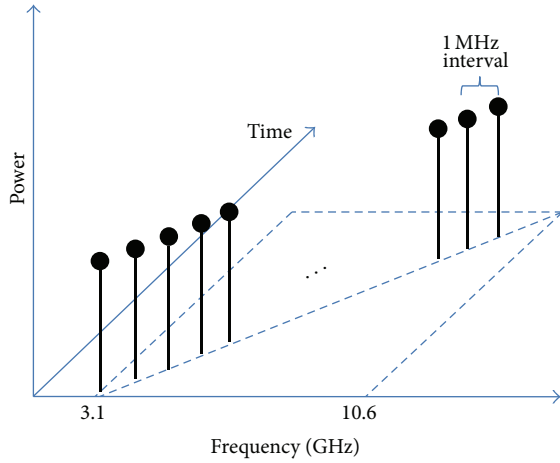


FIGURE 2: The proposed UWB signal for MIMO radar angle estimation.

fluctuating RCS. One of the most promising technologies with wideband capability is ultra wideband (UWB) systems. The usage of UWB signal for angle estimation in MIMO radar, however, has not been given much attention, limiting the study to medical imaging and through-the-wall radars [11, 12]. Application of conventional angle estimation methods (e.g., Capon, multiple signal classification (MUSIC), and estimation of signal parameters via rotational invariance (ESPRIT)) to a UWB signal is a challenge since those methods inherently assume narrowband signals.

The present authors proposed a joint DOD and DOA estimation in a UWB MIMO radar using the combination of a two-way MUSIC and angle histograms [13]. The basic idea in the proposed scheme was to treat the UWB signal as a summation of sinusoidal waves swept over the frequency band, and angle estimation was done at each of the frequency by means of two-way MUSIC [14]. The estimation results were then combined using majority decisions formulated

using angle histograms [15]. However, the report only investigated estimation performance when detecting targets with a constant RCS, which was unlikely in actual environments.

In this paper, we evaluate the performance of the proposed algorithm in detecting targets with fluctuating RCS. Here, it will be shown that combining the estimation at different frequencies through majority decisions will overcome the problem of poor estimation when detecting fluctuating targets. A comparison between the proposed technique and the conventional spectrum averaging is also presented. Numerical simulations and experimental results are presented.

It is important to mention here that the RCS fluctuation problem has been continuously studied in the radar community. Until recently, special attention has been given to the subject in the case of MIMO radar, since the usage of MIMO configuration offers further degrees of freedom in the forms of spatial, frequency, and also waveform diversity. For example, the works in [16–18] employed spatial and waveform diversity in MIMO radars to increase the probability of detection and direction finding performance when detecting fluctuating target. The present study employs different approach from those reports since we focused on the utilization of frequency diversity. Studies regarding MIMO radars utilizing frequency diversity in detecting fluctuating RCS were studied, for instance, in [19, 20], where several subbands with substantially wide frequency spacing were used for angle estimation. This study differs from those works from a point of view that we employ the diversity among a large number of subbands throughout the frequency bandwidth of a UWB system to enhance target localization performance and specifically demonstrated the application to MIMO radar.

The remainder of this paper is organized as follows. The next section discusses the proposed algorithm. Section 3 describes the numerical simulations, and Section 4 explained the results of experimental evaluations. Finally, the concluding remarks are presented in Section 5.

2. Proposed Scheme

2.1. Proposed Joint DOD and DOA Estimation Scheme. Consider a MIMO radar with M transmitting and N receiving elements, illuminating L uncorrelated targets located at the far field of transmit and receive arrays. At the transmit side, M orthogonal UWB signals are emitted, and each consists of multiple sinusoidal waves swept over the UWB bandwidth. Here, we define the complex transmit signal waveform vector by $\mathbf{s}(t) = [\mathbf{s}_1(t), \dots, \mathbf{s}_M(t)]$, where each term contains K frequency components. The orthogonality between the transmit signals can be achieved through time division scheme, where each transmitting antenna emits the UWB signal in separate time slots. Figure 2 illustrates an example of the transmitting signal which uses 3.1 to 10.6 GHz of sinusoidal waves in 1 MHz intervals. The receiving signal of the k th frequency component can be expressed by

$$\mathbf{x}_k(t) = [\mathbf{a}_t(\phi) \otimes \mathbf{a}_r(\theta)] \mathbf{s}^{(k)}(t) + \mathbf{n}(t), \quad (1)$$

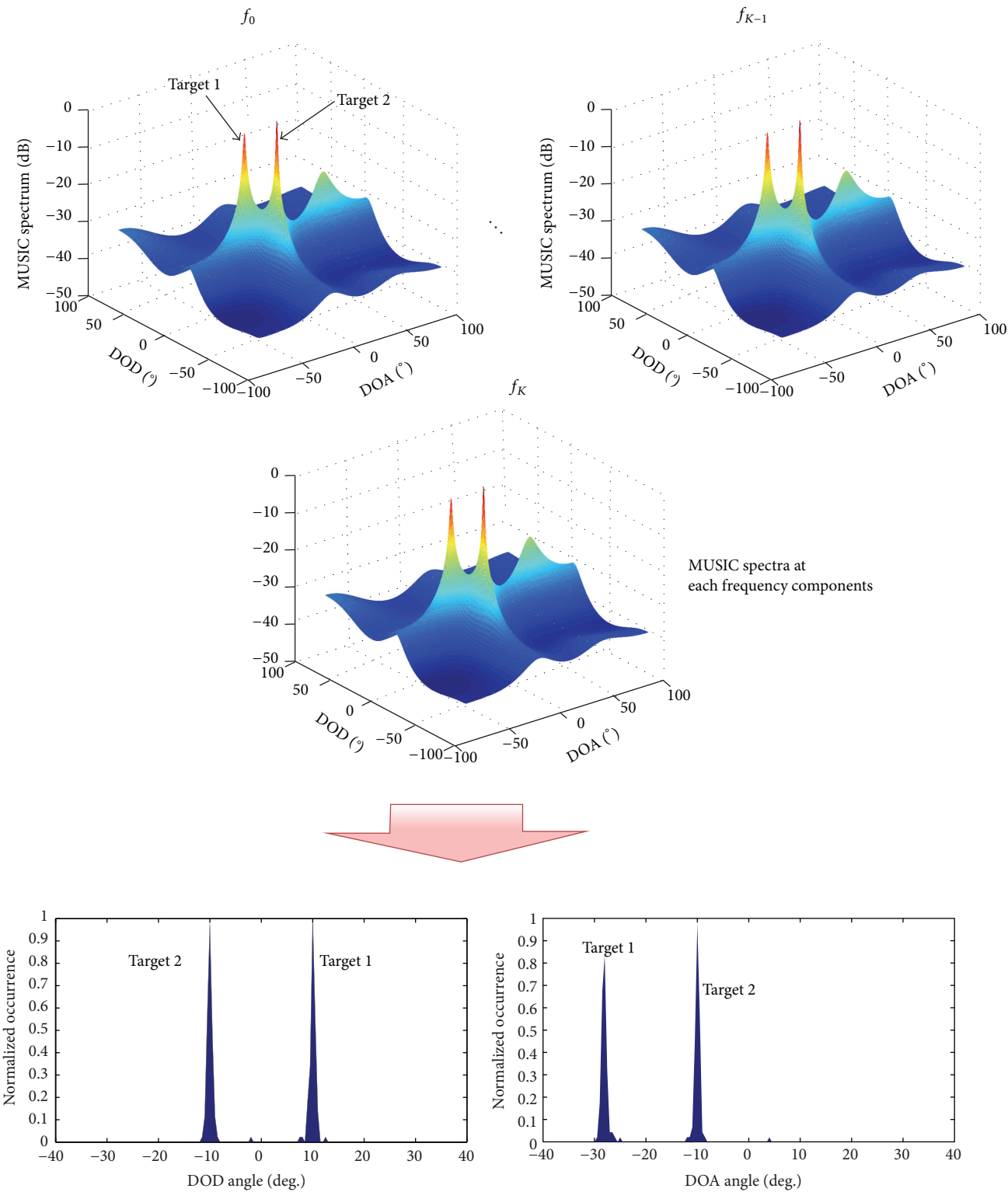


FIGURE 3: Formulation of angle histograms from two-way MUSIC spectra at each frequency component.

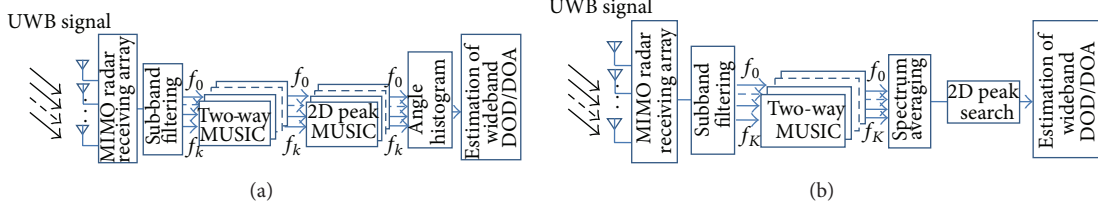
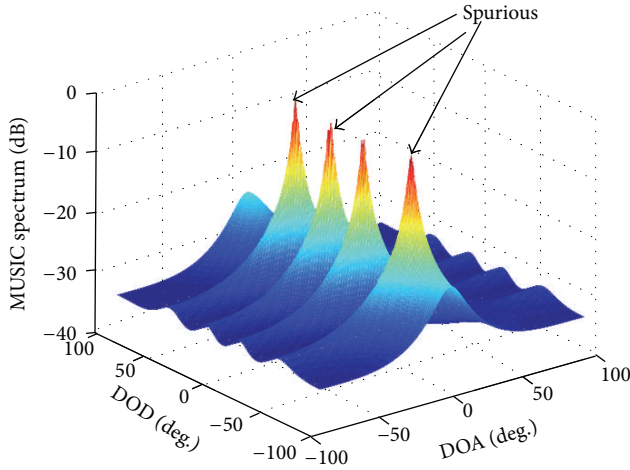


FIGURE 4: Block diagrams: (a) proposed and (b) conventional schemes.

FIGURE 5: Example of spurious peaks in a simulated MUSIC spectrum ($f_k = 5.0$ GHz).

where \otimes denotes the Kronecker product, \mathbf{a}_t and \mathbf{a}_r are the transmit and receive steering vectors, respectively, ϕ and θ are the corresponding transmit and receive angles, $\mathbf{s}^{(k)}(t)$ represents the k th frequency component of the transmit signal vector $\mathbf{s}(t)$, and $\mathbf{n}(t)$ is the total additive white Gaussian noise. The receiving signal covariance matrix of the k th frequency component is given by

$$\mathbf{R}_{xx,k} = E[\mathbf{x}_k(t) \cdot \mathbf{x}_k(t)^H], \quad (2)$$

where $E[\cdot]$ is the ensemble average and $[\cdot]^H$ represents the conjugate transpose operation. Here, singular value decomposition (SVD) of the covariance matrix gives

$$\mathbf{R}_{xx,k} = \mathbf{E}^{(k)} \mathbf{V}^{(k)} \mathbf{E}^{(k)H}, \quad (3)$$

where $\mathbf{V}^{(k)}$ is a diagonal matrix whose diagonal elements contain the signal and noise eigenvalues for the k th frequency and $\mathbf{E}^{(k)}$ is the corresponding eigenvectors of the signal and noise components. The two-dimensional spatial MUSIC spectrum at the k th frequency component can be constructed using the function

$$P_{\text{MU},k}(\phi, \theta) = \frac{1}{[\mathbf{a}_t(\phi) \otimes \mathbf{a}_r(\theta)]^H \mathbf{e}_N^{(k)} \mathbf{e}_N^{(k)H} [\mathbf{a}_t(\phi) \otimes \mathbf{a}_r(\theta)]}, \quad (4)$$

where $\mathbf{e}_N \mathbf{e}_N^H$ is the noise eigenvectors obtained from the eigendecomposition of the receive signal covariance matrix in (2). Here, we have the L largest peaks which correspond to the DOD and DOA of the targets at each frequency component. The wideband DOD and wideband DOA are decided by taking the majority of the estimated angles among all the estimates at each frequency. This is denoted by “majority decision” in this study. The majority decision is formulated by initially combining DOD and DOA estimates at the K frequencies into a vector and arranging them in the form of angle histograms [13], as depicted in Figure 3. The angle histogram can be viewed as a function of angle i from -90° to 90° at intervals of, for example, 0.5° . The normalized number of occurrence of the peak angle is then given by

$$\hat{r}^{(i)} = \frac{1}{z} p^{(i)}, \quad (5)$$

where $p^{(i)}$ is the number of occurrences of the angle i and z is the normalized coefficient given by

$$z = \arg \max \hat{r}^{(i)}. \quad (6)$$

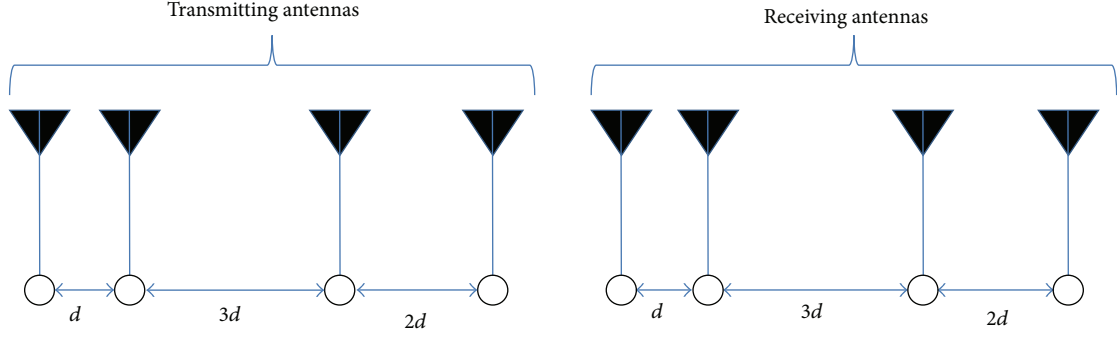
The majority decision is obtained by searching the peak of the histogram. As a benchmark, the performance of the proposed scheme will be compared with the conventional spectrum averaging method [21] used in existing subband processing scheme for angle estimation. The spectrum averaging method adopts an approach which takes the average of the estimated MUSIC spectra of all K frequency components:

$$P_{\text{MU,ave}}(\phi, \theta) = \frac{1}{K} \sum_{k=1}^K P_{\text{MU},k}(\phi, \theta). \quad (7)$$

Then the wideband DOD and DOA are estimated from the L largest peaks of $P_{\text{MU,ave}}$. We will demonstrate in Section 3 that the majority decision technique performs better than the spectrum averaging method. Figure 4 depicts the block diagrams of the proposed and conventional schemes.

2.2. MIMO Radar Array Configuration Used in this Study.

The main advantage of a MIMO radar system is that the degrees of freedom can be enhanced by using the concept of virtual array [22, 23]. When orthogonal signals were transmitted from different antennas, the back scatter returns of each orthogonal signal will carry independent phase information that forms a new virtual array steering vectors at the receiver.

FIGURE 6: Nonuniform array configuration used in the study ($d = 15$ mm).

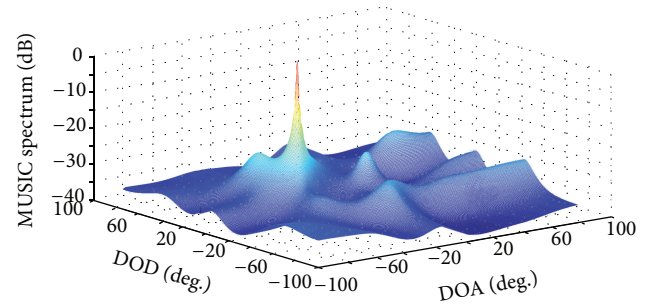
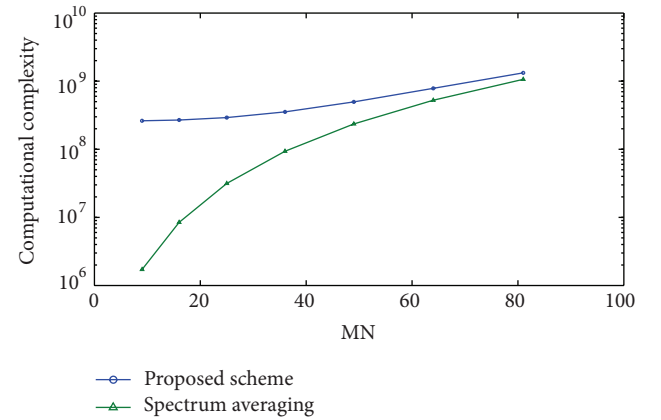
The virtual array can be characterized by convolution of the transmitting and receiving antenna positions [22]. Given a MIMO radar using M transmitting and N receiving antennas, it is possible to form a full virtual array with nonoverlapping MN elements, by optimizing the antenna positions. Larger numbers of M and N contribute to construction of longer virtual array, which means further enhancement in angle estimation performance. Thus, from a signal processing point of view, it is generally important to use a larger virtual array. However, in practical applications, it is often beneficial to limit the number of antennas for the sake of cost and space. In this study, we demonstrate the proposed algorithm using a 4×4 MIMO array and discuss the performance within that limitation.

A full MN virtual array can be constructed, for example, by using transmitting antennas with spacing of Nd and receiving antennas with d spacing [23], where d is the distance equal to the half wavelength.

However, as shown in Figure 5, utilizing a two-way MUSIC using this array configuration resulted in spurious peaks in the MUSIC spectrum, since the receiving array's spacing is much larger than the distance of half wavelength. This problem can be overcome by limiting the scan range, but in the cost of narrower coverage area.

In this study, we employed a nonuniform array configuration as shown in Figure 6 to reduce the spurious peaks. This array configuration was chosen due to the minimum number of redundant elements that could be obtained in the virtual MIMO array. Refer to the Appendix for further explanation. The basic antenna spacing of $d = 15$ mm (corresponds to half wavelength of 10 GHz) was used. Figure 7 depicts the resulting MUSIC spectrum using the nonuniform array, where we could observe that the spurious peaks were eliminated, and the resulting spectrum peak sharpness is comparable to a full MN array with limited range scan. The authors have previously reported in [13] that this array configuration outperforms the conventional uniform linear array.

2.3. Complexity Analysis. This subsection presents the analysis of the computational complexity of the proposed scheme. The computational burden of a conventional 2D-MUSIC has

FIGURE 7: Example of a MUSIC spectrum using the nonuniform array configuration ($f_k = 5.0$ GHz).FIGURE 8: Computational complexity of the proposed scheme against MN antennas ($K = 1000$, $L = 2$).

been reported in literatures, such as in [5]. For the sake of clarity, we broke down the complexity analysis of the proposed scheme in terms of SVD operation and searching algorithm computational costs, expressed using the O notation [24].

TABLE I: Simulation parameters.

Parameters	Description
Number of transmitting antennas, M	4
Number of receiving antennas, N	4
Number of targets, L	2
Signal to noise ratio, SNR	15 dB
Number of snapshots	50
Target positions	$(\phi_1, \theta_1) = (10^\circ, -28^\circ)$ $(\phi_2, \theta_2) = (-10^\circ, -10^\circ)$
Type of targets	Fixed point targets or Weibull targets

The conventional spectrum averaging method [21] was also analyzed for comparison.

Considering the dimensions of the covariance matrix $u \times v$ and the total K frequency components used, applying SVD operation on the receiving covariance matrix generally costs $O(K\{u^2v + v^3\})$. Here, from the receiving covariance matrix formulation, u and v are given by M^2 and N^2 , respectively. This is the same for both the proposed and the spectrum averaging schemes. In terms of peak search operation, the proposed scheme performs two-dimensional peak search on the MUSIC spectrum, which costs $O(i^2KL)$, where i is the number of angle bins during search operations. In addition, the majority decision routine costs $O(2\{i + K\}) + O(2\{iL\})$, where the first term corresponds to the histogram formulation of K total estimates, and the second term represents the one-dimensional peak search to identify the angles of L targets. On the other hand, the computational burden of the spectrum averaging method is $O(K) + O(i^2L)$, corresponding to the spectrum averaging and two-dimensional peak search of the averaged spectrum, respectively.

The computational complexity against MN antennas is plotted in Figure 8. It was shown that the proposed scheme marked larger computational burden than the spectral averaging method, particularly when the number of antennas is small. However, the difference of complexity is reduced with increasing number of antennas and converges when MN approaches 81. This is because the cost of SVD operation becomes dominant with larger dimension of receiving covariance matrix, thus resulting in similar order of total computational complexity in both methods.

3. Simulation Results

The proposed algorithm was simulated according to the parameters listed in Table I. As mentioned in the previous sections, the UWB signal considered in the proposed scheme contains multiple sinusoidal ranging from 3.1 to 10.6 GHz at 1 MHz intervals. Here, selection of the start and stop frequencies within the frequency range determines the total

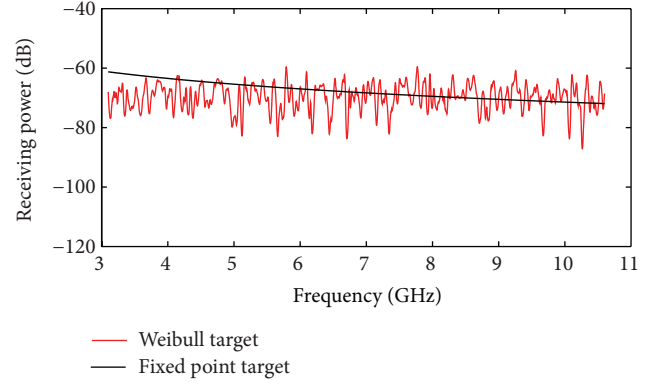


FIGURE 9: Simulated RCS of a simulated Weibull target in comparison with a fixed point target considering propagation loss in frequency domain.

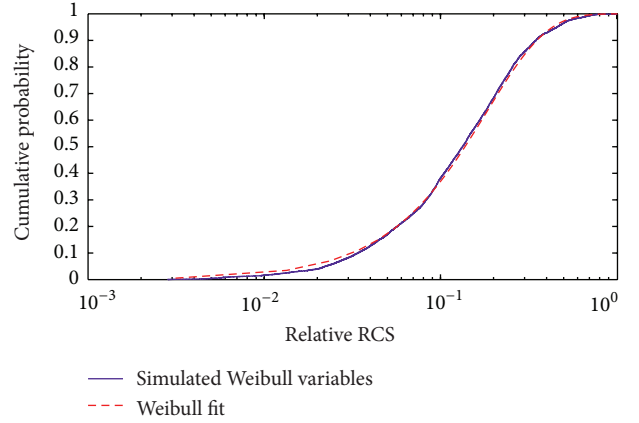


FIGURE 10: Cumulative distribution of the simulated RCS of a Weibull target in frequency domain.

bandwidth of the signal used. The signal bandwidth is defined by

$$\text{Bandwidth} = f_H - f_L, \quad (8)$$

where f_H and f_L are the highest and lowest frequency components, respectively. The simulations will be conducted while varying the signal bandwidth from 10 to 1000 MHz, at different center frequencies, f_c , for example, from 3.6, 5, and 8.4 to 10 GHz.

Two different scenarios were simulated, where the MIMO radar was detecting either a fixed point target or a target with fluctuating RCS. The fixed point target was modeled with a constant RCS, normalized by the free space propagation loss coefficient in each frequency. The targets with fluctuating RCS were modeled by Weibull distribution, since it was shown in literatures that measured RCS of complex targets such as automobiles and small cars follows Weibull distribution [25]. The measurement data also showed that at a given observation angle, the RCS against frequency (7 GHz bandwidth) also follows similar distribution. The targets considered in the simulation were modeled to have

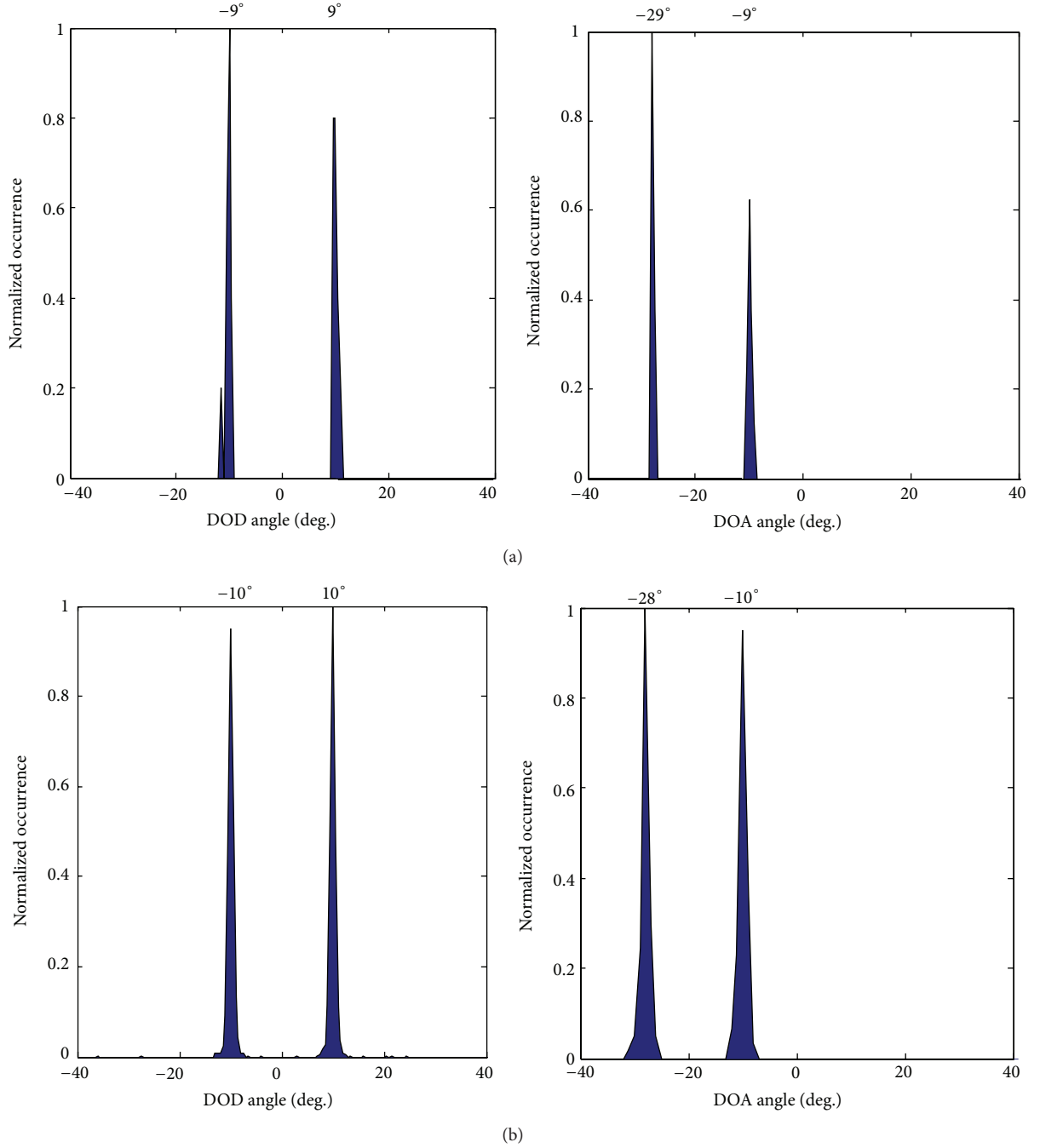


FIGURE 11: Angle histograms of estimated DODs and DOAs in detecting fixed point targets using a signal bandwidth of (a) 50 and (b) 1000 MHz.

Weibull distributed RCS throughout the UWB frequency range, whose cumulative distribution function is given by

$$f(x) = \begin{cases} 1 - \exp^{-(x/a)^b}, & x \geq 0, \\ 0, & x < 0, \end{cases} \quad (9)$$

where a and b are the shape and scale parameters, respectively. The values of a and b were selected so as to equal the RCS medians of the Weibull and fixed point targets. Figure 9

plots the RCS versus frequency (expressed in signal power), and Figure 10 depicts the corresponding cumulative distribution. We demonstrate the performance of the proposed scheme when detecting 2 targets located at $(\phi_1, \theta_1) = (10^\circ, -28^\circ)$ and $(\phi_2, \theta_2) = (-10^\circ, -10^\circ)$. The signal to noise ratio (SNR) was 15 dB, and the number of snapshots was 50.

Figure 11 shows the examples of angle histograms at $f_c = 3.6$ GHz, when the MIMO radar was detecting the fixed point targets. It can be observed that the angle histograms

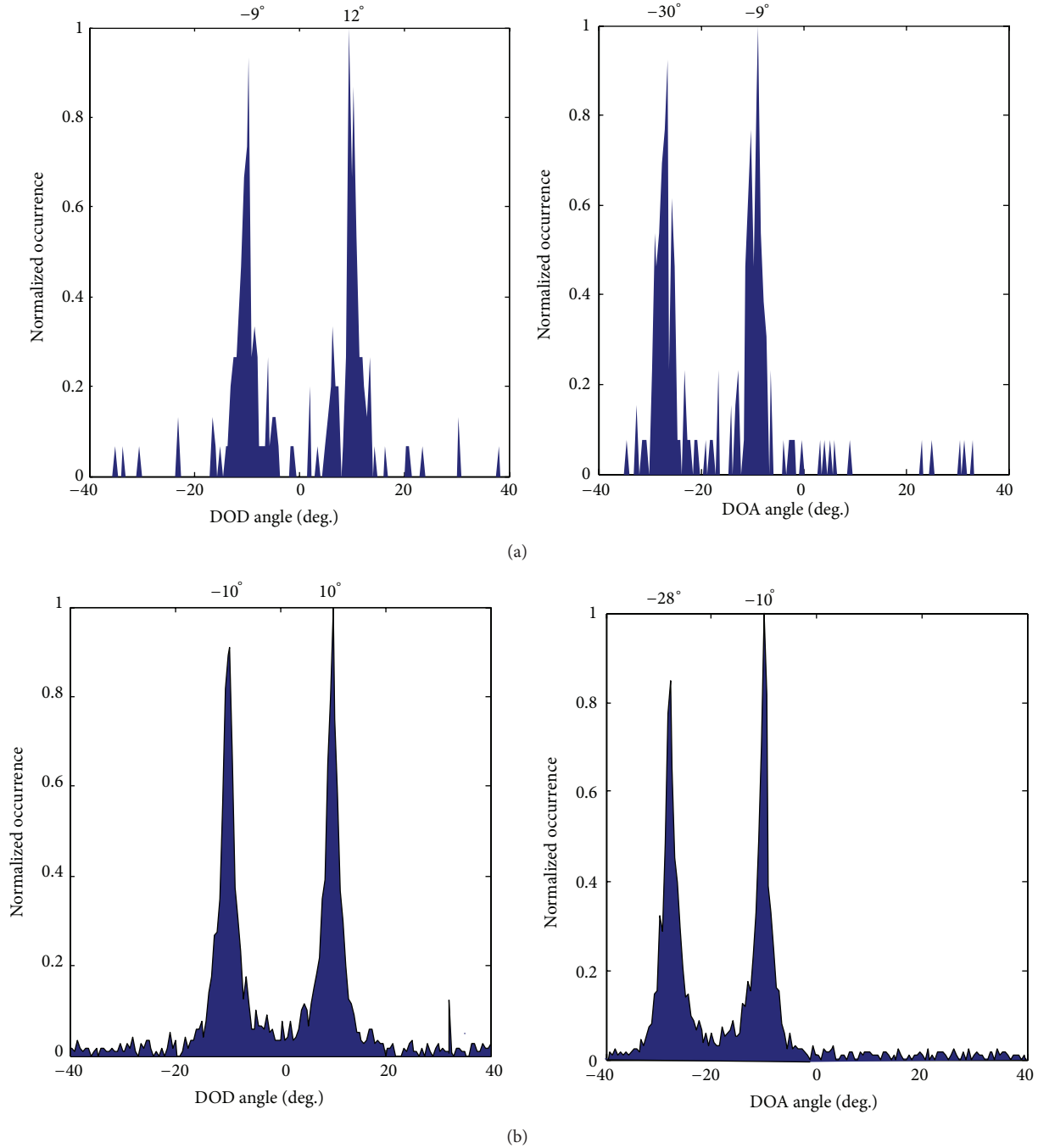


FIGURE 12: Angle histograms of estimated DODs and DOAs in detecting Weibull targets using a signal bandwidth of (a) 50 and (b) 1000 MHz.

were more or less similar when using either 1000 MHz or 50 MHz of signal bandwidths. Both cases marked sharp histogram peaks, which corresponds to the respective targets. This deduced that, when detecting fixed point targets, the bandwidth has minimal effects on the angle estimation performance. The estimation using a 50 MHz signal bandwidth, however, yielded an error of 1°. On the other hand, the angle estimation of the Weibull targets marked outstanding outliers in the angle histograms, particularly when using

a 50 MHz signal bandwidth, as depicted in Figure 12(a). These outliers were attributable to spurious peaks in the MUSIC spectrum due to small RCS values at certain frequencies. However, taking the majority decisions from the histograms, the targets were successfully estimated within 2° of estimation error. It was also shown in Figure 12(b) that, by taking a larger bandwidth, for example, 1 GHz, the peaks of the outliers were suppressed compared to using a 50 MHz signal bandwidth.

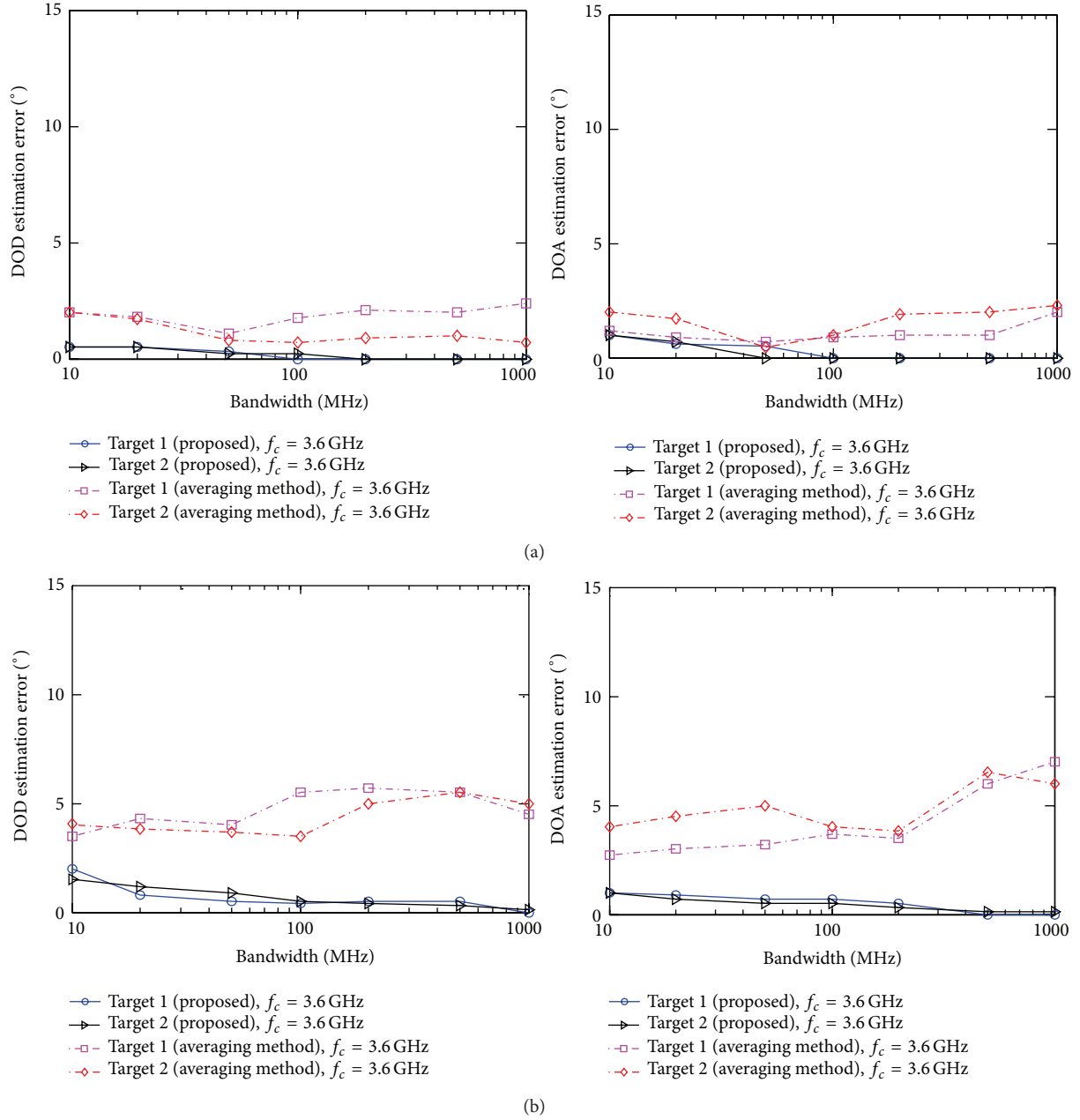


FIGURE 13: Estimation errors against bandwidth: (a) fixed point and (b) Weibull targets.

The performance of the proposed scheme was evaluated in terms of estimation error, defined by

$$\begin{aligned} \text{Error}_{\text{DOD}} &= \frac{1}{W} \sum_{w=1}^W |\phi - \phi_{\text{est}}|, \\ \text{Error}_{\text{DOA}} &= \frac{1}{W} \sum_{w=1}^W |\theta - \theta_{\text{est}}|, \end{aligned} \quad (10)$$

where W is the number of independent trials and ϕ_{est} and θ_{est} are the estimated DOD and DOA, respectively. The estimation error against signal bandwidth using $f_c = 3.6$ GHz was plotted in Figure 13, comparing the performance when detecting the fixed point and Weibull targets with 50 independent trials and SNR = 15 dB. Comparison with a conventional spectra averaging method [21] was also presented. It can be observed that the proposed scheme yielded improved estimation performance when taking larger signal bandwidth. This was true when detecting both types

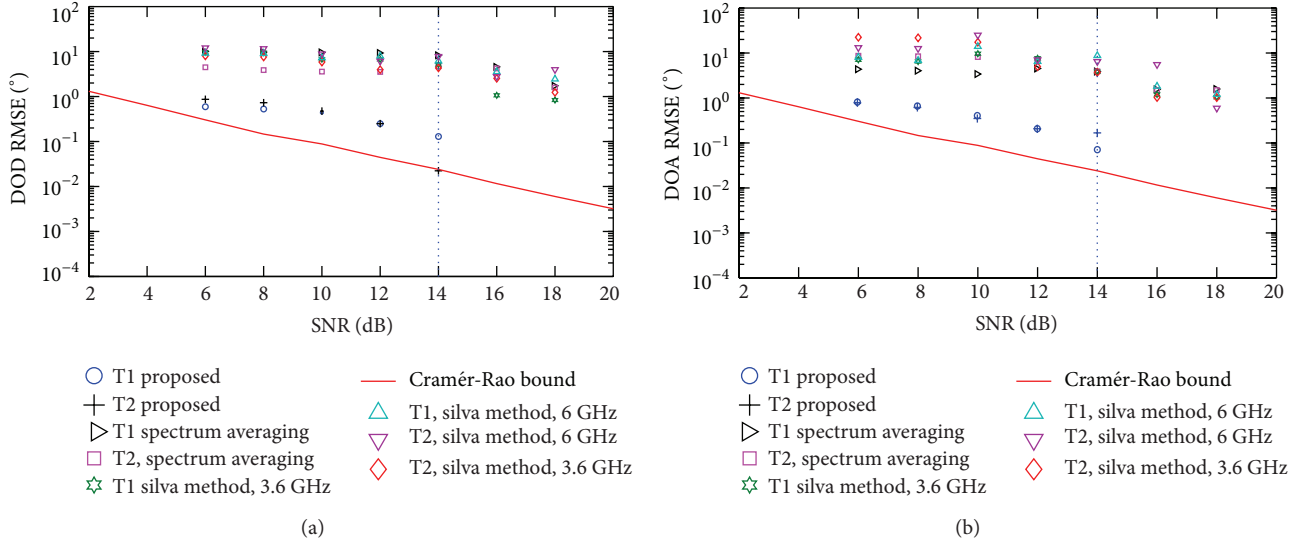
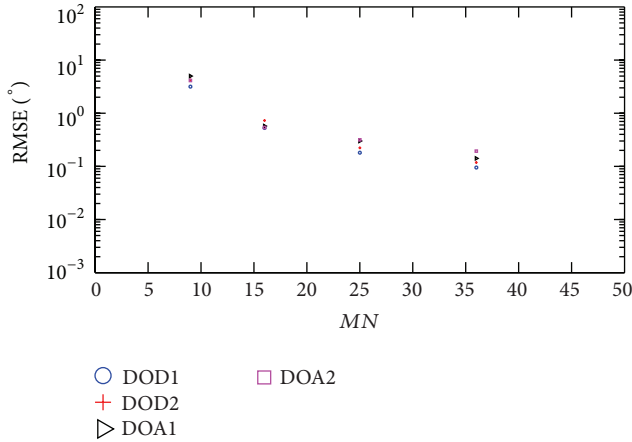


FIGURE 14: RMSE performance of the proposed scheme: (a) DOD and (b) DOA.

FIGURE 15: RMSE of the proposed scheme against MN (bandwidth = 1000 MHz, $L = 2$, SNR = 8 dB, and target = Weibull).

of targets; however, the improvement was more significant in the case of Weibull targets. On the other hand, the estimation error increased with larger bandwidth when conventional spectra averaging method was applied. This is attributed to large number of outliers which significantly influenced the averaging result. This result demonstrated the effectiveness of the proposed method in detecting targets with severely fluctuating RCS.

The performance of the proposed scheme in terms of root mean square error (RMSE) against SNR is plotted in Figure 14. Performance of the spectrum averaging method and another conventional method by de Silva and Seow [14] was also presented for benchmarking purposes. Simulation was carried out assuming that all methods use a 4×4 MIMO

nonuniform array detecting two Weibull targets. The performance of the proposed and spectrum averaging schemes was shown when they are using a 1000 MHz bandwidth with $f_c = 3.6$ GHz, while Silva's method was presented at several frequencies since it is a narrowband-based angle estimation. The performance bound calculated from the Cramér-Rao bound (CRB) when the DOD and DOA of a stationary target are estimated individually [26, 27] was also plotted for reference.

We could observe that the proposed scheme marked the best performance, which was the nearest to the CRB, and produced no estimation error when the SNR exceeds 14 dB. It was also shown that the performance of Silva method depended on the frequency for the targets with fluctuating RCS.

The impact of a number of antennas on the performance of the proposed scheme was plotted in Figure 15. The RMSE was computed in 50 independent trials against MN , when using a signal bandwidth of 1000 MHz and SNR = 8 dB. Specific cases of $M = N = 3, 4, 5$, and 6 were simulated. It is shown in the figure that increasing number of antennas yielded improvement in RMSE performance, even in the low SNR condition.

4. Experimental Results

Experiments were conducted to verify the results of the numerical simulations. The measurements were done in a radio anechoic chamber, using a measurement setup illustrated in Figure 16. The setup consists of a vector network analyzer (VNA) and GPIB-controlled scanners which were used to virtually construct the MIMO arrays at both transmitting and receiving sides. The VNA was used to generate UWB signals from 3.1 to 10.6 GHz in 1 MHz intervals, which were

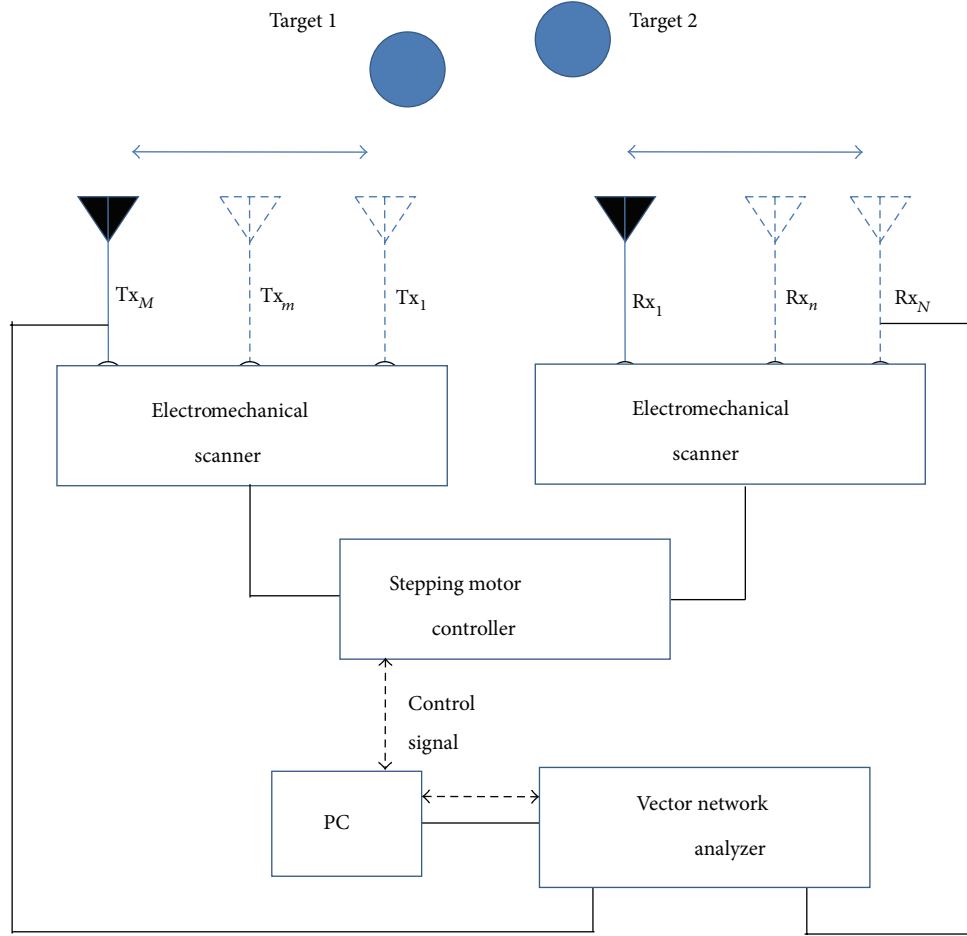


FIGURE 16: Measurement setup.

used as the transmitting signal. The VNA was adopted due to its good calibration functions and time gating capability to cancel out direct coupling effects between transmitting and receiving antennas. Wideband horn antennas with average gain of 12.5 dBi were used as both transmitting and receiving antennas. The SNR of the system is defined as the ratio of the receiving signal average power to the thermal noise.

The setup was used to localize two targets positioned at $(\phi_1, \theta_1) = (10^\circ, -28^\circ)$ and $(\phi_2, \theta_2) = (-10^\circ, -10^\circ)$, similar to the condition in previous simulations. Two types of targets were used, which were conductive spheres and complex shaped targets, both fabricated using polystyrenes and aluminum foil. The conductive spheres have 20 cm of diameters which yield RCS of approximately -10 dBm^2 . The complex targets were constructed so that they yield a fluctuating RCS in the frequency domain. An example of the complex target is shown in Figure 17. Figure 18 shows the measured frequency-domain data of the complex targets, where ψ is the monostatic angle of observation. From the figure, we could observe that the receive signal fluctuates severely against frequency, compared to that of sphere targets. The complex targets

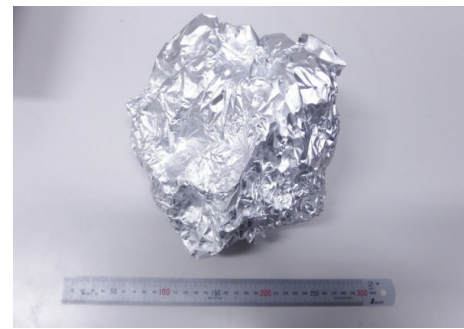


FIGURE 17: Example of a fabricated complex target.

marked several frequency regions with fluctuations of more than 15 dB at different angles, compared to sphere targets with only 5 dB of maximum fluctuations. The targets were positioned at 2.5 m from the baseline of the transmitter and receiver. The measurement scenario is depicted in Figure 19.

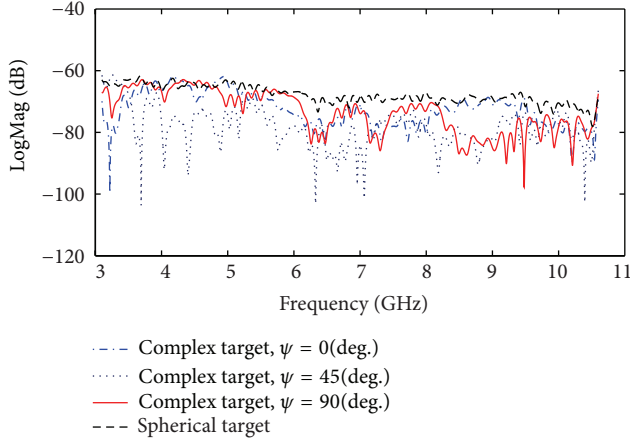


FIGURE 18: Measured frequency-domain data of the fabricated targets.

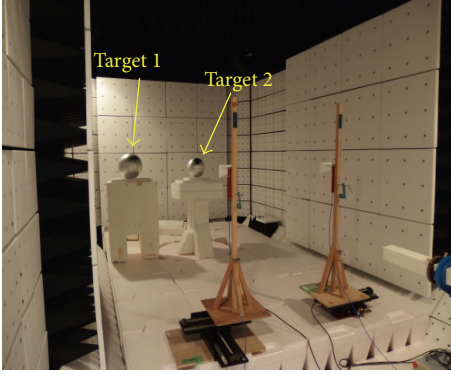


FIGURE 19: Measurement scenario in a radio anechoic chamber.

The estimation errors from measurement campaign were plotted in Figure 20. In the figure, the estimation errors were shown using signal bandwidths from 10 to 1000 MHz and f_c of 3.6, 5.0 and 8.4 GHz. As demonstrated in the numerical simulations, the measurement results also indicated a decreasing trend in estimation errors with increasing signal bandwidth, especially in the case of complex targets. The estimation errors of complex targets were worse than the sphere targets, where maximum of 7° of estimation errors was observed. Both cases marked poorer performance compared to the simulations since the experimental measurement included plane wave modeling errors and other maneuvering factors. Furthermore, no significant difference in estimation performance was observed when choosing different center frequencies.

A series of experiments was conducted to evaluate the localization performance of the proposed scheme. A single complex target was positioned in several locations in the radio anechoic chamber. The positions of the target are summarized in Table 2. The target was localized using the standard triangulation method, adopting the proposed scheme. In addition, localization using DOA and time of

TABLE 2: Target positions in a radio anechoic chamber.

Target positions	Actual DOD and DOA	Target distance from radar
A	$(\phi, \theta) = (15^\circ, -43^\circ)$	1.5 m
B	$(\phi, \theta) = (-3^\circ, -24^\circ)$	2.2 m
C	$(\phi, \theta) = (-17^\circ, -1^\circ)$	3.0 m
D	$(\phi, \theta) = (-21^\circ, 5^\circ)$	3.3 m

direction-of-arrival (TDOA) was also performed for comparison. The DOA-TDOA proposed method uses the DOA formulated from majority decisions of estimations at each subfrequency, and the TDOA was obtained from the time of arrival of the radar signal observed at Tx1-Rx1 antenna pair. The same MIMO array configuration as in the previous experiments was utilized, and the number of snapshots was 50. Considering the target location in an x - y plane, the localization errors are defined as

$$\Delta R = \sqrt{(\Delta x^2 + \Delta y^2)}, \quad (11)$$

where Δx and Δy are the ranging errors along the x and y axes. The results of the measurements were plotted in Figure 21. In the case of triangulation, less than 1 m of error was obtained when using signal bandwidth of 1000 MHz. Using a 50 MHz signal resulted in lower accuracy. The DOA-TDOA method also produced good results when using a 1000 MHz signal and marked poor accuracy when using a 50 MHz bandwidth, due to low range resolution of TDOA. Both localization methods showed slightly lower accuracy when the target is further away from the radar due to decrease in SNR.

5. Concluding Remarks

The performance of a joint DOD and DOA estimation in a UWB MIMO radar detecting fluctuating targets was evaluated through numerical simulations and experimental evaluations. From the investigation, it was found that in detecting targets with fluctuating RCS (in this case Weibull distributed RCS against frequency), it is essential to use large signal bandwidth to reduce the estimation error using the proposed algorithm. When taking wider signal bandwidth, the usage of majority decisions from the angle histograms resulted in good estimation performance compared to the conventional spectrum averaging method. We concluded based on the work that the proposed scheme was a suitable candidate to implement joint angle estimation in MIMO radar using ultra wideband signal. Although the resolution of target localization based on DOD and DOA estimations, in general, does not depend on the signal bandwidth, it was demonstrated that utilization of wider bandwidth in the proposed scheme leads to improvement of estimation performance, considering that the targets have fluctuating RCS in the frequency domain. Since the proposed scheme

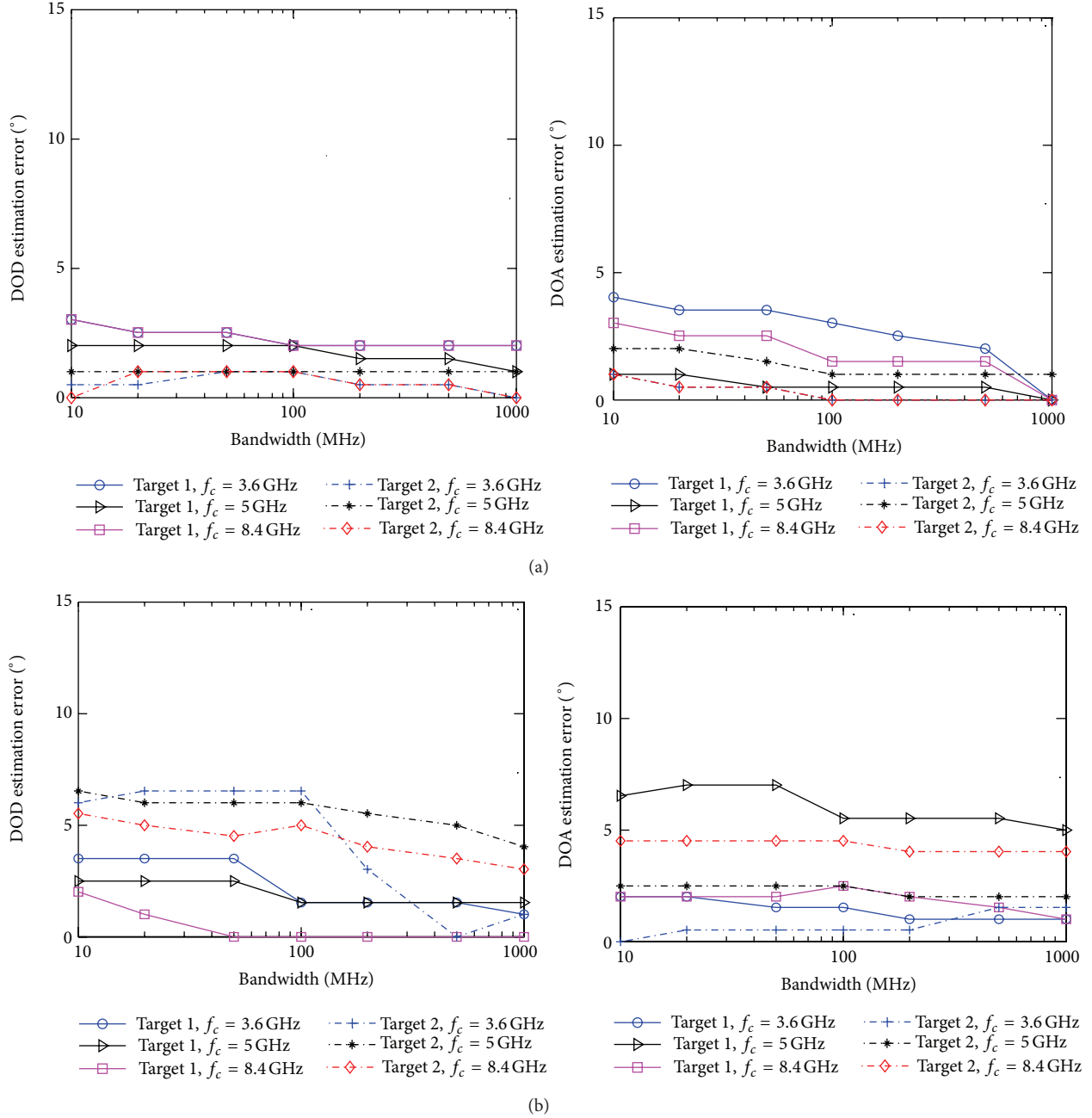


FIGURE 20: Estimation errors against bandwidth obtained from measurements: (a) spherical and (b) complex targets.

utilizes multiple subcarriers, it is suitable to be extended to an OFDM-based radar system.

Appendix

MIMO Radar Virtual Array Using Nonuniform Array Configuration

The MIMO antennas could be arranged in such a way that they produce a filled virtual array; however, the filled virtual array tends to consist of less number of unique

virtual elements due to redundant elements. A few examples are depicted in Figure 22. Here, we illustrate the physical transmitting and receiving antennas position using the notation $\{1111\}$, where each entry corresponds to the number of antennas at the particular location on the $\lambda/2$ grid, and $*$ is the convolutional operator. The results of the convolution of the transmitting and receiving antenna positions are shown on the right side of each figure. As depicted in Figure 22(a), the usage of uniform linear array on both transmitting and receiving arrays resulted in virtual arrays with significant number of redundant elements.

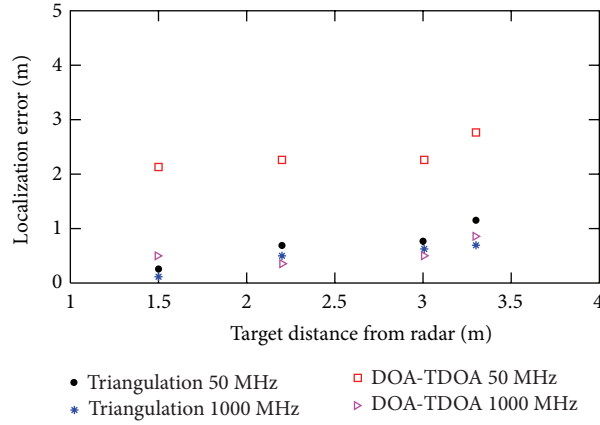


FIGURE 21: Localization errors from measurements in a radio anechoic chamber.

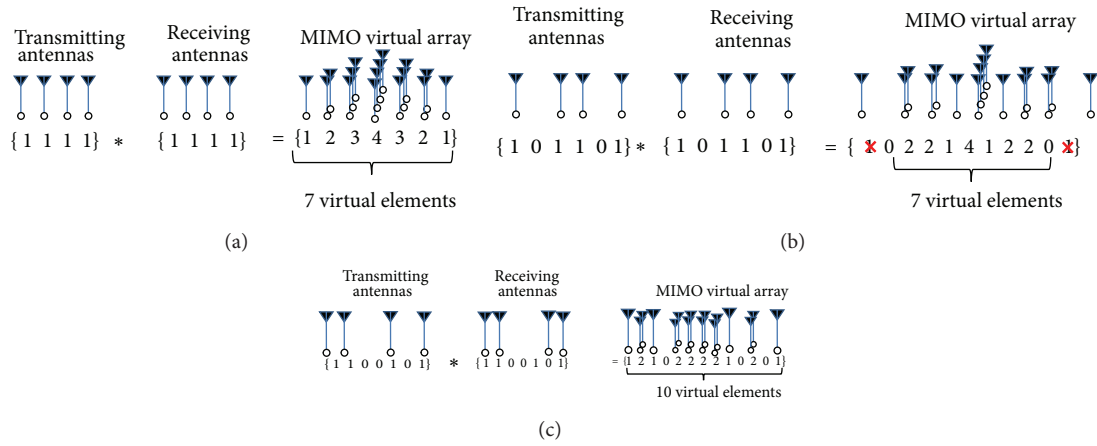


FIGURE 22: Illustration of examples of virtual arrays in MIMO radars: (a) uniform linear array, (b) truncated filled array, and (c) nonuniform array.

Configuration in Figure 22(b) produces a larger number of unique virtual elements. However, in order to obtain a filled array, truncation of the elements at the edge of the virtual array is required, thus reducing the array length. Meanwhile, the nonuniform MIMO array used in Figure 22(c) yielded a larger number of virtual antenna elements, since it has less number of redundant elements.

Conflict of Interests

The authors declare that there is no conflict of interests regarding the publication of this paper.

References

- [1] E. Fishler, A. Haimovich, R. S. Blum, L. J. Cimini Jr., D. Chizhik, and R. A. Valenzuela, "Spatial diversity in radars-models and detection performance," *IEEE Transactions on Signal Processing*, vol. 54, no. 3, pp. 823–838, 2006.
- [2] A. M. Haimovich, R. S. Blum, and L. J. Cimini, "MIMO radar with widely separated antennas," *IEEE Signal Processing Magazine*, vol. 25, no. 1, pp. 116–129, 2008.
- [3] J. Li and P. Stoica, "MIMO radar with colocated antennas," *IEEE Signal Processing Magazine*, vol. 24, no. 5, pp. 106–114, 2007.
- [4] X. H. Wu, A. A. Kishk, and A. W. Glisson, "MIMO-OFDM radar for direction estimation," *IET Radar, Sonar & Navigation*, vol. 4, no. 1, pp. 28–36, 2010.
- [5] X. Zhang, L. Xu, L. Xu, and D. Xu, "Direction of departure (DOD) and direction of arrival (DOA) estimation in MIMO radar with reduced-dimension mUSIC," *IEEE Communications Letters*, vol. 14, no. 12, pp. 1161–1163, 2010.
- [6] B. Yao, W. Wang, and Q. Yin, "DOD and DOA estimation in bistatic non-uniform multiple-input multiple-output radar systems," *IEEE Communications Letters*, vol. 16, no. 11, pp. 1796–1799, 2012.
- [7] G. Zheng, M. Yang, W. Guo, and B. Chen, "Joint DOD and DOA estimation for bistatic polarimetric MIMO radar," in *Proceedings of the IEEE 11th International Conference on Signal Processing (ICSP '12)*, pp. 329–332, Beijing, China, October 2012.
- [8] F. Liu and J. Wang, "AD-MUSIC for jointly DOA and DOD estimation in bistatic MIMO radar system," in *Proceedings of the*

- International Conference on Computer Design and Applications (ICCCA '10)*, pp. V4455–V4458, June 2010.
- [9] M. A. Haleem, A. Haimovich, and R. S. Blum, "Sidelobe mitigation in MIMO radar with multiple subcarriers," in *Proceedings of the IEEE Radar Conference (RADAR '09)*, pp. 1–6, May 2009.
 - [10] X. H. Wu, A. A. Kishk, and A. W. Glisson, "MIMO-OFDM radar for direction estimation," *IET Radar, Sonar and Navigation*, vol. 4, no. 1, pp. 28–36, 2010.
 - [11] X. Zhuge, A. G. Yarovoy, T. Savelyev, and L. Ligthart, "Modified kirchhoff migration for UWB MIMO array-based radar imaging," *IEEE Transactions on Geoscience and Remote Sensing*, vol. 48, no. 6, pp. 2692–2703, 2010.
 - [12] X. Zhuge and A. G. Yarovoy, "Study on two-dimensional sparse MIMO UWB arrays for high resolution near-field imaging," *IEEE Transactions on Antennas and Propagation*, vol. 60, no. 9, pp. 4173–4182, 2012.
 - [13] I. Pasya, N. Iwakiri, and T. Kobayashi, "Joint direction-of-departure and direction-of-arrival estimation in an ultra-wideband MIMO radar system," in *Proceedings of the IEEE Radio Wireless Symposium (RWS '14)*, pp. 52–54, Newport Beach, Calif, USA, 2014.
 - [14] P. de Silva and C. K. Seow, "Performance of MIMO RADAR using two-way music," in *Proceedings of the Progress in Electromagnetics Research Symposium (PIERS '13)*, pp. 84–87, March 2013.
 - [15] N. Iwakiri and T. Kobayashi, "Ultra-wideband time-of-arrival and angle-of-arrival estimation using a signal model based on measurements," *IEICE Transactions on Fundamentals of Electronics, Communications and Computer Sciences*, vol. 90, no. 11, pp. 2345–2353, 2007.
 - [16] W. Zhang, W. Liu, J. Wang, and S. Wu, "Joint transmission and reception diversity smoothing for direction finding of coherent targets in MIMO radar," *IEEE Journal of Selected Topics in Signal Process*, vol. 8, no. 1, pp. 115–124, 2014.
 - [17] D. Wilcox, M. Sellathurai, and T. Ratnarajah, "Subspace methods and spatial diversity in radars," in *Proceedings of the IEEE Radar Conference (RADAR '08)*, pp. 1–5, Rome, Italy, May 2008.
 - [18] Y. Chen, Y. Nijssure, C. Yuen, Y. H. Chew, Z. Ding, and S. Boussakta, "Adaptive distributed MIMO radar waveform optimization based on mutual information," *IEEE Transactions on Aerospace and Electronic Systems*, vol. 49, no. 2, pp. 1374–1385, 2013.
 - [19] V. Mangulis, "Frequency diversity in low-angle radar tracking," *IEEE Transactions on Aerospace and Electronic Systems*, vol. 17, no. 1, pp. 149–153, 1981.
 - [20] J. J. Zhang and A. Papandreou-Suppappola, "MIMO radar with frequency diversity," in *Proceedings of the International Waveform Diversity and Design Conference (WDD '09)*, pp. 208–212, February 2009.
 - [21] M. Fujimoto, S. Ohaka, and T. Hori, "DOA estimation without antenna characteristics calibration for UWB signal by using sub-band processing," in *Proceedings of the IEEE International Conference on Wireless Information Technology and Systems (ICWITS '10)*, pp. 1–4, September 2010.
 - [22] W.-Q. Wang, "Virtual antenna array analysis for MIMO synthetic aperture radars," *International Journal of Antennas and Propagation*, vol. 2012, Article ID 587276, 10 pages, 2012.
 - [23] L. Jian and P. Stoica, Eds., *MIMO Radar Signal Processing*, Wiley, New Jersey, NJ, USA, 2009.
 - [24] G. H. Golub and C. F. van Loan, *Matrix Computations*, Johns Hopkins University Press, Baltimore, Md, USA, 3rd edition, 1996.
 - [25] W. Buller, B. Wilson, L. Van Nieuwstadt, and J. Ebling, "Statistical modelling of measured automotive radar reflections," in *Proceedings of the IEEE International Instrumentation and Measurement Technology Conference (I2MTC '13)*, pp. 349–352, May 2013.
 - [26] H. W. Chen, D. Yang, H. Q. Wang, X. Li, and Z. W. Zhuang, "Direction Finding for bistatic MIMO radar using EM maximum likelihood algorithm," *Progress in Electromagnetics Research*, vol. 141, pp. 99–116, 2013.
 - [27] H. L. van Trees, *Optimum Array Processing*, Wiley, New York, NY, USA, 2009.

Research Article

LPI Optimization Framework for Target Tracking in Radar Network Architectures Using Information-Theoretic Criteria

Chenguang Shi,¹ Fei Wang,¹ Mathini Sellathurai,² and Jianjiang Zhou¹

¹ Key Laboratory of Radar Imaging and Microwave Photonics, Ministry of Education, Nanjing University of Aeronautics and Astronautics, No. 29, Yudao Street, Qinhuai District, Nanjing, Jiangsu 210016, China

² School of Engineering and Physical Sciences, Heriot-Watt University, Edinburgh, UK

Correspondence should be addressed to Jianjiang Zhou; zjje@nuaa.edu.cn

Received 26 February 2014; Revised 29 May 2014; Accepted 17 June 2014; Published 6 July 2014

Academic Editor: Shengqi Zhu

Copyright © 2014 Chenguang Shi et al. This is an open access article distributed under the Creative Commons Attribution License, which permits unrestricted use, distribution, and reproduction in any medium, provided the original work is properly cited.

Widely distributed radar network architectures can provide significant performance improvement for target detection and localization. For a fixed radar network, the achievable target detection performance may go beyond a predetermined threshold with full transmitted power allocation, which is extremely vulnerable in modern electronic warfare. In this paper, we study the problem of low probability of intercept (LPI) design for radar network and propose two novel LPI optimization schemes based on information-theoretic criteria. For a predefined threshold of target detection, Schleher intercept factor is minimized by optimizing transmission power allocation among netted radars in the network. Due to the lack of analytical closed-form expression for receiver operation characteristics (ROC), we employ two information-theoretic criteria, namely, Bhattacharyya distance and J-divergence as the metrics for target detection performance. The resulting nonconvex and nonlinear LPI optimization problems associated with different information-theoretic criteria are cast under a unified framework, and the nonlinear programming based genetic algorithm (NPGA) is used to tackle the optimization problems in the framework. Numerical simulations demonstrate that our proposed LPI strategies are effective in enhancing the LPI performance for radar network.

1. Introduction

Radar network architecture, which is often called as distributed multiple-input multiple-output (MIMO) radar, has been recently put forward and is becoming an inevitable trend for future radar system design [1–3]. The performance of radar network heavily depends on optimal power allocation and transmission waveform design, so enhanced improvements on target detection and information extraction would be realized by spatial and signal diversities.

Currently, system design for target detection and information extraction performance improvement has been a long-term research topic in the distributed radar network literature. In [4], Fishler et al. propose the distributed MIMO radar concept and analyze the target detection performance for distributed MIMO radar. Yang and Blum in [5] study the target identification and classification for MIMO radar employing mutual information (MI) and the minimum mean-square error (MMSE) criteria. The authors in [6]

investigate the problem of code design to improve the detection performance of multistatic radar in the presence of clutter. Niu et al. propose localization and tracking approaches for noncoherent MIMO radar, which provides significant performance enhancement over traditional phased array radar [7].

Power allocation problem in radar network architecture has been attracting contentiously growing attention, and some of the noteworthy publications include [8–14]. The work of [8] investigates the scheduling and power allocation problem in cognitive radar network for multiple-target tracking, in which an optimization criterion is proposed to find a suitable subset of antennas and optimal transmitted power allocation. Godrich et al. in [9–11] address the power allocation strategies for target localization in distributed multiple-radar configurations and propose some performance driven resource allocation schemes. In [12], the authors investigate target threatening level based optimal power allocation for LPI radar network, where two effective algorithms are

proposed to enhance the LPI performance for radar network. Furthermore, in [13, 14], several optimal power allocation algorithms for distributed MIMO radars with heterogeneous propagation losses are presented to enhance target detection and information extraction performance. However, up to now, the low probability of intercept (LPI) optimization for radar network architecture is still an open problem, which is playing an increasingly important role in modern electronic warfare [1, 15–18]. Therefore, it is an urgent task to investigate the LPI optimization problem in radar network.

This paper will extend the results in [6] and propose two novel LPI optimization algorithms based on information-theoretic criteria for radar network architecture. Our purpose is to minimize Schleher intercept factor by optimizing transmission power allocation among netted radars for a predefined threshold of target detection. Due to the lack of analytical closed-form expression for receiver operation characteristics (ROC), we employ two information-theoretic criteria including Bhattacharyya distance and J-divergence as the metrics for target detection performance. As demonstrated later, the proposed algorithms can provide significant LPI performance improvement for radar network. To the best of the authors' knowledge, no literature discussing the information-theoretic criteria based LPI optimization for radar network architecture was conducted prior to this work.

The remainder of this paper is organized as follows. Section 2 provides the radar network system model and binary hypothesis test. We first derive Schleher intercept factor for radar network in Section 3 and formulate the problems of information-theoretic criteria based LPI optimization, where the resulting nonconvex and nonlinear LPI optimization problems associated with different information-theoretic criteria are cast under a unified framework and solved through the nonlinear programming based genetic algorithm (NPGA). Numerical examples are provided in Section 4. Finally, conclusion remarks are drawn in Section 5.

2. System Model and the Optimal Detector

2.1. Radar Network SNR Equation. We consider a radar network architecture with N_t transmitters and N_r receivers, which can be broken down into $N_t \times N_r$ transmitter-receiver pairs each with a bistatic component contributing to the entirety of the radar network signal-to-noise ratio (SNR) [1]. Depicted in Figure 1 is an example of 4×4 radar network. All the radars have acquired and are tracking the target with their directional antenna beams. The netted radars *Radar1*, *Radar2*, *Radar3*, and *Radar4* transmit orthogonal waveforms (as solid lines) but receive and process all these echoes that are reflected from the target (as dotted lines) and send the estimates to one of the radars in the network for data fusion with data link.

For the radar network here, orthogonal polyphase codes are employed in the system, which have a large main lobe-to-side lobe ratio. These codes have a more complicated signal structure making it more difficult to be intercepted and detected by a hostile intercept receiver.

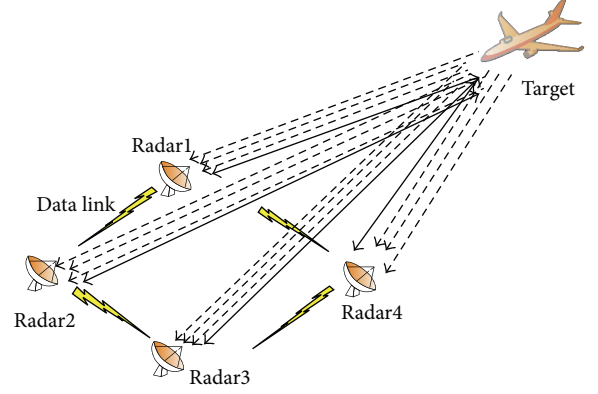


FIGURE 1: Example of an LPI radar network.

It is also supposed that the network system has a common precise knowledge of space and time. The radar network SNR can be calculated by summing up the SNR of each transmit-receive pair as [1] follows:

$$\text{SNR}_{\text{net}} = \sum_{i=1}^{N_t} \sum_{j=1}^{N_r} \frac{P_{ti} G_{ti} G_{rj} \sigma_{tij} \lambda_i^2}{(4\pi)^3 k T_{oij} B_{ri} F_{rj} R_{ti}^2 R_{rj}^2 L_{ij}}, \quad (1)$$

where the P_{ti} is the i th transmitter power, G_{ti} is the i th transmitting antenna gain, G_{rj} is the j th receiving antenna gain, σ_{tij} is the radar cross-section (RCS) of the target for the i th transmitter and j th receiver, λ_i is the i th transmitted wavelength, k is Boltzmann's constant, T_{oij} is the receiving system noise temperature at the j th receiver, B_{ri} is the bandwidth of the matched filter for the i th transmitted waveform, F_{rj} is the noise factor for the j th receiver, L_{ij} is the system loss between the i th transmitter and j th receiver, R_{ti} is the distance from the i th transmitter to the target, and R_{rj} is the distance from the target to the j th receiver.

2.2. Radar Network Signal Model. According to the discussions in [14], the path gain contains the target reflection coefficient g_{ij} and the propagation loss factor p_{ij} . Based on the central limit theorem, $g_{ij} \sim \text{CN}(0, R_g)$, where g_{ij} denotes the target reflection gain between radar i and radar j . The propagation loss factor p_{ij} is a function of radar antenna gain and waveform propagation distance, which is expressed as follows:

$$p_{ij} = \frac{\sqrt{G_{ti} G_{rj}}}{R_{ti} R_{rj}}. \quad (2)$$

It is supposed that the transmitted waveform of the i th netted radar is $\sqrt{P_{ti}} x_i(t)$, and then the collected signals at the j th receiver from a single point target can be written as follows:

$$y_j(t) = \sum_{i=1}^{N_t} p_{ij} g_{ij} \sqrt{P_{ti}} x_i(t - \tau_{ij}) + n_j(t), \quad (3)$$

where $\int |x_j(t)|^2 dt = 1$, τ_{ij} represents the time delay, $n_j(t)$ denotes the noise at receiver j , and the Doppler effect is negligible. At the j th receiver, the received signal is matched filtered by time response $x_k^*(-t)$, and the output signal can be expressed as follows:

$$\begin{aligned}\tilde{y}_{jk}(t) &= \int y_j(t) \cdot x_k^*(\tau - t) d\tau \\ &= p_{jk} g_{jk} \sqrt{P_{tk}} \int x_k(\tau - \tau_{kj}) \cdot x_k^*(\tau - t) d\tau + \tilde{n}_{jk}(t),\end{aligned}\quad (4)$$

where $\tilde{n}_{jk}(t) = \int n_j(\tau) \cdot x_k^*(\tau - t) d\tau$ and $\int x_j(\tau) \cdot x_k^*(\tau + t) d\tau = 0$ for $k \neq j$.

The discrete time signal for the j th receiver can be rewritten as follows:

$$r_{jk} \triangleq \tilde{y}_{jk}(\tau_{jk}) = p_{jk} g_{jk} \sqrt{P_{tk}} + \theta_{jk}, \quad (5)$$

where r_{kj} is the output of the matched filter at the receiver j sampled at τ_{jk} , $\theta_{jk} = \tilde{n}_{jk}(\tau_{jk})$, and $\theta_{jk} \sim \text{CN}(0, R_\theta)$. As mentioned before, we assume that all the netted radars have acquired and are tracking the target with their directional radar beams, and they transmit orthogonal waveforms while receiving and processing all these echoes that are reflected from the target. In this way, we can obtain τ_{jk} .

2.3. Binary Hypothesis Test. With all the received signals, the target detection for radar network system leads to a binary hypothesis testing problem:

$$\begin{aligned}H_0 : r_{ij} &= \theta_{ij} \\ H_1 : r_{ij} &= p_{ij} g_{ij} \sqrt{P_{ti}} + \theta_{ij},\end{aligned}\quad (6)$$

where $1 \leq i \leq N_t$, $1 \leq j \leq N_r$. The likelihood ratio test can be formulated as follows:

$$\begin{aligned}H_0 : T &\triangleq \prod_{i=1}^M \prod_{j=1}^N \frac{f(r_{ij} | H_1)}{f(r_{ij} | H_0)} < \delta, \\ H_1 : T &\triangleq \prod_{i=1}^M \prod_{j=1}^N \frac{f(r_{ij} | H_1)}{f(r_{ij} | H_0)} > \delta.\end{aligned}\quad (7)$$

As introduced in [14], the underlying detection problem can be equivalently rewritten as follows:

$$\begin{aligned}H_0 : r_{ij} &\sim \text{CN}(0, R_\theta), \\ H_1 : r_{ij} &\sim \text{CN}(0, R_\theta + P_{ti} R_g p_{ij}^2).\end{aligned}\quad (8)$$

Then, we have the optimal detector as follows:

$$\begin{aligned}H_0 : T &\triangleq \sum_{i=1}^{N_t} \sum_{j=1}^{N_r} |r_{ij}|^2 \frac{2P_{ti} p_{ij}^2}{R_\theta + P_{ti} R_g p_{ij}^2} < \delta, \\ H_1 : T &\triangleq \sum_{i=1}^{N_t} \sum_{j=1}^{N_r} |r_{ij}|^2 \frac{2P_{ti} p_{ij}^2}{R_\theta + P_{ti} R_g p_{ij}^2} > \delta,\end{aligned}\quad (9)$$

where δ denotes the detection threshold.

3. Problem Formulation

In this section, we aim to obtain the optimal LPI performance for radar network architecture by judiciously designing the transmission power allocation among netted radars in the network. We first derive Schleher intercept factor for radar network system and then formulate the LPI optimization problems based on information-theoretic criteria. For a predefined threshold of target detection, Schleher intercept factor is minimized by optimizing transmission power allocation among netted radars. It is indicated in [6] that the analytical closed-form expression for ROC does not exist. As such, we resort to information-theoretic criteria, namely, Bhattacharyya distance and J-divergence. In what follows, the corresponding LPI optimization problems associated with different information-theoretic criteria are cast under a unified framework and can be solved conveniently through NPGA.

3.1. Schleher Intercept Factor for Radar Network. For radar network, it is supposed that all signals can be separately distinguished at every netted radar node. Assuming that every transmitter-receiver combination in the network can be the same and $R_{\text{net}}^2 \triangleq R_{ti} \cdot R_{rj}$, in which case the radar network SNR equation (1) can be rewritten as follows (see Appendix A):

$$\text{SNR}_{\text{net}} = K_{\text{rad}} N_r \frac{P_t}{R_{\text{net}}^4}, \quad (10)$$

where

$$K_{\text{rad}} = \frac{G_t G_r \sigma_t \lambda^2}{(4\pi)^3 k T_o B_r F_r L}, \quad (11)$$

P_t is the total transmitting power of radar network system.

Note that, when $N_t = N_r = 1$, we can obtain the monostatic case

$$\text{SNR}_{\text{mon}} = K_{\text{rad}} \frac{P_t}{R_{\text{mon}}^4}, \quad (12)$$

where R_{mon} is the distance between the monostatic radar and the target, while, for intercept receiver, the SNR equation is

$$\text{SNR}_{\text{int}} = K_{\text{int}} \frac{P_t}{R_{\text{int}}^2}, \quad (13)$$

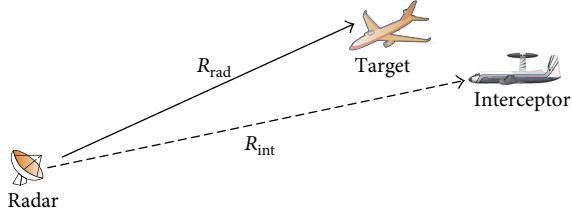


FIGURE 2: The geometry of radar, target, and interceptor.

where

$$K_{\text{int}} = \frac{G_t G_i \lambda^2}{(4\pi)^2 k T_o B_i F_i L_i}, \quad (14)$$

SNR_{int} is the SNR at the interceptor signal processor input, G'_t is the gain of the radar's transmitting antenna in the direction of the intercept receiver, G_i is the gain of the intercept receiver's antenna, F_i is the interceptor noise factor, B_i is the bandwidth of the interceptor, R_{int} is the range from radar network to the intercept receiver, and L_i refers to the losses from the radar antenna to the receiver. For simplicity, we assume that the intercept receiver is carried by the target. As such, the interceptor detects the radar emission from the main lobe; that is, $G'_t = G_t$.

Herein, Schleher intercept factor is employed to evaluate LPI performance for radar network. The definition of Schleher intercept factor can be calculated as follows:

$$\alpha = \frac{R_{\text{int}}}{R_{\text{rad}}}, \quad (15)$$

where R_{rad} is the detection range of radar and R_{int} is the intercept range of intercept receiver, as illustrated in Figure 2.

Based on the definition of Schleher intercept factor, if $\alpha > 1$, radar can be detected by the interceptor, while if $\alpha \leq 1$, radar can detect the target and the interceptor cannot detect the radar. Therefore, radar can meet LPI performance when $\alpha \leq 1$. Moreover, minimization of Schleher intercept factor leads to better LPI performance for radar network architecture.

With the derivation of Schleher intercept factor in Appendix B, it can be observed that, for a predefined target detection performance, the closer the distance between radar system and target is, the less power the radar system needs to transmit on guarantee of target detection performance. For simplicity, the maximum intercept factor $\alpha_{\text{mon}}^{\text{max}}$ is normalized to be 1 when the monostatic radar transmits the maximal power $P_{\text{tot}}^{\text{max}}$, and $\text{SNR}_{\text{net}} = \text{SNR}_{\text{mon}}$. Therefore, when the transmission power is P_t , the intercept factor for radar network system can be simplified as follows:

$$\alpha_{\text{net}} = \frac{\alpha_{\text{mon}}}{N_r^{1/4}} = \left(\frac{P_t}{P_{\text{tot}}^{\text{max}} \cdot N_r} \right)^{1/4}, \quad (16)$$

where α_{mon} is the Schleher intercept factor for monostatic radar. From (16), one can see that Schleher intercept factor α_{net} is reduced with the increase of the number of radar receivers N_r and the decrease of the total transmission power P_t in the network system.

3.2. Information-Theoretic Criteria Based LPI Optimization

3.2.1. Bhattacharyya Distance Based LPI Optimization Scheme. It is introduced in [6] that Bhattacharyya distance $B(p_0, p_1)$ measures the distance between two probability density functions (pdf) p_0 and p_1 . The Bhattacharyya distance provides an upper bound on the probability of false alarm P_{fa} and at the same time yields a lower bound on the probability of detection P_d .

Consider two multivariate Gaussian distributions P_0 and P_1 , $P_0 \sim \text{CN}(0, \sigma_0)$, and $P_1 \sim \text{CN}(0, \sigma_1)$; the Bhattacharyya distance $B(P_0, P_1)$ can be obtained as [6]

$$B(P_0, P_1) = \log \left\{ \frac{\det[0.5(\sigma_0 + \sigma_1)]}{\sqrt{\det(\sigma_0) \det(\sigma_1)}} \right\}. \quad (17)$$

Let $B[f(r | H_0), f(r | H_1)]$ represent Bhattacharyya distance between H_0 and H_1 , where $f(r | H_0)$ and $f(r | H_1)$ are the pdfs of \mathbf{r} under hypotheses H_0 and H_1 . For the binary hypothesis testing problem, we have that

$$\begin{aligned} B_{\text{net}} &\triangleq B[f(r | H_0), f(r | H_1)] \\ &= \sum_{i=1}^{N_t} \sum_{j=1}^{N_r} \log \left(\frac{1 + 0.5 \zeta_{ij}}{\sqrt{1 + \zeta_{ij}}} \right) \\ &= \sum_{i=1}^{N_t} \sum_{j=1}^{N_r} \log \left[\frac{1 + P_{ti} R_g p_{ij}^2 (2R_\theta)^{-1}}{\sqrt{1 + P_{ti} R_g p_{ij}^2 (R_\theta)^{-1}}} \right] \\ &= \sum_{i=1}^{N_t} \sum_{j=1}^{N_r} \log \left[\frac{1 + P_{ti} R_g G_{ti} G_{rj} (2R_\theta R_{ti}^2 R_{rj}^2)^{-1}}{\sqrt{1 + P_{ti} R_g G_{ti} G_{rj} (R_\theta R_{ti}^2 R_{rj}^2)^{-1}}} \right]. \end{aligned} \quad (18)$$

Based on the discussion in [6], maximization of the Bhattacharyya distance minimizes the upper bound on P_{fa} while it maximizes the lower bound on P_d . As expressed in (18), the Bhattacharyya distance derived here can be applied to evaluate the target detection performance of radar network as a function of different parameters, such as the transmitting power of each netted radar and the number of netted radars in the network. Intuitively, the greater the Bhattacharyya distance between the two distributions of the binary hypothesis testing problem, the better the capability of radar network system to detect the target, which would make the network system more vulnerable in modern electronic warfare. Therefore, the Bhattacharyya distance can provide guidance to the problem of LPI optimization for radar network architecture.

Here, we focus on the LPI optimization problem for radar network architecture, where Schleher intercept factor is minimized by optimizing transmission power allocation among netted radars in the network for a predetermined

Bhattacharyya distance threshold, such that the LPI performance is met on the guarantee of target detection performance. Eventually, the underlying LPI optimization problem can be formulated as follows:

$$\begin{aligned} \min_{\vec{P}_t} \quad & \alpha_{\text{net}}, \\ \text{s.t.:} \quad & B_{\text{net}} \geq B^{\text{th}}, \\ & \sum_{i=1}^{N_t} P_{ti} \leq P_{\text{tot}}^{\text{max}}, \\ & 0 \leq P_{ti} \leq P_{ti}^{\text{max}} \quad (\forall i), \end{aligned} \quad (19)$$

where $\vec{P}_t = [P_{t1}, P_{t2}, \dots, P_{tN_t}]^T$ is the transmitting power of radar network, B^{th} is the Bhattacharyya distance threshold for target detection, $P_{\text{tot}}^{\text{max}}$ is the maximum total transmission power of radar network, and P_{ti}^{max} (for all i) is the maximum transmission power of the corresponding netted radar node.

3.2.2. J-Divergence Based LPI Optimization Scheme. The J-divergence $J(p_0, p_1)$ is another metric to measure the distance between two pdfs p_0 and p_1 . It is defined as follows:

$$J(p_0, p_1) \triangleq D(p_0 \parallel p_1) + D(p_1 \parallel p_0), \quad (20)$$

where $D(\cdot)$ is the Kullback-Leibler divergence. It is shown in [19] that, for any fixed value of P_{fa} ,

$$D[f(r | H_0) \parallel f(r | H_1)] = \lim_{N \rightarrow \infty} \left[-\frac{1}{N} \log(1 - P_d) \right] \quad (21)$$

and, for any fixed value of P_d , we can obtain

$$D[f(r | H_1) \parallel f(r | H_0)] = \lim_{N \rightarrow \infty} \left[-\frac{1}{N} \log(P_{fa}) \right]. \quad (22)$$

From (21) and (22), we can observe that for any fixed P_{fa} the maximization of Kullback-Leibler divergence $D[f(r | H_0) \parallel f(r | H_1)]$ results in an asymptotic maximization of P_d , while for any fixed P_d the maximization of Kullback-Leibler divergence $D[f(r | H_1) \parallel f(r | H_0)]$ results in an asymptotic minimization of P_{fa} .

With the derivation in [6], we have that

$$\begin{aligned} J_{\text{net}} & \triangleq J[f(r | H_0), f(r | H_1)] \\ & = \sum_{i=1}^{N_t} \sum_{j=1}^{N_r} \frac{\zeta_{ij}^2}{1 + \zeta_{ij}} \end{aligned}$$

$$\begin{aligned} & = \sum_{i=1}^{N_t} \sum_{j=1}^{N_r} \frac{[P_{ti} R_g p_{ij}^2 (R_\theta)^{-1}]^2}{1 + P_{ti} R_g p_{ij}^2 (R_\theta)^{-1}} \\ & = \sum_{i=1}^{N_t} \sum_{j=1}^{N_r} \frac{[P_{ti} R_g G_{ti} G_{rj} (R_\theta R_{ti}^2 R_{rj}^2)^{-1}]^2}{1 + P_{ti} R_g G_{ti} G_{rj} (R_\theta R_{ti}^2 R_{rj}^2)^{-1}}. \end{aligned} \quad (23)$$

Consequently, the corresponding LPI optimization problem can be expressed as follows:

$$\begin{aligned} \min_{\vec{P}_t} \quad & \alpha_{\text{net}}, \\ \text{s.t.:} \quad & J_{\text{net}} \geq J^{\text{th}}, \\ & \sum_{i=1}^{N_t} P_{ti} \leq P_{\text{tot}}^{\text{max}}, \\ & 0 \leq P_{ti} \leq P_{ti}^{\text{max}} \quad (\forall i), \end{aligned} \quad (24)$$

where J^{th} is the J-divergence threshold for target detection.

3.3. The Unified Framework Based on NPGA. In this subsection, we cast the LPI optimization problems based on various information-theoretic criteria investigated earlier under a unified optimization framework. Furthermore, we formulate the following general form of the optimization problems in (19) and (24):

$$\begin{aligned} \min_{\vec{P}_t} \quad & \alpha_{\text{net}}, \\ \text{s.t.:} \quad & \gamma_{\text{net}} \geq \gamma^{\text{th}}, \\ & \sum_{i=1}^{N_t} P_{ti} \leq P_{\text{tot}}^{\text{max}}, \\ & 0 \leq P_{ti} \leq P_{ti}^{\text{max}} \quad (\forall i), \end{aligned} \quad (25)$$

where $\gamma_{\text{net}} \in \{B_{\text{net}}, J_{\text{net}}\}$ and γ^{th} is the corresponding threshold for target detection.

In this paper, we utilize the nonlinear programming based genetic algorithm (NPGA) to seek the optimal solutions to the resulting nonconvex, nonlinear, and constrained problem (25). The NPGA has a good performance on the convergence speed, and it improves the searching performance of ordinary genetic algorithm.

The NPGA procedure is illustrated in Figure 3, where the population initialization module is utilized to initialize the population according to the resulting problem, while the calculating fitness value module is to calculate the fitness values of individuals in the population. Selection, crossover, and mutation are employed to seek the optimal solution, where N is a constant. If the evolution is N 's multiples, we can use NP approach to accelerate the convergence speed.

So far, we have completed the derivation of Schleher intercept factor for radar network architecture and

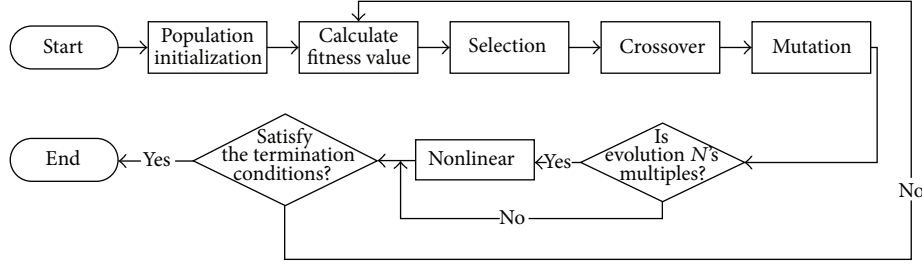


FIGURE 3: Flow diagram of NPGA procedure.

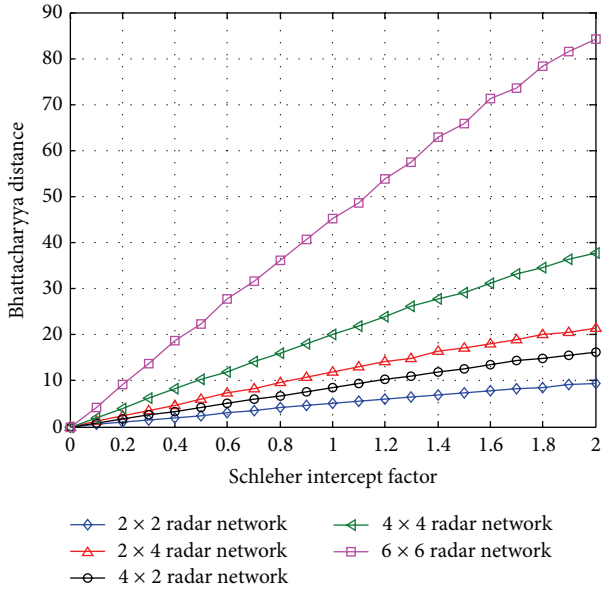
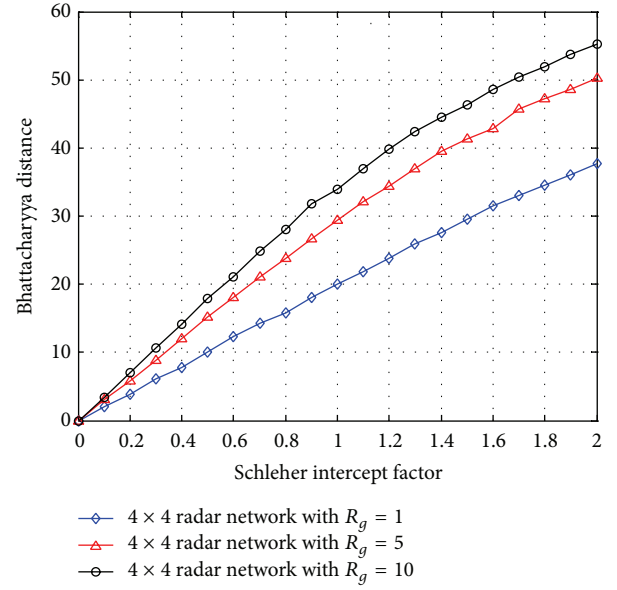


FIGURE 4: Bhattacharyya distance versus Schleher intercept factor for different radar network architectures.

FIGURE 5: Bhattacharyya distance versus Schleher intercept factor for different target scattering intensity with $N_t = N_r = 4$.

the information-theoretic criteria based LPI optimization schemes. In what follows, some numerical simulations are provided to confirm the effectiveness of our presented LPI optimization algorithms for radar network architecture.

4. Numerical Simulations

In this section, we provide several numerical simulations to examine the performance of the proposed LPI optimization algorithms as (19) and (24). Throughout this section, we assume that $P_{\text{tot}}^{\text{max}} = \sum_{i=1}^{N_t} P_{ti} = 24 \text{ KW}$, $G_t = G_r = 30 \text{ dB}$, $R_\theta = 10^{-10}$, and $R_g = 1$. The SNR is set to be 13 dB. The traditional monostatic radar can detect the target whose RCS is 0.05 m^2 in the distance $R_{\text{RMAX}} = 106.1 \text{ km}$ by transmitting the maximum power $P_{\text{tot}}^{\text{max}} = 24 \text{ KW}$, where the intercept factor is normalized to be 1 for simplicity.

4.1. LPI Performance Analysis. Figures 4 and 6 show the Bhattacharyya distance and logarithmic J-divergence versus Schleher intercept factor for different radar network architectures, respectively, which are conducted 10^6 Monte

Carlo trials. We can observe in Figures 4 and 6 that as Schleher intercept factor increases from $\alpha_{\text{net}} = 0$ to $\alpha_{\text{net}} = 2$ the achievable Bhattacharyya distance and logarithmic J-divergence are increased. This is due to the fact that as the intercept factor increases more transmission power would be allocated, which makes the achievable Bhattacharyya distance and logarithmic J-divergence increase correspondingly as theoretically proved in (18) and (23). Furthermore, it can be seen from Figures 4 and 6 that, with the same target detection threshold, Schleher intercept factor can be significantly reduced as the number of transmitters and receivers in the network system increases. Therefore, increasing the number of netted radars can effectively improve the LPI performance for radar network. This confirms the LPI benefits of the radar network architecture with more netted radars.

As shown in Figures 5 and 7, we illustrate the Bhattacharyya distance and logarithmic J-divergence versus Schleher intercept factor for different target scattering intensity with $N_t = N_r = 4$, respectively. It is depicted that as the target scattering intensity increases from $R_g = 1$ to $R_g = 10$ the achievable Bhattacharyya distance and logarithmic J-divergence are significantly increased. This is

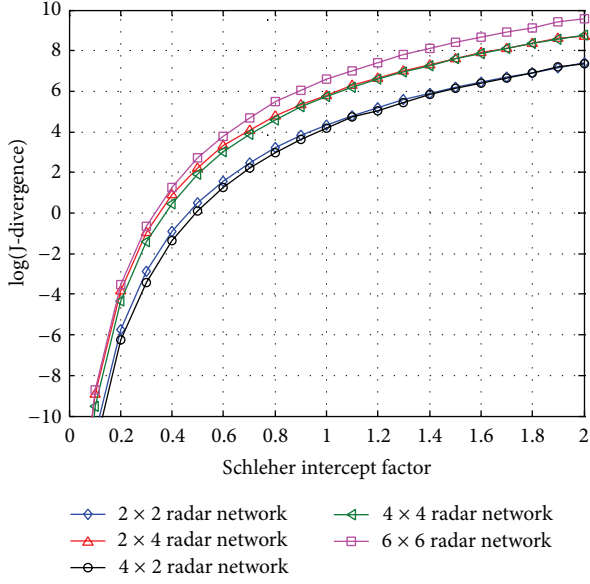


FIGURE 6: Logarithmic J-divergence versus Schleher intercept factor for different radar network architectures.

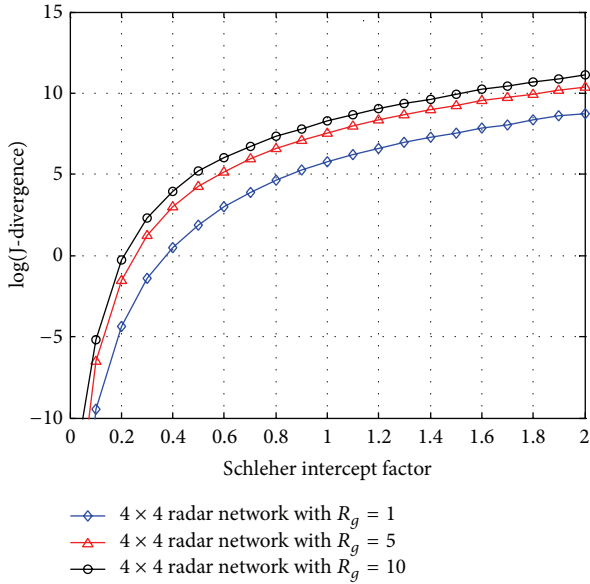


FIGURE 7: Logarithmic J-divergence versus Schleher intercept factor for different target scattering intensity with $N_t = N_r = 4$.

because the radar network system can detect the target with large scattering intensity easily with high P_d and low P_{fa} .

4.2. Target Tracking with LPI Optimization. In this subsection, we consider a 4×4 radar network system ($N_t = N_r = 4$) in the simulation, and it is widely deployed in modern battlefield. The target detection threshold γ^{th} can be calculated in the condition that the transmission power of each radar is 6 KW in the distance 150 km between the radar network and the target, which is the minimum value of the basic performance requirement for target detection. As

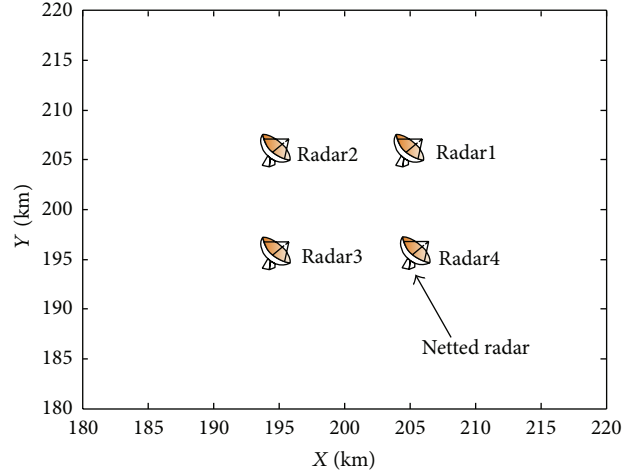


FIGURE 8: The radar network system configuration in two dimensions.

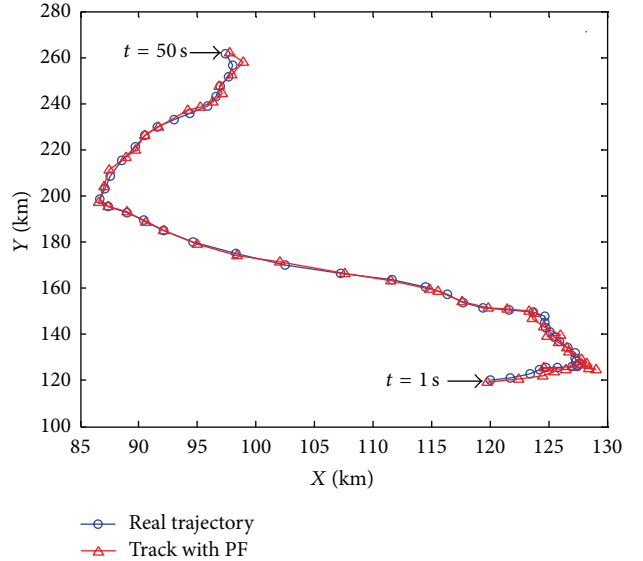


FIGURE 9: Target tracking scenario.

mentioned before, it is supposed that the intercept receiver is carried by the target. It is depicted in Figure 8 that the netted radars in the network are spatially distributed in the surveillance area at the initial time $t = 0$.

We track a single target by utilizing particle filtering (PF) method, where 5000 particles are used to estimate the target state. Figure 9 shows one realization of the target trajectory for 50 s, and the tracking interval is chosen to be 1 s. With the radar network configuration in Figure 8 and the target tracking scenario in Figure 9, we can obtain the distances changing curve between the netted radars and the target in the tracking process as depicted in Figure 10. Without loss of generality, we set *Radar1* as the distributed data fusion center and capitalize the weighted average approach to obtain the estimated target state.

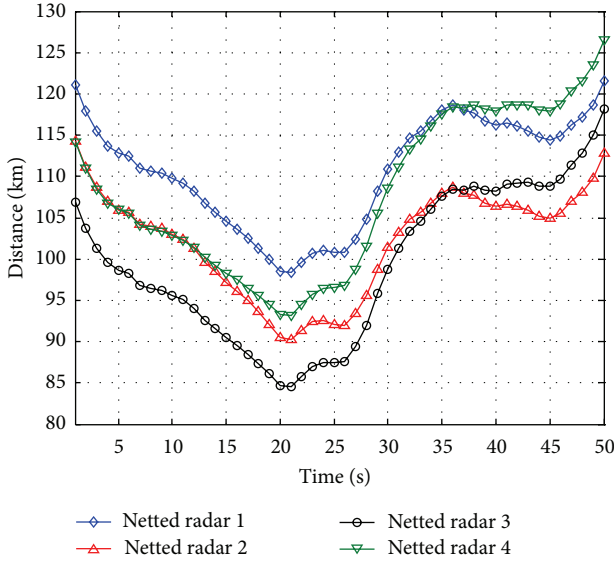


FIGURE 10: The distances between the netted radars and the target.

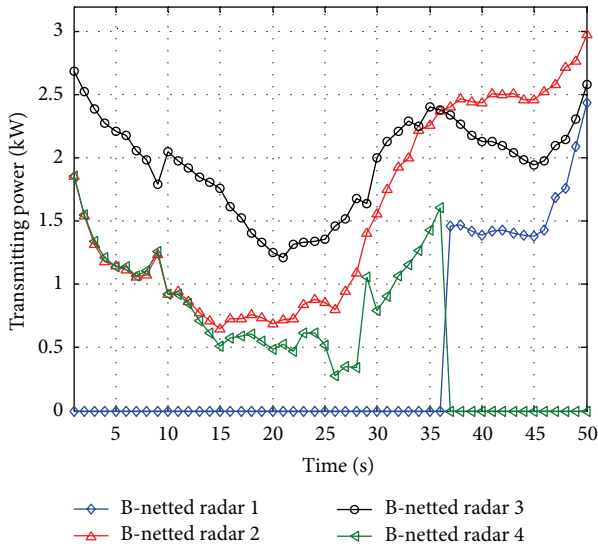


FIGURE 11: The transmitting power of netted radars utilizing Bhatlacharya distance based LPI optimization in the tracking process.

To obtain the optimal transmission power allocation of radar network, we utilize NPGA to solve (19) and (24). Let the population size be 100, let the crossover probability be 0.6, and let the mutation probability be 0.01. The population evolves 10 generations. Figure 11 shows the transmitting power of netted radars utilizing Bhatlacharya distance based LPI optimization in the tracking process, while Figure 12 depicts the J-divergence based case. Before $t = 36$ s, netted radars 2, 3, and 4 are selected to track the target, which are the ones closest to the target, while netted radar 1 is selected instead of radar 2 after $t = 36$ s, which is because netted radars 1, 2, and 3 have the best channel conditions in the network. From Figures 11 and 12, we can see that the transmission power allocation is determined by the locations of single

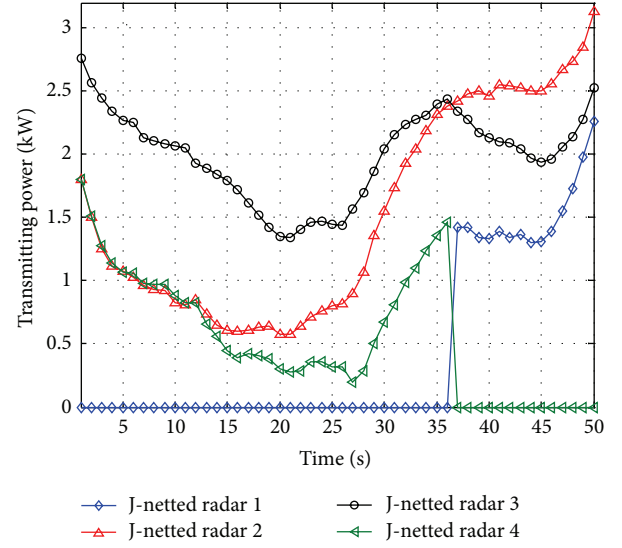


FIGURE 12: The transmitting power of netted radars utilizing J-divergence based LPI optimization in the tracking process.

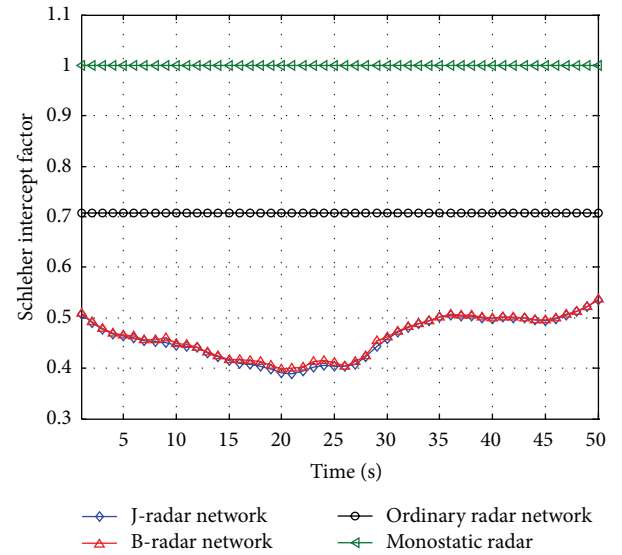


FIGURE 13: The normalized Schleher intercept factor comparison in the tracking process.

target relative to the netted radars and their propagation losses. To be specific, in the LPI optimization process, more transmitting power is allocated to the radar nodes that are located closer to the target; this is due to the fact that they suffer less propagation losses.

Figure 13 demonstrates the advantage of our proposed optimization problems based on information-theoretic criteria. The traditional monostatic radar transmits 24 KW constantly, while the ordinary radar network has a constant sum of transmitted power 24 KW and each radar node transmits uniform power. One can see that Schleher intercept factor for radar network employing the information-theoretic criteria based LPI optimization strategies is strictly smaller

than that of traditional monostatic radar and ordinary radar network across the whole region, which further shows the LPI enhancement by exploiting our presented LPI optimization schemes in radar network to defend against passive intercept receiver. Moreover, it can be seen in Figure 13 that, in terms of the same system constraints and fundamental quantity, Bhattacharyya distance based LPI optimization is asymptotically equivalent to the J-divergence based case.

4.3. Discussion. According to Figures 4–13, we can deduce the following conclusions for radar network architecture.

- (1) From Figures 4 to 7, we can observe that as the predefined threshold of target detection increases more transmission power would be allocated for radar network to meet the detection performance, while the intercept factor is increased subsequently, which is vulnerable in electronic warfare. In other words, there exists a tradeoff between LPI and target detection performance in radar network system, and the LPI performance would be sacrificed with target detection consideration.
- (2) In the numerical simulations, we observe that the proposed optimization schemes (19) and (24) can be employed to enhance the LPI performance for radar network. Based on the netted radars' spatial distribution with respect to the target, we can improve the LPI performance by optimizing transmission power allocation among netted radars. As indicated in Figures 11 and 12, netted radars with better channel conditions are favorable over others. In addition, it can be observed that exploiting our proposed algorithms can effectively improve the LPI performance of radar network to defend against intercept receiver, and Bhattacharyya distance based LPI optimization algorithm is asymptotically equivalent to the J-divergence based case under the same system constraints and fundamental quantity.

5. Conclusions

In this paper, we investigated the problem of LPI design in radar network architecture, where two LPI optimization schemes based on information-theoretic criteria have been proposed. The NPGA was employed to tackle the highly nonconvex and nonlinear optimization problems. Simulations have demonstrated that our proposed strategies are effective and valuable to improve the LPI performance for radar network, and it is indicated that these two optimization problems are asymptotically equivalent to each other under the same system constraints. Note that only single target was considered in this paper. Nevertheless, it is convenient to be extended to multiple targets scenario, and the conclusions obtained in this study suggest that similar LPI benefits would be obtained for the multiple targets case. Future work will look into the adaptive threshold design of target detection performance in radar network architectures.

Appendices

A.

Assume that every transmitter-receiver combination in the network can be the same and $R_{\text{net}}^2 \triangleq R_{ti} \cdot R_{rj}$, where the radar network SNR (1) can be written as follows:

$$\text{SNR}_{\text{net}} = K_{\text{rad}} \sum_{i=1}^{N_t} \sum_{j=1}^{N_r} \frac{P_{ti}}{R_{\text{net}}^4}, \quad (\text{A.1})$$

where

$$K_{\text{rad}} = \frac{G_t G_r \sigma_t \lambda^2}{(4\pi)^3 k T_o B_r F_r L}. \quad (\text{A.2})$$

Assume that the sum of the effective radiated power (ERP) from all the radars in the network is equivalent to that of monostatic radar; that is,

$$\text{ERP} = \sum_{i=1}^{N_t} P_{ti} G_{ti} = P_t G_t, \quad (\text{A.3})$$

where P_t and G_t are the transmitting power and transmitting antenna gain of the monostatic radar, respectively. For $G_{ti} = G_t$ (for all i), we can rewrite (A.1) as follows:

$$\text{SNR}_{\text{net}} = K_{\text{rad}} N_t \frac{P_t}{R_{\text{net}}^4}. \quad (\text{A.4})$$

B.

According to (15), we can derive the intercept factor for radar network as

$$\alpha_{\text{net}} = \frac{R_{\text{int}}}{R_{\text{net}}} = \left(\frac{P_t \cdot K_{\text{int}}^2 \cdot \text{SNR}_{\text{net}}}{K_{\text{rad}} \cdot N_r \cdot \text{SNR}_{\text{int}}^2} \right)^{1/4} \quad (\text{B.1})$$

and the intercept factor for conventional monostatic radar as

$$\alpha_{\text{mon}} = \frac{R_{\text{int}}}{R_{\text{mon}}} = \left(\frac{P_t \cdot K_{\text{int}}^2 \cdot \text{SNR}_{\text{mon}}}{K_{\text{rad}} \cdot \text{SNR}_{\text{int}}^2} \right)^{1/4}. \quad (\text{B.2})$$

When $\text{SNR}_{\text{net}} = \text{SNR}_{\text{mon}}$, we can readily obtain the relationship between the intercept factors for radar network α_{net} and for the monostatic case α_{mon} :

$$\alpha_{\text{net}} = \frac{\alpha_{\text{mon}}}{N_r^{1/4}}. \quad (\text{B.3})$$

Furthermore, for monostatic radar, we can assume that

$$\text{SNR}_{\text{mon}} = K_{\text{rad}} \frac{P_t}{R_{\text{mon}}^4} = K_{\text{rad}} \frac{P_{\text{tot}}^{\text{max}}}{R_{\text{RMAX}}^4}, \quad (\text{B.4})$$

where $P_{\text{tot}}^{\text{max}}$ is the maximal power of the monostatic radar and R_{RMAX} is the corresponding maximal detection range. Then, we can obtain

$$\frac{R_{\text{mon}}}{R_{\text{RMAX}}} = \left(\frac{P_t}{P_{\text{tot}}^{\text{max}}} \right)^{1/4}. \quad (\text{B.5})$$

Similarly, for intercept receiver, we have the following:

$$\text{SNR}_{\text{int}} = K_{\text{int}} \frac{P_t}{R_{\text{int}}^2} = K_{\text{int}} \frac{P_{\text{tot}}^{\text{max}}}{R_{\text{IMAX}}^2}, \quad (\text{B.6})$$

$$\frac{R_{\text{int}}}{R_{\text{IMAX}}} = \left(\frac{P_t}{P_{\text{tot}}^{\text{max}}} \right)^{1/2}, \quad (\text{B.7})$$

where R_{IMAX} is the intercept range when the transmitting power of radar is $P_{\text{tot}}^{\text{max}}$.

Using (15), (B.5), and (B.7), we can obtain the following expression:

$$\frac{\alpha_{\text{mon}}}{\alpha_{\text{mon}}^{\text{max}}} = \frac{R_{\text{int}}/R_{\text{mon}}}{R_{\text{IMAX}}/R_{\text{RMAX}}} = \left(\frac{P_t}{P_{\text{tot}}^{\text{max}}} \right)^{1/4}, \quad (\text{B.8})$$

where $\alpha_{\text{mon}}^{\text{max}}$ is Schleher intercept factor corresponding to the maximal transmitting power $P_{\text{tot}}^{\text{max}}$.

Conflict of Interests

The authors declare that there is no conflict of interests regarding the publication of this paper.

Acknowledgments

The authors would like to thank the anonymous reviewers for their comments that help to improve the quality of this paper. The support provided by the National Natural Science Foundation of China (Grant no. 61371170), Funding of Jiangsu Innovation Program for Graduate Education (CX LX13.154), the Fundamental Research Funds for the Central Universities, the Priority Academic Program Development of Jiangsu Higher Education Institutions (PADA), and Key Laboratory of Radar Imaging and Microwave Photonics, Ministry of Education, Nanjing University of Aeronautics and Astronautics, Nanjing, China, is gratefully acknowledged.

References

- [1] E. P. Phillip, *Detecting and Classifying Low Probability of Intercept Radar*, Artech House, Boston, Mass, USA, 2009.
- [2] A. M. Haimovich, R. S. Blum, and L. J. Cimini Jr., "MIMO radar with widely separated antennas," *IEEE Signal Processing Magazine*, vol. 25, no. 1, pp. 116–129, 2008.
- [3] A. L. Hume and C. J. Baker, "Netted radar sensing," in *Proceedings of the 2001 CIE International Conference on Radar*, pp. 23–26, 2001.
- [4] E. Fishler, A. Haimovich, R. S. Blum, L. J. Cimini Jr., D. Chizhik, and R. A. Valenzuela, "Spatial diversity in radars-Models and detection performance," *IEEE Transactions on Signal Processing*, vol. 54, no. 3, pp. 823–838, 2006.
- [5] Y. Yang and R. S. Blum, "MIMO radar waveform design based on mutual information and minimum mean-square error estimation," *IEEE Transactions on Aerospace and Electronic Systems*, vol. 43, no. 1, pp. 330–343, 2007.
- [6] M. M. Naghsh, M. H. Mahmoud, S. P. Shahram, M. Soltanalian, and P. Stoica, "Unified optimization framework for multi-static radar code design using information-theoretic criteria," *IEEE Transactions on Signal Processing*, vol. 61, no. 21, pp. 5401–5416, 2013.
- [7] R. Niu, R. S. Blum, P. K. Varshney, and A. L. Drozd, "Target localization and tracking in noncoherent multiple-input multiple-output radar systems," *IEEE Transactions on Aerospace and Electronic Systems*, vol. 48, no. 2, pp. 1466–1489, 2012.
- [8] P. Chavali and A. Nehorai, "Scheduling and power allocation in a cognitive radar network for multiple-target tracking," *IEEE Transactions on Signal Processing*, vol. 60, no. 2, pp. 715–729, 2012.
- [9] H. Godrich, A. Petropulu, and H. V. Poor, "Optimal power allocation in distributed multiple-radar configurations," in *Proceeding of the IEEE International Conference on Acoustics, Speech, and Signal Processing (ICASSP '11)*, pp. 2492–2495, Prague, Czech Republic, May 2011.
- [10] H. Godrich, A. P. Petropulu, and H. V. Poor, "Power allocation strategies for target localization in distributed multiple-radar architectures," *IEEE Transactions on Signal Processing*, vol. 59, no. 7, pp. 3226–3240, 2011.
- [11] H. Godrich, A. Petropulu, and H. V. Poor, "Estimation performance and resource savings: tradeoffs in multiple radars systems," in *Proceedings of the IEEE International Conference on Acoustics, Speech, and Signal Processing (ICASSP '12)*, pp. 5205–5208, Kyoto, Japan, March 2012.
- [12] C. G. Shi, J. J. Zhou, F. Wang, and J. Chen, "Target threatening level based optimal power allocation for LPI radar network," in *Proceedings of the 2nd International Symposium on Instrumentation and Measurement, Sensor Network and Automation (IMSNA '13)*, pp. 634–637, Toronto, Canada, December 2013.
- [13] X. Song, P. Willett, and S. Zhou, "Optimal power allocation for MIMO radars with heterogeneous propagation losses," in *Proceedings of the IEEE International Conference on Acoustics, Speech, and Signal Processing (ICASSP '12)*, pp. 2465–2468, Kyoto, Japan, March 2012.
- [14] X. F. Song, P. Willett, S. Zhou, and J. Glaz, "MIMO radar detection with heterogeneous propagation losses," in *Proceedings of the IEEE Statistical Signal Processing Workshop (SSP '12)*, pp. 776–779, August 2012.
- [15] D. C. Schleher, "LPI radar: fact or fiction," *IEEE Aerospace and Electronic Systems Magazine*, vol. 21, no. 5, pp. 3–6, 2006.
- [16] D. Lynch Jr., *Introduction to RF Stealth*, Sci Tech Publishing, 2004.
- [17] A. G. Stove, A. L. Hume, and C. J. Baker, "Low probability of intercept radar strategies," *IEEE Proceedings Radar, Sonar and Navigation*, vol. 151, no. 5, pp. 249–260, 2004.
- [18] D. E. Lawrence, "Low probability of intercept antenna array beamforming," *IEEE Transactions on Antennas and Propagation*, vol. 58, no. 9, pp. 2858–2865, 2010.
- [19] T. Kailath, "The divergence and Bhattacharyya distance measures in signal detection," *IEEE Transaction on Communication Technology*, vol. 15, no. 2, pp. 52–60, 1967.

Research Article

Computationally Efficient DOA Tracking Algorithm in Monostatic MIMO Radar with Automatic Association

Huaxin Yu,¹ Xiaofei Zhang,^{1,2} Xueqiang Chen,¹ and Hailang Wu¹

¹ College of Electronic and Information Engineering, Nanjing University of Aeronautics & Astronautics, Nanjing 210016, China

² Laboratory of Modern Acoustic of Ministry of Education, Nanjing University, Nanjing 210093, China

Correspondence should be addressed to Xiaofei Zhang; njxnd88@126.com

Received 16 March 2014; Revised 23 May 2014; Accepted 10 June 2014; Published 3 July 2014

Academic Editor: Frankie KitWing Chan

Copyright © 2014 Huaxin Yu et al. This is an open access article distributed under the Creative Commons Attribution License, which permits unrestricted use, distribution, and reproduction in any medium, provided the original work is properly cited.

We consider the problem of tracking the direction of arrivals (DOA) of multiple moving targets in monostatic multiple-input multiple-output (MIMO) radar. A low-complexity DOA tracking algorithm in monostatic MIMO radar is proposed. The proposed algorithm obtains DOA estimation via the difference between previous and current covariance matrix of the reduced-dimension transformation signal, and it reduces the computational complexity and realizes automatic association in DOA tracking. Error analysis and Cramér-Rao lower bound (CRLB) of DOA tracking are derived in the paper. The proposed algorithm not only can be regarded as an extension of array-signal-processing DOA tracking algorithm in (Zhang et al. (2008)), but also is an improved version of the DOA tracking algorithm in (Zhang et al. (2008)). Furthermore, the proposed algorithm has better DOA tracking performance than the DOA tracking algorithm in (Zhang et al. (2008)). The simulation results demonstrate effectiveness of the proposed algorithm. Our work provides the technical support for the practical application of MIMO radar.

1. Introduction

Multiple-input multiple-output (MIMO) radar employs multiple antennas to simultaneously transmit diverse waveforms and utilizes multiple antennas to receive the reflected signals [1–5]. Direction of arrival (DOA) algorithms in MIMO radar have been recently investigated in [6–24], which contain estimation of signal parameters via rotational invariance technique (ESPRIT) algorithms [6–8], Capon algorithms [10, 11], multiple signal classification (MUSIC) algorithms [9, 12–15], parallel factor (PARAFAC) analysis algorithms [16–18], propagator method [19, 20], quaternion method [21, 22], compressive sampling methods [23, 24], and so on. However, the algorithms mentioned above are, generally, used in offline situation, and they are not applicable for tracking moving targets. The online algorithms can be used for real-time application of MIMO radar.

DOA tracking for array antenna has been investigated for a long time, which contains projection approximation and subspace tracking (PAST) algorithm [25], projection approximation and subspace tracking of deflation (PASTd)

algorithm [26], Bi-iterative least-square method [27], Bi-iteration single value decomposition [28], and others [29, 30]. The DOA tracking algorithms in [25–30] have a high computational complexity. A low-complexity method was proposed in [31, 32] to track DOA of moving sources using the elements of the covariance matrix of the received signal in array signal processing, and the DOA tracking algorithm can implement automatic association, which is a key technique in DOA tracking [33].

DOA tracking for MIMO radar is to track the DOA of the moving targets. PARAFAC adaptive algorithms [17, 18] and PASTd [34] were used for DOA tracking for MIMO radar, but an extra data association is required. Kalman-PASTd was proposed in [35] for DOA tracking for monostatic MIMO Radar with automatic association. PARAFAC adaptive algorithm, PASTd algorithm, and Kalman-PASTd algorithm have high computational complexity. In the paper, we propose a computationally efficient DOA tracking algorithm in monostatic MIMO radar with automatic association.

In this paper, we reference the array-signal-processing DOA tracking idea in [31] to propose a DOA tracking

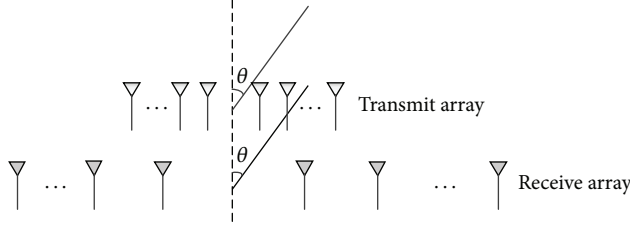


FIGURE 1: The array structure of monostatic MIMO radar.

algorithm which is suitable for MIMO radar. Using the reduced-dimension transformation for the received signal of MIMO radar, we obtain the covariance matrix of reduced-dimension transformation signal, and then we adopt an improved version for DOA tracking. The proposed algorithm can realize automatic association in DOA tracking. Error analysis and Cramér-Rao lower bound (CRLB) are also derived in this paper. Finally, the simulation results demonstrate the effectiveness and robustness of the proposed algorithm.

There are some differences between the work in [31] and the proposed algorithm. (1) Reference [31] proposed an effective DOA tracking algorithm in array signal processing, while we address DOA tracking problem for MIMO radar in the paper. (2) The DOA tracking algorithm in array signal processing in [31] requires the direction matrix of Vandermonde form. The direction matrix in MIMO radar is not a Vandermonde matrix, and the DOA tracking algorithm in [31] cannot be used directly for DOA tracking in MIMO radar. We employ the reduced-dimension transformation for the received signal to obtain the reduced-dimension direction matrix of Vandermonde form. (3) Our work improves the DOA tracking algorithm in [31] to enhance the DOA tracking performance in MIMO radar, since it fully uses the Toeplitz matrix property to eliminate the noise. Therefore, the proposed algorithm not only can be regarded as an extension of the work in [31], but also is an improved algorithm. Simulation results show that the proposed algorithm has much better DOA tracking performance than the DOA tracking algorithm in [31].

The reminder of this paper is structured as follows. Section 2 develops the data model for monostatic MIMO radar. Section 3 establishes our DOA tracking algorithm based on the elements of the covariance matrix of the reduced-dimension transformation signal. In Section 4, error analysis and Cramér-Rao lower bound (CRLB) are derived. In Section 5, simulation results are presented to verify the effectiveness of the proposed algorithm, while the conclusions are made in Section 6.

Notation. $(\cdot)^T, (\cdot)^H, (\cdot)^{-1}$, and $(\cdot)^+$ denote transpose, conjugate-transpose, inverse, and pseudoinverse operations, respectively. $\text{diag}(\mathbf{v})$ stands for diagonal matrix whose diagonal is a vector \mathbf{v} ; \mathbf{I}_K is a $K \times K$ identity matrix; \otimes , \circ , and \oplus are the Kronecker product, Khatri-Rao product, and Hadamard product, respectively. $E(\cdot)$ denotes the expectation operator. $\hat{\mathbf{X}}$ denotes the estimated value of \mathbf{X} .

2. Data Model

We consider a monostatic MIMO radar system equipped with both uniform linear arrays (ULAs) for the transmit/receive array, in which M elements and N elements are arranged with half-wavelength spacing between adjacent antennas, respectively. The array structure of monostatic MIMO radar is shown in Figure 1. We assume that there are K uncorrelated targets. At time t , the output of the matched filters at the receiver can be expressed as [9]

$$\begin{aligned} \mathbf{r}(t) &= [\mathbf{a}_r(\theta_{t,1}) \otimes \mathbf{a}_t(\theta_{t,1}), \dots, \mathbf{a}_r(\theta_{t,K}) \otimes \mathbf{a}_t(\theta_{t,K})] \mathbf{s}(t) + \mathbf{n}(t) \\ &= \mathbf{A}_t \mathbf{s}(t) + \mathbf{n}(t), \end{aligned} \quad (1)$$

where $\theta_{t,k}$ is the DOA of the k th target at time t . $\mathbf{a}_r(\theta_{t,k}) = [1, \exp(-j\pi \sin \theta_{t,k}), \dots, \exp(-j(M-1)\pi \sin \theta_{t,k})]^T$, $\mathbf{a}_t(\theta_{t,k}) = [1, \exp(-j\pi \sin \theta_{t,k}), \dots, \exp(-j(N-1)\pi \sin \theta_{t,k})]^T$. $\mathbf{s}(t) = [s_1(t), s_2(t), \dots, s_K(t)]^T$, and $s_k(t) = \rho_k e^{j2\pi f_k t}$ with f_k being Doppler frequency and ρ_k being the amplitude. We assume that $s_i(t)$ and $s_j(t)$ are uncorrelated for the different targets. $\mathbf{n}(t)$ is the received additive white Gaussian noise with noise vector of zeros mean and covariance matrix $\sigma^2 \mathbf{I}_{MN}$ an $MN \times 1$ noise vector. \otimes stands for Kronecker product. The matrix \mathbf{A}_t is

$$\mathbf{A}_t = [\mathbf{a}_r(\theta_{t,1}) \otimes \mathbf{a}_t(\theta_{t,1}), \dots, \mathbf{a}_r(\theta_{t,K}) \otimes \mathbf{a}_t(\theta_{t,K})]. \quad (2)$$

During the interval $((t-1)T_s, tT_s]$, $\theta_{t,k}$ is a constant and J snapshots of sensor data are available for the signal processing.

3. DOA Tracking Algorithm

The DOA tracking algorithm of array signal processing in [31] requires the direction matrix of Vandermonde form. The direction matrix \mathbf{A}_t in (2) is not a Vandermonde matrix, and the DOA tracking algorithm of array signal processing in [31] cannot be used directly for DOA tracking in MIMO radar. We employ the reduced-dimension transformation for the received signal to obtain the reduced-dimension direction matrix of Vandermonde form. In this paper, we reference the array-signal-processing DOA tracking idea in [31] to propose a low complexity DOA tracking algorithm which is suitable for MIMO radar.

3.1. Reduced-Dimension Transformation. $\mathbf{a}_r(\theta_{t,k}) \otimes \mathbf{a}_t(\theta_{t,k})$ can be expressed by [9]

$$\mathbf{a}_r(\theta_{t,k}) \otimes \mathbf{a}_t(\theta_{t,k}) = \mathbf{G}\mathbf{b}(\theta_{t,k}), \quad (3)$$

where $\mathbf{b}(\theta_{t,k}) = [1, \exp(-j\pi \sin \theta_{t,k}), \dots, \exp(-j\pi(M+N-2) \sin \theta_{t,k})]^T$, and

$$\mathbf{G} = \begin{bmatrix} \begin{matrix} 1 & 0 & \cdots & 0 & 0 & \cdots & 0 \\ 0 & 1 & \cdots & 0 & 0 & \cdots & 0 \\ \vdots & \vdots & \ddots & \vdots & \vdots & \ddots & \vdots \\ 0 & 0 & \cdots & 1 & 0 & \cdots & 0 \\ 0 & 1 & \cdots & 0 & 0 & \cdots & 0 \\ 0 & 0 & 1 & 0 & 0 & \cdots & 0 \\ \vdots & \vdots & \vdots & \ddots & \vdots & \ddots & \vdots \\ 0 & 0 & \cdots & 0 & 1 & 0 & 0 \end{matrix} & \left. \begin{matrix} \\ \\ \\ \\ \\ \\ \\ \end{matrix} \right\} M \\ \vdots \\ \begin{matrix} 0 & \cdots & 0 & 1 & 0 & \cdots & 0 \\ 0 & \cdots & 0 & 0 & 1 & \cdots & 0 \\ \vdots & \ddots & \vdots & \vdots & \vdots & \ddots & \vdots \\ 0 & \cdots & 0 & 0 & 0 & \cdots & 1 \end{matrix} & \left. \begin{matrix} \\ \\ \\ \\ \end{matrix} \right\} M \end{bmatrix} \in \mathbb{C}^{MN \times (M+N-1)}. \quad (4)$$

Then we define $\mathbf{W} \triangleq \mathbf{G}^H \mathbf{G}$ as follows:

$$\mathbf{W} = \text{diag} \left(1, 2, \dots, \underbrace{\min(M, N), \dots, \min(M, N)}_{|M-N|+1}, \dots, 2, 1 \right). \quad (5)$$

Using the reduced-dimension transformation $\mathbf{W}^{-1} \mathbf{G}^H$ for the receiver signal $\mathbf{r}(t)$, we obtain

$$\begin{aligned} \mathbf{y}(t) &= \mathbf{W}^{-1} \mathbf{G}^H \mathbf{r}(t) \\ &= \mathbf{W}^{-1} \mathbf{W} [\mathbf{b}(\theta_{t,1}), \dots, \mathbf{b}(\theta_{t,K})] \mathbf{s}(t) + \mathbf{W}^{-1} \mathbf{G}^H \mathbf{n}(t) \\ &= \mathbf{B}_t \mathbf{s}(t) + \mathbf{W}^{-1} \mathbf{G}^H \mathbf{n}(t), \end{aligned} \quad (6)$$

where

$$\mathbf{B}_t = [\mathbf{b}(\theta_{t,1}), \dots, \mathbf{b}(\theta_{t,K})] \in \mathbb{C}^{(M+N-1) \times K}. \quad (7)$$

$\mathbf{B}_t \in \mathbb{C}^{(M+N-1) \times K}$ is the direction matrix of Vandermonde form. Since the reduced-dimension matrix is sparse, its transformation adds less computational load.

The covariance matrix of $\mathbf{y}(t)$ in (6) is $\mathbf{R}_t \in \mathbb{C}^{(M+N-1) \times (M+N-1)}$. Consider

$$\begin{aligned} \mathbf{R}_t &= E[\mathbf{y}(t) \mathbf{y}^H(t)] \\ &= \mathbf{B}_t \mathbf{R}_s \mathbf{B}_t^H + \mathbf{R}_n'(t), \end{aligned} \quad (8)$$

where $\mathbf{R}_s = E[\mathbf{s}(t) \mathbf{s}^H(t)] = \text{diag}(|\rho_1|^2, |\rho_2|^2, \dots, |\rho_K|^2)$ and $\mathbf{R}_n'(t) = \mathbf{W}^{-1} \mathbf{G}^H \mathbf{R}_n \mathbf{G} \mathbf{W}^{-1}$ with $\mathbf{R}_n = E[\mathbf{n}(t) \mathbf{n}^H(t)]$.

3.2. DOA Tracking. The direction matrix in the reduced-dimension signal in (6) is a Vandermonde matrix, and we use the improved version of the DOA tracking in [31] for DOA tracking of MIMO radar.

We assume that $\theta_{t,k}$ is slowly varying. The DOA of the K targets at time t is $\theta_t = [\theta_{t,1}, \theta_{t,2}, \dots, \theta_{t,K}]$. Similarly, the DOA

at time $t+1$ is $\theta_{t+1} = [\theta_{t+1,1}, \theta_{t+1,2}, \dots, \theta_{t+1,K}]$, with $\theta_{t+1,k}$ being the DOA of the k th target at time $t+1$. We define

$$\Delta\theta_t = \theta_{t+1} - \theta_t, \quad (9)$$

where $\Delta\theta_t = [\Delta\theta_{t,1}, \Delta\theta_{t,2}, \dots, \Delta\theta_{t,K}]$ with $\Delta\theta_{t,k} = \theta_{t+1,k} - \theta_{t,k}$.

We define \mathbf{R}_{t+1} as the covariance matrices of the signal $\mathbf{y}(t)$ at time $t+1$. The covariance matrix is

$$\mathbf{R}_{t+1} = \mathbf{B}_{t+1} \mathbf{R}_s \mathbf{B}_{t+1}^H + \mathbf{R}_n'(t+1), \quad (10)$$

where $\mathbf{B}_{t+1} = [\mathbf{b}(\theta_{t+1,1}), \dots, \mathbf{b}(\theta_{t+1,K})]$ is the direction matrix at time $t+1$ and $\mathbf{b}(\theta_{t+1,k}) = [1, \exp(-j\pi \sin \theta_{t+1,k}), \dots, \exp(-j\pi(M+N-2) \sin \theta_{t+1,k})]^T$. $\mathbf{R}_n'(t+1)$ is the covariance matrix of the noise.

Then we can obtain [31, 36]

$$\Delta\mathbf{R}_t = \mathbf{R}_{t+1} - \mathbf{R}_t. \quad (11)$$

$\Delta\mathbf{R}_t$ is denoted by

$$\Delta\mathbf{R}_t = (\mathbf{B}_{t+1} \mathbf{R}_s \mathbf{B}_{t+1}^H - \mathbf{B}_t \mathbf{R}_s \mathbf{B}_t^H) + (\mathbf{R}_n'(t+1) - \mathbf{R}_n'(t)). \quad (12)$$

We assume that the noise covariance matrix at time $t+1$ is approximately equal to that at time t , and then we have

$$\Delta\mathbf{R}_t \approx \mathbf{B}_{t+1} \mathbf{R}_s \mathbf{B}_{t+1}^H - \mathbf{B}_t \mathbf{R}_s \mathbf{B}_t^H. \quad (13)$$

Using the Vandermonde characteristic of the matrices \mathbf{B}_t and \mathbf{B}_{t+1} , the noiseless $\Delta\mathbf{R}_t$ in (13) can be denoted by [31, 32, 36]

$$\Delta\mathbf{R}_t = \begin{bmatrix} 0 & b_1 & b_2 & \cdots & b_{M+N-2} \\ b_1^* & 0 & b_1 & \cdots & b_{M+N-3} \\ b_2^* & b_1^* & 0 & \cdots & b_{M+N-4} \\ \vdots & \vdots & \vdots & \ddots & \vdots \\ b_{M+N-2}^* & b_{M+N-3}^* & b_{M+N-4}^* & \cdots & 0 \end{bmatrix}, \quad (14)$$

where

$$b_n = \sum_{i=1}^K s_i (e^{jn\pi \sin(\theta_{t,i} + \Delta\theta_{t,i})} - e^{jn\pi \sin \theta_{t,i}}), \quad (15)$$

$$n = 1, 2, \dots, M+N-2,$$

where s_i is the (i, i) element of the matrix \mathbf{R}_s and $s_i = |\rho_i|^2$. b_n in (15) can be expanded as $b_n = \sum_{i=1}^K s_i (e^{jn\pi [\sin \theta_{t,i} \cos \Delta\theta_{t,i} + \cos \theta_{t,i} \sin \Delta\theta_{t,i}]} - e^{jn\pi \sin \theta_{t,i}})$. Considering that $\Delta\theta_{t,i}$ is very small,

$$\sin(\theta_{t,i} + \Delta\theta_{t,i}) \approx \sin \theta_{t,i} + \Delta\theta_{t,i} \cos \theta_{t,i}. \quad (16)$$

Then b_n in (15) can be denoted by

$$\begin{aligned} b_n &\approx \sum_{i=1}^K s_i \left(e^{jn\pi(\sin \theta_{t,i} + \Delta \theta_{t,i} \cos \theta_{t,i})} - e^{jn\pi \sin \theta_{t,i}} \right) \\ &= \sum_{i=1}^K s_i e^{jn\pi \sin \theta_{t,i}} \left(e^{jn\pi \Delta \theta_{t,i} \cos \theta_{t,i}} - 1 \right). \end{aligned} \quad (17)$$

Considering that x is very small, $e^x - 1 \approx x$. And then b_n in (17) can be rewritten as

$$b_n \approx \sum_{i=1}^K s_i e^{jn\pi \sin \theta_{t,i}} (jn\pi \Delta \theta_{t,i} \cos \theta_{t,i}). \quad (18)$$

According to (18), we can construct the following matrix:

$$\underbrace{\begin{bmatrix} b_1 \\ \vdots \\ b_{M+N-2} \\ b_1^* \\ \vdots \\ b_{M+N-2}^* \end{bmatrix}}_{\mathbf{b}} = \underbrace{\begin{bmatrix} s_1 e^{j\pi \sin \theta_{t,1}} j\pi \cos \theta_{t,1} & \cdots & s_K e^{j\pi \sin \theta_{t,K}} j\pi \cos \theta_{t,K} \\ \vdots & \ddots & \vdots \\ s_1 e^{j(M+N-2)\pi \sin \theta_{t,1}} j(M+N-2)\pi \cos \theta_{t,1} & \cdots & s_K e^{j(M+N-2)\pi \sin \theta_{t,K}} j(M+N-2)\pi \cos \theta_{t,K} \\ -s_1 e^{-j\pi \sin \theta_{t,1}} j\pi \cos \theta_{t,1} & \cdots & -s_K e^{-j\pi \sin \theta_{t,K}} j\pi \cos \theta_{t,K} \\ \vdots & \ddots & \vdots \\ -s_1 e^{-j(M+N-2)\pi \sin \theta_{t,1}} j(M+N-2)\pi \cos \theta_{t,1} & \cdots & -s_K e^{-j(M+N-2)\pi \sin \theta_{t,K}} j(M+N-2)\pi \cos \theta_{t,K} \end{bmatrix}}_{\mathbf{V}_t} \underbrace{\begin{bmatrix} \Delta \theta_{t,1} \\ \Delta \theta_{t,2} \\ \vdots \\ \Delta \theta_{t,K} \end{bmatrix}}_{\Delta \theta_t}. \quad (19)$$

Equation (19) can be rewritten with matrix form

$$\mathbf{V}_t \Delta \theta_t = \mathbf{b}. \quad (20)$$

From (14), we find that $\Delta \mathbf{R}_t$ is a Toeplitz matrix, whose elements in a straight line paralleled to the principal diagonal are equal. We take the following processing to estimate b_n and b_n^* ($n = 1, \dots, M+N-2$) to eliminate the noise. Consider

$$\begin{aligned} \hat{b}_n &= \frac{1}{M+N-1-n} \sum_{i=1}^{M+N-1-n} \Delta \mathbf{R}_t(i, n+i) \\ \hat{b}_n^* &= \frac{1}{M+N-1-n} \sum_{i=1}^{M+N-1-n} \Delta \mathbf{R}_t(n+i, i), \end{aligned} \quad (21)$$

where $\Delta \mathbf{R}_t(i, j)$ is the (i, j) element of the matrix $\Delta \mathbf{R}_t$. In the DOA tracking algorithm in [31], \hat{b}_n and \hat{b}_n^* are obtained through $\hat{b}_n = \Delta \mathbf{R}_t(1, n+1)$ and $\hat{b}_n^* = \Delta \mathbf{R}_t(n+1, 1)$, respectively. The proposed algorithm fully uses the Toeplitz matrix property of $\Delta \mathbf{R}_t$ to eliminate the noise and improves the parameter estimation performance.

Using the method of least square, we get

$$\Delta \hat{\theta}_t = (\mathbf{V}_t^H \mathbf{V}_t)^{-1} \mathbf{V}_t^H \hat{\mathbf{b}}, \quad (22)$$

where $\hat{\mathbf{b}} = [\hat{b}_1 \cdots \hat{b}_{M+N-2} \hat{b}_1^* \cdots \hat{b}_{M+N-2}^*]^T$.

Through the above analysis, the angles at time of t and $t+1$ are automatically associated, and the proposed algorithm avoids an extra data association.

For the finite samples, the covariance matrix in (8) is estimated by $\hat{\mathbf{R}}_t = \sum_{l=1}^L \mathbf{y}(t_l) \mathbf{y}^H(t_l)$, and we also get $\hat{\mathbf{R}}_{t+1}$,

which is the estimate of the covariance matrix at time $t+1$. We estimate b_n and b_n^* as follows:

$$\hat{b}_n = \frac{1}{M+N-1-n} \sum_{i=1}^{M+N-1-n} \Delta \hat{\mathbf{R}}_t(i, n+i) \quad (23a)$$

$$\hat{b}_n^* = \frac{1}{M+N-1-n} \sum_{i=1}^{M+N-1-n} \Delta \hat{\mathbf{R}}_t(n+i, i), \quad (23b)$$

where $\Delta \hat{\mathbf{R}}_t = \hat{\mathbf{R}}_{t+1} - \hat{\mathbf{R}}_t$. We use (22) to estimate $\Delta \theta_t$, where $\hat{\mathbf{b}} = [\hat{b}_1 \cdots \hat{b}_{M+N-2} \hat{b}_1^* \cdots \hat{b}_{M+N-2}^*]^T$, whose element is estimated via (23a) and (23b).

Till now, we show the major steps of DOA tracking algorithm for monostatic radar as follows.

Step 1. Use reduced-dimension matrix $\mathbf{W}^{-1} \mathbf{G}^H$ for the received signal $\mathbf{r}(t)$ and estimate the covariance matrix $\hat{\mathbf{R}}_t$.

Step 2. Get covariance matrix $\hat{\mathbf{R}}_{t+1}$ at time $t+1$, and we calculate $\Delta \hat{\mathbf{R}}_t = \hat{\mathbf{R}}_{t+1} - \hat{\mathbf{R}}_t$.

Step 3. We compute \hat{b}_n and \hat{b}_n^* via (23a) and (23b) and construct $\hat{\mathbf{b}} = [\hat{b}_1 \cdots \hat{b}_{M+N-2} \hat{b}_1^* \cdots \hat{b}_{M+N-2}^*]^T$.

Step 4. We estimate $\Delta \hat{\theta}_t$ via (22), and the DOA at time $t+1$ is $\hat{\theta}_{t+1} = \hat{\theta}_t + \Delta \hat{\theta}_t$.

Step 5. Repeat Steps 1–4 to estimate DOA at next time.

Remark 1. In this paper, the number of targets in MIMO radar is assumed to be preknown. If we have no knowledge about it, we may use the existing source-number estimation technique in [37] to obtain an estimate of the number of targets.

TABLE 1: Complexity comparison.

Algorithm	Computational complexity
PAST [25]	$O((3MNK + K^2)J + 3K^2M(N - 1) + K^3)$
PASTd [26]	$O((4MNK + K)J + 3K^2M(N - 1) + K^3)$
The proposed algorithm	$O((M + N - 1)^2J + 2K^2(M + N - 2) + K^3 + 2K(M + N - 2) + K^2)$

Remark 2. The initial angles in DOA tracking are obtained by ESPRIT algorithm or other DOA algorithms. The initial DOA is $\hat{\theta}_1$, and we get angles $\hat{\theta}_m = \hat{\theta}_1 + \sum_{i=1}^{m-1} \Delta\hat{\theta}_i$.

Remark 3. We assume that the noise covariance matrices of adjacent time are approximately equal. The noise component in (12) will be eliminated no matter which type of noise. The proposed algorithm still works well for the case of the colored noise.

Remark 4. The proposed algorithm works well in condition of small value of $\Delta\theta_{t,k}$. When $\Delta\theta_{t,k}$ becomes large, the proposed algorithm may fail to work.

3.3. Complexity Analysis and Advantages of the Proposed Algorithm. Since the reduced-dimension matrix is sparse, its transformation adds less computational load. The proposed algorithm does not require eigenvalue decomposition of the covariance matrix and avoids an extra data association. For the proposed algorithm, the calculation of the covariance matrix requires $O((M + N - 1)^2J)$, and the computation of $(\mathbf{V}_t^H \mathbf{V}_t)^{-1} \mathbf{V}_t^H \mathbf{b}$ needs $(2K^2(M + N - 2) + K^3 + 2K(M + N - 2) + K^2)$. The major computational complexity of the proposed algorithm is $O((M + N - 1)^2J + 2K^2(M + N - 2) + K^3 + 2K(M + N - 2) + K^2)$. Table 1 and Figure 2 show the computational complexity comparison among the proposed algorithm and other DOA tracking algorithms. We find that the proposed algorithm has much lower computational load than PAST in [25] and PASTd in [26].

The advantages of the proposed algorithm can be presented as follows.

- (1) The proposed algorithm does not require eigenvalue decomposition of the covariance matrix and has lower complexity than the conventional DOA tracking algorithms including PAST and PASTd.
- (2) The proposed algorithm can implement automatic association of DOA for monostatic MIMO radar.
- (3) The proposed algorithm has much better DOA tracking performance than the DOA tracking algorithm in [31], which will be shown in Section 5.

4. Error Analysis and CRLB

In this section, we derive the variance of DOA tracking and CRLB. We assume that the observation noise variances are almost the same at adjacent time. When computing $\Delta\theta$, we use some approximate calculations such as $e^x - 1 \approx x$ and

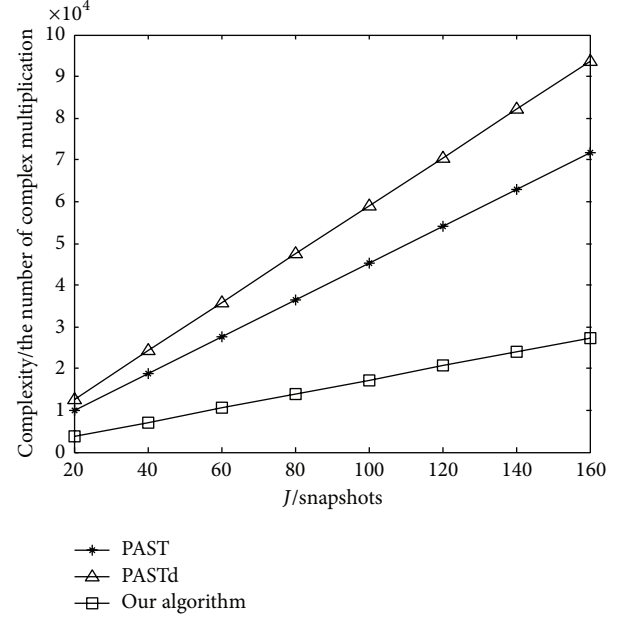


FIGURE 2: Complexity comparison with $M = 8$, $N = 6$, $K = 3$, and different J .

$\sin x \approx x$ when x is smaller. This leads to a little difference compared with the perfect value. Consider

$$\sin x = x - \frac{x^3}{3!} + \Lambda \quad (24a)$$

$$\cos x = 1 - \frac{x^2}{2!} + \Lambda' \quad (24b)$$

$$e^x - 1 = x + \Lambda'', \quad (24c)$$

where $\Lambda, \Lambda', \Lambda''$ are the high-order expansion terms.

According to (16), (17), (18), (24a), (24b), and (24c), we have

$$\begin{aligned}
 b_n &= \sum_{i=1}^K s_i \left(e^{jn\pi[\sin \theta_{t,i} \cos \Delta\theta_{t,i} + \cos \theta_{t,i} \sin \Delta\theta_{t,i}]} - e^{jn\pi \sin \theta_{t,i}} \right) \\
 &= \sum_{i=1}^K s_i \left(e^{jn\pi[\sin \theta_{t,i}(1 - (\Delta\theta_{t,i}^2/2!) + \Lambda') + \cos \theta_{t,i}(\Delta\theta_{t,i} - (\Delta\theta_{t,i}^3/3!) + \Lambda)]} \right. \\
 &\quad \left. - e^{jn\pi \sin \theta_{t,i}} \right) \\
 &= \sum_{i=1}^K s_i \left(e^{jn\pi[\sin \theta_{t,i} + \cos \theta_{t,i} \Delta\theta_{t,i}]} \right. \\
 &\quad \left. \times e^{jn\pi[\sin \theta_{t,i}(-(\Delta\theta_{t,i}^2/2!) + \Lambda') + \cos \theta_{t,i}(-(\Delta\theta_{t,i}^3/3!) + \Lambda)]} \right. \\
 &\quad \left. - e^{jn\pi \sin \theta_{t,i}} \right) \\
 &= \sum_{i=1}^K s_i e^{jn\pi \sin \theta_{t,i}} \\
 &\quad \times \left(e^{jn\pi \cos \theta_{t,i} \Delta\theta_{t,i}} \right.
 \end{aligned}$$

$$\begin{aligned}
& \times e^{jn\pi[\sin\theta_{t,i}(-(\Delta\theta_{t,i}^2/2!)+\Lambda')+\cos\theta_{t,i}(-(\Delta\theta_{t,i}^3/3!)+\Lambda)]-1}) \\
& = \sum_{i=1}^K s_i e^{jn\pi \sin\theta_{t,i}} \\
& \quad \times \left(jn\pi \cos\theta_{t,i} \Delta\theta_{t,i} \right. \\
& \quad \left. + jn\pi \left[\sin\theta_{t,i} \left(-\frac{\Delta\theta_{t,i}^2}{2!} + \Lambda' \right) \right. \right. \\
& \quad \left. \left. + \cos\theta_{t,i} \left(-\frac{\Delta\theta_{t,i}^3}{3!} + \Lambda \right) + j\Lambda'' \right] \right. \\
& \quad \left. + j\Lambda'' \right) \\
& = \sum_{i=1}^K s_i e^{jn\pi \sin\theta_{t,i}} jn\pi \cos\theta_{t,i} \Delta\theta_{t,i} \\
& \quad + \sum_{i=1}^K s_i e^{jn\pi \sin\theta_{t,i}} \left(jn\pi \left[\sin\theta_{t,i} \left(-\frac{\Delta\theta_{t,i}^2}{2!} + \Lambda' \right) \right. \right. \\
& \quad \left. \left. + \cos\theta_{t,i} \left(-\frac{\Delta\theta_{t,i}^3}{3!} + \Lambda \right) \right] \right. \\
& \quad \left. + j\Lambda'' \right). \tag{25}
\end{aligned}$$

∂b_n is estimation error of b_n , and ∂b_n can be shown as follows:

$$\begin{aligned}
\partial b_n = \sum_{i=1}^K s_i e^{jn\pi \sin\theta_{t,i}} & \left(jn\pi \left[\sin\theta_{t,i} \left(-\frac{\Delta\theta_{t,i}^2}{2!} + \Lambda' \right) \right. \right. \\
& \left. \left. + \cos\theta_{t,i} \left(-\frac{\Delta\theta_{t,i}^3}{3!} + \Lambda \right) \right] + j\Lambda'' \right). \tag{26}
\end{aligned}$$

According to (26) and (22), the variance of Δb_n is denoted by

$$\begin{aligned}
E[|\partial b_n|^2] & = \frac{1}{M+N-1-n} \\
& \times \sum_{i=1}^K s_i^2 \left[n\pi \sin\theta_{t,i} \left(-\frac{\Delta\theta_{t,i}^2}{2!} + \Lambda' \right) \right. \\
& \left. + n\pi \cos\theta_{t,i} \left(-\frac{\Delta\theta_{t,i}^3}{3!} + \Lambda \right) + \Lambda'' \right]^2. \tag{27a}
\end{aligned}$$

And we have

$$E[\partial b_i \partial b_j^*] = 0, \quad \forall i \neq j \tag{27b}$$

$$E[\partial b_n^2] = 0. \tag{27c}$$

We define that $\partial \mathbf{b}$ is the estimation error of \mathbf{b} . $\partial \mathbf{b} = [\partial b_1, \dots, \partial b_{M+N-2}, \partial b_1^*, \dots, \partial b_{M+N-2}^*]^T$. Then the variance of $\partial \mathbf{b}$ is

$$\begin{aligned}
E[|\partial \mathbf{b}|^2] & = \begin{bmatrix} E[|\partial b_1|^2] \\ \vdots \\ E[|\partial b_{M+N-2}|^2] \\ E[|\partial b_1|^2] \\ \vdots \\ E[|\partial b_{M+N-2}|^2] \end{bmatrix} = \begin{bmatrix} \frac{1}{M+N-2} \sum_{i=1}^K s_i^2 \left[\pi \sin\theta_{t,i} \left(-\frac{\Delta\theta_{t,i}^2}{2!} + \Lambda' \right) + \pi \cos\theta_{t,i} \left(-\frac{\Delta\theta_{t,i}^3}{3!} + \Lambda \right) + \Lambda'' \right]^2 \\ \vdots \\ \sum_{i=1}^K s_i^2 \left[(M+N-2) \pi \sin\theta_{t,i} \left(-\frac{\Delta\theta_{t,i}^2}{2!} + \Lambda' \right) + (M+N-2) \pi \cos\theta_{t,i} \left(-\frac{\Delta\theta_{t,i}^3}{3!} + \Lambda \right) + \Lambda'' \right]^2 \\ \frac{1}{M+N-2} \sum_{i=1}^K s_i^2 \left[\pi \sin\theta_{t,i} \left(-\frac{\Delta\theta_{t,i}^2}{2!} + \Lambda' \right) + \pi \cos\theta_{t,i} \left(-\frac{\Delta\theta_{t,i}^3}{3!} + \Lambda \right) + \Lambda'' \right]^2 \\ \vdots \\ \sum_{i=1}^K s_i^2 \left[(M+N-2) \pi \sin\theta_{t,i} \left(-\frac{\Delta\theta_{t,i}^2}{2!} + \Lambda' \right) + (M+N-2) \pi \cos\theta_{t,i} \left(-\frac{\Delta\theta_{t,i}^3}{3!} + \Lambda \right) + \Lambda'' \right]^2 \end{bmatrix}. \tag{28}
\end{aligned}$$

According to [38], we get the variance of $\Delta\theta_{t,i}$

$$\text{var}[\Delta\theta_{t,i}] = \frac{E[|\mathbf{V}_{t,i}^+ \partial \mathbf{b}|^2] + \text{Re}(E[\mathbf{V}_{t,i}^+ \partial \mathbf{b}])}{2}, \tag{29}$$

where $\mathbf{V}_{t,i}^+$ denotes the i th row of \mathbf{V}_t^+ and \mathbf{V}_t^+ is the pseudoinverse of \mathbf{V}_t . According to (27a), (27b), and (27c), we get

$$\begin{aligned}
\text{var}[\Delta\theta_{t,i}] & = \frac{\mathbf{V}_{t,i}^+ \text{diag}(E[|\partial \mathbf{b}|^2]) \mathbf{V}_{t,i}^{+H} + \text{Re}(\mathbf{V}_{t,i}^+ E[\partial \mathbf{b} \partial \mathbf{b}^T] \mathbf{V}_{t,i}^{+T})}{2}
\end{aligned}$$

$$= \frac{\mathbf{V}_{t,i}^+ \text{diag} \left(E[|\partial \mathbf{b}|^2] \right) \mathbf{V}_{t,i}^{+H}}{2}, \quad (30)$$

where $E[|\partial \mathbf{b}|^2]$ is shown in (28).

According to [39], we derive the CRLB for DOA estimation in monostatic MIMO-radar at time t . Consider

$$\text{CRLB}(t) = \frac{\sigma^2}{2J} \left\{ \text{Re} \left[\left(\mathbf{D}^H \Pi_{\mathbf{A}_t}^\perp \mathbf{D} \right) \oplus \mathbf{P}^T \right]^{-1} \right\}, \quad (31)$$

where $\Pi_{\mathbf{A}_t}^\perp = \mathbf{I}_{MN} - \mathbf{A}_t(\mathbf{A}_t^H \mathbf{A}_t)^{-1} \mathbf{A}_t^H$, $\mathbf{D} = [\mathbf{d}_1, \mathbf{d}_2, \dots, \mathbf{d}_K]$, $\mathbf{d}_k = \partial(\mathbf{a}_r(\theta_{t,k}) \otimes \mathbf{a}_t(\theta_{t,k}) / \partial \theta_{t,k})$, and

$\mathbf{P} = (1/J) \sum_{n=1}^J \mathbf{s}(t_n) \mathbf{s}^H(t_n)$. \oplus stands for Hadamard product.

Then we can define the average CRLB as follows:

$$\text{CRLB} = \frac{1}{T} \sum_{t=1}^T \text{CRLB}(t), \quad (32)$$

where T is the total tracking time.

5. Simulation Results

The Monte Carlo simulations are adopted to assess DOA tracking performance of the proposed algorithm. We suppose that there are three moving targets. We define root-mean square error (RMSE) as

$$\text{RMSE} = \frac{1}{K} \sum_{k=1}^K \sqrt{\frac{1}{F} \sum_{f=1}^F \left[\frac{1}{T} \sum_{t=1}^T (\hat{\theta}_{k,f,t} - \theta_{k,f,t})^2 \right]}, \quad (33)$$

where $\hat{\theta}_{k,f,t}$ is the estimate of DOA $\theta_{k,f,t}$ of the f th Monte Carlo trial. F is the times of Monte Carlo trial and $F = 1000$. We note that M , N , and K are the number of transmit antennas, receive antennas, and targets, respectively. During the tracking procedure, the targets are tracked over an interval of 100 s with $T_s = 1$ s. During each 1 s interval, J snapshots of sensor data are generated and used to estimate DOA.

Figure 3 depicts the DOA tracking result of the proposed algorithm for $M = 8$, $N = 6$, $K = 3$, $J = 100$, and SNR = 15 dB. It is shown that the proposed algorithm can track the DOA in monostatic MIMO radar effectively.

Figures 4-5 show the DOA tracking result of the proposed algorithm for other moving trajectories of targets with $M = 8$, $N = 6$, $K = 3$, $J = 100$, and SNR = 15 dB. From Figures 4-5 we find that the proposed algorithm can work well, which proves the robustness of the proposed algorithm.

Figure 6 shows the DOA tracking performance comparison with $M = 8$, $N = 6$, and $K = 3$, where we compare the proposed algorithm against the DOA tracking algorithm in [31], Kalman-PASTd algorithm in [35], and CRLB. It is shown in Figure 6 that the proposed algorithm has better DOA tracking performance than the DOA tracking algorithm in [31], since the proposed algorithm fully uses the Toeplitz matrix property of $\Delta \mathbf{R}_t$ to eliminate the noise and improves

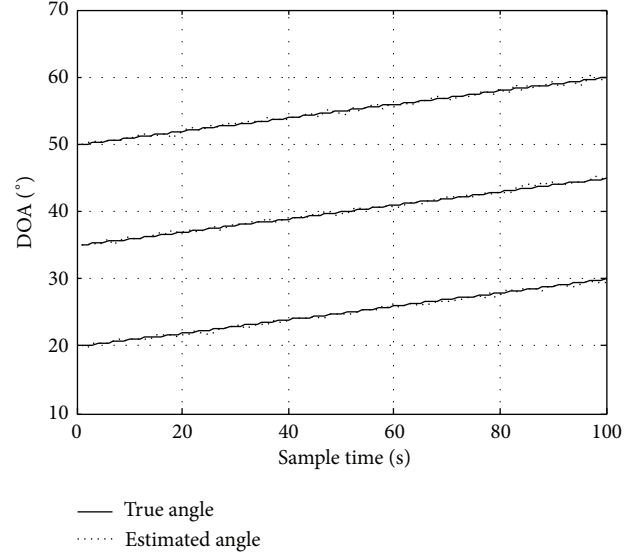


FIGURE 3: DOA tracking results of the proposed algorithm at SNR = 15 dB (Scene 1).

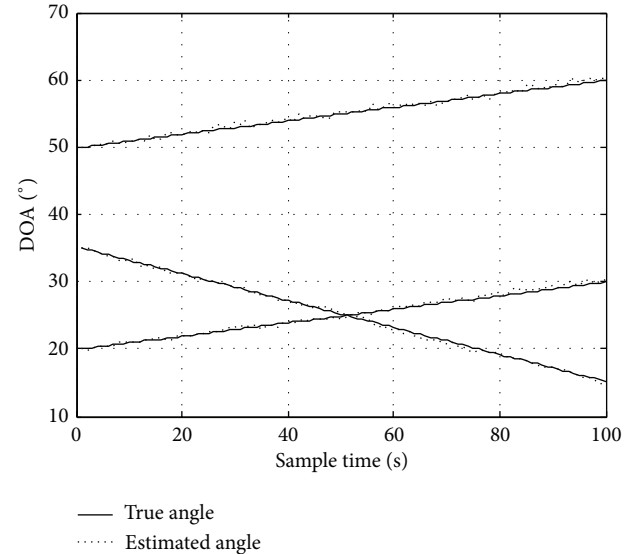


FIGURE 4: DOA tracking results of the proposed algorithm at SNR = 15 dB (Scene 2).

the estimation performance. The proposed algorithm has less DOA tracking performance than Kalman-PASTd algorithm, which has a heavy computational complexity.

Figure 7 investigates the DOA tracking performance of the proposed algorithm with different values of K . From Figure 7 we find that DOA tracking performance of the proposed algorithm improves with the decreasing of K . When K increases, the interference will enhance.

Figures 8-9 show DOA tracking performance with different M/N . It is clear that the DOA tracking performance of the proposed algorithm is improved as the number of transmit/receive antennas increases. Multiple transmit/receive

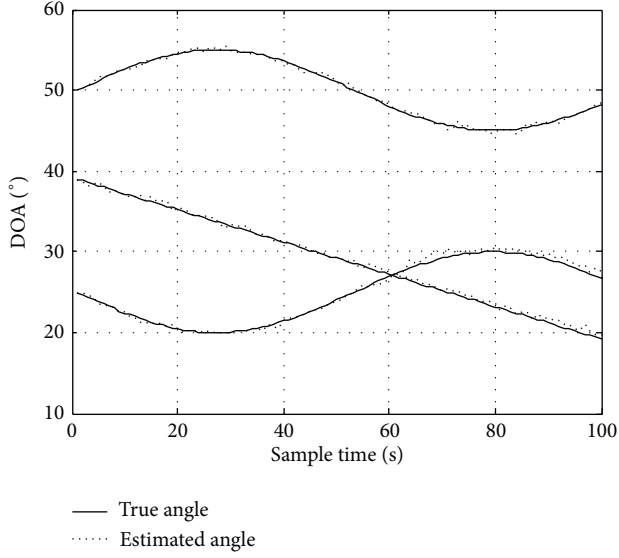


FIGURE 5: DOA tracking results of the proposed algorithm at SNR = 15 dB (Scene 3).

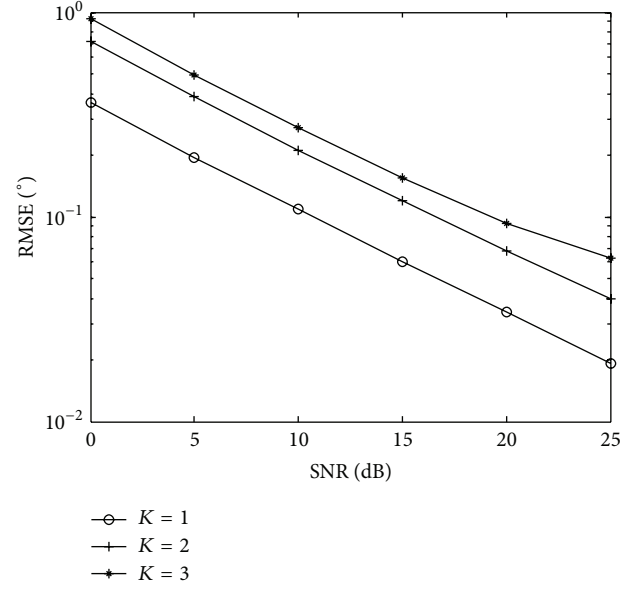


FIGURE 7: DOA tracking with different values of K .

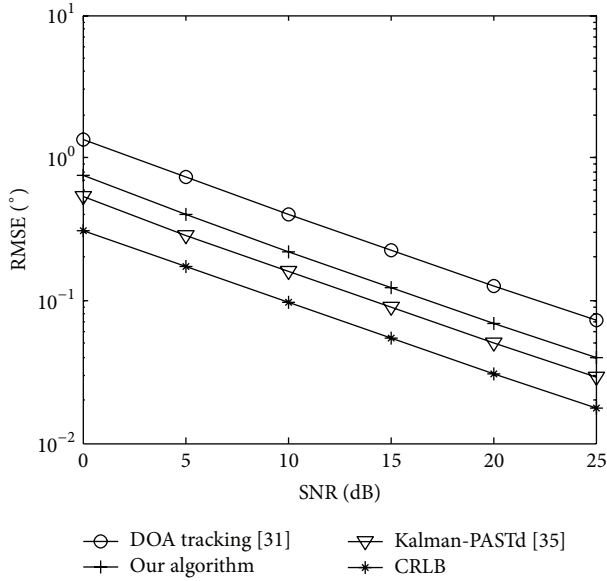


FIGURE 6: DOA tracking performance comparison with $M = 8$ and $N = 6$.

antennas improve DOA tracking performance because of diversity gain.

Figure 10 depicts the DOA tracking performance of the proposed algorithm with $M = 8$, $N = 6$, $K = 3$, $J = 100$, and SNR = 15 dB, and the different DOA spacing between two consecutive observations is considered. It is shown in Figure 10 that the angle tracking performance of the proposed algorithm degrades with increasing of DOA spacing between two consecutive observations.

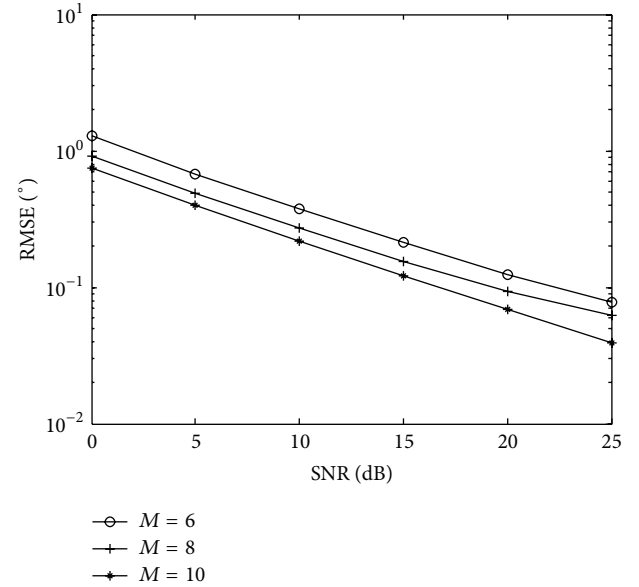


FIGURE 8: DOA tracking with different values of M .

6. Conclusions

In this paper we have presented the DOA tracking of multiple moving targets for monostatic MIMO radar. The proposed algorithm obtains DOA estimation of the target via the difference in previous and current covariance matrix of the reduced-dimension transformation signals, and the proposed algorithm reduces the computational complexity and realizes automatic association of DOA. Error analysis and CRLB of DOA tracking are derived in the paper. The simulation results demonstrate effectiveness and robustness of the proposed algorithm. Our research provides technical support for the practical application of MIMO radar.

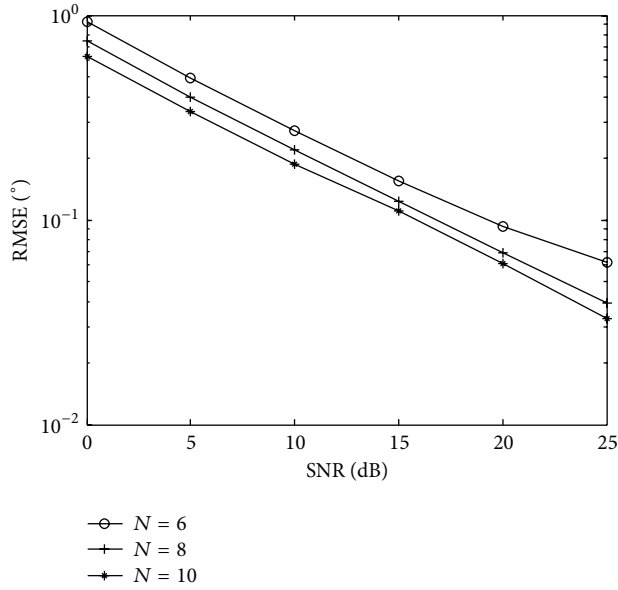
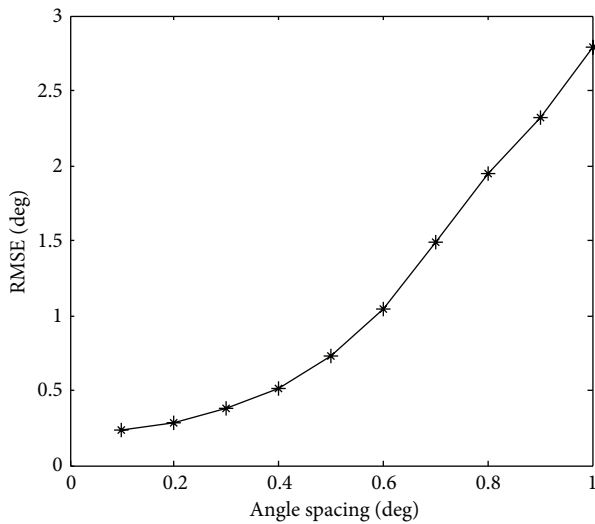
FIGURE 9: DOA tracking with different values of N .

FIGURE 10: DOA tracking performance with different angle spacing.

Conflict of Interests

The authors declare that there is no conflict of interests regarding the publication of this paper.

Acknowledgments

This work is supported by China NSF Grants (61371169, 61301108, and 61071164), Jiangsu Planned Projects for Post-doctoral Research Funds (1201039C), China Postdoctoral Science Foundation (2012M521099 and 2013M541661), Open Project of Key Laboratory of Modern Acoustic of Ministry of Education (Nanjing University), Aeronautical Science Foundation of China (20120152001), Qing Lan Project, Priority Academic Program Development of Jiangsu High Education

Institutions, and Fundamental Research Funds for the Central Universities (NS2013024, kfj130114, and kfj130115).

References

- [1] E. Fishler, A. Haimovich, R. Blum, D. Chizhik, L. Cimini, and R. Valenzuela, "MIMO radar: an idea whose time has come," in *Proceedings of the IEEE Radar Conference*, pp. 71–78, April 2004.
- [2] X. Li, Z. Zhang, W. Mao, X. Wang, J. Lu, and W. Wang, "A study of frequency diversity MIMO radar beamforming," in *Proceedings of the IEEE 10th International Conference on Signal Processing (ICSP '10)*, pp. 352–356, Beijing, China, October 2010.
- [3] J. Li and P. Stoica, "MIMO radar-diversity means superiority," in *Proceedings of 14th Annual Workshop Adaptive Sensor Array Processing*, Lexington, Mass, USA, June 2006.
- [4] J. Li and P. Stoica, "MIMO radar with colocated antennas," *IEEE Signal Processing Magazine*, vol. 24, no. 5, pp. 106–114, 2007.
- [5] A. M. Haimovich, R. S. Blum, and L. J. Cimini, "MIMO radar with widely separated antennas," *IEEE Signal Processing Magazine*, vol. 25, no. 1, pp. 116–129, 2008.
- [6] C. Jinli, G. Hong, and S. Weimin, "Angle estimation using ESPRIT without pairing in MIMO radar," *Electronics Letters*, vol. 44, no. 24, pp. 1422–1423, 2008.
- [7] J. Li and X. Zhang, "Performance analysis of ESPRIT for angle estimation in bistatic MIMO radar," in *Proceedings of the International Conference on Computer, Electrical, and Systems Sciences (CESSE '11)*, pp. 400–403, Wuhan, China, 2011.
- [8] M. L. Bencheikh and Y. Wang, "Joint DOD-DOA estimation using combined ESPRIT-MUSIC approach in MIMO radar," *Electronics Letters*, vol. 46, no. 15, pp. 1081–1083, 2010.
- [9] M. L. Bencheikh, Y. Wang, and H. He, "Polynomial root finding technique for joint DOA DOD estimation in bistatic MIMO radar," *Signal Processing*, vol. 90, no. 9, pp. 2723–2730, 2010.
- [10] X. Zhang and D. Xu, "Angle estimation in MIMO radar using reduced-dimension Capon," *Electronics Letters*, vol. 46, no. 12, pp. 860–861, 2010.
- [11] X. Zhang, Y. Huang, C. Chen, J. Li, and D. Xu, "Reduced-complexity Capon for direction of arrival estimation in a monostatic multiple-input multiple-output radar," *IET Radar, Sonar and Navigation*, vol. 6, no. 8, pp. 796–801, 2012.
- [12] X. Gao, X. Zhang, G. Feng, Z. Wang, and D. Xu, "On the MUSIC-derived approaches of angle estimation for bistatic MIMO radar," in *Proceedings of the International Conference on Wireless Networks and Information Systems (WNIS '09)*, pp. 343–346, Shanghai, China, December 2009.
- [13] J. Li and X. Zhang, "Improved Joint DOD and DOA estimation for mimo array with velocity receive sensors," *IEEE Signal Processing Letters*, vol. 18, no. 12, pp. 717–720, 2011.
- [14] X. Zhang, L. Xu, and D. Xu, "Direction of departure (DOD) and direction of arrival (DOA) estimation in MIMO radar with reduced-dimension MUSIC," *IEEE Communications Letters*, vol. 14, no. 12, pp. 1161–1163, 2010.
- [15] F. Liu and J. Wang, "AD-MUSIC for jointly DOA and DOD estimation in bistatic MIMO radar system," in *Proceedings of the International Conference on Computer Design and Applications (ICCD '10)*, pp. 455–458, Qinhuaogdao, China, June 2010.
- [16] X. Zhang, Z. Xu, L. Xu, and D. Xu, "Trilinear decomposition-based transmit angle and receive angle estimation for multiple-input multiple-output radar," *IET Radar, Sonar & Navigation*, vol. 5, no. 6, pp. 626–631, 2011.

- [17] H. Wu and X. Zhang, "DOA tracking in monostatic MIMO radar using PARAFAC-RLST algorithm," in *Proceedings of the 3rd International Conference on Information and Systems Engineering (ICISE '11)*, pp. 958–961, Amsterdam, The Netherlands, July 2011.
- [18] D. Nion and N. D. Sidiropoulos, "Adaptive algorithms to track the PARAFAC decomposition of a third-order tensor," *IEEE Transactions on Signal Processing*, vol. 57, no. 6, pp. 2299–2310, 2009.
- [19] X. Zhang, H. Wu, J. Li, and D. Xu, "Computationally efficient DOD and DOA estimation for bistatic MIMO radar with propagator method," *International Journal of Electronics*, vol. 99, no. 9, pp. 1207–1221, 2012.
- [20] Z. D. Zheng and J. Y. Zhang, "Fast method for multi-target localisation in bistatic MIMO radar," *Electronics Letters*, vol. 47, no. 2, pp. 138–139, 2011.
- [21] J. Li and X. Zhang, "2D-angle estimation algorithm using quaternion theory in bistatic MIMO-radar," in *Proceedings of the 3rd International Conference on Information Science and Engineering (ICISE '11)*, pp. 752–755, 2011.
- [22] J. Li, X. Zhang, and F. Wang, "Quaternion root-MUSIC algorithm for angle estimation in bistatic MIMO radar," *Journal of Electronics and Information Technology*, vol. 34, no. 2, pp. 300–304, 2012.
- [23] Y. Yu, A. P. Petropulu, and H. V. Poor, "MIMO radar using compressive sampling," *IEEE Journal on Selected Topics in Signal Processing*, vol. 4, no. 1, pp. 146–163, 2010.
- [24] Y. Liu, M. Y. Wu, and S. J. Wu, "Fast OMP algorithm for 2D angle estimation in MIMO radar," *Electronics Letters*, vol. 46, no. 6, pp. 444–445, 2010.
- [25] B. Yang, "Projection approximation subspace tracking," *IEEE Transactions on Signal Processing*, vol. 43, no. 1, pp. 95–107, 1995.
- [26] B. Yang, "Extension of the PASTd algorithm to both rank and subspace tracking," *IEEE Signal Processing Letters*, vol. 2, no. 9, pp. 179–182, 1995.
- [27] S. Ouyang and Y. Hua, "Bi-iterative least-square method for subspace tracking," *IEEE Transactions on Signal Processing*, vol. 53, no. 8, part 2, pp. 2984–2996, 2005.
- [28] P. Strobach, "Bi-iteration SVD subspace tracking algorithms," *IEEE Transactions on Signal Processing*, vol. 45, no. 5, pp. 1222–1240, 1997.
- [29] S. B. Park, C. S. Ryu, and K. K. Lee, "Multiple target angle tracking algorithm using predicted angles," *IEEE Transactions on Aerospace and Electronic Systems*, vol. 30, no. 2, pp. 643–648, 1994.
- [30] C. K. Sword, M. Simaan, and E. W. Kamen, "Multiple target angle tracking using sensor array outputs," *IEEE Transactions on Aerospace and Electronic Systems*, vol. 26, no. 2, pp. 367–373, 1990.
- [31] H. Zhang, L. Zhang, S. Wu, and Y. Liu, "A new multiple targets angle tracking method," *Journal of Electronics and Information Technology*, vol. 29, no. 12, pp. 2840–2842, 2007.
- [32] H. Zhang, S. Wu, L. Zhang, and Y. Liu, "Multiple targets angle tracking algorithm based on the elements of the covariance matrix," *Journal of Xidian University*, vol. 35, no. 5, pp. 785–792, 2008.
- [33] C. R. Rao, L. Zhang, and L. C. Zhao, "Multitarget angle tracking an algorithm for data association," *IEEE Transactions on Signal Processing*, vol. 42, no. 2, pp. 459–462, 1994.
- [34] H. Wu and X. Zhang, "DOD and DOA tracking algorithm for bistatic MIMO radar using PASTD without additional angles pairing," in *Proceedings of the IEEE 5th International Conference on Advanced Computational Intelligence (ICACI '12)*, pp. 1132–1136, October 2012.
- [35] X. F. Zhang, J. F. Li, G. P. Feng, and H. L. Wu, "Kalman-PASTd based DOA tracking algorithm for monostatic MIMO radar," in *Proceedings of the International Conference on Information, Services and Management Engineering (ISME '11)*, pp. 220–224, 2011.
- [36] W. Hailang, *Multi-target angle estimation and tracking in monostatic MIMO radar system [M.S. thesis]*, Nanjing University of Aeronautics and Astronautics, 2013.
- [37] J. Xin, N. Zheng, and A. Sano, "Simple and efficient nonparametric method for estimating the number of signals without eigendecomposition," *IEEE Transactions on Signal Processing*, vol. 55, no. 4, pp. 1405–1420, 2007.
- [38] B. D. Rao and K. V. S. Hari, "Performance analysis of ESPRIT and TAM in determining the direction of arrival of plane waves in noise," *IEEE Transactions on Speech and Signal Processing*, vol. 37, no. 12, pp. 1990–1995, 1989.
- [39] P. Stoica and A. Nehorai, "Performance study of conditional and unconditional direction-of-arrival estimation," *IEEE Transactions on Acoustics, Speech, and Signal Processing*, vol. 38, no. 10, pp. 1783–1795, 1990.

Research Article

Transmit Waveform Optimization for Spatial-Frequency Diversity MIMO Radar in the Presence of Clutter

Yonghao Tang, Xiaofeng Ma, Weixing Sheng, and Yubing Han

School of Electronic and Optical Engineering, Nanjing University of Science and Technology, Nanjing 210094, China

Correspondence should be addressed to Xiaofeng Ma; maxiaofeng@njust.edu.cn

Received 25 February 2014; Revised 1 June 2014; Accepted 16 June 2014; Published 1 July 2014

Academic Editor: Mathini Sellathurai

Copyright © 2014 Yonghao Tang et al. This is an open access article distributed under the Creative Commons Attribution License, which permits unrestricted use, distribution, and reproduction in any medium, provided the original work is properly cited.

Benefitting from the independent target echoes of diversity channels, diversity MIMO radar can efficiently improve system performance, such as target detection and parameter estimation. Due to the fact that the RCS (radar cross section) of complex target may vary with the different transmitted carrier frequencies and array geometries, many recent researches study at the background of diversity MIMO radar equipped with widely separated array antennas or working at multiple carrier frequencies, respectively. In this paper, a new MIMO radar system combining the spatial and frequency diversities is investigated in the presence of signal-dependent clutter, which is called spatial-frequency diversity MIMO radar. With the prior information of target and clutter, a new method for joint optimization of transmitted waveforms and receiving filters is proposed to enhance the target detection ability of spatial-frequency diversity MIMO radar. Inspired by the MIMO communication system, the water-filling algorithm is introduced into the transmitted energy allocation problem for each carrier frequency channel. Simulation results show that the proposed system has a better performance in output signal-to-clutter-noise ratio (SCNR) compared to conventional diversity MIMO radar system.

1. Introduction

Recently, the transmitted waveforms optimization problem of MIMO radar is a very popular issue in radar research field [1–5]. In conventional MIMO radar, the target diversity information of independent channels can be extracted by matched filters. The extra degrees of freedom brought by diversity information enable the system to obtain better performance in target detection and parameter estimation [6–8]. However, in the presence of clutter, the conventional MIMO radar is unable to suppress clutter effectively for the reason of the intrinsic correlation between the clutter and target echoes. Consequently, the joint optimization of transmitted waveforms and receiving filters for MIMO radar to suppress the clutter has attracted the attention of more and more researchers [9–11].

Because of its ability to transmit arbitrary waveforms, MIMO radar can obtain plenty of diversity information of target echoes. It is possible to suppress the clutters effectively by properly utilizing the diversity information. According to the types of diversity information, diversity MIMO radar can be divided into two types: spatial diversity MIMO radar

[12, 13] and frequency diversity MIMO radar [14, 15]. For spatial diversity MIMO radar, in order to observe target from different directions, the array antennas are often widely distributed. According to [7, 16], MIMO radar system will obtain the different RCS of target from different directions when the spacing between every two antennas satisfies

$$d_t \geq \frac{\lambda D}{d}, \quad (1)$$

where d_t denotes the spacing between two antennas, λ is the wavelength of carrier frequency, D is the target distance departed to array, and d represents target size. For frequency diversity MIMO radar, the system obtains the independent target echoes by transmitting probing signals of different carrier frequencies. Even though the array antennas may be co-located distributed, the frequency diversity can be obtained only if the working frequency difference of two frequency channels satisfies [16, 17]

$$\Delta f \geq \frac{c}{2d}, \quad (2)$$

where Δf denotes the carrier frequency difference of two frequency channels and c represents the speed of light.

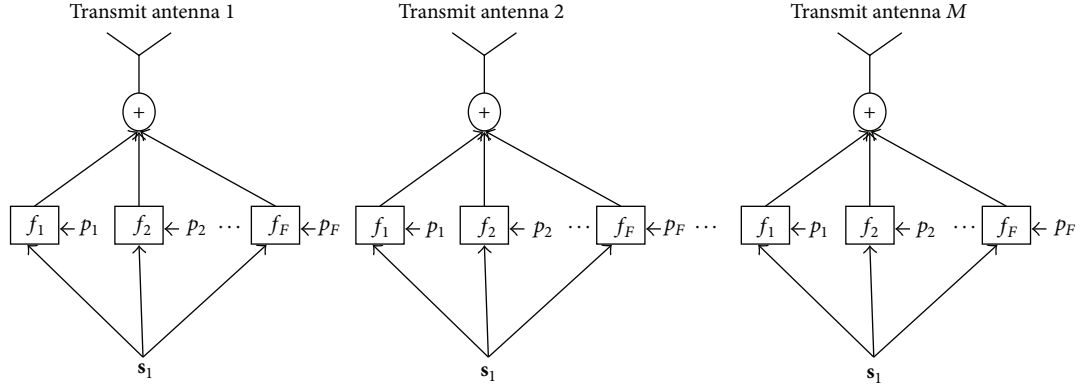


FIGURE 1: The structure of transmit array.

In this paper, spatial-frequency diversity MIMO radar system is investigated, which combines the advantages brought by spatial and frequency diversities. The structure of spatial-frequency diversity MIMO radar is shown in Figures 1 and 2. The array antennas are widely distributed. The spacing between every two antennas satisfies (1), so that the spatial diversity information can be obtained. Meanwhile, each antenna transmits probing signals of F carrier frequencies. The frequency difference of every two frequency channels satisfies (2) to obtain the frequency diversity information. So much diversity information provides much more extra degrees of freedom to design transmitted waveforms, receiving filters and energy allocation of frequency channels, which makes it possible for spatial-frequency diversity MIMO radar to achieve better system performance than conventional diversity MIMO radar. However, the difficulty is that the joint optimization of transmitted waveforms and receiving filters is not a convex optimization problem, which cannot get the closed-form solution easily. In addition, the energy allocation optimization of different frequency channels is a new problem that is faced by spatial-frequency diversity MIMO radar.

So far, the transmitted waveforms optimization techniques are mostly developed for MIMO radar with widely distributed antennas, which only take advantage of the spatial diversity information [1, 3, 4, 12, 13, 18]. In order to improve the performance of parameter estimation, the MMSE, NMSE, and MI methods are investigated for spatial diversity MIMO radar in [1] and the references therein. The methods proposed in [18] are also developed for spatial diversity MIMO radar to improve the target detection performance. Unfortunately, all these methods are not extended to spatial-frequency diversity MIMO radar yet. Unlike these references, this paper proposes a joint optimization method of transmitted waveforms and receiving filters for spatial-frequency diversity MIMO radar to improve the target detection performance against clutters. A similar iteration algorithm designed for traditional radar system is proposed in [19]. However, it cannot be directly applied in MIMO radar especially the proposed spatial-frequency diversity MIMO radar. In the proposed method, the rule of maximum output SCNR is applied to optimize the transmitted waveforms and receiving filters jointly. Under

the premise that the target and clutter are known as priors, an iterative algorithm is proposed to maximize the output SCNR of system by optimizing the transmitted waveforms and receiving filters alternatively. The output SCNR in each step of the iterative algorithm is nondecreasing, so that the convergence of the proposed method is guaranteed. Meanwhile, inspired by the MIMO communication theory, the water-filling algorithm is introduced to the optimization problem of energy allocation for different frequency channels. Simulation results show that the water-filling algorithm significantly improves the system performance. Combining these methods, spatial-frequency diversity MIMO radar achieves a greatly improved target detection performance compared to conventional MIMO radar systems.

The paper is organized as follows. In Section 2, the signal model of spatial-frequency diversity MIMO radar is briefly introduced. In Section 3, the water-filling algorithm is introduced to energy allocation problem of frequency channels firstly. Then, an iterative algorithm is proposed to optimize the transmitted waveforms and receiving filters alternatively in Section 4. The simulations results that show the advantages of spatial-frequency diversity MIMO radar are presented in Section 5 which is followed by the conclusions in Section 6.

2. Signal Model of Spatial-Frequency Diversity MIMO Radar

Consider the proposed spatial-frequency diversity MIMO radar system equipped with a transmit array of M antennas and a receive array of N antennas. Assume that the baseband waveform transmitted by each transmit antenna is \mathbf{s}_m ($m = 1, 2, \dots, M$), with the snapshots of L . The total energy of waveforms is normalized. Each waveform \mathbf{s}_m will be transmitted by F different carrier frequencies at the same time (as shown in Figure 1). The energy of each carrier frequency is represented as p_f ($f = 1, \dots, F$), and the total transmit energy is set as E . As shown in Figure 2, the received signal of each receive antenna is down-converted with F different carrier frequencies, respectively, and summed together in baseband. Then the synthetic baseband data go through the receiving filters \mathbf{h}_n ($n = 1, 2, \dots, N$).

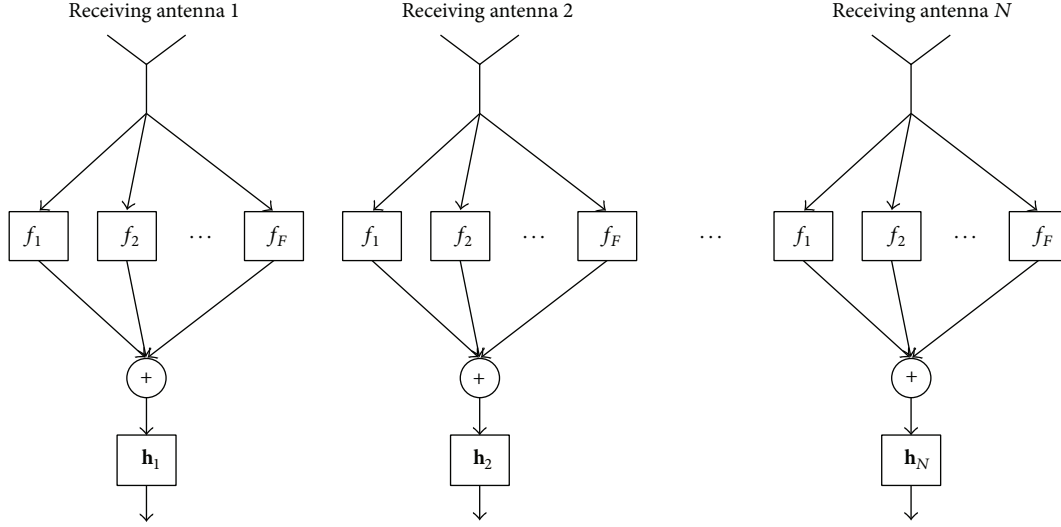


FIGURE 2: The structure of receive array.

As the proposed system satisfies (1) and (2) simultaneously, the received data of MNF channels are independent. Assume that t_{fmn} ($f = 1, 2, \dots, F$, $m = 1, 2, \dots, M$, $n = 1, 2, \dots, N$) represents target reflection and attenuation coefficient between m th transmit antenna and n th receive antenna at f th frequency channel. If the target reflection and attenuation coefficients change so slowly that they can be deemed to remain constant in the L snapshots duration, the received baseband target echoes at f th frequency channel can be written as

$$\mathbf{X}_{tf} = \sqrt{p_f} \mathbf{T}_f \mathbf{S}, \quad (3)$$

where

$$\mathbf{T}_f = \begin{bmatrix} t_{f11} & t_{f12} & \cdots & t_{f1M} \\ t_{f21} & t_{f22} & \cdots & t_{f2M} \\ \vdots & \vdots & \ddots & \vdots \\ t_{fN1} & t_{fN2} & \cdots & t_{fNM} \end{bmatrix}, \quad (4)$$

$$\mathbf{S} = [\mathbf{s}_1, \mathbf{s}_2, \dots, \mathbf{s}_M]^T.$$

The received baseband target echoes in (3) can be vectorized as

$$\mathbf{x}_{tf} = \text{vec}(\mathbf{X}_{tf}) = \sqrt{p_f} (\mathbf{I}_L \otimes \mathbf{T}_f) \cdot \text{vec}(\mathbf{S}) = \sqrt{p_f} \tilde{\mathbf{T}}_f \mathbf{s}, \quad (5)$$

where $\text{vec}(\cdot)$ denotes vectorized operator, \otimes denotes Kronecker product, and \mathbf{I}_L is $L \times 1$ identity matrix. Note that if target reflection and attenuation coefficients change so quickly that they will vary within the L snapshots, $\tilde{\mathbf{T}}_f$ should be redefined as

$$\tilde{\mathbf{T}}_f = \begin{bmatrix} \mathbf{T}_{f1} & \mathbf{0} & \cdots & \mathbf{0} \\ \mathbf{0} & \mathbf{T}_{f2} & \cdots & \mathbf{0} \\ \vdots & \vdots & \ddots & \vdots \\ \mathbf{0} & \mathbf{0} & \cdots & \mathbf{T}_{fL} \end{bmatrix}_{NL \times ML}. \quad (6)$$

In this case, the target reflection and attenuation coefficients \mathbf{T}_f can be assumed as stochastic processes of MN random variables under the f th frequency, and the MN random variables may be assumed independent and identically distributed (i.i.d.), with distribution $\mathcal{CN}(\mathbf{0}, \mathbf{R}_{\mathbf{T}_f})$.

Then, the sum of received baseband target echoes of all the frequency channels can be described as

$$\mathbf{x}_t = \sum_{f=1}^F \mathbf{x}_{tf} = \sum_{f=1}^F \sqrt{p_f} \tilde{\mathbf{T}}_f \mathbf{s}. \quad (7)$$

Defining $\mathbf{T} = \sum_{f=1}^F \sqrt{p_f} \tilde{\mathbf{T}}_f$, (7) can be rewritten as

$$\mathbf{x}_t = \mathbf{T} \mathbf{s}. \quad (8)$$

Similarly, the clutter coefficients of MN channels under f th frequency also can be assumed as stochastic processes, with distribution $(\mathbf{0}, \mathbf{R}_{\mathbf{C}_f})$. By defining the clutter coefficients matrix $\tilde{\mathbf{C}}_f$ which has the same structure as $\tilde{\mathbf{T}}_f$ and $\mathbf{C} = \sum_{f=1}^F \sqrt{p_f} \tilde{\mathbf{C}}_f$, the sum of received baseband clutters of all the frequency channels can be described as

$$\mathbf{x}_c = \mathbf{C} \mathbf{s}. \quad (9)$$

Then, the complete received baseband data can be expressed as

$$\mathbf{x} = \mathbf{x}_t + \mathbf{x}_c + \mathbf{w} = \mathbf{T} \mathbf{s} + \mathbf{C} \mathbf{s} + \mathbf{w}, \quad (10)$$

where \mathbf{w} denotes Gaussian noise with energy of σ_w^2 . Let the received baseband data go through the receiving filters \mathbf{h}_n ($n = 1, 2, \dots, N$). The output of the filters can be written as

$$\mathbf{y} = \mathbf{h}^T \mathbf{x} = \mathbf{h}^T \mathbf{T} \mathbf{s} + \mathbf{h}^T \mathbf{C} \mathbf{s} + \tilde{\mathbf{w}}, \quad (11)$$

where $\mathbf{h} = [\mathbf{h}_1^T, \mathbf{h}_2^T, \dots, \mathbf{h}_N^T]^T$ with a size of $NL \times 1$.

Note that when F is chosen as 1, the signal model proposed above will be equal to the model in [18] which is based on spatial diversity MIMO radar. Consequently, the signal model of spatial diversity MIMO radar can be regarded as a special case of the proposed signal model in this paper.

3. Energy Allocation of Frequency Channels

In some clutter scenarios, such as ground clutters and sea clutters, the clutter coefficients may vary with different frequencies. Especially when the frequency difference Δf is large enough, the clutter coefficients of different frequency channels will be particularly different [20]. As a result, conventional uniform energy distribution method for frequency channels cannot achieve the best performance of spatial-frequency diversity MIMO radar.

Water-filling algorithm is widely applied in energy allocation in multichannel wireless communications, which can allot adaptively transmitted energy according to the channel condition [21, 22]. Inspired by the theory in MIMO communication system, we introduce the water-filling algorithm to the energy allocation problem of frequency channels for spatial-frequency diversity MIMO radar. According to [22], the capacity of all the frequency channels can be described as

$$I = \sum_{f=1}^F \log_2 \left(1 + \frac{p_f \lambda_f}{\sigma_f^2} \right), \quad (12)$$

where $\lambda_f \triangleq \text{trace}(\mathbf{R}_{Tf})$, $\sigma_f^2 \triangleq \text{trace}(\mathbf{R}_{Cf}) + \sigma_w^2$, and $\text{trace}(\cdot)$ denotes the trace of a matrix.

With the channel knowledge known, the maximum capacity of MIMO channel can be achieved by applying water-filling principle on the channel energy allocation. The optimal energy allocation p_f is decided according to the water-filling rule [23]:

$$p_f = \max \left(\mu - \frac{\sigma_f^2}{\lambda_f}, 0 \right), \quad (13)$$

where μ is a constant which guarantees the energy constraint at transmitter that

$$\sum_{f=1}^F p_f = E. \quad (14)$$

4. Joint Optimization of Transmitted Waveforms and Receiving Filters

Spatial-frequency diversity MIMO radar provides much more extra degrees of freedom to design transmitted waveforms and receiving filters. Even in clutter environment, it is possible to improve the output SCNR of the proposed system, as long as the transmitted waveforms and receiving filters are designed properly. In this section, the rule of maximizing the output SCNR is applied to optimize the transmitted waveforms and receiving filters jointly.

Define the output SCNR of system as

$$\text{SCNR} = \frac{E \left[|\mathbf{h}^T \mathbf{T} \mathbf{s}|^2 \right]}{E \left[|\mathbf{h}^T \mathbf{C} \mathbf{s}|^2 \right] + E \left[|\tilde{\mathbf{w}}|^2 \right]}. \quad (15)$$

As the rule of maximizing SCNR is applied, the optimization problem can be expressed as

$$\max_{\mathbf{s}, \mathbf{h}} \frac{\mathbf{h}^T E \left[\mathbf{T} \mathbf{s} \mathbf{s}^T \mathbf{T}^T \right] \mathbf{h}}{\mathbf{h}^T E \left[\mathbf{C} \mathbf{s} \mathbf{s}^T \mathbf{C}^T \right] \mathbf{h} + E \left[|\tilde{\mathbf{w}}|^2 \right]} \quad \text{s.t. } \|\mathbf{s}\|^2 = 1. \quad (16)$$

Obviously, the optimization is not a convex problem and cannot get its global optimal solutions easily. However, several local optimal solutions may be found within the feasible solution space. In this paper, an iterative algorithm which optimizes the transmitted waveforms \mathbf{s} and receiving filters \mathbf{h} alternatively is proposed to improve the SCNR. The numerical simulation results show that each step of the proposed algorithm is nondecreasing, so that the convergence of the proposed method is guaranteed. Although the final results of the iteration algorithm may be just local optimum, they will be global optimum with respect to \mathbf{s} dimension and \mathbf{h} dimension, respectively. As a result, the optimized result is the best one among the multiple local optimal solutions.

Firstly, we solve \mathbf{h} in terms of \mathbf{s} . In this case, the optimization problem above can be written as

$$\max_{\mathbf{h}} \frac{\mathbf{h}^T E \left[\mathbf{T} \mathbf{s} \mathbf{s}^T \mathbf{T}^T \right] \mathbf{h}}{\mathbf{h}^T E \left[\mathbf{C} \mathbf{s} \mathbf{s}^T \mathbf{C}^T \right] \mathbf{h} + \mathbf{h}^T E \left[\mathbf{w} \mathbf{w}^T \right] \mathbf{h}}. \quad (17)$$

Define

$$\begin{aligned} \mathbf{R}_{Ts} &\triangleq E \left[\mathbf{T} \mathbf{s} \mathbf{s}^T \mathbf{T}^T \right], \\ \mathbf{R}_{Cs} &\triangleq E \left[\mathbf{C} \mathbf{s} \mathbf{s}^T \mathbf{C}^T \right], \\ \mathbf{R}_w &\triangleq E \left[\mathbf{w} \mathbf{w}^T \right]. \end{aligned} \quad (18)$$

Then, (17) can be rewritten as

$$\max_{\mathbf{h}} \frac{\mathbf{h}^T \mathbf{R}_{Ts} \mathbf{h}}{\mathbf{h}^T (\mathbf{R}_{Cs} + \mathbf{R}_w) \mathbf{h}}. \quad (19)$$

It is obvious that (19) is the well-known Rayleigh quotient problem [24] and the solution to this problem is the principal generalized eigenvector of \mathbf{R}_{Ts} and $(\mathbf{R}_{Cs} + \mathbf{R}_w)$; that is,

$$\tilde{\mathbf{h}} = \lambda_{\max} (\mathbf{R}_{Ts}, \mathbf{R}_{Cs} + \mathbf{R}_w), \quad (20)$$

where $\lambda_{\max}(\mathbf{A}, \mathbf{B})$ denotes the generalized eigenvector corresponding to the maximum generalized eigenvalue of \mathbf{A} and \mathbf{B} .

To solve \mathbf{s} in terms of \mathbf{h} , the optimization problem can be rewritten as

$$\max_{\mathbf{s}} \frac{\mathbf{s}^T E \left[\mathbf{T}^T \mathbf{h} \mathbf{h}^T \mathbf{T} \right] \mathbf{s}}{\mathbf{s}^T E \left[\mathbf{C}^T \mathbf{h} \mathbf{h}^T \mathbf{C} \right] \mathbf{s} + \mathbf{h}^T E \left[\mathbf{w} \mathbf{w}^T \right] \mathbf{h}} \quad \text{s.t. } \|\mathbf{s}\|^2 = 1. \quad (21)$$

Similarly, define

$$\begin{aligned} \mathbf{R}_{Th} &\triangleq E \left[\mathbf{T}^T \mathbf{h} \mathbf{h}^T \mathbf{T} \right], \\ \mathbf{R}_{Ch} &\triangleq E \left[\mathbf{C}^T \mathbf{h} \mathbf{h}^T \mathbf{C} \right]. \end{aligned} \quad (22)$$

Then, (21) can be rewritten as

$$\max_{\mathbf{s}} \frac{\mathbf{s}^T \mathbf{R}_{Th} \mathbf{s}}{\mathbf{s}^T \mathbf{R}_{Ch} \mathbf{s} + \mathbf{h}^T \mathbf{R}_w \mathbf{h}} \quad \text{s.t. } \|\mathbf{s}\|^2 = 1. \quad (23)$$

Unfortunately, the structure of (23) is slightly different from (19), and it is not a standard Rayleigh quotient problem. However, noting the fact that the constraint satisfies $\|\mathbf{s}\|^2 = \mathbf{s}^T \mathbf{s} = 1$, the optimization problem (23) is equal to

$$\max_{\mathbf{s}} \frac{\mathbf{s}^T \mathbf{R}_{Th} \mathbf{s}}{\mathbf{s}^T \mathbf{R}_{Ch} \mathbf{s} + \mathbf{s}^T (\mathbf{h}^T \mathbf{R}_w \mathbf{h} \cdot \mathbf{I}_{ML}) \mathbf{s}}, \quad (24)$$

where \mathbf{I}_{ML} denotes identity matrix with a size of ML . Equation (24) is a Rayleigh quotient problem and its solution satisfies the constraint $\|\mathbf{s}\|^2 = 1$. As a result, the optimal solution to (23) can be computed by

$$\tilde{\mathbf{s}} = \lambda_{\max} (\mathbf{R}_{Th}, \mathbf{R}_{Ch} + \mathbf{h}^T \mathbf{R}_w \mathbf{h} \cdot \mathbf{I}_{ML}). \quad (25)$$

All steps of the proposed algorithm are summarized as follows.

- (1) Compute transmitted energy allocation p_f of different frequency channels by (13).
- (2) Initialize the transmitted waveforms \mathbf{s} (e.g., random waveforms).
- (3) Compute \mathbf{R}_{Ts} , \mathbf{R}_{Cs} , and \mathbf{R}_w by (18).
- (4) Compute \mathbf{h} by (20).
- (5) Compute \mathbf{R}_{Th} and \mathbf{R}_{Ch} by (22).
- (6) Compute \mathbf{s} by (25).
- (7) Compute the SCNR by (15), and compute the difference σ between the two adjacent iterative results of SCNR.
- (8) Repeat steps 3–7 until the difference σ is less than a very small value (e.g., 10^{-4}).

5. Simulation Results

In this section, some simulations are performed to show the performance of spatial-frequency diversity MIMO radar against clutters. Throughout our experiments, a MIMO radar system with a transmit array of $M = 4$ and a receive array of $N = 4$ is assumed. The configurations of arrays satisfy (1) and (2). The number of snapshots is set as $L = 16$ and the energy of Gaussian noise is assumed as $\sigma_w^2 = 1$. In the experiments of SCNR versus CNR (clutter-to-noise ratio), each method has completed 200 independent runs.

Experiment 1. In this experiment, the number of carrier frequencies are assumed as $F = 3$. The transmitted waveforms are initialized as random waveforms. The total transmitted energy of all frequency channels are set as $E = 1$. The coefficients $\{t_{fmn}\}$ are generated as independent and identically distributed Gaussian random variables with unity variance;

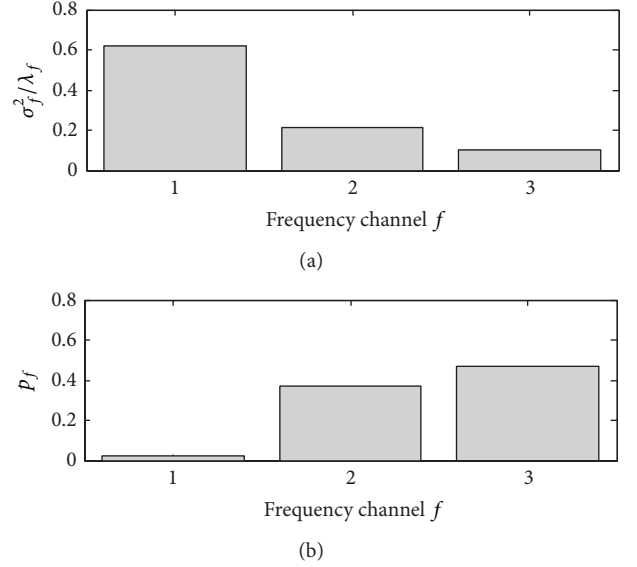


FIGURE 3: The conditions and transmitted energy allocation of frequency channels.

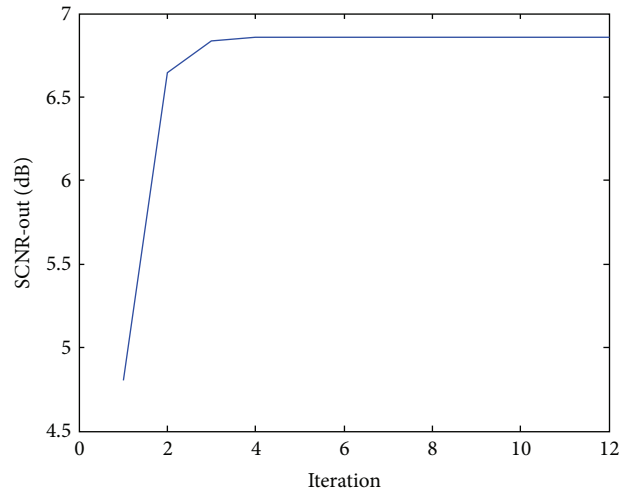


FIGURE 4: The output SCNR versus the number of iterations.

namely, $\mathbf{R}_{Tf} = \mathbf{I}_{MN}$. The covariance matrixes \mathbf{R}_{Cf} of clutters under each frequency channel are generated by

$$\mathbf{R}_{Cf} = \mathbf{B} \mathbf{A}^f \mathbf{B}, \quad f = 1, 2, 3, \quad (26)$$

where \mathbf{A} is a positive semidefinite matrix with a size of 16×16 whose maximum spectral radius is no more than 1 and \mathbf{B} is a unitary matrix with a size of 16×16 . Note that (26) with superscript f applied here is just for the aim of generating the different clutter covariance matrixes in different frequency channels.

By applying the water-filling algorithm, the energy allocation of each frequency channel is shown in Figure 3. According to the condition of each frequency channel, the energy is no longer uniformly distributed. Then, the proposed iterative algorithm (from (18) to (25)) is applied to optimize the system output SCNR. Figure 4 shows the trends of SCNR

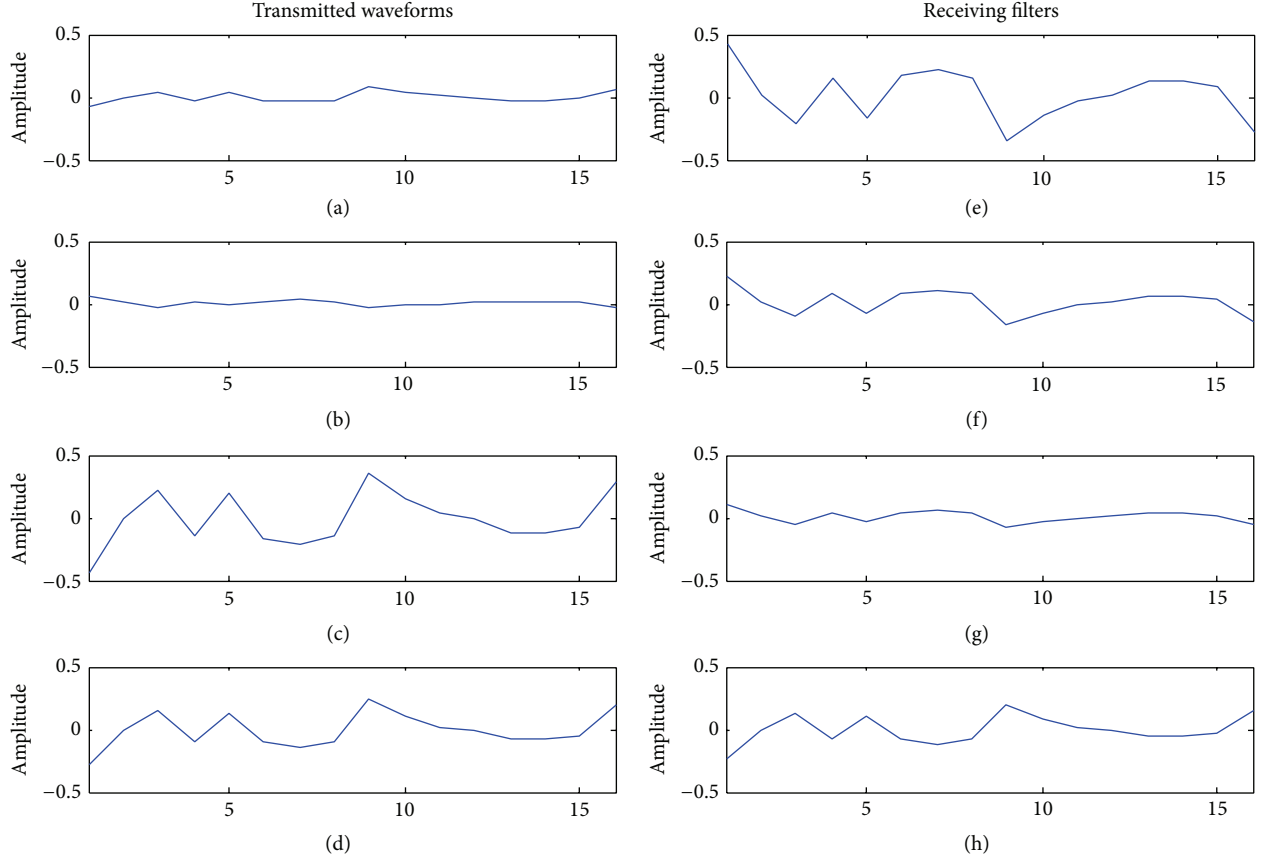


FIGURE 5: The optimized results: (a)–(d) are transmitted waveforms and (e)–(f) are receiving filters.

versus iterative number. It can be found that the SCNR in each step of the proposed iterative algorithm is nondecreasing and rapid convergence of the method is guaranteed. The optimized transmitted waveforms and receiving filters are shown in Figure 5.

Experiment 2. In order to illustrate the effects of water-filling algorithm and the number F of frequency channels on the performance of the system, we also perform the simulations of the output SCNR versus input CNR in five cases: (i) $F = 2$ with applying the water-filling algorithm; (ii) $F = 3$ with applying the water-filling algorithm; (iii) $F = 2$ with applying uniform energy allocation method; (iv) $F = 3$ with applying uniform energy allocation method; (v) the method for spatial diversity MIMO radar in [18] ($F = 1$).

For simplicity, the target coefficients are assumed as

$$t_{fmm} = 1, \quad n, m = 1, \dots, 4, \quad f = 1, 2, 3. \quad (27)$$

The clutter covariance matrixes \mathbf{R}_{Cf} are generated similarly to that in Experiment 1. The total transmitted energy of all frequency channels are set as $E = 1$. However, the input CNR varies in the range $[-5 \text{ dB}, 30 \text{ dB}]$. The simulation results of the output SCNR versus input CNR in the cases of $F = 2$ and $F = 3$ with applying water-filling algorithm or uniform energy allocation method are shown in Figure 6. Obviously, the two cases which apply the water-filling algorithm have

better performance than the other two with uniform energy allocation. It is demonstrated that the water-filling algorithm works very well in spatial-frequency diversity MIMO radar. Besides, the performance in the case of $F = 3$ is also much better than that in the cases of $F = 1$ and 2, which shows that more frequency diversities will make more contributions to the system performance. Nevertheless, we could not increase the number of carrier frequencies without restrictions. The reason is that the increased number of carrier frequencies will not only result in extra hardware cost and increased usage of electromagnetic spectrum but also lead to the increase of computational complexity. Consequently, it is still a problem that is worthy of further study to seek the balance among the number of carrier frequencies, hardware cost, computational complexity, and the increase of system performance.

Experiment 3. In [3, 4], the authors also proposed a method to design optimal waveforms by only exploiting spatial diversity. In their proposed algorithm, water-filling algorithm is used to optimize the transmitted power from different antennas, whereas similar algorithm is used to optimize the transmitted power from different frequency channels in our method. Besides, their method can also achieve the closed-form optimal solution; namely, the left singular vectors of the optimal waveform should be the eigenvectors of the covariance matrix of colored noise and the right singular vectors should be eigenvectors of the covariance matrix

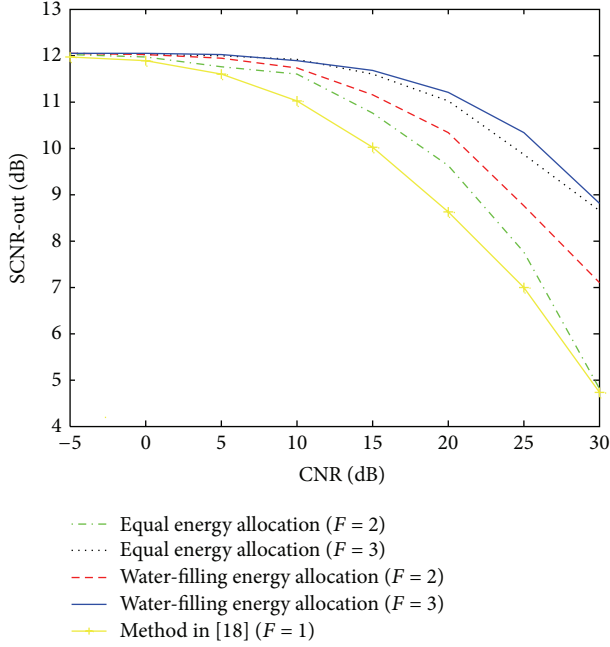


FIGURE 6: The output SCNR versus input CNR under five cases.

of target. To illustrate the superiority of our method, the comparison in signal-dependent scenario of the two methods under the rule of maximizing SCNR is performed. Note that the application scenario discussed in this paper is signal-dependent clutter suppression, so that the comparison of signal-independent noise suppression performance for the two methods is not considered here.

In this experiment, the MIMO radar equipped with $M = 4$ widely distributed arrays is assumed. The eigenvalues of covariance matrix of target \mathbf{R}_H (which is defined in [4]) are set as $\{7, 5, 2, 1\}$. The clutter covariance matrixes \mathbf{R}_{Cf} and noise are generated similarly to that in Experiment 2. The input CNR varies in the range $[-5 \text{ dB}, 30 \text{ dB}]$. The total transmit energy is set as $E = 100$. Note that the signal-dependent clutter and noise here are treated as the colored noise part \mathbf{W} (which is defined in [4]) in the simulation of the method in [4]. In our method, the number of carrier frequencies is set as $F = 3$. The trends of SCNR versus CNR of the two methods are shown in Figure 7. The result of the method applying orthogonal waveforms and matched filters is also drawn in Figure 7. It is obvious that the performance of our proposed method is much better than that in [4], and the performance of the method in [4] is similar to the matched filters method with no anticlutter measures applied. It demonstrates that the method in [4] is unable to suppress the signal-dependent clutter effectively, although it works well in the colored noise suppression application (where the noise part is independent of transmit signal). In signal-dependent clutter suppression application, the performance of the method we proposed is much better than conventional MIMO radar and those in [4]. However, the computational complexity of our method will increase linearly with the number of iterations. Compared with the

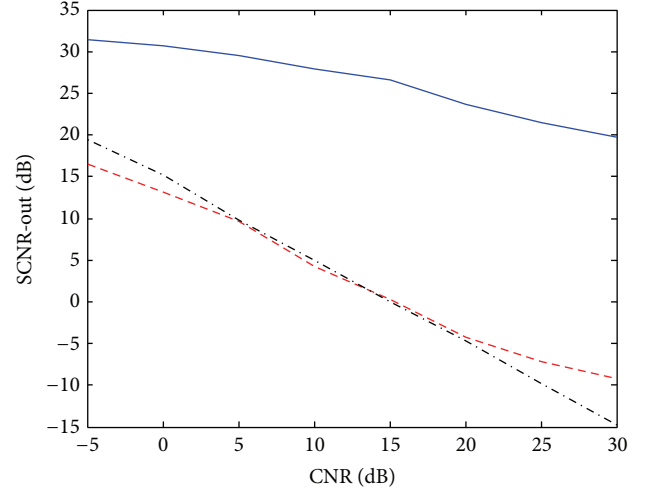


FIGURE 7: The comparison of the SCNR versus CNR.

closed-form solution in [4], more computing resources are needed in the proposed method.

Experiment 4. In this experiment, two application scenes for the proposed method are investigated: the target reflection and attenuation coefficients slowly changed case and quickly changed case. For the slowly changed target case, the coefficients $\{t_{fmm}\}$ are deemed to remain constant in L snapshots duration, so that the FMN coefficients are assumed as independent and identically distributed Gaussian random variables with unity variance. For the quickly changed target case, the coefficients $\{t_{fmm}\}$ will vary within L snapshots. Similarly to Experiment 1, the $LFMN$ coefficients in this case are generated as independent and identically distributed Gaussian random variables with unity variance too. For both cases, the F is set as 3. Under the same MIMO radar system and clutter assumption in Experiment 2, the simulation results of the output SCNR versus input CNR in both cases are shown in Figure 8. It shows that our method has a better performance in quickly changed target case, for the reason that more RCS samples of quickly changed target are obtained in time domain. It is demonstrated once again that MIMO radar has the ability to suppress the target scintillation effectively and the advantages of diversity information brought by MIMO radar can effectively improve the target detection performance.

6. Conclusions

In this paper, the spatial and frequency diversities are combined in one MIMO radar system, namely, spatial-frequency diversity MIMO radar. By taking full advantages of the extra degrees of freedom brought by plenty of spatial and frequency diversities, we investigate the application of spatial-frequency

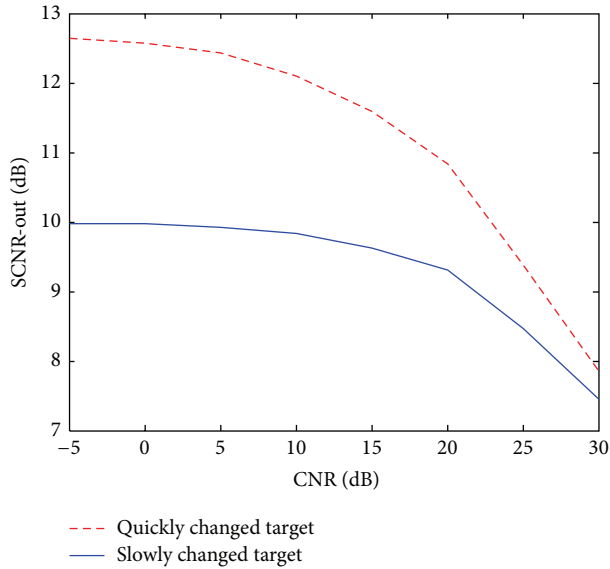


FIGURE 8: The output SCNR versus input CNR in slowly and quickly changed target cases.

diversity MIMO radar in clutter scenarios. Firstly, the water-filling algorithm is introduced to the energy allocation problem of frequency channels. The simulation result shows that it works well to improve the system performance. Then, an iterative algorithm which optimizes the transmitted waveforms and receiving filters alternatively is proposed to maximize the output SCNR, which will improve the target detection performance in the presence of clutters. Simulation results show that the methods we proposed can effectively suppress the clutters with spatial-frequency diversity MIMO radar. Compared with existing methods, the proposed method has a superior performance in the presence of clutter. In addition, it is demonstrated once again in our simulation results that MIMO radar can suppress the target scintillation effectively.

Conflict of Interests

The authors declare that there is no conflict of interests regarding the publication of this paper.

Acknowledgments

This work is supported in part by the National Natural Science Foundation of China (Grant no. 11273017), the College Graduate Scientific Research Innovation Fund in Jiangsu Province of China (Grant no. CXZZ13.0205), and the Shanghai Aerospace Science and Technology Innovation Fund of China (Grant no. SAST201356).

References

- [1] W. Zhang and L. Yang, "Communications-inspired sensing: a case study waveform design," *IEEE Transactions on Signal Processing*, vol. 58, no. 2, pp. 792–803, 2010.
- [2] Y. Yang and R. S. Blum, "MIMO radar waveform design based on mutual information and minimum mean-square error estimation," *IEEE Transactions on Aerospace and Electronic Systems*, vol. 43, no. 1, pp. 330–343, 2007.
- [3] B. Tang, J. Tang, and Y. Peng, "MIMO radar waveform design in colored noise based on information theory," *IEEE Transactions on Signal Processing*, vol. 58, no. 9, pp. 4684–4697, 2010.
- [4] B. Tang, J. Tang, and Y. Peng, "Waveform optimization for MIMO radar in colored noise: further results for estimation-oriented criteria," *IEEE Transactions on Signal Processing*, vol. 60, no. 3, pp. 1517–1522, 2012.
- [5] Y. C. Wang, X. Wang, H. Liu, and Z. Luo, "On the design of constant modulus probing signals for MIMO radar," *IEEE Transactions on Signal Processing*, vol. 60, no. 8, pp. 4432–4438, 2012.
- [6] F. Daum and J. Huang, "MIMO radar: snake oil or good idea?" in *Proceedings of the IEEE International Waveform Diversity and Design Conference (WDD '09)*, pp. 113–117, Kissimmee, Fla, USA, February 2009.
- [7] E. Fishler, A. Haimovich, R. Blum, D. Chizhik, L. Cimini, and R. Valenzuela, "MIMO radar: an idea whose time has come," in *Proceedings of the IEEE Radar Conference*, pp. 71–78, April 2004.
- [8] C. Du, J. S. Thompson, and Y. R. Petillot, "Detector and waveform design for MIMO radar system with noisy channel estimation," *IEEE Transactions on Aerospace and Electronic Systems*, vol. 48, no. 3, pp. 2332–2348, 2012.
- [9] T. Naghibi and F. Behnia, "MIMO radar waveform design in the presence of clutter," *IEEE Transactions on Aerospace and Electronic Systems*, vol. 47, no. 2, pp. 770–781, 2011.
- [10] Y. Yang and R. S. Blum, "Minimax robust MIMO radar waveform design," *IEEE Journal on Selected Topics in Signal Processing*, vol. 1, no. 1, pp. 147–155, 2007.
- [11] E. Grossi, M. Lops, and L. Venturino, "Robust waveform design for MIMO radars," *IEEE Transactions on Signal Processing*, vol. 59, no. 7, pp. 3262–3271, 2011.
- [12] A. M. Haimovich, R. S. Blum, and L. J. Cimini, "MIMO radar with widely separated antennas," *IEEE Signal Processing Magazine*, vol. 25, no. 1, pp. 116–129, 2008.
- [13] E. Fishler, A. Haimovich, R. S. Blum, L. J. Cimini Jr., D. Chizhik, and R. A. Valenzuela, "Spatial diversity in radars—models and detection performance," *IEEE Transactions on Signal Processing*, vol. 54, no. 3, pp. 823–838, 2006.
- [14] V. Ravenni, "Performance evaluations of frequency diversity radar system," in *Proceedings of the 37th IEEE European Microwave Conference (EUMC '07)*, pp. 1715–1718, October 2007.
- [15] J. J. Zhang and A. Papandreou-Suppappola, "MIMO radar with frequency diversity," in *Proceedings of the International Waveform Diversity and Design Conference (WDD '09)*, pp. 208–212, IEEE, Kissimmee, Fla, USA, February 2009.
- [16] S. H. Zhou and H. W. Liu, "Target statistical correlation characteristic for spatial-frequency jointly diversity multiple-input multiple-output radar," *IET Radar, Sonar and Navigation*, vol. 5, no. 6, pp. 638–649, 2011.
- [17] E. F. Nathanson, P. J. Reilly, and M. N. Cohen, "Radar design principles-Signal processing and the Environment," *NASA STI/Recon Technical Report A*, vol. 91, article 46747, 1991.
- [18] B. Friedlander, "Waveform design for MIMO radars," *IEEE Transactions on Aerospace and Electronic Systems*, vol. 43, no. 3, pp. 1227–1238, 2007.

- [19] A. Aubry, A. Demaio, A. Farina, and M. Wicks, "Knowledge-aided (potentially cognitive) transmit signal and receive filter design in signal-dependent clutter," *IEEE Transactions on Aerospace and Electronic Systems*, vol. 49, no. 1, pp. 93–117, 2013.
- [20] M. I. Skolnik, *Radar Handbook*, 1970.
- [21] X. Ling, B. Wu, H. Wen, L. Pan, and F. Luo, "Fast and efficient parallel-shift water-filling algorithm for power allocation in orthogonal frequency division multiplexing-based underlay cognitive radios," *IET Communications*, vol. 7, no. 12, pp. 1269–1278, 2013.
- [22] A. Yoshimoto and T. Hattori, "Area coverage of a multi-link MIMO system with water filling power allocation strategy," in *Proceedings of the 66th IEEE Vehicular Technology Conference (VTC '07)*, pp. 1137–1141, IEEE, October 2007.
- [23] T. M. Cover and J. A. Thomas, *Elements of Information Theory*, John Wiley & Sons, 2012.
- [24] R. A. Horn and C. R. Johnson, *Matrix Analysis*, Cambridge University Press, 2012.

Research Article

An Efficient Signal Reconstruction Algorithm for Stepped Frequency MIMO-SAR in the Spotlight and Sliding Spotlight Modes

Jiajia Zhang, Guangcai Sun, Mengdao Xing, Zheng Bao, and Fang Zhou

Key Laboratory for Radar Signal Processing, Xidian University, Xi'an 710071, China

Correspondence should be addressed to Jiajia Zhang; zjjreal@126.com

Received 25 January 2014; Revised 13 June 2014; Accepted 16 June 2014; Published 26 June 2014

Academic Editor: Mathini Sellathurai

Copyright © 2014 Jiajia Zhang et al. This is an open access article distributed under the Creative Commons Attribution License, which permits unrestricted use, distribution, and reproduction in any medium, provided the original work is properly cited.

Multiple-input multiple-output (MIMO) synthetic aperture radar (SAR) using stepped frequency (SF) waveforms enables a high two-dimensional (2D) resolution with wider imaging swath at relatively low cost. However, only the stripmap mode has been discussed for SF MIMO-SAR. This paper presents an efficient algorithm to reconstruct the signal of SF MIMO-SAR in the spotlight and sliding spotlight modes, which includes Doppler ambiguity resolving algorithm based on subaperture division and an improved frequency-domain bandwidth synthesis (FBS) method. Both simulated and constructed data are used to validate the effectiveness of the proposed algorithm.

1. Introduction

According to the minimum antenna area constraint, high resolution and wide swath (HRWS) pose contradicting requirements on synthetic aperture radar (SAR) system design [1]. This system-inherent limitation can be overcome by single-input multiple-output (SIMO) SAR system [2], which has been extended to multiple SAR modes, such as spotlight and sliding spotlight, to fulfill the different requirements of spatial resolution and coverage in future SAR missions [3–5]. In high-resolution SAR, wide bandwidth signals are needed to obtain a high range resolution. However, the direct transmission of a wide bandwidth signal may lead to a high cost of the hardware [6–8]. A solution to this problem is the transmission of stepped frequency (SF) waveforms in combination with bandwidth synthesis technologies [6–8].

The SF multiple-input multiple-output (MIMO)-SAR, which is defined as the MIMO-SAR system transmitting and receiving a class of SF subband signals simultaneously by multiple azimuth channels, respectively, combines the advantages of the SIMO system and SF waveforms and enables HRWS imaging at relatively low cost [9, 10]. However, only the stripmap mode SF MIMO-SAR has been discussed.

In the spotlight and sliding spotlight modes, the steering of the antenna beams leads to an increase of the azimuth bandwidth and thus raises difficulties for both azimuth reconstruction and bandwidth synthesis. Furthermore, the HRWS leads to a great amount of data, which may cause high computational burden, so an efficient signal reconstruction algorithm is required.

In this paper, an efficient algorithm is presented to reconstruct SF MIMO-SAR signal for the spotlight and sliding spotlight modes. Firstly, a Doppler ambiguity resolving algorithm based on the azimuth subaperture division is presented for azimuth reconstruction of each SF subband signal. Then, an improved frequency-domain bandwidth synthesis method without upsampling in range is proposed to efficiently synthesize the subband signals.

This paper is organized as follows. In Section 2, the signal model of SF MIMO-SAR is introduced. In Section 3, the Doppler ambiguity resolving algorithm based on subaperture division is described. An improved FBS method without upsampling in range is proposed and the flowchart of the signal reconstruction algorithm is shown in Section 4. In Section 5, simulation and real data processing results are presented. Finally, the conclusion is presented in Section 6.

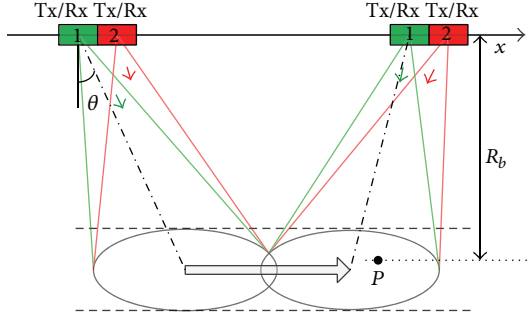


FIGURE 1: Imaging geometry of SF MIMO-SAR (sliding spotlight).

2. Signal Model

Consider a SF MIMO-SAR system with N transmit/receive (Tx/Rx) channels in azimuth by which a class of SF subband signals are transmitted at the same time, respectively. The carrier frequencies of this class of subband signals increase from subband to subband by a fixed frequency step Δf_c , and then the center frequency of the subband n can be represented by

$$f_n = f_c + \Delta f_c \left[n - \frac{(N+1)}{2} \right] = f_c + \Delta f_{c,n}, \quad (1)$$

where f_c is the center frequency of the whole synthesized bandwidth signal and $\Delta f_{c,n}$ denotes the center frequency interval between the n th subband signal and the whole bandwidth signal.

Figure 1 shows the imaging geometry of sliding spotlight SF MIMO-SAR with two channels as an example. The radar moves along the x -axis with a constant velocity v , and the main beams of N transmit/receive (Tx/Rx) channels in azimuth are steered from forward to backward, respectively, pointing to the rotation center of the corresponding mode. The echoes are received by all the N channels simultaneously, so N channels data are achieved for each subband signal. If the azimuth multichannel samples of each subband signal do not coincide, the PRF will be improved N times after azimuth reconstruction, so the equivalent PRF after azimuth reconstruction is $N \cdot \text{PRF}$. In order to ensure relative wide range coverage, the PRF is set to ensure the equivalent PRF after azimuth reconstruction to be lower than the total Doppler bandwidth B_{azi} and slightly greater than the instantaneous Doppler bandwidth B_{ins} [4, 5].

Suppose that X_n and X_m , respectively, denote the relative positions in azimuth of the n th transmit channel (Tx n) and the m th ($m = 1, 2, \dots, N$) receive channel (Rx m). The multichannel data of each subband signal can be converted into equivalent self-transmitting and self-receiving data corresponding to the effective phase centers (EPCs) by compensating the phase errors [8]. The compensating function for the subband n signal received by Rx m is denoted by $H_{1,n}(m)$. After the compensation of the phase errors,

N EPCs signal can be achieved for subband n signal, whose azimuth coordinate can be given as

$$X'_{nm} = \frac{(X_n + X_m)}{2}. \quad (2)$$

The EPC corresponding to Tx1 and Rx1 is defined as the reference EPC, whose azimuth coordinate is set to be zero. It is shown in (2) that, due to different positions of transmit channels, the EPCs of different subband signals corresponding to a same Rx channel are of different azimuth coordinates. These geometry differences between subband signals should be removed for the bandwidth synthesis.

After range compression, the signal of a point target $P(X, R_b)$ transmitted by Tx n and received by Rx m can be expressed as

$$\begin{aligned} s_{1,n}(t, t_a, m) = & w_r \left(t - \frac{2}{c} R_{nm}(t_a) \right) \\ & \times w_{\text{azi}} \left(t_a + \frac{X'_{nm} - X}{v} \right) \\ & \times \exp \left(-j \frac{4\pi f_n}{c} R_{nm}(t_a) \right), \end{aligned} \quad (3)$$

where $R_{nm}(t_a) = \sqrt{R_b^2 + (vt_a + X'_{nm} - X)^2}$ is the slant range from point P to the EPC corresponding to Tx n and Rx m , c is the speed of light, t is the fast time, t_a is the slow time, and $w_r(\cdot)$ and $w_{\text{azi}}(\cdot)$ denote the range window function and the azimuth window function, respectively.

3. Doppler Ambiguity Resolving Based on Subaperture Division

In the spotlight and sliding spotlight modes, the time-variant squint angle inevitably leads to an extension of the azimuth spectrum [4, 5]. The time-frequency distribution (TFD) of the sliding spotlight mode is shown in Figure 2(a). The azimuth reconstruction processing based on the subaperture division for the sliding spotlight SIMO SAR [4] can be extended to SF MIMO-SAR in the spotlight and sliding spotlight modes to resolve Doppler ambiguity of each subband signal. The subaperture division of subband signals should ensure that the processed Doppler bandwidth of the whole bandwidth signal is smaller than the equivalent PRF. Since the whole bandwidth is very wide to obtain a high resolution, the influence of range frequency on the processed Doppler bandwidth should be taken into account, which is different from the case in [4].

The beam central frequency varying with slow time t_a and range frequency can be expressed as

$$f_{dc}(f) = \frac{2v \sin[\theta(t_a)]}{c} f, \quad (4)$$

where $f \in [f_c - N\Delta f_c/2, f_c + N\Delta f_c/2]$ is the range frequency, which covers all the subbands and θ denotes the time-variant azimuth squint angle. From Figure 2(b), the processed

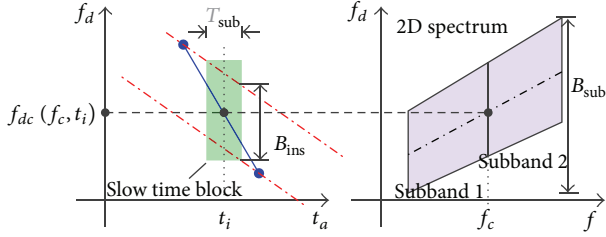


FIGURE 2: The subaperture division. (a) The TFD of sliding spotlight. (b) 2D spectrum of the whole bandwidth signal.

azimuth bandwidth B_{sub} of the whole bandwidth signal can be approximately expressed as

$$B_{sub} \approx B_{ins} + k_{rot} T_{sub} + f_{dc,i} \left(f_c + \frac{N \Delta f_c}{2} \right) - f_{dc,i} \left(f_c - \frac{N \Delta f_c}{2} \right), \quad (5)$$

where $k_{rot} = 2v^2 f_c / c R_{rot}$ denotes the slope rate of the variation of the beam central Doppler frequency, R_{rot} is the rotational distance, and $f_{dc,i}$ denotes the Doppler center of the i th subaperture, which varies with the range frequency. To reconstruct the Doppler spectrum of the whole bandwidth signal, the duration of each slow time block T_{sub} is chosen to ensure that the processed bandwidth B_{sub} in each block is less than $N \cdot PRF$.

After the subaperture division, the signal described by (5) is multiplied by a Doppler shift function $H_{2,n}(t_a, m) = \exp(-j2\pi t_a f_{dc,i}(f_c))$ to move the Doppler spectrum to the Doppler baseband. Then, the Doppler ambiguity can be resolved by spatial filtering [3–5] for each subband signal. The spatial filtering is a weighting operation of a multichannel signal for each subband in the Doppler domain. Considering the great amount of SF MIMO-SAR data, in order to reduce the computational burden of weight vectors of spatial filtering, the signals are multiplied by compensating functions to make the weight vectors independent of specific Doppler frequency [5], and the compensating functions can be constructed as

$$H_{3,n}(f_a, m) = \exp \left(-j2\pi \frac{X'_{nm}}{v} (f_a + f_{dc,i}(f_c)) \right), \quad (6)$$

where $f_a \in (-N \cdot PRF/2, -(N-1) \cdot PRF/2)$ is the Doppler frequency. Then the weight vectors of the spatial filter can be obtained by

$$[\mathbf{w}_n(1), \dots, \mathbf{w}_n(m), \dots, \mathbf{w}_n(N)] = \mathbf{A}_n^{-1}, \quad (7)$$

where

$$\mathbf{A}_n = [\mathbf{a}_n(1), \mathbf{a}_n(2), \dots, \mathbf{a}_n(N)]^T, \quad (8)$$

$$\mathbf{a}_m = \left[1, \exp \left(j2\pi \frac{X_m}{v} PRF \right), \dots, \exp \left(j2\pi \frac{X_m}{v} (N-1) PRF \right) \right]^T. \quad (9)$$

Then, the Doppler spectrum can be reconstructed by

$$S_{2,n}(t, f_a + m \cdot PRF) = \mathbf{S}_{1,n} \mathbf{w}_n(m), \quad (10)$$

where $\mathbf{S}_{1,n} = [S_{1,n}(t, f_a, 1), \dots, S_{1,n}(t, f_a, N)]$ is the multi-channel signal vector of subband n . It can be observed from (9) that $\mathbf{a}_n(m)$ is independent of specific Doppler bin, and thus $\mathbf{w}_n(m)$ does not need to be updated with azimuth Doppler bins, which can sufficiently reduce the computation burden.

After the Doppler ambiguity resolving, the Doppler spectrum of subband n signal can be expressed as

$$\begin{aligned} S_{2,n}(t, f_d) &= w_r \left(t - \frac{2}{c} R_{ref}(f_d) \right) W_{azi}(f_d) \\ &\times \exp \left(-j2\pi (f_d + f_{dc,i}(f_c)) \frac{X}{v} \right) \\ &\times \exp \left(-j \frac{2\pi}{v} R_b \sqrt{\left(\frac{2v}{c} f_n \right)^2 - (f_d + f_{dc,i}(f_c))^2} \right), \end{aligned} \quad (11)$$

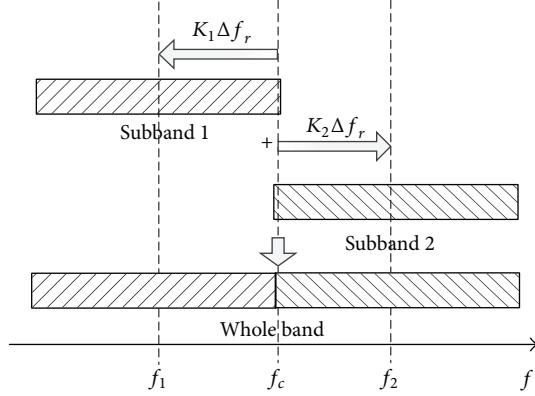
where $f_d \in (-N \cdot PRF/2, N \cdot PRF/2)$ denotes the Doppler frequency. From (11), we can see that each subband signal is equivalent to a single channel signal, and the geometry differences between different subband signals are removed. Then the bandwidth synthesis can be performed in Doppler domain.

4. Improved FBS Method in Doppler Domain

In general, there are two popular methods for the bandwidth synthetic of SAR signal: the synthetic the time-domain bandwidth synthesis (TBS) method and the FBS method. The TBS method is accurate, but the long duration of the synthetic pulse causes a high computation burden making it inefficient [6]. The FBS method is also accurate and more efficient, so it is widely used for bandwidth synthesis of SAR signal [7, 8].

The FBS method proposed in [7] transforms the subband signals to range frequency domain and then shifts the spectrum of subband n signal by $\Delta f_{c,n}$ and performs coherent summation to obtain the whole bandwidth signal. However, considering the signals are discrete, the spectrum can only be shifted by an integer number of frequency bins in frequency domain. So this method is precise only if the residual fractional part of $\Delta f_{c,n}$ is zero. A solution to this problem is N times upsampling and then multiplying the signal of subband n by a frequency shift function in time domain to shift the spectrum by $\Delta f_{c,n}$ [8]. However, the processing of upsampling adds an extra FFT, N times zero-padding in frequency domain, and an extra IFFT to the processing of bandwidth synthesis, which is inefficient with respect to both the use of data space and processing time.

To avoid signal upsampling in range, an improved FBS method in Doppler domain is proposed. Firstly, a slight shift of the range frequency spectrum is performed. The shift

FIGURE 3: The spectrum shift and coherent summation ($N = 2$).

amount is the value of the fractional part of $\Delta f_{c,n}$, so the frequency shift functions can be constructed as

$$H_{4,n}(t) = \exp[j2\pi t(\Delta f_{c,n} - K_n \Delta f_r)], \quad (12)$$

where Δf_r denotes the frequency interval of a frequency bin and K_n is the integer part of $\Delta f_{c,n}/\Delta f_r$. Note that the frequency shifting amount is smaller than the value of a frequency bin, so that the range frequency spectrums do not alias.

Then, after the spectrum shift, the signals are transformed into range frequency domain. The center frequency distance between subband n signal and the whole bandwidth signal spans over K_n frequency bins, so spectrum shift and precise coherent summation can be performed as shown in Figure 3. Therefore, in comparison to the FBS method used in [8], the proposed improved FBS method can perform bandwidth synthesis precisely without upsampling of signal and thus lowers the computation load. After the coherent summation, the whole bandwidth signal in 2D frequency domain is obtained, which can be processed by conventional SAR imaging algorithms for corresponding modes [4, 11].

Figure 4 shows the flowchart of the proposed algorithm in the case of $N = 2$. It consists of three parts: subaperture division, Doppler ambiguity resolving, and bandwidth synthesis.

Suppose L_r and L_a denote the range and azimuth sampling numbers of each subband signal, respectively. According to the flow of the proposed algorithm, the computational load of improved FBS method can be written as $(1/2)NL_a \log_2 L_r + NL_a L_r$, while the computational load of FBS method presented in [8] is $(1/2)NL_a \log_2 L_r + NL_a \log_2 NL_r + N^2 L_a L_r$. Therefore, the proposed improved FBS method can sufficiently lower the computational load of bandwidth synthesis.

5. Simulation and Raw Data Results

In this section, point targets simulation and constructed data processing results are carried out to verify the validity of the proposed algorithm.

TABLE 1: Main system parameters of point target simulation.

Number of Tx/Rx	2
Pulse duration	10 μ s
Acquisition time	6 s
Rotational distance	800 km
PRF	1598 Hz
Step frequency	250 MHz
Center frequency of subband 1	9.65 GHz
Azimuth baseline	2.3 m
Platform velocity	7390 m/s
Center distance of scene	617 km

5.1. Simulation. The main parameters of a sliding spotlight SF MIMO-SAR system are given in Table 1. A 3×3 point target array, of which the targets are uniformly distributed in a scene of $2 \text{ km} \times 2 \text{ km}$ in azimuth and range directions, is set in the illustrated scene.

After the subaperture division, the subband 1 signal in the 2D frequency domain before and after the spatial filtering is shown in Figures 5(a) and 5(b), respectively. It can be observed that the Doppler ambiguity is resolved by the spatial filtering, and the Doppler spectrum without aliasing is reconstructed for each subband signal. Then the improved FBS method is performed to combine the two subband signals, and the whole bandwidth signal in the 2D frequency domain is shown in Figure 6(a). Figure 6(b) shows the range images of a point target before and after bandwidth synthesis, from which one can see that the high range resolution is achieved after bandwidth synthesis. Then the imaging algorithm proposed in [11] is used to process the 2D reconstructed signal and the imaging result is obtained. The interpolated contour plots of three of the point targets are shown in Figure 7. These three point targets are denoted by P_1 , P_2 , and P_3 , respectively, and their 2D coordinates are $(-1 \text{ km}, 616 \text{ km})$, $(0 \text{ km}, 617 \text{ km})$, and $(1 \text{ km}, 618 \text{ km})$. The plots show that the point targets are well focused. The key image quality parameters, namely, the integrated sidelobe ratios (IRWs), the peak sidelobe ratios (PSLRs), and the integrated sidelobe ratios (ISLRs), are measured and shown in Table 2, which further verify the performance of the proposed algorithm.

5.2. Constructed Data Experiment. Since there are no SF MIMO-SAR data available for us, a single channel airborne Spotlight SAR data is used to construct SF MIMO-SAR data. The airborne Spotlight SAR data was collected on July, 2008, the main system parameters of which are given in Table 3.

Firstly, the original data is transformed into range frequency domain and the whole range bandwidth is divided into two subbands, and then the subband 2 data is transformed into Doppler domain and multiplied by a slow time delay function to simulate an EPC difference from subband 1. Finally, the two subband data are downsampled by a factor of two into equivalent two channel undersampled data, respectively. Then a two-input two-output MIMO-SAR data in spotlight mode with two subbands is obtained. The main

TABLE 2: Image quality of point targets.

Target	IRW (m)	Range PSLR (dB)	ISLR (dB)	IRW (m)	Azimuth PSLR (dB)	ISLR (dB)
P ₁	0.255	-13.29	-10.01	0.280	-13.39	-10.48
P ₂	0.254	-13.30	-10.08	0.278	-13.41	-10.60
P ₃	0.255	-13.30	-10.03	0.281	-13.41	-10.51

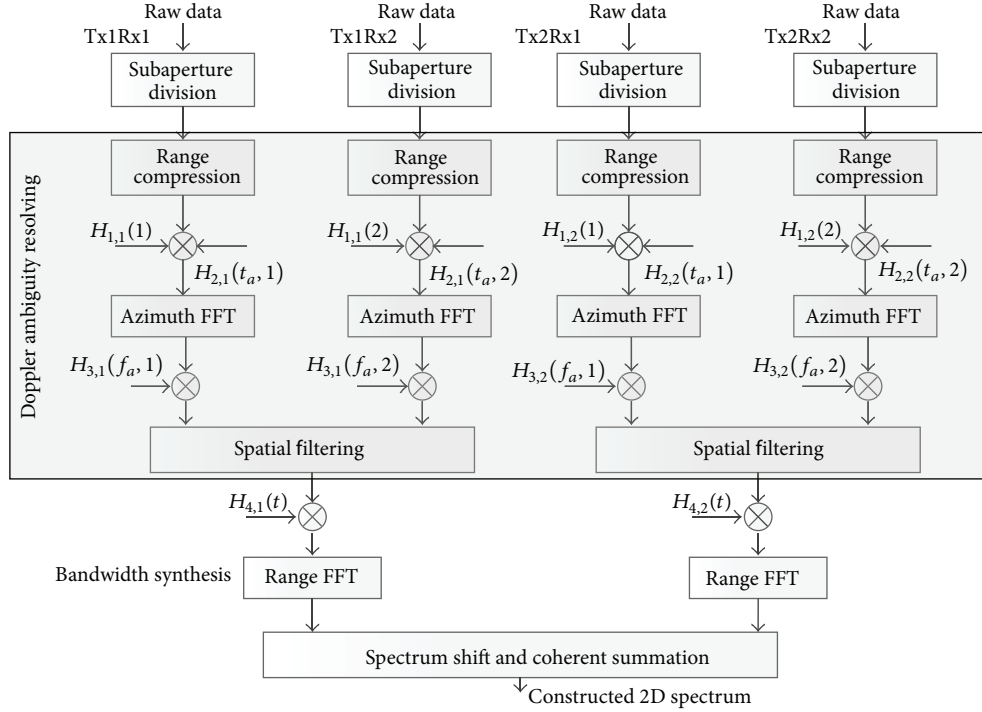
FIGURE 4: Flowchart of the proposed algorithm ($N = 2$).

TABLE 3: Main system parameters of original data.

Center frequency	9.6 GHz
Acquisition time	10 s
PRF	900 Hz
Signal bandwidth	600 MHz
Platform velocity	97 m/s
Center distance of scene	20 km

parameters of the constructed SF MIMO-SAR data are given in Table 4.

Figure 8(a) shows the focused image of subband 1 data after Doppler ambiguity resolving, from which one can see that no ghost exists in azimuth. The focused image of the synthesized bandwidth signal is shown in Figure 8(b), and the comparison between the range images of a point target in the amplified area before and after bandwidth synthesis is shown in Figure 8(c), from which one can see that the range resolution is improved by the proposed improved FBS method. Therefore, the result of constructed real data processing also proves the effectiveness of the proposed algorithm.

TABLE 4: Main system parameters of constructed data.

Center frequency	9.6 GHz
Acquisition time	10 s
PRF	450 Hz
Center frequency of subband 1	9.45 GHz
Step frequency	300 MHz
Platform velocity	97 m/s
Center distance of scene	20 km
Azimuth baseline	0.22 m

6. Conclusion

This paper presents an efficient algorithm to reconstruct SF MIMO-SAR signal in the spotlight and sliding spotlight modes. A Doppler ambiguity resolving method based on the subaperture division is presented to reconstruct the Doppler spectrum of each subband signal. Then, considering the high computation load of SF MIMO-SAR signal synthesis, an improved FBS method is proposed to avoid upsampling of data and thus lower the computation load of bandwidth synthesis. Results of point targets simulation and constructed

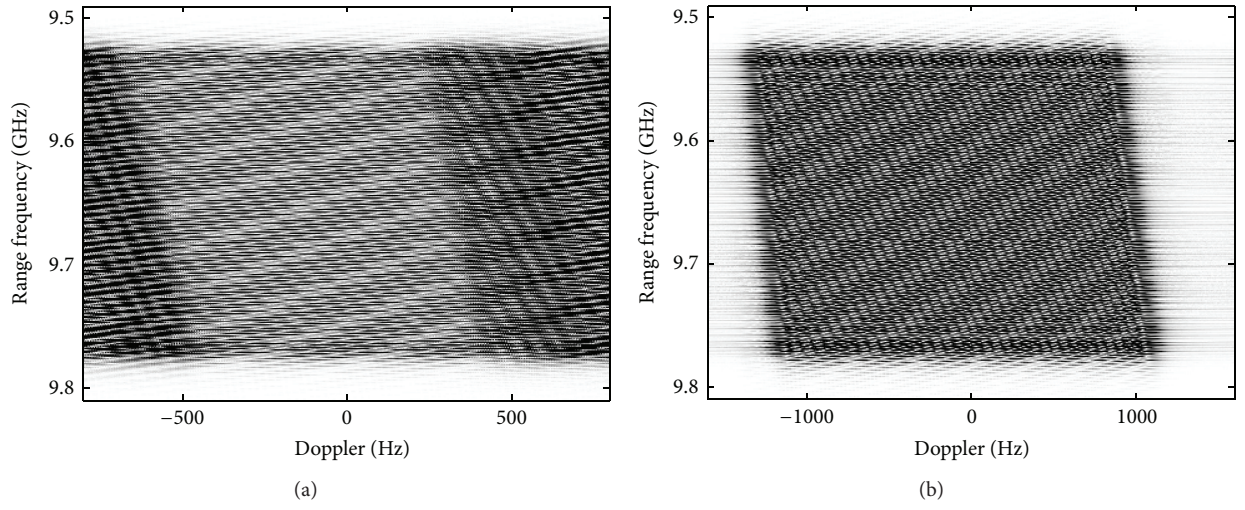


FIGURE 5: 2D spectrum (a) before and (b) after spatial filtering.

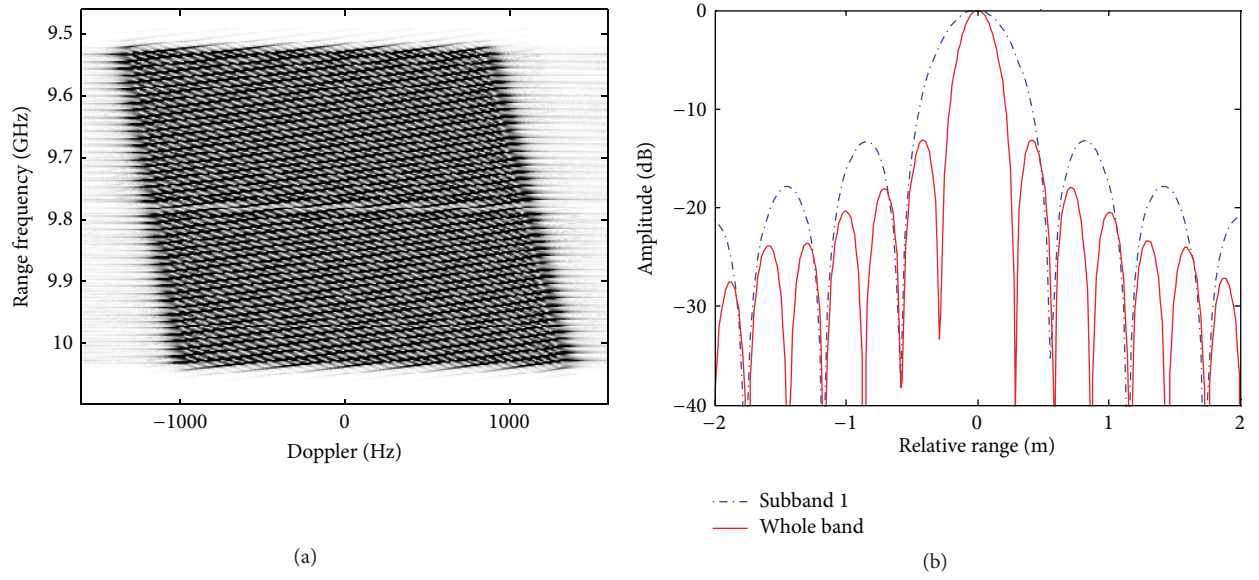


FIGURE 6: (a) 2D spectrum of the whole bandwidth signal. (b) Range images of a point target before and after bandwidth synthesis.

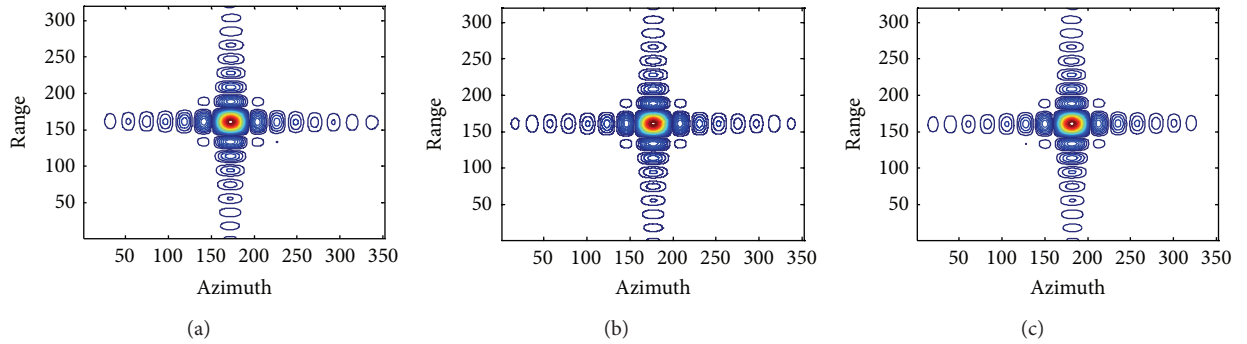


FIGURE 7: Contour plots of targets.

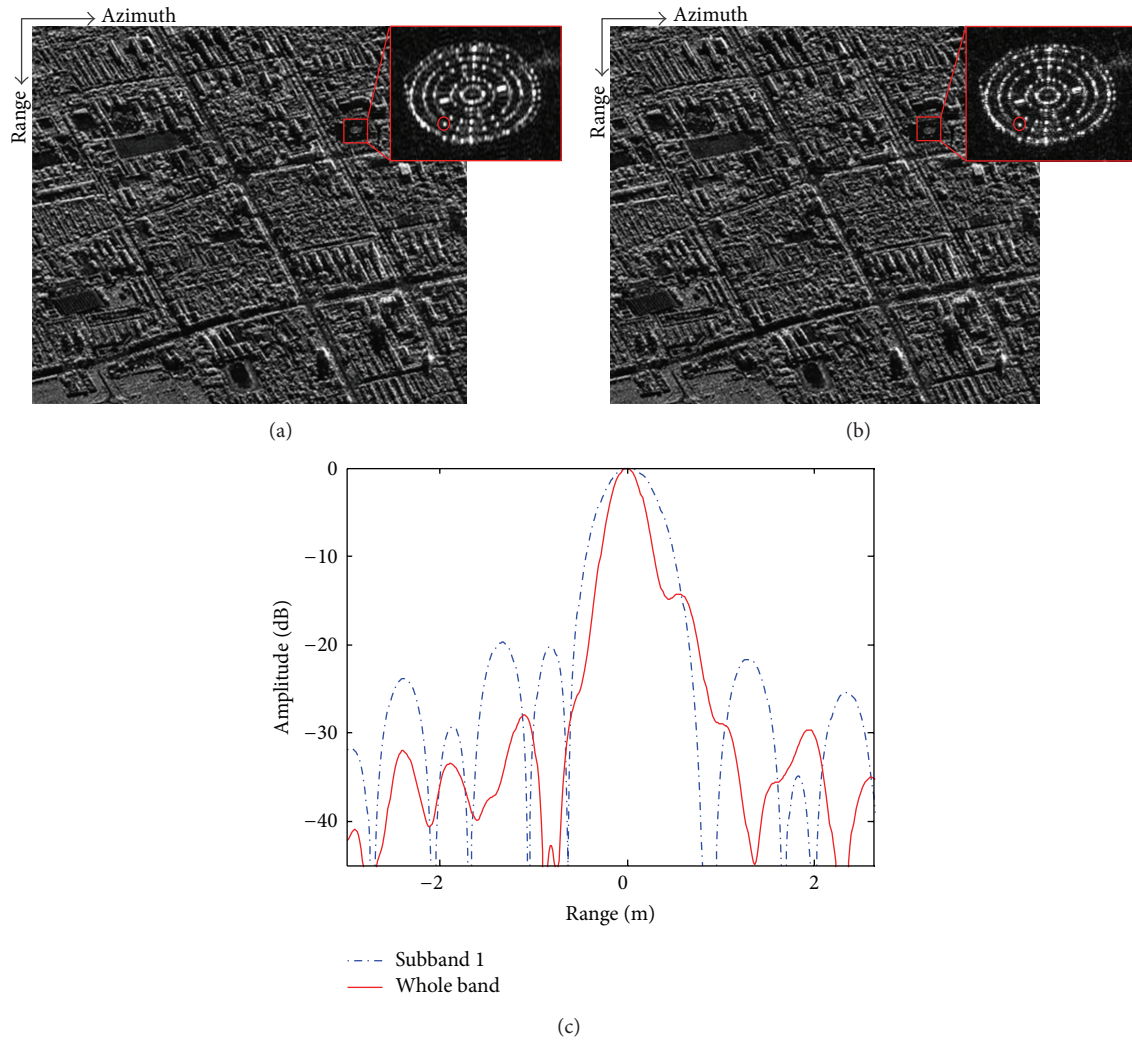


FIGURE 8: Results from an airborne spotlight SAR. (a) The image of subband 1 data after Doppler ambiguity resolving. (b) The image of the synthesized bandwidth data. (c) The range comparison of a point target in the amplified area.

data processing have validated the effectiveness of the proposed algorithm.

Conflict of Interests

The authors declare that there is no conflict of interests regarding the publication of this paper.

Acknowledgment

This work was supported by the National Natural Science Foundation of China under Grant 61301292.

References

- [1] A. Freeman, W. T. K. Johnson, B. Huneycutt et al., "The myth of the minimum SAR antenna area constraint," *IEEE Transactions on Geoscience and Remote Sensing*, vol. 38, no. 1, pp. 320–324, 2000.
- [2] A. Currie and M. A. Brown, "Wide-swath SAR," *IEE Proceedings F: Radar and Signal Processing*, vol. 139, no. 2, pp. 122–135, 1992.
- [3] N. Gebert, G. Krieger, and A. Moreira, "Multichannel azimuth processing in ScanSAR and TOPS mode operation," *IEEE Transactions on Geoscience and Remote Sensing*, vol. 48, no. 7, pp. 2994–3008, 2010.
- [4] Q. Chen, Y. Deng, R. Wang, and Y. Liu, "Investigation of multichannel sliding spotlight SAR for ultrahigh-resolution and wide-swath imaging," *IEEE Geoscience and Remote Sensing Letters*, vol. 10, no. 6, pp. 1339–1343, 2013.
- [5] G. Sun, M. Xing, X. Xia, Y. Wu, P. Huang, and Z. Bao, "Multichannel Full-aperture Azimuth Processing for beam steering SAR," *IEEE Transactions on Geoscience and Remote Sensing*, vol. 51, no. 9, pp. 4761–4778, 2013.
- [6] P. Berens, "SAR with ultra-high range resolution using synthetic bandwidth," in *Proceedings of the IEEE International Geoscience and Remote Sensing Symposium (IGARSS '99)*, vol. 3, pp. 1752–1754, Hamburg, Germany, July 1999.
- [7] A. J. Wilkinson, R. T. Lord, and M. R. Inggs, "Stepped-frequency processing by reconstruction of target reflectivity spectrum," in

Proceedings of the South African Symposium on Communications and Signal Processing (COMSIG '98), pp. 101–104, Rondebosch, South Africa, September 1998.

- [8] Y. Deng, H. Zheng, R. Wang, J. Feng, and Y. Liu, “Internal calibration for stepped-frequency chirp SAR imaging,” *IEEE Geoscience and Remote Sensing Letters*, vol. 8, no. 6, pp. 1105–1109, 2011.
- [9] Q. Wu, M. Xing, Z. Bao, and H. Shi, “Wide swath, high range resolution imaging with MIMO-SAR,” in *IET International Radar Conference*, April 2009.
- [10] X. Luo, R. Wang, Y. Deng, and W. Xu, “Influences of channel errors and interference on the OFDM-MIMO SAR,” in *Proceedings of the IEEE Radar Conference*, 2013.
- [11] G. Sun, M. Xing, Y. Wang, Y. Wu, Y. Wu, and Z. Bao, “Sliding spotlight and TOPS SAR data processing without subaperture,” *IEEE Geoscience and Remote Sensing Letters*, vol. 8, no. 6, pp. 1036–1040, 2011.

Research Article

The PARAFAC-MUSIC Algorithm for DOA Estimation with Doppler Frequency in a MIMO Radar System

Nan Wang,¹ Wenguang Wang,¹ Fan Zhang,² and Yunneng Yuan¹

¹ School of Electronic and Information Engineering, Beihang University, Beijing 100191, China

² College of Information Science & Technology, Beijing University of Chemical Technology, Beijing 100029, China

Correspondence should be addressed to Wenguang Wang; wwenguang@ee.buaa.edu.cn

Received 26 February 2014; Accepted 10 June 2014; Published 23 June 2014

Academic Editor: Wei Xu

Copyright © 2014 Nan Wang et al. This is an open access article distributed under the Creative Commons Attribution License, which permits unrestricted use, distribution, and reproduction in any medium, provided the original work is properly cited.

The PARAFAC-MUSIC algorithm is proposed to estimate the direction-of-arrival (DOA) of the targets with Doppler frequency in a monostatic MIMO radar system in this paper. To estimate the Doppler frequency, the PARAFAC (parallel factor) algorithm is firstly utilized in the proposed algorithm, and after the compensation of Doppler frequency, MUSIC (multiple signal classification) algorithm is applied to estimate the DOA. By these two steps, the DOA of moving targets can be estimated successfully. Simulation results show that the proposed PARAFAC-MUSIC algorithm has a higher accuracy than the PARAFAC algorithm and the MUSIC algorithm in DOA estimation.

1. Introduction

Recently, there has been a growing interest in multiple-input multiple-output radar which utilizes multiple antennas at both transmitter and receiver. According to the array configuration, MIMO radar can be classified into two main types, the first of which is called distributed MIMO radar. It is composed of widely separated transmit antennas which transmit the linearly independent signals. Based on the sufficient distribution space and linearly independent signals, the distributed MIMO radar is able to obtain rich scattering properties of the targets and to mitigate radar cross-section (RCS) fluctuations. The second type is called collocated MIMO radar, in which the transmit elements are collocated. By transmitting independent waveforms and capitalizing on the MIMO spatial signature, the collocated MIMO can estimate the parameters of interest via coherent processing.

On the other hand, an accurate estimation of signal DOA has made a great sense in radar system of military and commercial application. Many algorithms were proposed on DOA estimation in MIMO radar system as it provides waveform diversity and spatial distribution of flexibility. In [1], the Capon algorithm, proposed in 1969, is a main lobe

self-adaptive algorithm which is stable but poor at low SNR. ESPRIT (estimation signal parameter via rotational invariance techniques) algorithm in [2] exploits the invariance property for DOA estimation in MIMO radar system. In [3], MUSIC algorithm, one of the most popular algorithms for DOA estimation, utilizes subspace analysis and has a good performance.

Although these algorithms introduced above are useful for DOA estimation, they are poor when the Doppler frequency is taken into consideration. As the target always moves, DOA estimation of moving targets is extremely essential. In [4, 5], PARAFAC algorithm exploits the iteration of TALS (trilinear alternating least square) to estimate the frequency and DOA. PARAFAC algorithm has a better performance than Capon, ESPRIT, and MUSIC when considering Doppler frequency. PARAFAC-MUSIC algorithm, proposed in this paper, utilizes the PARAFAC algorithm to estimate the Doppler frequency and then exploits MUSIC algorithm to estimate the DOA after the Doppler effect is eliminated. Simulation shows that PARAFAC-MUSIC algorithm is also able to solve the problem generated from Doppler frequency and may have a better performance than PARAFAC algorithm.

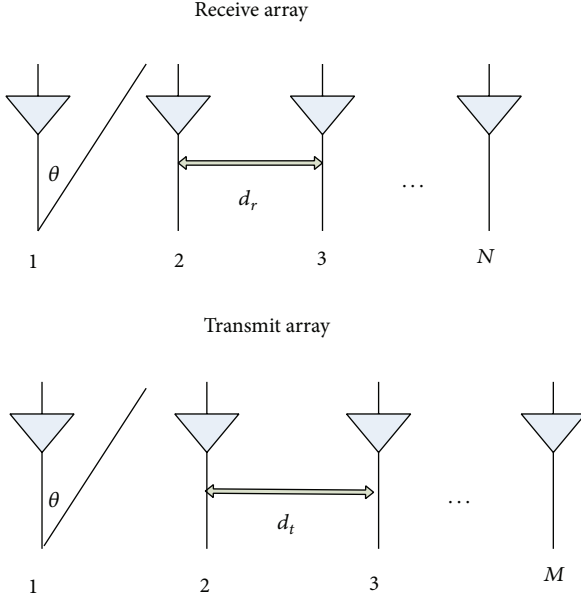


FIGURE 1: Transmit and receive antennas.

2. Signal Model

Assume that there is a monostatic MIMO radar system with M collocated transmit antennas and N collocated receive antennas, both of which are uniform linear arrays (ULA), shown in Figure 1. Since the transmit array and the receive array are assumed to be close to each other, the DOD (direction of departure) and the DOA are approximately equal, denoted by θ . d_t and d_r are the interelement spacing at the transmitter and receiver. The M transmit antennas transmit orthogonal waveforms simultaneously while the N receive antennas receive the signals reflected from the targets. It is supposed that there are P targets in the far field, each of which can be considered as a point source. And the RCS of each target is assumed as a constant during a pulse period.

The received signal at time t before match filters can be expressed as

$$\mathbf{x}(t) = \sum_{p=1}^P \mathbf{a}_r(\theta_p) \times \mathbf{a}_t(\theta_p)^T \times \mathbf{s}_p(t) + \mathbf{n}_x(t), \quad (1)$$

where $\mathbf{a}_r(\theta_p) = [1, e^{-j2\pi d_r \sin \theta_p / \lambda}, \dots, e^{-j2\pi(N-1)d_r \sin \theta_p / \lambda}]^T$ is the receive steering vector and $\mathbf{a}_t(\theta_p) = [1, e^{-j2\pi d_t \sin \theta_p / \lambda}, \dots, e^{-j2\pi(M-1)d_t \sin \theta_p / \lambda}]^T$ is the transmit steering vector. λ denotes the wavelength. Consider $\mathbf{s}_p(t) = [\beta_p e^{-j2\pi f_{dp} t} s_1(t), \dots, \beta_p e^{-j2\pi f_{dp} t} s_M(t)]^T$, where β_p is the reflection coefficient depending on the RCS of the target p , f_{dp} is Doppler frequency of the target p , and $s_m(t)$ is the transmit signal of each transmit antenna. $\mathbf{n}_x(t)$ is a complex Gaussian white noise vector with zero mean and covariance matrix $\sigma^2 \mathbf{I}$. $[\cdot]^T$ represents transpose operator.

As the transmit waveforms are orthogonal from each other, the output of the match filters at time t is

$$\mathbf{y}(t) = [\mathbf{A}_t(\theta) \odot \mathbf{A}_r(\theta)] \mathbf{c}(t) + \mathbf{n}_y(t), \quad (2)$$

where

$$\begin{aligned} \mathbf{A}_t(\theta) &= [\mathbf{a}_t(\theta_1), \dots, \mathbf{a}_t(\theta_P)], \\ \mathbf{A}_r(\theta) &= [\mathbf{a}_r(\theta_1), \dots, \mathbf{a}_r(\theta_P)], \end{aligned} \quad (3)$$

$\mathbf{c}(t) = [\beta_1 e^{j2\pi f_{d1} t}, \dots, \beta_P e^{j2\pi f_{dP} t}]^T$, and “ \odot ” represents the Khatri-Rao product.

So the received signal before the match filters can be expressed by matrix as

$$\mathbf{X} = \sum_{p=1}^P [\mathbf{a}_r(\theta_p) \times \mathbf{a}_t(\theta_p)^T \times \mathbf{S}] + \mathbf{W}_x, \quad (4)$$

where $\mathbf{S} = [\mathbf{s}_1, \mathbf{s}_2, \mathbf{s}_3, \dots, \mathbf{s}_L]$ and L denotes the number of snapshot. \mathbf{W}_x is complex Gaussian white noise matrix.

The output at match filters can be expressed by matrix as

$$\mathbf{Y} = [\mathbf{A}_t(\theta) \odot \mathbf{A}_r(\theta)] \mathbf{C}^T + \mathbf{W}_y, \quad (5)$$

where $\mathbf{Y} = [\mathbf{y}_1, \mathbf{y}_2, \mathbf{y}_3, \dots, \mathbf{y}_L]$ is a $MN \times L$ matrix and $\mathbf{C}^T = [c_1, c_2, c_3, \dots, c_L]$ is a $P \times L$ matrix. Consider $c_l = [\beta_1 e^{-j2\pi f_{d1} l T}, \dots, \beta_P e^{-j2\pi f_{dP} l T}]^T$, in which T is sampling time. \mathbf{W}_y is complex Gaussian white noise matrix.

3. PARAFAC-MUSIC Algorithm

PARAFAC-MUSIC algorithm combines the advantages of PARAFAC algorithm and MUSIC algorithm. It exploits PARAFAC algorithm to estimate the Doppler frequency, then eliminates the effect in received signal generated from Doppler frequency, and finally utilizes MUSIC algorithm to estimate the DOA.

As known from formula (5), the output \mathbf{Y} at match filters possesses the character of three-way model. Therefore, it can be expressed as set \mathbf{Y}_L composed of L sections \mathbf{Y}_l , each of which is a $M \times N$ matrix. \mathbf{Y}_l can be expressed as

$$\mathbf{Y}_l = \mathbf{A}_t(\theta) \times D_l[\mathbf{C}] \times \mathbf{A}_r(\theta)^T + \mathbf{w}_l, \quad (6)$$

where $D_j[\cdot]$ represents the diagonal matrix composed of the elements obtained from the j th row of the matrix.

In the same way, \mathbf{Y} can be expressed as a set \mathbf{Y}_N composed of N sections \mathbf{Y}_n or a set \mathbf{Y}_M composed of M sections \mathbf{Y}_m . \mathbf{Y}_n and \mathbf{Y}_m can be, respectively, expressed as

$$\begin{aligned} \mathbf{Y}_n &= \mathbf{C} \times D_n[\mathbf{A}_r(\theta)] \times \mathbf{A}_t(\theta)^T + \mathbf{w}_n, \\ \mathbf{Y}_m &= \mathbf{A}_r(\theta) \times D_m[\mathbf{A}_t(\theta)] \times \mathbf{C}^T + \mathbf{w}_m. \end{aligned} \quad (7)$$

So \mathbf{Y}_L , \mathbf{Y}_N , and \mathbf{Y}_M can be, respectively, expressed as

$$\begin{aligned}
 \mathbf{Y}_L &= \begin{bmatrix} \mathbf{Y}_1 \\ \mathbf{Y}_2 \\ \vdots \\ \mathbf{Y}_L \end{bmatrix} \\
 &= \begin{bmatrix} \mathbf{A}_t(\theta) \times D_1 [\mathbf{C}] \\ \mathbf{A}_t(\theta) \times D_2 [\mathbf{C}] \\ \vdots \\ \mathbf{A}_t(\theta) \times D_L [\mathbf{C}] \end{bmatrix} \mathbf{A}_r(\theta)^T + \begin{bmatrix} \mathbf{w}_1 \\ \mathbf{w}_2 \\ \vdots \\ \mathbf{w}_L \end{bmatrix} \\
 &= [\mathbf{C} \odot \mathbf{A}_t(\theta)] \mathbf{A}_r(\theta)^T + \mathbf{W}_L, \\
 \mathbf{Y}_N &= \begin{bmatrix} \mathbf{Y}_1 \\ \mathbf{Y}_2 \\ \vdots \\ \mathbf{Y}_N \end{bmatrix} \\
 &= \begin{bmatrix} \mathbf{C} \times D_1 [\mathbf{A}_r(\theta)] \\ \mathbf{C} \times D_2 [\mathbf{A}_r(\theta)] \\ \vdots \\ \mathbf{C} \times D_N [\mathbf{A}_r(\theta)] \end{bmatrix} \mathbf{A}_t(\theta)^T + \begin{bmatrix} \mathbf{w}_1 \\ \mathbf{w}_2 \\ \vdots \\ \mathbf{w}_N \end{bmatrix} \quad (8) \\
 &= [\mathbf{A}_r(\theta) \odot \mathbf{C}] \mathbf{A}_t(\theta)^T + \mathbf{W}_N, \\
 \mathbf{Y}_M &= \begin{bmatrix} \mathbf{Y}_1 \\ \mathbf{Y}_2 \\ \vdots \\ \mathbf{Y}_M \end{bmatrix} \\
 &= \begin{bmatrix} \mathbf{A}_r(\theta) \times D_1 [\mathbf{A}_t(\theta)] \\ \mathbf{A}_r(\theta) \times D_2 [\mathbf{A}_t(\theta)] \\ \vdots \\ \mathbf{A}_r(\theta) \times D_M [\mathbf{A}_t(\theta)] \end{bmatrix} \mathbf{C}^T + \begin{bmatrix} \mathbf{w}_1 \\ \mathbf{w}_2 \\ \vdots \\ \mathbf{w}_M \end{bmatrix} \\
 &= [\mathbf{A}_t(\theta) \odot \mathbf{A}_r(\theta)] \mathbf{C}^T + \mathbf{W}_M.
 \end{aligned}$$

When the three-way array is obtained, it is common to utilize TALS [5] to estimate $\hat{\mathbf{A}}_t(\theta)$, $\hat{\mathbf{A}}_r(\theta)$, and $\hat{\mathbf{C}}$. TALS is a popular method in data detection of three-way array model which updates one estimated matrix in each step after obtaining the initial estimated matrixes. Least square (LS) algorithm always works in estimated matrix update that takes the estimated matrix to be updated as a variable and other estimated matrixes as constants in each step. When all the estimated matrixes are updated, it will carry on the next iteration until convergence. Specific steps of TALS are stated as follows.

Step 1. Construct the three-way array \mathbf{Y}_L , \mathbf{Y}_N , \mathbf{Y}_M based on the output at match filters.

Step 2. Initialize all the estimated matrixes $\hat{\mathbf{A}}_{t0}(\theta)$, $\hat{\mathbf{A}}_{r0}(\theta)$, and $\hat{\mathbf{C}}_0$.

Step 3. Substitute $\hat{\mathbf{A}}_{t(k-1)}(\theta)$, $\hat{\mathbf{C}}_{k-1}$ into formula (9) to obtain $\hat{\mathbf{A}}_{rk}(\theta)$ shown as formula (10). $[\cdot]_F$, $\#$ represents Frobenius norm and the pseudo inverse operation. k represents the iterations

$$\hat{\mathbf{A}}_{rk}(\theta) = \arg \min_{\hat{\mathbf{A}}_r} \|\mathbf{Y}_L - [\hat{\mathbf{C}}_{k-1} \odot \hat{\mathbf{A}}_{t(k-1)}(\theta)] \hat{\mathbf{A}}_{rk}^T(\theta)\|_F^2, \quad (9)$$

$$\hat{\mathbf{A}}_{rk}(\theta) = \mathbf{Y}_L^T \left[(\hat{\mathbf{C}}_{k-1} \odot \hat{\mathbf{A}}_{t(k-1)}(\theta))^\# \right]^T. \quad (10)$$

Step 4. Substitute $\hat{\mathbf{A}}_{rk}(\theta)$, $\hat{\mathbf{C}}_{k-1}$ into formula (11) to obtain $\hat{\mathbf{A}}_{tk}(\theta)$ shown as formula (12). Consider

$$\hat{\mathbf{A}}_{tk}(\theta) = \arg \min_{\hat{\mathbf{A}}_t} \|\mathbf{Y}_N - [\hat{\mathbf{A}}_{rk}(\theta) \odot \hat{\mathbf{C}}_{k-1}] \hat{\mathbf{A}}_{tk}^T(\theta)\|_F^2, \quad (11)$$

$$\hat{\mathbf{A}}_{tk}(\theta) = \mathbf{Y}_N^T \left[(\hat{\mathbf{A}}_{rk}(\theta) \odot \hat{\mathbf{C}}_{k-1})^\# \right]^T. \quad (12)$$

Step 5. Substitute $\hat{\mathbf{A}}_{tk}(\theta)$, $\hat{\mathbf{A}}_{rk}(\theta)$ into formula (13) to obtain $\hat{\mathbf{C}}_k$ shown as formula (14). Then calculate $\delta_k = \sum_{l=1}^L \|\mathbf{Y}_l - \hat{\mathbf{A}}_{tk}(\theta) D_l[\mathbf{C}] \hat{\mathbf{A}}_{rk}(\theta)^T\|_F^2$. If $|\delta_k - \delta_{k-1}| > \varepsilon$ (ε is error threshold), repeat Step 3 to Step 5; otherwise, go to Step 6. Consider

$$\hat{\mathbf{C}}_k = \arg \min_{\hat{\mathbf{C}}} \|\mathbf{Y}_M - [\hat{\mathbf{A}}_{tk}(\theta) \odot \hat{\mathbf{A}}_{rk}(\theta)] \hat{\mathbf{C}}_k^T\|_F^2, \quad (13)$$

$$\hat{\mathbf{C}}_k = \mathbf{Y}_M^T \left[(\hat{\mathbf{A}}_{tk}(\theta) \odot \hat{\mathbf{A}}_{rk}(\theta))^\# \right]^T. \quad (14)$$

Step 6. $\hat{\mathbf{A}}_t(\theta)$, $\hat{\mathbf{A}}_r(\theta)$, and $\hat{\mathbf{C}}$ are obtained after iteration. Then \hat{f}_{dp} can be calculated by the following formula:

$$\hat{f}_{dp} = \frac{1}{2\pi T(L-1)} \sum_{i=1}^{L-1} \text{angle} \left(\frac{\hat{c}_{i,p}(\theta)}{\hat{c}_{i+1,p}(\theta)} \right), \quad (15)$$

where $\hat{c}_{i,p}(\theta)$ presents the element in $\hat{\mathbf{C}}^T$ and i and p are the indexes of row and column. $\text{angle}(\cdot)$ represents phase obtain operation.

When the Doppler frequency has been estimated, it can be used to eliminate the Doppler effect to received signal \mathbf{X} . The signal after preprocessing can be expressed as

$$\vec{\mathbf{X}} = [\vec{\mathbf{x}}_1, \vec{\mathbf{x}}_2, \vec{\mathbf{x}}_3, \dots, \vec{\mathbf{x}}_L], \quad (16)$$

where $\vec{\mathbf{x}}_l = \vec{\mathbf{x}}(lT)$, $\vec{\mathbf{x}}(t) = \sum_{p=1}^P [\mathbf{x}_p(t)/f_p(t)]$. $\mathbf{x}_p(t) = \mathbf{a}_r(\theta_p) \times \mathbf{a}_t(\theta_p)^T \times \mathbf{s}_p(t) + \mathbf{n}_p(t)$, $f_p(t)$ represents the compensatory phase of target p and can be expressed as

$$f_p(t) = e^{-j2\pi \hat{f}_{dp} t}. \quad (17)$$

So the output of match filters can be expressed as

$$\bar{\mathbf{X}} = \text{vec} \left(\frac{\vec{\mathbf{X}} \mathbf{S}^H}{L} \right), \quad (18)$$

where $[\cdot]^H$ represents Hermit operation and $\text{vec}(\cdot)$ represents vector obtain operation.

The covariance of $\bar{\mathbf{X}}$ can be expressed as

$$\mathbf{R}_{\bar{\mathbf{X}}\bar{\mathbf{X}}} = E[\bar{\mathbf{X}}\bar{\mathbf{X}}^H]. \quad (19)$$

Then eigendecomposition is carried on for $\mathbf{R}_{\bar{\mathbf{X}}\bar{\mathbf{X}}}$ shown in formula (20). Consider

$$\mathbf{R}_{\bar{\mathbf{X}}\bar{\mathbf{X}}} = \mathbf{U} \Sigma \mathbf{U}^H, \quad (20)$$

where $\Sigma = \text{diag}(\alpha_1, \alpha_2, \dots, \alpha_{M \times N})$ and α_{ij} denotes eigenvalue of $\mathbf{R}_{\bar{\mathbf{X}}\bar{\mathbf{X}}}$.

Since the first p eigenvalues are composed of variance of signal and Gaussian white noise while the remaining eigenvalues are only composed of variance of Gaussian white noise, the first p eigenvalues are larger than the rest at high SNR. The first p eigenvalues are defined as “signal eigenvalues” and the rest are defined as “noise eigenvalues.” So the eigenvector matrix \mathbf{U} can be classified into two parts in the following formula:

$$\mathbf{U} = [\mathbf{G}_s | \mathbf{G}_n], \quad (21)$$

where $\mathbf{G}_s = [\mathbf{u}_1, \mathbf{u}_2, \dots, \mathbf{u}_p]$ is composed of the signal eigenvectors and $\mathbf{G}_n = [\mathbf{u}_{p+1}, \mathbf{u}_{p+2}, \dots, \mathbf{u}_{M \times N}]$ is composed of the noise eigenvectors.

So the spectrum estimation formula of MUSIC is expressed as

$$P_{\text{MUSIC}}(\theta) = \frac{1}{\boldsymbol{\omega}(\theta)^H \mathbf{G}_n \mathbf{G}_n^H \boldsymbol{\omega}(\theta)}, \quad (22)$$

where $\boldsymbol{\omega}(\theta) = \mathbf{a}_r(\theta) \otimes \mathbf{a}_t(\theta)$. “ \otimes ” represents the Kronecker product.

Then the estimated DOA can be obtained according to the position of the spectral peak.

4. Results and Discussion

In order to state that PARAFAC-MUSIC algorithm has a better performance in DOA estimation with Doppler frequency, simulation is carried on with MATLAB software to compare PARAFAC-MUSIC algorithm with PARAFAC algorithm and MUSIC algorithm.

Assume that there are two targets in the far field and a MIMO radar system with 8 collocated transmit antennas and 8 collocated receive antennas. The frequency of the transmit signals is 4 GHz. The array structure is the same as Figure 1 with $d_t = 0.5\lambda \times M$ space between adjacent transmit elements and $d_r = 0.5\lambda$ space between adjacent receive elements. The targets are at 5° and 15° , respectively, relative to the MIMO radar system with the same velocity $v_t = 300$ m/s and the same RCS $\beta = 1$ m². The sampling frequency is 100 KHz. The number of snapshots is $L = 80$. Additionally, results shown below are obtained from 500 Monte Carlo experiments at each SNR.

Figures 2 and 3 show the two targets' mean errors of the estimated DOAs obtained from PARAFAC algorithm,

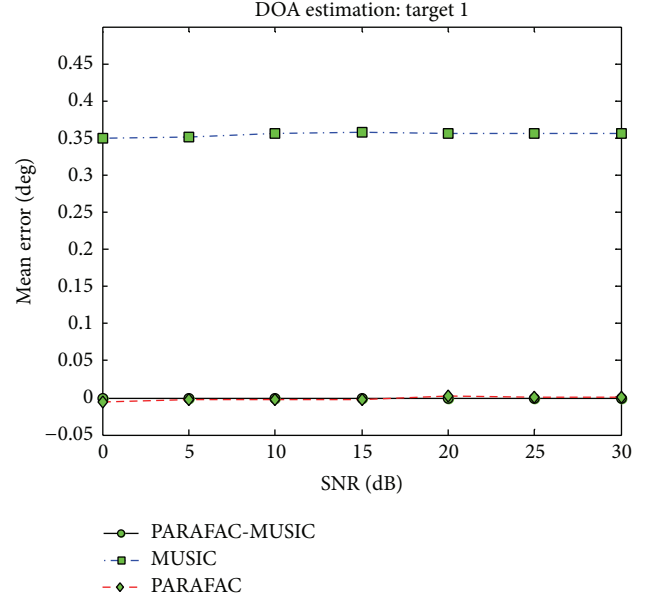


FIGURE 2: Mean error of target 1.

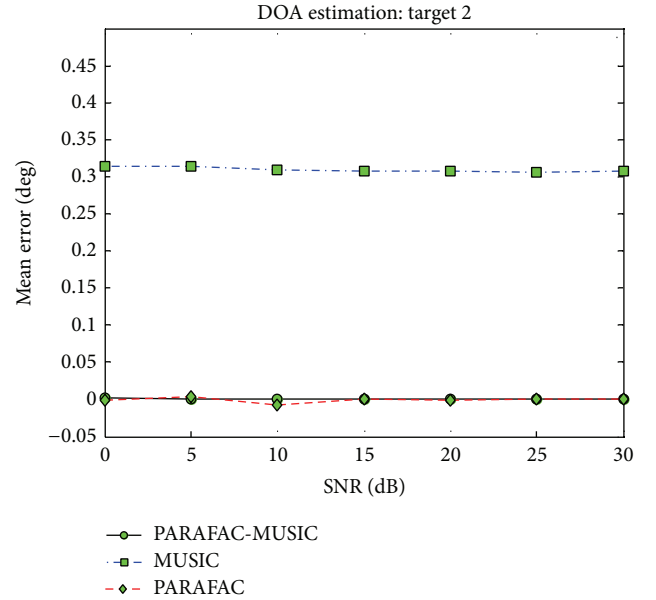


FIGURE 3: Mean error of target 2.

MUSIC algorithm, and proposed algorithm. It is apparent to find that the mean error of target 1 obtained from MUSIC algorithm fluctuates near 0.36° and converges on 0.36° gradually with the increasing SNR, and the mean error of target 2 obtained from MUSIC algorithm fluctuates near 0.31° and converges on 0.31° gradually with the increasing SNR. The results show that the MUSIC algorithm cannot provide an accurate estimation because of the Doppler frequency. Nevertheless, as far as the PARAFAC algorithm and the proposed algorithm are concerned, the mean error of two targets fluctuates near 0° and converges on 0° gradually with

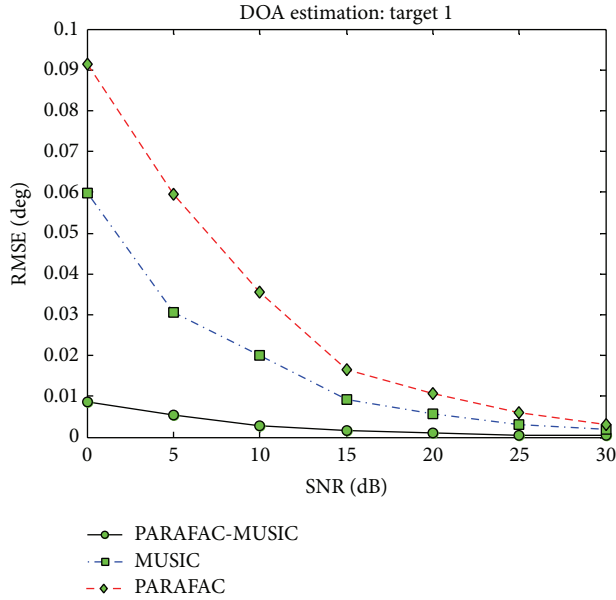


FIGURE 4: RMSE of target 1.

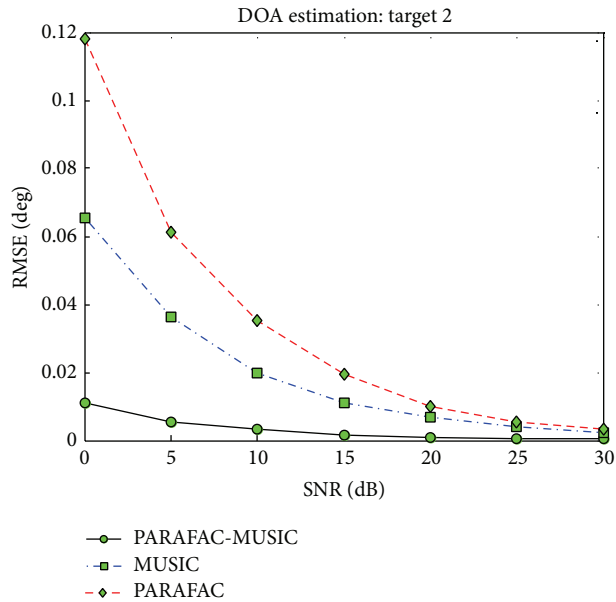


FIGURE 5: RMSE of target 2.

the increasing SNR. But the mean error of the proposed algorithm in both figures is closer to 0° than the one of PARAFAC algorithm which means that the proposed algorithm has a better performance than the PARAFAC algorithm.

Figures 4 and 5 illustrate the two targets' root mean square errors (RMSE) of the estimated DOAs obtained from PARAFAC algorithm, MUSIC algorithm, and proposed algorithm. RMSE of the estimated DOAs in both figures decreases gradually with the increasing SNR. Though the RMSE of the estimated DOAs in both figures obtained from the MUSIC algorithm, the PARAFAC algorithm and the proposed algorithm tend to 0° with the increasing SNR;

the RMSE of the proposed algorithm is smaller than the other two algorithms which means that the proposed algorithm has a smaller fluctuation in DOA estimation.

Simulation results state that MUSIC algorithm suffers from Doppler frequency seriously and cannot provide an accurate DOA estimation to moving target. Besides, the PARAFAC-MUSIC is able to estimate the DOA with a higher accuracy than the PARAFAC algorithm to moving targets.

5. Conclusions

In this paper, some algorithms in DOA estimation are reviewed first. Then a new algorithm named PARAFAC-MUSIC is proposed to estimate the DOA with Doppler frequency in a MIMO radar system. The proposed algorithm is able to estimate DOAs of multiple targets. Finally simulation results confirm that the MUSIC algorithm is not suitable for DOA estimation with Doppler frequency while PARAFAC-MUSIC algorithm is very popular for DOA estimation with Doppler frequency and has a higher accuracy than the PARAFAC algorithm and the MUSIC algorithm.

Conflict of Interests

The authors declare that there is no conflict of interests regarding the publication of this paper.

Acknowledgment

The authors would like to thank the Pre-research Foundation for the support of their research (no. 9140C800202120C80279).

References

- [1] J. Capon, "High-resolution frequency-wavenumber spectrum analysis," *Proceedings of the IEEE*, vol. 57, no. 8, pp. 1408–1418, 1969.
- [2] C. Duofang, C. Baixiao, and Q. Guodong, "Angle estimation using ESPRIT in MIMO radar," *Electronics Letters*, vol. 44, no. 12, pp. 770–771, 2008.
- [3] A. Zahernia, M. J. Dehghani, and R. Javidan, "MUSIC algorithm for DOA estimation using MIMO arrays," in *Proceedings of the 6th International Conference on Telecommunication Systems, Services, and Applications (TSSA '11)*, pp. 149–153, October 2011.
- [4] D. Nion and N. D. Sidiropoulos, "A PARAFAC-based technique for detection and localization of multiple targets in a MIMO radar system," in *Proceedings of the IEEE International Conference on Acoustics, Speech, and Signal Processing (ICASSP '09)*, pp. 2077–2080, April 2009.
- [5] Z. Jianyun, Z. Zhidong, and L. Xiaobo, "Joint DOD, DOA and doppler frequency estimation for bistatic MIMO radar system," *Journal of Electronics & Information Technology*, vol. 32, no. 8, pp. 1009–5896, 2010.

Research Article

Transmit Beampattern Synthesis with Constant Beamwidth and Sidelobe Control for Wideband MIMO Radar

Pengcheng Gong and Zhenhai Shao

*Greating-UESTC Joint Experiment Engineering Center, School of Communication and Information Engineering,
University of Electronic Science and Technology of China, Chengdu 611731, China*

Correspondence should be addressed to Zhenhai Shao; shao_zh@uestc.edu.cn

Received 7 January 2014; Revised 10 May 2014; Accepted 13 May 2014; Published 22 June 2014

Academic Editor: Shengqi Zhu

Copyright © 2014 P. Gong and Z. Shao. This is an open access article distributed under the Creative Commons Attribution License, which permits unrestricted use, distribution, and reproduction in any medium, provided the original work is properly cited.

A beampattern synthesis approach is proposed to design the power spectral density matrix (PSDM), which is chosen to achieve a given transmit beampattern in wideband multiple-input multiple-output (MIMO) radar systems. The proposed approach focuses on transmit beampattern synthesis with constant beamwidth and sidelobe control. Moreover, the design problem is further converted to a convex optimization problem, which is solved efficiently via the modeling system CVX. In comparison to these recently developed wideband MIMO beampattern synthesis methods, the proposed approach maintains a constant beamwidth across the entire frequency band and provides a great improvement in sidelobe control. Numerical simulation results are obtained to validate the effectiveness of this approach.

1. Introduction

Transmit beampattern synthesis is a well-studied topic in standard phased-array radars [1–3]. Recently, several transmit beampattern design approaches for narrowband MIMO radars have been reported [4–9]. The main idea of these approaches is to design the proper probing signals according to the desired transmit beampattern. A relationship between the spatial beampattern and the covariance matrix of the transmit waveforms derived in [4, 5] shows that it is possible to design a covariance matrix to synthesize the desired beampattern. This work is further extended in [6, 7] to solve the beampattern design problem by a semidefinite quadratic programming (SQP) algorithm.

However, the discussion is limited to transmit beampattern synthesis for wideband MIMO radar. Antonio and Fuhrmann have designed the signal cross-spectral density matrixes (CSDM) in order to approximate the desired transmit beampattern in [10]. He et al. [11] also have proposed a wideband beampattern formation via iterative techniques (WBFIT) to synthesize wideband MIMO waveforms, which satisfy some practical constraints such as constant-modulus or low peak-to-average power ratio (PAPR). In WBFIT, the

beamwidth of the designed beampattern tends to shrink as the frequency increases for one narrow mainbeam. The method in [12] performs similarly as WBFIT, but with much lower computational costs.

Although these methods [10–12] have discussed the wideband beampattern synthesis problem, so little attention has been paid to the case of the constant beamwidth and the sidelobe attenuation. In this paper, we propose a beampattern synthesis approach to design power spectral density matrix (PSDM) in order to match a transmit energy distribution in both space and frequency for wideband MIMO radar. In our proposed approach, the mainlobe of the designed beampattern has an almost constant beamwidth for different frequencies and the sidelobe level of the designed beampattern is strictly below a desired sidelobe value. In addition, the proposed approach is converted to second-order cone programming (SOCP) problem, which is easily solved by the convex optimization toolbox CVX. Simulation results show that the proposed approach significantly outperforms the existing WBFIT approach in terms of both frequency invariant property and sidelobe attenuation.

The rest of this paper is organized as follows. The problem is formulated in Section 2. In Section 3, the proposed

approach is developed. Design examples and simulation results are shown in Section 4 and concluded remarks are given in Section 5.

Notation 1. We denote vectors and matrices by lowercased and uppercased letters, respectively. $(\cdot)^H$ denotes the vector or matrix conjugate transpose operation, $(\cdot)^T$ denotes the transpose operation, $(\cdot)^*$ denotes the conjugate operation, $\text{diag}(\cdot)$ denotes diagonals of a matrix, $|\cdot|$ denotes the absolute value operation, $\|\cdot\|_2$ denotes the Euclidean norm, and $\text{rank}(\cdot)$ refers to the rank operation.

2. Problem Formulation

When a MIMO radar system employs M transmit antennas with the interelement spacing d , the signal transmitted by the m th antenna is given by

$$s_m(t) = x_m(t) \cdot e^{j2\pi f_c t}, \quad (1)$$

where f_c denotes the carrier frequency of the transmitted signal and $x_m(t)$ is the baseband signal, whose time support is $[0, \tau]$.

In this case, the far-field signal at target angle θ can be written as

$$z_\theta(t) = \sum_{m=0}^{M-1} s_m(t - \tau_m), \quad t \in [0, \tau], \quad (2)$$

where τ_m is the time needed by the signal emitted from the m th transmit antenna to the target. Substituting (1) into (2), (2) is then modified as

$$z_\theta(t) = \sum_{m=0}^{M-1} x_m(t - \tau_m) \cdot e^{j2\pi f_c(t - \tau_m)}, \quad t \in [0, \tau]. \quad (3)$$

Assuming that the Fourier transform (FT) of $x_m(t)$ is $y_m(f)$, (3) can be rewritten as

$$z_\theta(t) = \int_{-B/2}^{B/2} Y(\theta, f) e^{j2\pi(f + f_c)t} df, \quad (4)$$

where

$$Y(\theta, f) = \sum_{m=0}^{M-1} y_m(f) \cdot e^{-j2\pi(f + f_c)\tau_m} = a^H(\theta, f) \cdot y(f), \quad (5)$$

$$a(\theta, f) = [1, e^{j2\pi(f + f_c)\tau_0}, \dots, e^{j2\pi(f + f_c)\tau_m}, \dots, e^{j2\pi(f + f_c)\tau_{M-1}}]^T, \quad (6)$$

$$y(f) = [y_0(f), y_1(f), \dots, y_m(f), \dots, y_{M-1}(f)]^T. \quad (7)$$

Enlightened by these approaches proposed in [10, 11], the beampattern at spatial angle θ and frequency $f + f_c$ is redefined as (see [13] for details)

$$P(\theta, f + f_c) = a^H(\theta, f) \cdot y(f) \cdot y^H(f) \cdot a(\theta, f), \quad (8)$$

where the baseband frequency $f \in [-B/2, B/2]$ and the spatial angle $\theta \in [0, \pi]$. In the case when wideband signals are used, the PSDM is defined as [14]

$$S(f) = y(f) \cdot y^H(f). \quad (9)$$

Then (8) can be rewritten as

$$P(\theta, f + f_c) = a^H(\theta, f) \cdot S(f) \cdot a(\theta, f). \quad (10)$$

In practical applications, the baseband signal and the spatial angle need to be discretized, so that (6) and (7) can be rewritten, respectively, as follows:

$$\begin{aligned} a_{kp} &= a\left(\theta_k, \frac{p}{NT_s}\right) \\ &= [1, e^{j2\pi(f + p/NT_s)\tau_0}, \dots, e^{j2\pi(f + p/NT_s)\tau_m}, \\ &\quad \dots, e^{j2\pi(f + p/NT_s)\tau_{M-1}}]^T, \end{aligned} \quad (11)$$

$$y_p = [y_0(p), y_1(p), \dots, y_m(p), \dots, y_{M-1}(p)]^T,$$

where $\{\theta_k\}_{k=1}^K$ is a fine grid of points that cover the spatial angle interval $[0, \pi]$. Note that $\{y_p\}_{p=-N/2}^{N/2-1}$ represents the discrete Fourier transform (DFT) of

$$\begin{aligned} x(n) &= [x_0(n), \dots, x_m(n), \dots, x_{M-1}(n)]^T, \\ n &= 0, \dots, N-1, \end{aligned} \quad (12)$$

where N denotes the number of samples and is assumed to be even.

So, the beampattern in (8) can be expressed on the discrete angle-frequency grid as

$$P_{kp} = a_{kp}^H S(p) a_{kp}, \quad (13)$$

where $k \in [1, K]$, $p \in [-N/2, \dots, 0, \dots, N/2 - 1]$,

$$S(p) = y_p y_p^H. \quad (14)$$

In this paper, when the transmit beampattern and a desired beampattern are defined as (13) and d_{kp} , respectively, the goal is to choose the appropriate PSDM $S(p)$ ($p \in [-N/2, \dots, 0, \dots, N/2 - 1]$), under some constraints, so that the beampattern in (13) matches the desired one d_{kp} .

3. The Proposed Transmit Beampattern Design

In this section, how to synthesize wideband transmit beampattern with constant beamwidth across the entire frequency band and sidelobe control is described. Here, the beampattern synthesis goal is to minimize the error between the designed beampattern and the desired one over the mainlobe region and to maintain the sidelobe region to be lower than

a given threshold value. Mathematically, such beampattern synthesis problem can be formulated as follows:

$$\begin{aligned} \min_{\{S(p)\}} \quad & \left\{ \sum_{m'=1}^{M'} \sum_{p=-N/2}^{N/2-1} |\alpha d_{m'p} - a_{m'p}^H S(p) a_{m'p}|^2 \right\} \\ \text{subject to} \quad & \theta_{m'} \in \Theta_{M'L}, \quad m' = 1, \dots, M' \\ & |a_{sp}^H S(p) a_{sp}| \leq \sigma, \quad \theta_s \in \Theta_{SL}, \quad s = 1, \dots, S, \end{aligned} \quad (15)$$

where $\theta_{m'} \in \Theta_{M'L}$ ($m' = 1, \dots, M'$) and $\theta_s \in \Theta_{SL}$ ($s = 1, \dots, S$) that denote that a fine grid (uniform or nonuniform) of points covers mainlobe region and sidelobe region of interest, respectively. $d_{m'p}$ and σ denote the mainlobe region and the desired sidelobe value of a desired beampattern, respectively. And $\alpha > 0$ is a variable to control the magnitude of the desired beampattern.

In (15), the PSDM cannot be chosen freely and should satisfy the following constraints:

$$C_1 : \sum_{n=0}^{N-1} |x_m(n)|^2 = \frac{c}{M}, \quad m = 0, \dots, M-1; \quad (16a)$$

$$C_2 : S(p) \geq 0, \quad p \in \left[-\frac{N}{2}, \frac{N}{2} - 1\right], \quad (16b)$$

where c/M is the transmitted power from each antenna, and c is a total transmit power for M antennas. The first constraint C_1 means that transmit power from all the antenna elements should be the same, and the second constraint C_2 ensures that $S(p)$ is a positive semidefinite matrix.

Using the Parseval equality, the first constraint C_1 on $\{x_m(n)\}$ imposes the following constraint on $\{y_m(p)\}$:

$$\begin{aligned} \sum_{p=-N/2}^{N/2-1} |y_m(p)|^2 &= N \sum_{n=0}^{N-1} |x_m(n)|^2 = \frac{Nc}{M}, \\ m &= 0, \dots, M-1. \end{aligned} \quad (17)$$

Therefore, C_1 in (16a) can be rewritten as

$$\sum_{p=-N/2}^{N/2-1} S_m(p) = \frac{Nc}{M}, \quad m = 0, \dots, M-1. \quad (18)$$

Combining (15) with the above PSDM constraints in (16a) and (16b), the beampattern design problem can be formulated as

$$\begin{aligned} \min_{\{S(p)\}} \quad & \left\{ \sum_{m'=1}^{M'} \sum_{p=-N/2}^{N/2-1} |\alpha d_{m'p} - a_{m'p}^H S(p) a_{m'p}|^2 \right\} \\ \text{subject to} \quad & \theta_{m'} \in \Theta_{M'L}, \quad m' = 1, \dots, M' \\ & |a_{sp}^H S(p) a_{sp}| \leq \sigma, \quad \theta_s \in \Theta_{SL}, \quad s = 1, \dots, S \end{aligned}$$

$$\sum_{p=-N/2}^{N/2-1} S_m(p) = \frac{Nc}{M}, \quad m = 0, \dots, M-1$$

$$S(p) \geq 0, \quad p \in \left[-\frac{N}{2}, \frac{N}{2} - 1\right].$$

(19)

Next, it will be shown that the optimal design problem (19) can be converted to a second-order cone programming (SOCP) [15] and can be efficiently solved by the well-established interior point method [16], such as public domain software CVX toolbox [17].

Introducing new variables τ_p ($p \in [-N/2, N/2 - 1]$), (19) can be converted to the following form:

$$\begin{aligned} \min_{\{S(p)\}} \quad & \sum_{p=-N/2}^{N/2-1} \tau_p \\ \text{subject to} \quad & \left\{ \sum_{m'=1}^{M'} |\alpha d_{m'p} - a_{m'p}^H S(p) a_{m'p}|^2 \right\} \leq \tau_p, \\ & \theta_{m'} \in \Theta_{M'L}, \quad m' = 1, \dots, M' \end{aligned} \quad (20)$$

$$|a_{sp}^H S(p) a_{sp}| \leq \sigma, \quad \theta_s \in \Theta_{SL}, \quad s = 1, \dots, S$$

$$\sum_{p=-N/2}^{N/2-1} S_m(p) = \frac{Nc}{M}, \quad m = 0, \dots, M-1$$

$$S(p) \geq 0, \quad p \in \left[-\frac{N}{2}, \frac{N}{2} - 1\right].$$

The first constraint and the second constraint in (20) can be rewritten as the following compact form, respectively:

$$\begin{aligned} \|\alpha d_p - \text{diag}(A_p S(p) A_p^H)\| &\leq \sqrt{\tau_p} \\ \|\text{diag}(\bar{A}_p S(p) \bar{A}_p^H)\| &\leq \sigma, \end{aligned} \quad (21)$$

where $A_p = [a_{1p}^*, \dots, a_{m'p}^*, \dots, a_{M'p}^*]^T$ is the steering matrix of the mainlobe region, $\bar{A}_p = [a_{1p}^*, \dots, a_{sp}^*, \dots, a_{Sp}^*]^T$ is the steering matrix of the sidelobe region, and $d_p = [d_{1p}, \dots, d_{m'p}, \dots, d_{M'p}]^T$.

Based on (21), the beampattern design in (19) can be expressed as the following minimization problem:

$$\begin{aligned} \min_{\{S(p)\}} \quad & \sum_{p=-N/2}^{N/2-1} \tau_p \\ \text{subject to} \quad & \|\alpha d_p - \text{diag}(A_p S(p) A_p^H)\| \leq \sqrt{\tau_p} \\ & \|\text{diag}(\bar{A}_p S(p) \bar{A}_p^H)\| \leq \sigma \\ & \sum_{p=-N/2}^{N/2-1} S_m(p) = \frac{Nc}{M}, \quad m = 0, \dots, M-1 \end{aligned} \quad (22)$$

$$S(p) \geq 0, \quad p \in \left[-\frac{N}{2}, \frac{N}{2} - 1\right].$$

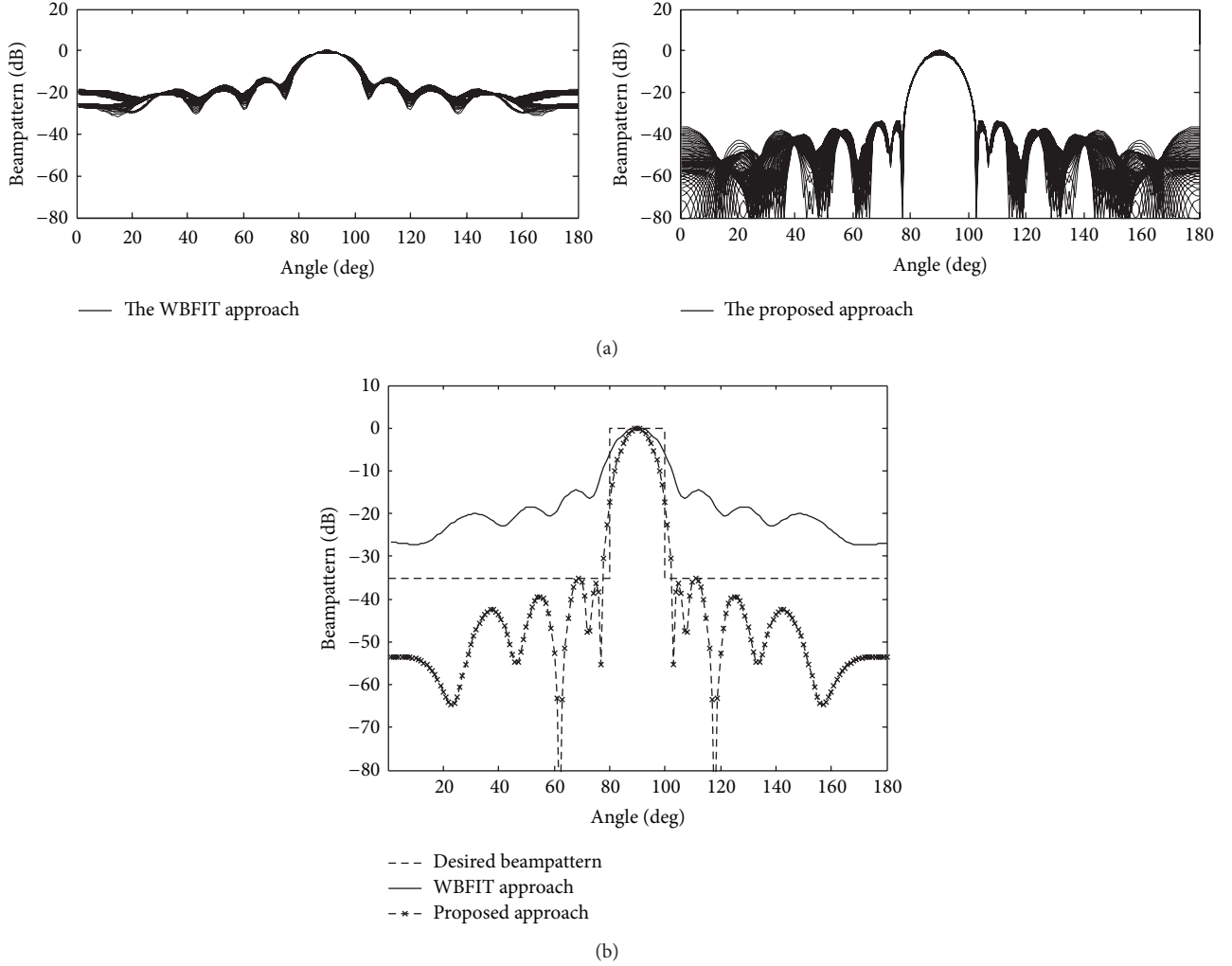


FIGURE 1: Comparison of the synthesized beam pattern. The desired beam pattern is given in (23). (a) Plot at all the 64 frequencies using the WBFIT approach and the proposed approach. (b) Plot at center frequency.

It can be observed that, by introducing new variables, the optimal design problem in (19) can be converted to the SOCP problem (22), which is a convex optimization problem [15]. The second-order cone, $Q^m = \{(x, y) \in R^m \times R \mid \|x\|_2 \leq y\}$, can be solved using CVX in MATLAB with the code given in “ $\{x, y\} \langle \text{In} \rangle \text{complex_lorentz} (m)$.” We therefore emphasize more on convex problem formulation (22) and the computational complexity analysis for the solution is not provided.

Now, if $S(p)$ is of rank one, an optimal solution to (14) can be obtained. However, if the corresponding rank is greater than one, we need to resort to randomization techniques to extract a feasible solution [18].

Let $S(p) = \sum_{i=1}^r \lambda_i q_i q_i^T$ denote the eigenvalue decomposition of $S(p)$, where $r = \text{rank}[S(p)]$, the eigenvalues are $\lambda_1 \geq \lambda_2 \geq \dots \geq \lambda_r > 0$, and q_1, \dots, q_r are the respective eigenvectors. We choose $y_p = \sqrt{\lambda_1} q_1$ as our candidate vector to (14).

Hence the proposed approach works as follows. Firstly, the frequency band occupied by the wideband signal is divided into a certain number of narrowband bins. Secondly, PSDM of the signal vectors at each frequency bin is designed via proposed approach in (22). Then, a feasible solution to (14) from a solution $S(p)$ is extracted.

4. Numerical Results

This section focuses on demonstrating the performances of the proposed approach using an $M = 10$ MIMO radar system with uniform linear array (ULA), where the interelement spacing d is given by half-wavelength. The parameters for simulations are set as follows: $f_c = 1$ GHz, $B = 200$ MHz, $N = 64$, $K = 180$, and the total transmit power is $c = 1$. Although the design of multiple beams is not considered in these simulations, it can be achieved via the proposed

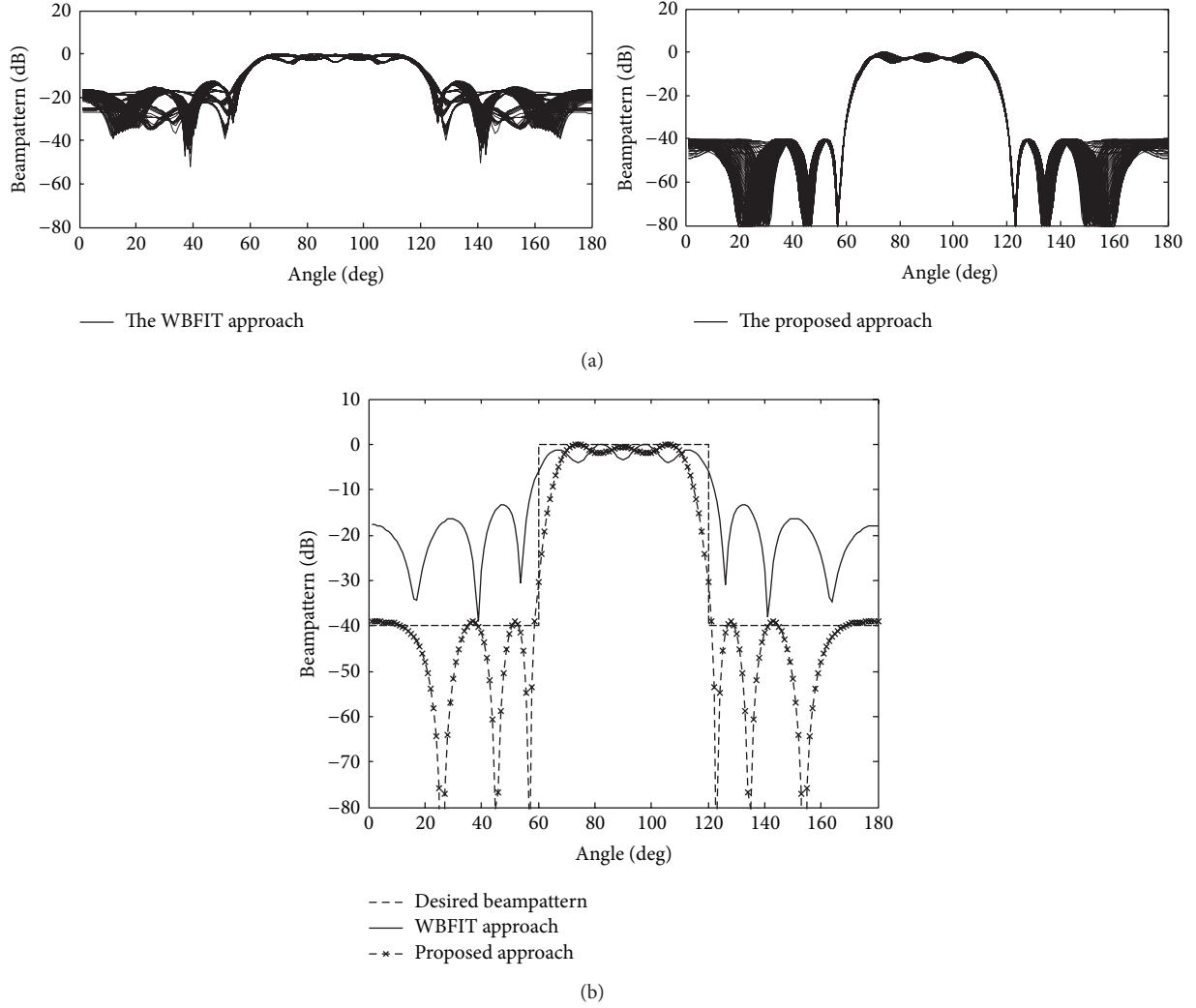


FIGURE 2: Comparison of the synthesized beam pattern. The desired beam pattern is given in (24). (a) Plot using the WBFIT approach and the proposed approach. (b) Plot at center frequency.

approach. So, it is sufficient only to discuss the single beam design.

Firstly, the desired beam pattern which is synthesized using the proposed approach denotes the following:

$$d(\theta, f) = \begin{cases} 1, & 80^\circ \leq \theta_k \leq 100^\circ \\ 0, & \text{others,} \end{cases} \quad (23)$$

$$f \in \left[-\frac{B}{2} + f_c, \frac{B}{2} + f_c \right].$$

Here the mainlobe region is set to $\Theta_{M'L} = [80^\circ, 100^\circ]$; that is, the beamwidth of the desired beam pattern is 20° , and the sidelobe region is $\Theta_{SL} = [1^\circ, 79^\circ] \cup [101^\circ, 180^\circ]$, with 1° increment between adjacent grid points.

Figure 1(a) shows the obtained beam patterns at all the 64 frequencies using the WBFIT approach of [11] and the proposed approach in (19). In this case, the desired sidelobe value is set to $\sigma = -35$ dB. From the plots, it can be seen that the beam pattern obtained by proposed approach shows

a clean mainlobe at 90° across the entire frequency range, and the main beamwidth synthesized by proposed approach keeps fixed for all in-band frequency. Figure 1(b) compares the beam pattern designed by the proposed approach with the WBFIT approach at center frequency. From Figure 1(b), it is noted that the designed beam pattern using the proposed approach has a sidelobe level of -35 dB.

Secondly, the following desired beam pattern with a wider mainlobe is considered:

$$d(\theta, f) = \begin{cases} 1, & 60^\circ \leq \theta_k \leq 120^\circ \\ 0, & \text{others,} \end{cases} \quad (24)$$

$$f \in \left[-\frac{B}{2} + f_c, \frac{B}{2} + f_c \right].$$

Similarly, Figure 2(a) shows the obtained beam patterns at all the 64 frequencies using the WBFIT approach and the proposed approach. Figure 2(b) compares the beam pattern designed by the proposed approach with the WBFIT

approach at center frequency. The desired sidelobe value and the beamwidth of the desired beampattern are set to $\sigma = -40$ dB and 60° , respectively.

It can be clearly seen that the designed beampattern, using the proposed approach, maintains a constant beamwidth across the entire frequency band from Figure 2(a), and more importantly, the designed sidelobe level is strictly below -40 dB from Figure 2(b).

From these simulation examples, compared with the existing WBFIT approach, the proposed approach has achieved significant improvement in both frequency invariant property and sidelobe attenuation. Therefore, the merit of the proposed approach is validated.

5. Conclusions

In this paper, a modified approach has been proposed to successfully synthesize the PSDM according to the desired transmit beampattern in wideband MIMO radar systems. With the proposed approach, the mainlobe of the designed beampattern has an almost constant beamwidth for different frequencies and the sidelobe level of the designed beampattern is strictly below a desired sidelobe value (e.g., -35 dB and -40 dB). Numerical results were provided to illustrate the effectiveness and validity of the proposed approach.

Conflict of Interests

The authors declare that there is no conflict of interests regarding the publication of this paper.

Acknowledgment

This work was supported in part by the Fundamental Research Funds for the Central Universities under Grant no. ZYGX2011YB002.

References

- [1] B. P. Ng, M. H. Er, and C. A. Kot, "Flexible array synthesis method using quadratic programming," *IEEE Transactions on Antennas and Propagation*, vol. 41, no. 11, pp. 1541–1550, 1993.
- [2] S. E. Nai, W. Ser, Z. L. Yu, and H. Chen, "Beampattern synthesis for linear and planar arrays with antenna selection by convex optimization," *IEEE Transactions on Antennas and Propagation*, vol. 58, no. 12, pp. 3923–3930, 2010.
- [3] D. P. Scholnik and J. O. Coleman, "Optimal design of wideband array patterns," in *Proceedings of the IEEE International Radar Conference*, pp. 172–177, Alexandria, VA, USA, May 2000.
- [4] D. R. Fuhrmann and G. S. Antonio, "Transmit beamforming for MIMO radar systems using partial signal correlation," in *Proceedings of the 38th Asilomar Conference on Signals, Systems and Computers*, pp. 295–299, November 2004.
- [5] D. R. Fuhrmann and G. San Antonio, "Transmit beamforming for MIMO radar systems using signal cross-correlation," *IEEE Transactions on Aerospace and Electronic Systems*, vol. 44, no. 1, pp. 171–186, 2008.
- [6] J. Li, P. Stoica, and Y. Xie, "On probing signal design for MIMO radar," in *Proceedings of the 40th Asilomar Conference on Signals, Systems, and Computers*, pp. 31–35, Pacific Grove, Calif, USA, 2006.
- [7] P. Stoica, J. Li, and Y. Xie, "On probing signal design for MIMO radar," *IEEE Transactions on Signal Processing*, vol. 55, no. 8, pp. 4151–4161, 2007.
- [8] S. Ahmed, J. S. Thompson, Y. R. Petillot, and B. Mulgrew, "Unconstrained synthesis of covariance matrix for MIMO radar transmit beampattern," *IEEE Transactions on Signal Processing*, vol. 59, no. 8, pp. 3837–3849, 2011.
- [9] Y.-C. Wang, X. Wang, H. Liu, and Z.-Q. Luo, "On the design of constant modulus probing signals for MIMO radar," *IEEE Transactions on Signal Processing*, vol. 60, no. 8, pp. 4432–4438, 2012.
- [10] G. S. Antonio and D. R. Fuhrmann, "Beampattern synthesis for wideband MIMO radar systems," in *Proceedings of the 1st International Workshop on Computational Advances in Multi-Sensor Adaptive Processing*, pp. 105–108, Puerto Vallarta, Mexico, December 2005.
- [11] H. He, P. Stoica, and J. Li, "Wideband MIMO systems: signal design for transmit beampattern synthesis," *IEEE Transactions on Signal Processing*, vol. 59, no. 2, pp. 618–628, 2011.
- [12] T. Yang, T. Su, and Z. Wu, "Fast frequency invariant transmit beampattern synthesis for wideband MIMO radar," in *Proceedings of the IET International Conference on Radar Systems (Radar '12)*, pp. 1–5, Glasgow, UK, October 2012.
- [13] P. Gong, Z. Shao, G. Tu, and J. Zhou, "Low PAPR waveform design based on transmit beampattern synthesis for wideband MIMO radars," *Science China Information Sciences*, vol. 43, no. 3, pp. 429–444, 2013.
- [14] H. He, P. Stoica, and J. Li, "Designing unimodular sequence sets with good correlations—including an application to MIMO radar," *IEEE Transactions on Signal Processing*, vol. 57, no. 11, pp. 4391–4405, 2009.
- [15] S. Boyd and L. Vandenberghe, *Convex Optimization*, Cambridge University Press, 2004.
- [16] J. F. Sturm, "Using SeDuMi 1.02, a MATLAB toolbox for optimization over symmetric cones," *Optimization Methods and Software*, vol. 11, no. 1, pp. 625–653, 1999.
- [17] M. Grant and S. Boyd, "CVX: Matlab software for disciplined convex programming (web page and software)," September 2008, <http://cvxr.com/cvx/>.
- [18] Z.-Q. Luo, W.-K. Ma, A. So, Y. Ye, and S. Zhang, "Semidefinite relaxation of quadratic optimization problems," *IEEE Signal Processing Magazine*, vol. 27, no. 3, pp. 20–34, 2010.

Research Article

Channel Phase Error Compensation for MIMO-SAR

Lei Zhang,^{1,2} Yunkai Deng,¹ and Robert Wang¹

¹ Department of Spaceborne Microwave Remote Sensing System, Institute of Electronics, Chinese Academy of Sciences, Beijing 100190, China

² University of Chinese Academy of Sciences, Chinese Academy of Sciences, Beijing 100190, China

Correspondence should be addressed to Lei Zhang; 314forever@163.com

Received 27 February 2014; Accepted 2 June 2014; Published 22 June 2014

Academic Editor: Wen-Qin Wang

Copyright © 2014 Lei Zhang et al. This is an open access article distributed under the Creative Commons Attribution License, which permits unrestricted use, distribution, and reproduction in any medium, provided the original work is properly cited.

Multi-input multioutput (MIMO) is a novel technique to achieve high-resolution as well as wide swath in synthetic aperture radar (SAR) systems. Channel imbalance is inevitable in multichannel systems that it declines the imaging quality. Generally, the imbalance cannot be fully compensated by simple internal calibration in a MIMO-SAR system. In this paper, a new algorithm based on raw data is presented to remove the channel phase error. Based on the error source, this approach models the phase error as two parts: the transmit phase error and the receive phase error. The receive phase error is removed using cost function at the azimuth processing stage, whereas the transmit phase error is estimated with correlation. Point target simulations confirm the influence of channel phase error and the validation of the proposed approach. Besides, the performance is also investigated.

1. Introduction

Synthetic aperture radar (SAR) is a powerful microwave instrument for remote sensing [1]. 2D even 3D [2] image of the terrestrial surface can be obtained independent of weather and sunlight illumination. High-resolution as well as wide swath (HRWS) is one of the main goals of the system engineers [3, 4].

For the sake of high azimuth resolution, people have developed spotlight mode [5, 6] in which the antenna points toward the same region during the whole data acquisition. While obtaining large imaging swath, ScanSAR mode [7] is proposed in which the antenna directivity is fixed, swapping between different strips. Limited by the minimum-antenna-area constraint [1], conventional spaceborne SAR is hard to achieve high-resolution in azimuth meanwhile wide imaging swath. High azimuth resolution requires large Doppler bandwidth, which means a high pulse repetition frequency (PRF) to comply with the Nyquist theory, whereas, wide imaging swath demands wide range beam width in which the PRF must be low to guarantee the echo's completeness. Modes such as sliding-spotlight and TOPS [8, 9] are the trade-off between the two demands.

In range direction, SAR transmits chirp pulse. The resolution is proportional to the signal bandwidth, which is defined as

$$\sigma_r = \frac{c}{2B}, \quad (1)$$

where σ_r is the range resolution, c is the velocity of light, and B is the signal bandwidth. For 0.1 m resolution in slant range, 1.5 GHz bandwidth is necessary. This implies at least 1.8 GHz sampling rate (with oversampling rate 20%). The high quality, that is, radiation hardened, A/D convertor is quite difficult to manufacture.

Multi-input multioutput (MIMO) technique provides an opportunity to break through these constraints [10, 11]. The antenna being divided into several apertures, each aperture transmits pulses at different center frequencies simultaneously and all apertures receive the echoes. In this way, numerous effective phase centers are formed. These effective phase centers may be overlapped in spacetime or in frequency. Then using the signal processing technique signals with large bandwidth (both in range and in Doppler) as well as wide swath are obtained [12, 13].

Channel imbalance is inevitable in multichannel system due to the effects of the qualities of modules, the construction of the system, and the atmosphere. The imbalance presents in echo data in terms of amplitude error and phase error. These errors impair the signal synthesis in which the final SAR image will be ambiguous even unrecognized.

Channel imbalance can be removed by means of system internal calibration [1] or analyzing through raw data. Methods based on internal calibration are precise but cannot calibrate the phase errors caused by the antenna, whereas literature belonging to the latter is rare to see. In this paper, an algorithm based on raw data to handle channel phase imbalance in MIMO-SAR system is proposed. The method models phase imbalance as two parts: the transmit phase error (TXE) and the receive phase error (RXE). The transmit phase error is estimated by correlation operation, whereas the receive phase error is removed using cost function at the azimuth processing stage.

This paper is organized as follows. In Section 2, the signal mode is introduced. The proposed method is presented in Section 3 with simulations and discussions in Section 4. Section 5 will give the conclusion.

2. Signal Mode

Figure 1 is a diagram of a MIMO-SAR system with five channels in azimuth. Antennas of each channel and the corresponding phase-centers are marked with rectangles and triangles, respectively. Each channel transmits pulse simultaneously and receives the echoes transmitted by not only itself but also the others. Suppose channel m transmits pulse at center frequency $f_{c,m}$. By compensating a known constant phase between channels, the received echo-signal can be converted into the equivalent self-transmit and self-receive signal [14]. In Figure 1(b), the effective phase-centers are marked with circles which are located halfway in between the transmitting and the respective receiving phase-centers. The effective phase-centers of different center frequencies are marked with distinct colors. Theoretically, if a MIMO-SAR transmits pulse with M channels and receives with N , the total effective phase-centers is $M \cdot N$.

The signal transmitted by channel m is

$$s_{t,m}(\tau, \eta) = \text{rect}\left(\frac{\tau}{T}\right) \exp\left\{j2\pi\left(f_{c,m}\tau + \frac{1}{2}K_r\tau^2\right)\right\}, \quad (2)$$

where τ is the fast time, η is the slow time, T is the pulse length, and K_r is the chirp rate. Then the signal after mixing with center frequency $f_{c,m}$ received by channel n is

$$\begin{aligned} s_{r,n,m}(\tau, \eta) = & \sigma \cdot \text{rect}\left(\frac{\tau - 2R_{n,m}(\eta)/c}{T}\right) \\ & \times \exp\left\{-j\frac{4\pi R_{n,m}(\eta)f_{c,m}}{c}\right\} \\ & \times \exp\left\{j\pi K_r\left(\tau - \frac{2R_{n,m}(\eta)}{c}\right)^2\right\}, \end{aligned} \quad (3)$$

where σ is the backscattering coefficient of the target, c is the velocity of light, and $R_{n,m}(\eta)$ is the slant range

$$R_{n,m}(\eta) = \sqrt{R_0^2 + \left(V_r\eta + \frac{(n-1) \cdot d}{2} + \frac{(m-1) \cdot d}{2}\right)^2}, \quad (4)$$

where R_0 is the nearest range, V_r is the platform velocity, d is the antenna length in azimuth of a single channel, and m and n ranges from 1 to M . In (4), the reference channel is channel 1; that is, the reference slant range is $R_{1,1}(\eta) = \sqrt{R_0^2 + V_r^2\eta^2}$.

Consider the signals with a specific center frequency. They can be treated as the azimuth multichannel SAR signals. Usually, all channels have the same the antenna lengths. According to the slow time delay, after compensating the known constant phase, the received signals have

$$s_{r,n,m}(\tau, \eta) = s_{r,1,m}\left(\tau, \eta + \frac{(n-1) \cdot d}{2V_r}\right). \quad (5)$$

If the radar platform velocity and the PRF have a relationship

$$\text{PRF} = \frac{Md}{2V_r}, \quad (6)$$

where M is the number of receive channels and d is the antenna length of a single channel, the effective phase-centers are distributed uniformly in azimuth. However, (6) is hard to meet strictly in practical SAR systems because of the timing restriction, and therefore the effective phase-centers are nonuniform distribution as the upper part of Figure 1(b) shows. Using the signal processing technique such as system filters [14] or STAP [15] (the matrices are identical indeed), the data can be reconstructed as uniformly sampled. The lower part of Figure 2(b) is the effective phase-centers after reconstruction where the dashed line denotes the zero delay. It is interesting that the time delays are different for each $f_{c,m}$ because (4) associates with m .

From Figure 1(b), it can be seen that the effective phase-centers of different $f_{c,m}$ are overlapped after reconstruction. If the pulse bandwidth of all transmit channels is identical and $f_{c,m}$ steps following

$$f_{c,m} - f_{c,m-1} \leq B, \quad (7)$$

where B is the chirp bandwidth, then a chirp signal with large bandwidth can be obtained using the subband synthesis technique with the overlapped samples [16]. Subband synthesis can be realized either in the range time domain or in the range frequency domain. Besides, synthesis can be before range compression or after compression.

In summary, the MIMO-SAR processing steps followed by this paper are

- (1) samples reconstruction in azimuth;
- (2) imaging each subband;
- (3) subband synthesis in range.

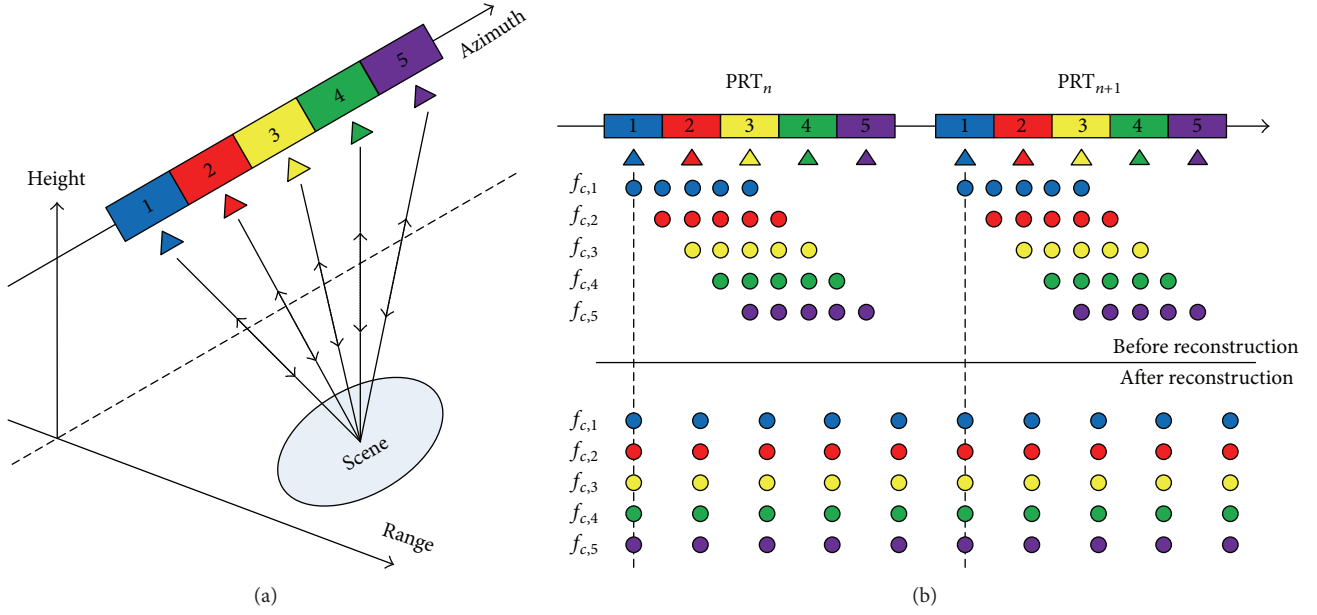


FIGURE 1: Diagram of a MIMO-SAR system. (a) System geometry. (b) Phase sequence.

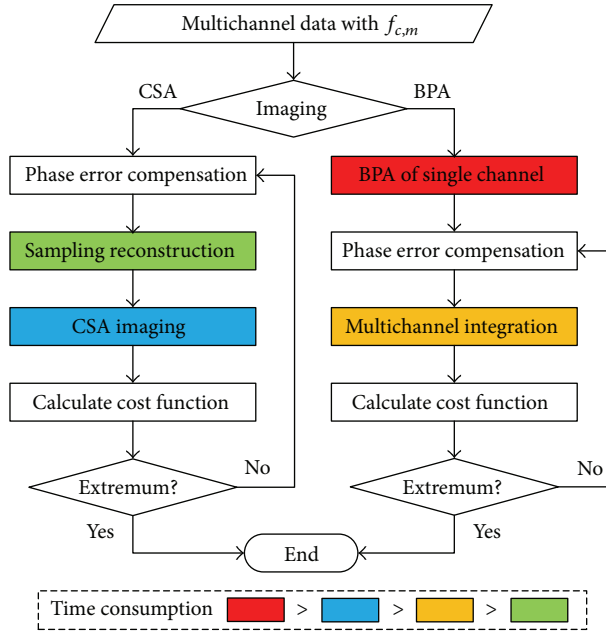


FIGURE 2: Flow chart of removing RXE.

3. Phase Error and the Compensation

Channel imbalance is inevitable in multichannel system, not expecting MIMO-SAR. It presents in echo data in terms of amplitude error and phase error. We only focus on phase error in this paper. Denote the transmission characteristic of each transmit channel as $\Delta\psi_1, \Delta\psi_2, \dots, \Delta\psi_M$ and each receive channel as $\Delta\phi_{1,1}, \Delta\phi_{1,2}, \dots, \Delta\phi_{1,M}, \Delta\phi_{2,1}, \Delta\phi_{2,2}$

$\dots, \Delta\phi_{2,M}, \dots, \Delta\phi_{M,1}, \Delta\phi_{M,2}, \dots, \Delta\phi_{M,M}$, respectively. Here, the substrip of $\Delta\psi$ indicates the transmit channel number, and $\Delta\phi_{n,m}$ indicates the characteristic of channel n receiving the signals with center frequency $f_{c,m}$. The actual signals received are

$$s_{r,n,m}(\tau, \eta) = \Delta\psi_m \cdot \Delta\phi_{n,m} \cdot s_{r,1,m} \left(\tau, \eta + \frac{(n-1) \cdot d}{2V_r} \right). \quad (8)$$

3.1. The Receive Phase Errors. Consider the signals with center frequency $f_{c,m}$ and suppose channel 1 is the reference channel. Define the phase error

$$\Delta\epsilon_{r,n,m} = \frac{\Delta\varphi_{n,m}}{\Delta\varphi_{1,m}}, \quad n = 2, \dots, M \quad (9)$$

the receive phase error (RXE). RXE is range invariant and if arranged along azimuth, it periodically changes over a cycle of M samples. It can be treated as some form of phase error introduced by motion errors in airborne SAR system; therefore RXE brings blurring on subband imaging that the images are ambiguous and defocused in the azimuth.

The compensation of RXE can be treated as a special case of autofocus. There are numerous autofocus methods; however not all are suitable for RXE removing. Because the azimuth reconstruction will disturb the phase error, the phase estimated by autofocus is usually not the original one. We resort to the method using cost function [17] in which the phase error is trial rather than directly derived from the imagery.

Generally, the value of cost function relates to the extent of an image into focus. The broaden mainlobe of a point target and the ghosts along azimuth are the two main characteristics blurred images caused by RXE exhibited [18]. Although defocused, the ghosts share the same shape with the actual targets. According to these two characteristics, we develop a new cost function called image self-correlation in azimuth (ISCA):

$$\text{CF}_{\text{ISCA}}(k) = \frac{E_m \{I(p, q) \cdot I^*(p, q + r)\}}{E_m \{I(p, q) \cdot I^*(p, q)\}}, \quad (10)$$

where $I(p, q)$ is a grey-scale SAR image, p and q are the range coordinate and the azimuth one, respectively, r is the azimuth offset, $*$ denotes conjugation, and E_m implies average in range. ISCA is normalized by the denominator in which the maximum value is 1 which happens only when $k = 0$.

ISCA describes the RXE in two ways. First, the ISCA of a focused image descends faster around $k = 0$ (zero peak) than that of a defocused one; that is, the zero peak is sharper, because the mainlobe is wider on the defocused image. Second, besides the zero peak, the curve of self-correlation may have other couples of peaks (nonzero peak). When the image is fully focused, the ghosts are suppressed that these nonzero peaks become flat.

Thus, the estimation of RXE can be described as an optimization procedure

$$\Delta\hat{\epsilon}_{r,m} = \arg \text{ext}_{\Delta\epsilon_{r,m}} \text{CF}_{\text{ISCA}}, \quad (11)$$

where $\Delta\hat{\epsilon}_{r,m}$ is the optimal solution, $\Delta\epsilon_{r,m} = [\Delta\epsilon_{r,2,m}, \Delta\epsilon_{r,3,m}, \dots, \Delta\epsilon_{r,M,m}]$, and operator ext denotes judging via the width of the zero peak or with the height of nonzero peaks of ISCA.

As the optimization in (11) has no closed-form solution, an iterative method called coordinate descent algorithm [19] is adopted in which the elements of $\Delta\epsilon_{r,m}$ are obtained in sequence. The iterative processes as well as the computational

burden are distinctively different according to the imaging algorithm applied.

The iteration flow, when frequency domain imaging algorithm such as the familiar chirp scaling (CSA) [20] is chosen, is shown on the left of Figure 2. Because some time-consuming progresses are involved in iteration, the time consumption of the whole iteration will be quite large especially when the number of channels is big. This is the inherent limitation of cost function autofocus.

Situations will turn better when time domain imaging algorithm such as back projection imaging algorithm (BPA) [21] is used. Integrating along the target track precisely, BPA can be used in almost all SAR working modes. Resembling the idea of fast factorized BP (FFBP), the data of each single channel are imaged first and then integrated as the right of Figure 2 shows. As only multichannel integration is involved in iteration, less time is required. After each single channel is imaged for the first time, we can select some range bins with highest contrast as a new data set for the iteration ahead. This will speed up the iteration further.

3.2. The Transmit Phase Errors. When RXE is compensated, we obtain M frame focused images with different center frequencies and (8) becomes

$$s'_{r,n,m}(\tau, \eta) = \Delta\psi_m \cdot \Delta\varphi_{1,m} \cdot s_{r,1,m} \left(\tau, \eta + \frac{(n-1) \cdot d}{2V_r} \right). \quad (12)$$

Similarly, suppose channel 1 is the reference channel. Define the phase error

$$\Delta\epsilon_{t,m} = \frac{\Delta\psi_m \Delta\varphi_{1,m}}{\Delta\psi_1 \Delta\varphi_{1,m}}, \quad m = 2, \dots, M \quad (13)$$

the transmit phase error (TXE). TXE will reduce the performance of subband synthesis in which the peak sidelobe level ratio (PSLR) and the integrated sidelobe level ratio (ISLR) are worsened [22].

On the focused images, the target is compressed as

$$s_{c,n,m}(\tau, \eta) = A \cdot \Delta\psi_m \cdot \Delta\varphi_{1,m} \cdot p_r \left(\tau - \frac{2R_{n,m}(\eta)}{c} \right) p_a(\eta) \times \exp \left\{ -j \frac{4\pi R_{n,m}(\eta) f_{c,m}}{c} \right\} \exp \{ j2\pi f_{dc} \eta \}, \quad (14)$$

where A is a irrespective coefficient, p_r and p_a are the amplitude of impulse response; that is, the sinc function, f_{dc} is the Doppler center. $R_{n,m}(\eta)$ is known as (4); so the estimation of TXE is simple compared to RXE in which

$$\Delta\epsilon_{t,m} = \frac{s_{c,n,m}(\tau, \eta)}{s_{c,n,1}(\tau, \eta)} \cdot \exp \left\{ j \frac{4\pi (R_{n,m}(\eta) f_{c,m} - R_{n,1}(\eta) f_{c,1})}{c} \right\}. \quad (15)$$

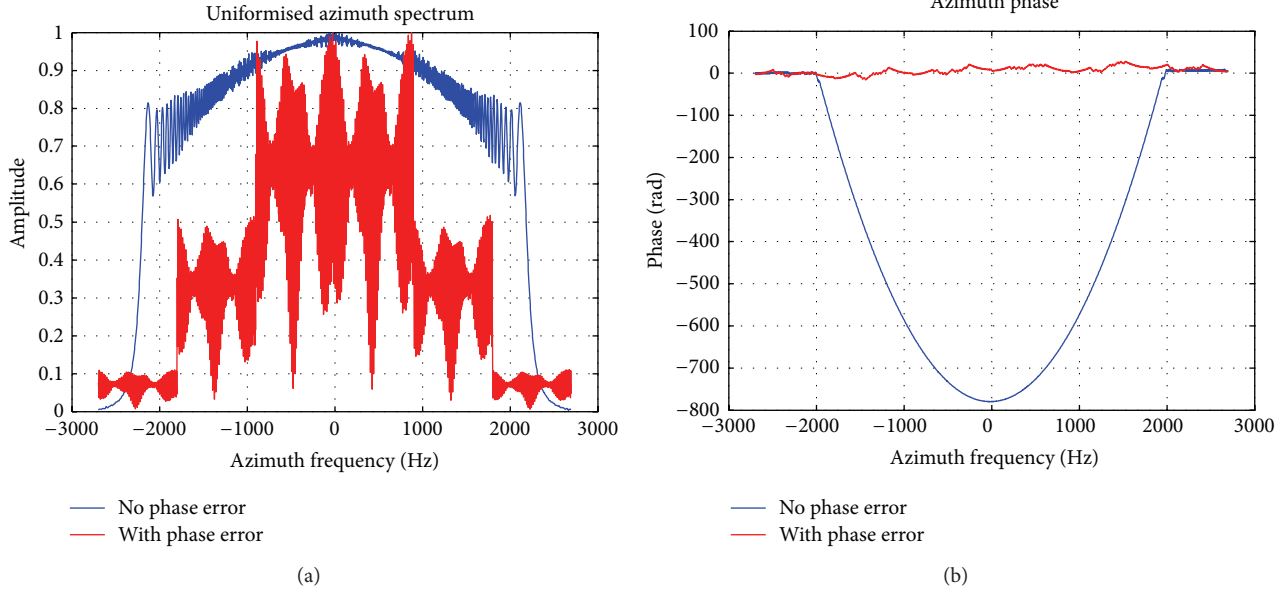


FIGURE 3: Results of azimuth reconstruction. (a) Azimuth spectrum. (b) Phase.

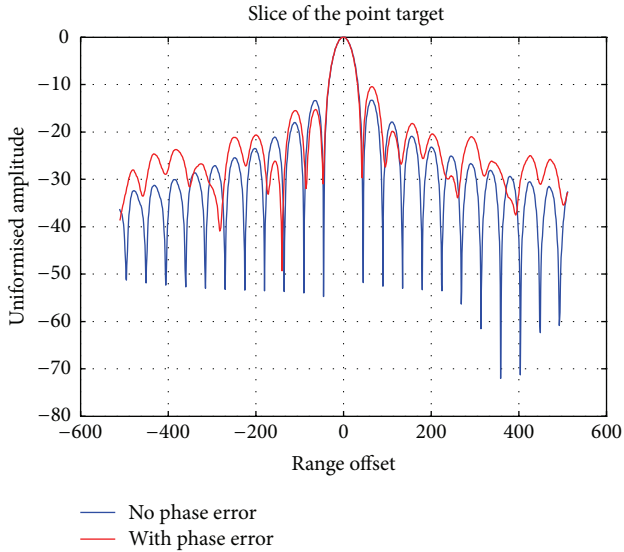


FIGURE 4: Results of subband synthesis.

To make the estimation more precisely and fast, not the whole image but parts of the image with high signal to cluster ratio (SCR) are used. A rectangular sliding window of appropriate size is traveled throughout the image, with the variance of the pixels in the window calculated, those high SCR targets are likely to exist in the windows with high variance [23].

4. Simulation

In this Section, point target simulations are introduced to analyze the proposed algorithm. The simulation parameters are listed in Table 1. The system has 6 channels in azimuth

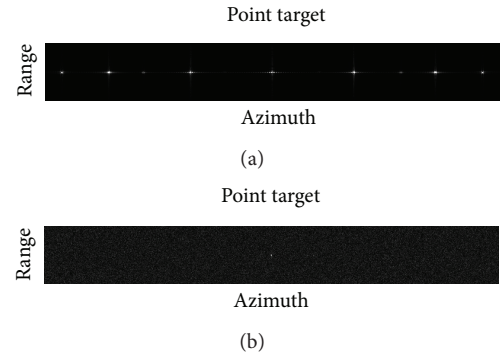


FIGURE 5: Imaging of the target point. (a) With phase errors. (b) Without phase errors.

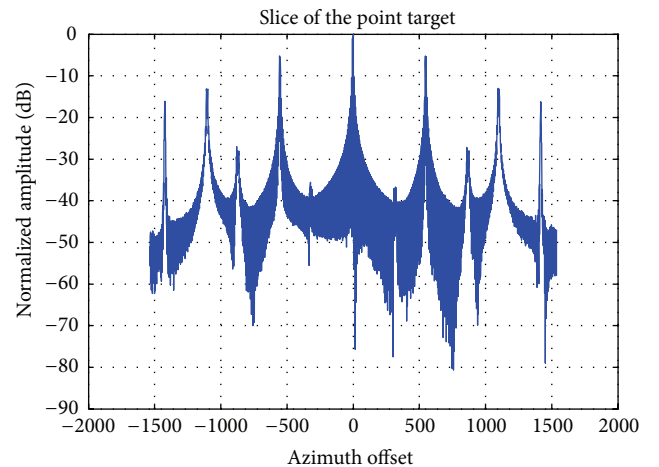


FIGURE 6: Slice of the point target in Figure 5(a).

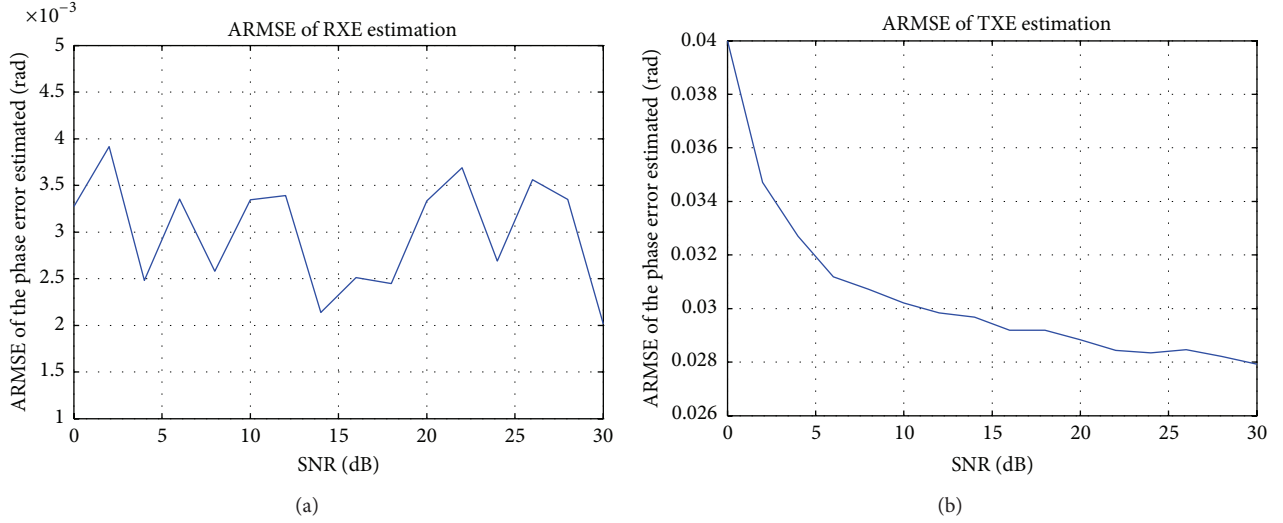


FIGURE 7: Results of Monte Carlo simulation. (a) Results of RXE estimation. (b) Results of TXE estimation.

TABLE 1: Simulation parameters.

Parameter	Value
Channels	6
Center frequency	9.35 GHz~9.85 GHz
Chirp bandwidth	100 MHz
Pulse length	20 us
Platform velocity	7000 m/s
PRF	900 Hz
Antenna length (full)	6 m
Range	800 km

with center frequency ranged from 9.35 GHz to 9.85 GHz stepped by 100 MHz, in which the overlapped ratio of sub-band in range frequency is zero. The full antenna length is 6 m in azimuth which means each aperture can share one out of six.

First, impacts of the phase error on azimuth reconstruction as well as range matched filtering are confirmed. Figure 3 gives the results of azimuth reconstruction. The RXEs added are 0.030π , -0.055π , 0.041π , -0.035π , and -0.018π , respectively. It is clear that the energy is confused across the spectrum as the existence of RXE. And the most important influence is that the phase no longer holds the form of quadratic which means the azimuth compression will fail. Figure 4 gives the results of subband synthesis. The TXEs added are 0.50π , -0.55π , -0.21π , 0.09π , and -0.47π , respectively. As mentioned in Section 3.2, the sidelobe indicators are worsened that the shape is distorted and no longer symmetrical, whereas the mainlobe remains the same; that is, the range resolution is not declined. Comparing the order of RXE with that of TXE, it can be found that azimuth reconstruction is more sensitive to the phase error.

Second, the validation of the proposed algorithm is verified. The system SNR is set to 20 dB. As only point target is involved in the simulations, the computation cost

of frequency domain imaging algorithm is acceptable. Thus the chirp scaling algorithm is used. Figure 5 gives the imaging results. The ghost targets are clearly seen on Figure 5(a) and Figure 6 in which the real target is defocused without doubt. After the compensation, the ambiguity is suppressed; see Figure 5(b). The estimation results are given in Table 2.

At last, the performance of the proposed algorithm is investigated using Monte Carlo experiment. The TXE interval as well as that of RXE is set to $[-0.5\pi, 0.5\pi]$ with uniform distribution. The system SNR is set from 0 dB to 30 dB with step of 2 dB. For each SNR, the experiment is carried out 100 times. The experiment results are given by Figure 7, where the averaged root-mean-square error (ARMSE) is defined by

$$\text{ARMSE} = \frac{1}{M-1} \sum_{m=2}^M \left(\frac{1}{N} \sqrt{\sum_{n=1}^N (\hat{\varepsilon}_{m,n} - \varepsilon_m)^2} \right), \quad (16)$$

where M is the total channels, N is the simulation times, ε is the error set and $\hat{\varepsilon}$ is the error estimated, and subscript m and n indicate the channel and the sample, respectively. From Figure 6, it is shown that ARMSE of RXE estimation is almost independent on system SNR. This is because the cost function is obtained from SAR image where the energy is focused, and noise is greatly suppressed by the defined cost function ISCA (10). However, ARMSE of TXE estimation is dependent on system SNR which means that (16) has room for improvement. The ARMSE order of TXE is bigger than that of RXE because the estimation of RXE is prior to that of TXE; that is, the estimation error propagates.

5. Conclusion

MIMO technique offers an opportunity to map wider image swaths with improved spatial resolution in SAR system. Aiming at the inevitable channel imbalance of multichannel system, this paper has described a new algorithm for compensating the phase errors in MIMO-SAR systems based on

TABLE 2: The phase errors added and estimated.

Channel	TXE					RXE				
	2	3	4	5	6	2	3	4	5	6
Error	0.50π	-0.55π	-0.21π	0.09π	-0.47π	0.030π	-0.055π	0.041π	-0.035π	-0.018π
Estimation	0.512π	-0.601π	-0.213π	0.078π	-0.455π	0.0321π	-0.0564π	0.0440π	-0.0372π	-0.0203π

raw data. Compared with the internal calibration, not only the transmitter and the receiver phase imbalances but also the antenna phase imbalances can be removed. The phase error is classified as transmit phase error or receive phase error which is compensated separately. Simulations confirm the contribution of different kinds of error to image quality decline. Meanwhile the performance with different SNR is also investigated. Algorithm considering gain errors will be our future research focus.

Conflict of Interests

The authors declare that there is no conflict of interests regarding the publication of this paper.

References

- [1] J. C. Curlander and R. N. McDonough, *Synthetic Aperture Radar-Systems and Signal Processing*, John Wiley & Sons, Hoboken, NJ, USA, 1991.
- [2] J. Klare, A. Brenner, and J. Ender, "A new airborne radar for 3D imaging-Image formation using the ARTINO principle," in *Proceedings of the 6th European Conference on Synthetic Aperture Radar (EUSAR '06)*, pp. 16–18, 2006.
- [3] A. Currie and M. A. Brown, "Wide-swath SAR," *IEEE Proceedings F: Radar and Signal Processing*, vol. 139, no. 2, pp. 122–135, 1992.
- [4] J.-H. Kim, M. Younis, P. Prats-Iraola, M. Gabele, and G. Krieger, "First spaceborne demonstration of digital beamforming for azimuth ambiguity suppression," *IEEE Transactions on Geoscience and Remote Sensing*, vol. 51, no. 1, pp. 579–590, 2013.
- [5] W. G. Carrara, R. S. Goodman, and R. M. Majewski, *Spotlight Synthetic Aperture Radar*, Artech House, Norwood, Mass, USA, 1995.
- [6] J. Mittermayer, A. Moreira, and O. Loffeld, "Spotlight SAR data processing using the frequency scaling algorithm," *IEEE Transactions on Geoscience and Remote Sensing*, vol. 37, no. 5, pp. 2198–2214, 1999.
- [7] R. K. Moore, J. P. Claassen, and Y. H. Lin, "Scanning spaceborne synthetic aperture radar with integrated radiometer," *IEEE Transactions on Aerospace and Electronic Systems*, vol. 17, no. 3, pp. 410–421, 1981.
- [8] P. Prats, R. Scheiber, J. Mittermayer, A. Meta, and A. Moreira, "Processing of sliding spotlight and TOPS SAR data using baseband azimuth scaling," *IEEE Transactions on Geoscience and Remote Sensing*, vol. 48, no. 2, pp. 770–780, 2010.
- [9] W. Xu, P. Huang, R. Wang, and Y. Deng, "Processing of multichannel sliding spotlight and TOPS synthetic aperture radar data," *IEEE Transactions on Geoscience and Remote Sensing*, vol. 51, no. 8, pp. 4417–4429, 2013.
- [10] W.-Q. Wang, "Space-time coding MIMO-OFDM SAR for high-resolution imaging," *IEEE Transactions on Geoscience and Remote Sensing*, vol. 49, no. 8, pp. 3094–3104, 2011.
- [11] W.-Q. Wang, "Virtual antenna array analysis for MIMO synthetic aperture radars," *International Journal of Antennas and Propagation*, vol. 2012, Article ID 587276, 10 pages, 2012.
- [12] S. Yuepeng and Y. Ruliang, "High resolution, wide swath SAR using sub-aperture sub-band technique," in *Proceedings of the CIE International Conference on Radar (ICR '06)*, Shanghai, China, October 2006.
- [13] J. H. G. Ender and J. Klare, "System architectures and algorithms for radar imaging by MIMO-SAR," in *Proceedings of the IEEE Radar Conference*, Pasadena, Calif, USA, May 2009.
- [14] G. Krieger, N. Gebert, and A. Moreira, "Unambiguous SAR signal reconstruction from nonuniform displaced phase center sampling," *IEEE Geoscience and Remote Sensing Letters*, vol. 1, no. 4, pp. 260–264, 2004.
- [15] W. Jing, M. Xing, C.-W. Qiu, Z. Bao, and T.-S. Yeo, "Unambiguous reconstruction and high-resolution imaging for multiple-channel SAR and Airborne experiment results," *IEEE Geoscience and Remote Sensing Letters*, vol. 6, no. 1, pp. 102–106, 2009.
- [16] R. T. Lord and M. R. Inggs, "High resolution SAR processing using stepped-frequencies," in *Proceedings of the IEEE International Geoscience and Remote Sensing Symposium (IGARSS '97)*, pp. 490–492, August 1997.
- [17] F. Berizzi and G. Corsim, "Autofocusing of inverse synthetic aperture radar images using contrast optimization," *IEEE Transactions on Aerospace and Electronic Systems*, vol. 32, no. 3, pp. 1185–1191, 1996.
- [18] C. G. Gao, *Study on new techniques for high-resolution and wide-swath synthetic aperture radar [Ph.D. thesis]*, University of Chinese Academy of Sciences, 2012.
- [19] J. K. Thomas, "Monotonic iterative algorithm for minimum-entropy autofocus," in *Proceedings of the Adaptive Sensor Array Processing Workshop (ASAP '06)*, June 2006.
- [20] I. G. Cumming and F. H. Wong, *Digital Signal Processing of Synthetic Aperture Radar Data: Algorithms and Implementation*, Artech House, Norwood, Mass, USA, 2004.
- [21] M. D. Desai and W. K. Jenkins, "Convolution backprojection image reconstruction for spotlight mode synthetic aperture radar," *IEEE Transactions on Image Processing*, vol. 1, no. 4, pp. 505–517, 1992.
- [22] Q. Chen, *Study on new techniques for high-resolution and wide-swath spaceborne synthetic aperture radar [Ph.D. thesis]*, University of Chinese Academy of Sciences, 2013.
- [23] R. C. Gonzalez and R. E. Woods, *Digital Image Processing*, Prentice Hall, 3rd edition, 2007.

Research Article

Multiband Microwave Imaging Analysis of Ionosphere and Troposphere Refraction for Spaceborne SAR

Fan Zhang, Guojun Li, Wei Li, and Wei Hu

College of Information Science & Technology, Beijing University of Chemical Technology, Beijing 100029, China

Correspondence should be addressed to Fan Zhang; zhangf@mail.buct.edu.cn

Received 28 February 2014; Revised 14 April 2014; Accepted 22 April 2014; Published 20 May 2014

Academic Editor: Wen-Qin Wang

Copyright © 2014 Fan Zhang et al. This is an open access article distributed under the Creative Commons Attribution License, which permits unrestricted use, distribution, and reproduction in any medium, provided the original work is properly cited.

Ionosphere has different stratification at the different height. Troposphere has different refractivity at the different height. When microwave signals transmit through the ionosphere and the troposphere, the real propagation path is not an ideal straight line, but a slightly curved straight line. For the synthetic aperture radar (SAR) system, the actual distance errors will result in phase errors, which impact range section and azimuth section of SAR raw data. Consequently, the imaging precision has been decreased by imprecise slant range history. In this paper, we simulate the propagation path between satellite and the target according to Snell's law and analyze how the ionospheric and tropospheric refraction impact the spaceborne SAR imaging performance at L-band and X-band. The simulation results show that the two refraction effects should be compensated in low frequency band for better image focusing performance.

1. Introduction

As the microwave signals transmit between SAR and targets, the imaging results are inevitably affected by the ionosphere and troposphere. The ionizing is at the height of 70 km to 500 km from the ground. Low frequency signal often suffers ionosphere influences severely, such as dispersion, Faraday rotation, refraction, rotation of polarization caused by irregularities, and so on [1–4]. For example, the ionized ionosphere induces Faraday rotation (FR) that affects radar polarization and causes signal path delays, and all of these can be ignored at high frequencies (10 GHz) [5]. These effects all have strong relationship with the TEC (total electron content). Observations show that the electron density of the ionosphere presents a structure of stratification. Generally, we call the electron concentration distribution with height as the electron density profile. In recent years, there has been an increasing interest in the analysis of the impact of propagation link on low frequency and wide-bandwidth spaceborne SAR imaging [5]. Chen et al. put forward an operation mode for topside ionospheric sounding based on spaceborne high

frequency SAR (HF-SAR) [6]. Theoretical analysis indicates that the azimuth resolution can be improved to tens of meters. Liu et al. develop a numerical model to investigate the SAR image degradation caused by an inhomogeneous ionosphere [7]. Both horizontal and vertical structures of the ionosphere are considered in this model. Although they do not study a method to compensate for the ionospheric effects on SAR, the numerical model they have developed is useful for testing different mitigation techniques. And they develop two numerical models about the ionosphere acting on the propagation characteristics of the spaceborne SAR [8]. One of the models simulates the ray-bending effects on the SAR system. Their results show substantial image shift due to this effect at *P*-band or lower frequency band. Wang et al. present the analytical study and numerical simulation to investigate the ionospheric effects on SAR imaging with Gaussian white noise at *P*-band [9]. They use the IRI 2001 model to generate the electron density profile and use the two-parameter spectrum to generate the horizontal electron density profile, which are also used in this paper.

Troposphere is under the altitude of about 12 km. It is the closest layer to the ground and a mixture of kinds of gases (nitrogen, oxygen, carbon dioxide, and so on) and water vapor. The dielectric properties of the troposphere vary with time and space. So the microwave signals transmit in the troposphere differently from in the vacuum [10]. The effect of troposphere on SAR imaging is usually ignored for that the early moderate resolution imaging would not be affected by the relative minor tropospheric path error. Consequently, there are few thorough analysis and validation related to the troposphere in SAR field. Currently, the spaceborne SAR imaging resolution has reached half a meter level. So the troposphere environmental factor has become one of the factors that cannot be ignored on spaceborne SAR imaging with high resolution. Sun et al. introduce the impact of atmospheric refraction on the high resolution airborne SAR which mainly reflects on azimuth resolution [10]. The changes of atmosphere refractive index in troposphere with the Hopfield refractive model are analyzed, and the calculation of the apparent range between radar and ground targets is given. The algorithm mentioned in paper has certain reference value to the performance and imaging analysis of the high resolution airborne SAR system which is level of centimeter. The refraction effects are addressed with assuming a horizontally nonhomogeneous troposphere [11]. The impact of the range refractivity on a terrestrial radio link is investigated in terms of radio horizon range. By acquiring simultaneous weather radar data over the test site, it is possible to flag affected SAR images and exclude them from the procedure.

Through the above introduction, the index of refraction will vary with the height both in ionosphere and troposphere [12]. According to Snell's law, the propagation of radio waves in the multilayer medium will be bent and not straight as we expected. The path error will cause many problems in SAR imaging. Therefore, we will simulate and analyze the impact of the multiband microwave propagation errors caused by the ionosphere and troposphere on SAR imaging in the following contents.

In this paper, we focus on the propagation path's bending caused by ionosphere and troposphere refraction, which are seldom synthetically considered before. First, we discuss the effects of ionospheric and tropospheric refraction on SAR imaging. In Section 2, we introduce the background of the ionospheric and tropospheric refractive model. The structure of ionosphere can be analyzed from two aspects: vertical profile and horizontal profile. In Section 3, we use the path tracing method to calculate the actual distance according to Snell's law. In Section 4, we perform SAR imaging simulation with the path errors and analyze the imaging performance. In Section 5, we draw a conclusion and put forward some plans for future research.

2. Atmosphere Structure

As Figure 1 shows, troposphere is at the height of 0 to 12 km. The layer between 60 km and 90 km is the D region and

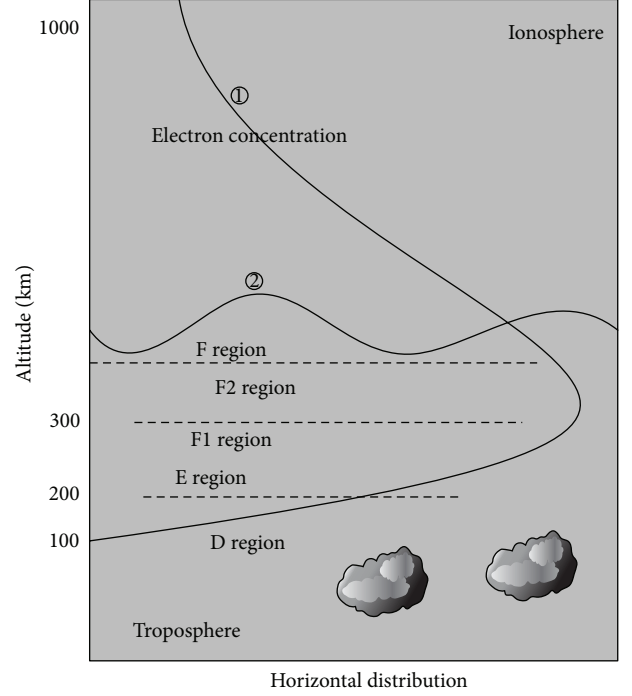


FIGURE 1: Sketch map of ionosphere and troposphere.

from 90 km to 140 km is the E region. The F region is at the height above 140 km. In Figure 1, curve ① represents the profile of vertical electron density; curve ② represents the profile of horizontal electron density. Because the sketch map is just used to indicate the atmosphere structure, the vertical and horizontal electron density profile are rough. We can see that the electron concentration varies with different heights and different horizontal distribution, which will lead to the change of the ionosphere refraction. Moreover, there are kinds of gases in the troposphere, and the tropospheric index of refraction will vary with different heights as well. So there must be path errors in the propagation of microwaves.

2.1. Basic Structure of Ionosphere. The basic structure of ionosphere can be discussed from two aspects: vertical TEC profile and horizontal TEC profile.

2.1.1. Vertical TEC Profile. According to Appleton-Hatreek, we can get the simplified formula about the refractive index of ionosphere [13, 14]:

$$n = \sqrt{1 - \frac{80.6N_e}{f^2}}, \quad (1)$$

where N_e is the electron concentration and f is the wave frequency in Hz.

In this paper, we use the engineering ionospheric electron density profile model IRI 2001 to calculate N_e [15, 16]. The model is expressed as below [17]:

$$N_e(h) = \begin{cases} N_m E \left[1 - \left(\frac{h_m E - h}{y_m E} \right)^2 \right], & h_m E - y_m E \leq h \leq h_m E \\ \frac{N_j - N_m E}{h_j - h_m E} h + \frac{(N_m E) h_j - N_j (h_m E)}{h_j - h_m E}, & h_m E < h \leq h_j \\ N_m F_2 \left[1 - \left(\frac{h_m F_2 - h}{y_m F_2} \right)^2 \right], & h_j < h < h_m F_2 \\ N_m F_2 \exp \left[\frac{1}{2} \left(1 - \frac{h - h_m F_2}{H} - e^{-(h - h_m F_2)/H} \right) \right], & h_m F_2 < h \leq 1000 \text{ km}, \end{cases} \quad (2)$$

where N_m is the largest electronic concentration of each layer, N_j is for F_1 layer, h is the height corresponding to the largest electronic concentration of each layer, and h_j is for F_1 layer. y_m is the half-thickness for each layer, f_0 is the critical frequency for each layer, and f_j is for F_1 layer. $h_m E$ is 115 km; $y_m E$ is 20 km [18].

The vertical electron concentration is shown in Figure 2.

2.1.2. Horizontal TEC Profile. As shown in Figure 3, the horizontal TEC varies with the different latitudes and longitudes. Since the spaceborne SAR aperture size is at least tens of kilometers, the horizontal TEC gradient will impact the SAR imaging performance.

In this paper, we use the two-parameter spectrum to generate the horizontal profile of electron concentration [19, 20]. $V(k)$ can be expressed as [7]

$$V(k) = \begin{cases} \frac{\pi A}{v_1 - 1} \frac{1}{(k^2 + k_0^2)^{v_1 - 1}} \\ - \frac{\pi A}{(k_b^2 + k_0^2)^{v_1 - 1}} \left(\frac{1}{v_1 - 1} - \frac{1}{v_2 - 1} \right), & k \leq k_b, \\ \frac{\pi A (k_b^2 + k_0^2)^{v_2 - v_1}}{v_2 - 1} \frac{1}{(k^2 + k_0^2)^{v_2 - 1}}, & k > k_b, \end{cases} \quad (3)$$

where $k_b = 2\pi/L_b$, $k_0 = 2\pi/L_0$, k_b is the interrupt wave number, $L_0 = 10$ km, $L_b = 500$ m, and $2v_1 = 3.5$, $2v_2 = 5.5$.

To generate the horizontal profile of electron concentration, a sequence of normally distributed random numbers is used in the phase of the profile spectrum. Using the discrete Fourier transform, the relationship between the electron density profile and the profile spectrum is described in the following equations:

$$f(x) = \frac{1}{L} \sum_{n=N/2}^{N/2-1} F(k_n) \exp(ik_n x), \quad (4)$$

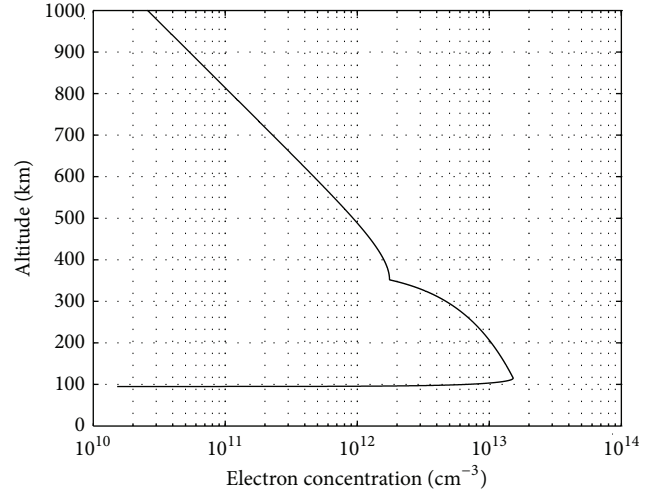


FIGURE 2: Vertical electron density profile model.

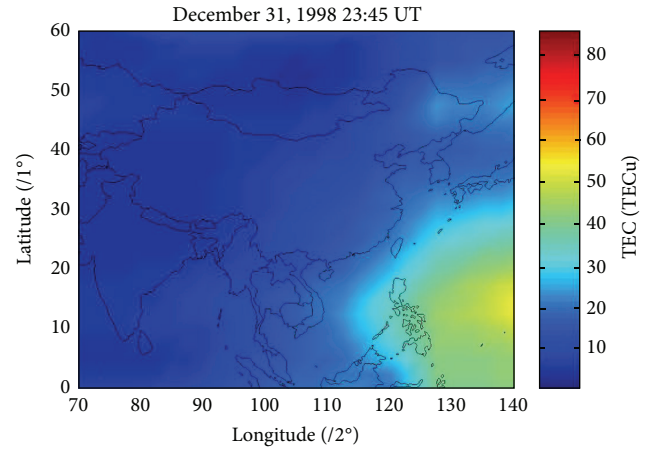


FIGURE 3: Horizontal electron density profile model.

where

$$F(k_n) = \sqrt{2\pi LV(k_n)} \begin{cases} \frac{1}{\sqrt{2}} [N(0, 1) + iN(0, 1)], & n \neq 0, \frac{N}{2} \\ N(0, 1), & n = 0, \frac{N}{2} \end{cases} \quad (5)$$

and $K_n = 2\pi n/L$, L is a total length of a profile. $N(0, 1)$ denotes a sequence of normally distributed numbers in $[0, 1]$ with zero mean and unity standard deviation. The horizontal electron concentration is shown in Figure 4.

2.2. Model for Tropospheric Refractivity. As for troposphere, we often use the statistical model of the refractive index. In this paper, we use the Hopfield model [12], which includes mainly two parts. The first one is the so-called wet part, which is related to the concentration of water vapor. The other part is the so-called dry part, which is related to the gaseous nature

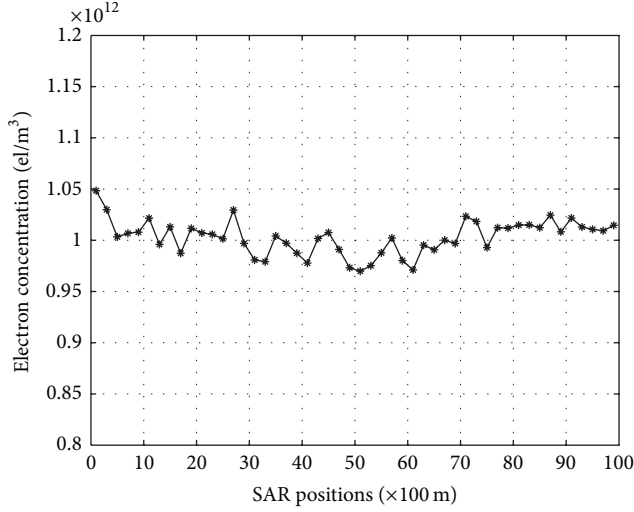


FIGURE 4: The propagation path of microwave signals.

of the lower part of the atmosphere. The dry parts and the wet parts are in form of function of fourth power [21].

$$N(h) = N_d + N_w \quad (6)$$

$$N_d = \begin{cases} N_{0d} \left(\frac{H_d - h}{H_d - h_0} \right)^4, & h < H_d \\ 0, & h \geq H_d \end{cases} \quad (7)$$

$$N_w = \begin{cases} N_{0w} \left(\frac{H_w - h}{H_w - h_0} \right)^4, & h < H_w \\ 0, & h \geq H_w, \end{cases} \quad (8)$$

where the subscripts d and w represent dry and wet parts; N_{0d} and N_{0w} are the ground atmospheric refractivity; H_d and H_w are the height where the dry and wet section of atmospheric refractivity decay to 0; h_0 is the height of ground.

Then, we can calculate the ground atmospheric refractivity as below:

$$N_{0d} = 77.6 \frac{P_0}{(t_s + 273.15)} \quad (9)$$

$$N_{0w} = 3.37 \times 10^3 \frac{RH \times a}{(t_s + 273.15)^2} \exp\left(\frac{bt_s}{c + t_s}\right).$$

Then, we can calculate the refractive index of troposphere by (6).

3. Calculation of the Path Error

When the microwave signals transmit through the ionosphere and troposphere, the path will become bent because of refraction as Figure 5 shows. We can calculate the actual distance according to Snell's law. Assuming that the radar situated at a height of h , radar's depression angle is θ_0 ,

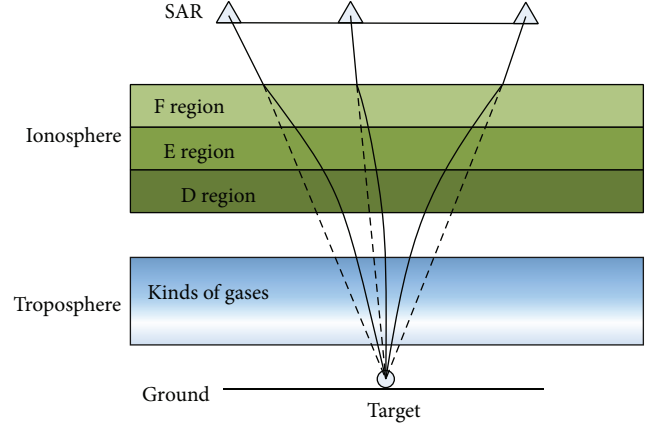


FIGURE 5: Path tracing course.

the refractive index at the height of h is n_0 . Then, the actual distance of the radar and the target is

$$R = \int_0^h \frac{n^2(z)}{\sqrt{n^2(z) - n_0^2 \cos^2 \theta_0}} dz. \quad (10)$$

In (10), $n(z)$ is the refractive index of space, including ionosphere and troposphere. Due to the fact that different models are used, we independently calculate the actual distance in ionosphere and troposphere refraction. Furthermore, the ionospheric refraction includes two parts: vertical TEC section and horizontal TEC section.

Accordingly, the horizontal distance between radar and the target is y_0 :

$$y_0 = \int_0^h \frac{n_0 \cos \theta_0}{\sqrt{n^2(z) - n_0^2 \cos^2 \theta_0}} dz. \quad (11)$$

According the equations above, we use the method of path tracing to calculate the actual distance of radar and the target. First, we substitute y_0 into (11) as a known quantity; thus we can get radar's depression angle θ_0 . Then, we substitute the θ_0 into (10), and get the actual distance of radar and the target. The flowchart of the course of path tracing is expressed in Figure 6.

SAR imaging geometry is shown as Figure 7. Spaceborne SAR is at the height of h and moves at a speed of v_a along the x -axis direction; the instant time is t_m . When it comes to the synthetic aperture center, $t_m = 0$. The shadow is the footprint, the horizontal width of the beam is β , and the vertical width is φ . At the t_m moment, the actual distance between SAR and the target is $R(t_m)$.

If the ionospheric and tropospheric environment can be ignored, the actual distance is equal to the theoretical distance between SAR and the targets, which can be calculated as [22]

$$R(t_m) = \sqrt{h^2 + r_0^2 + (v_a t_m)^2}. \quad (12)$$

So the path error is

$$\Delta R(t_m) = R(t_m, n(z)) - R(t_m). \quad (13)$$

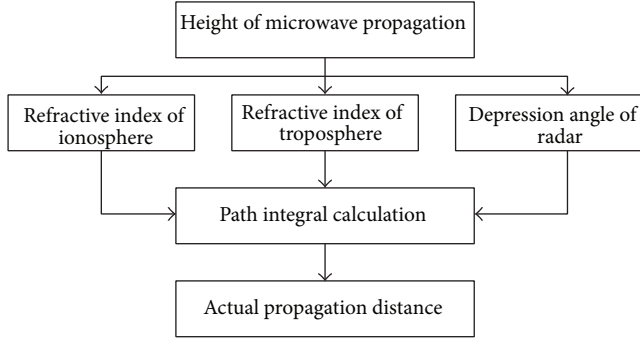


FIGURE 6: SAR imaging geometry.

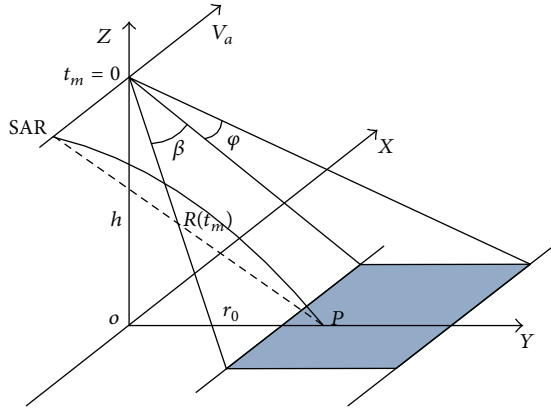


FIGURE 7: An example of horizontal TEC map over China and adjacent regions.

The phase error caused by path error is

$$\Delta\varphi(t_m) = \frac{-4\pi\Delta R(t_m)}{\lambda}. \quad (14)$$

Assuming that the total synthetic aperture time is T_a , the time of range section is τ and the radar signal is chirp signal. We can get the echo that the radar receives from the target as below:

$$s(t_m, \tau) = \sigma w_a^2(\theta) \text{rect}\left(\frac{\tau - 2R(t_m)/c}{T_a}\right) \cdot \exp\left(-j\frac{4\pi}{\lambda}R(t_m)\right) \cdot \exp\left(j\pi K\left(\tau - \frac{2R(t_m)}{c}\right)^2\right), \quad (15)$$

where t is the azimuth slow time, τ is the range fast time, K is chirp rate, $w_a(\theta)$ is the azimuth antenna illumination envelop, σ is the backscatter coefficient, c is the speed of light, and R is the distance from antenna phase center to the target.

The echo signals that the radar receives from the target are related to the actual distance between the radar and the target. So the path error will lead to the delay and the offset error in range section.

On the other hand, we can do quadratic Taylor expansion on the actual distance $R(t_m, n(z))$ around $t_c = r_0/v_a$:

$$R(t_m, n(z)) \approx R((t_m - t_c), n(z)) + \Delta t * R'((t_m - t_c), n(z)) + 0.5\Delta t^2 * R''((t_m - t_c), n(z))^2. \quad (16)$$

In (16), there is a quadratic term. There must be quadratic phase error in azimuth section when the distance errors are considered. Obviously, the quadratic phase error will lead to the elevated sidelobe energy, thus affecting the SAR image quality. In summary, the path error will lead to two problems in SAR imaging: the offset error in range section and quadratic phase error in azimuth section, which can be illustrated as Figure 8.

4. Multiband Spaceborne SAR Imaging Simulation with Refraction Path Error

To analyze the refraction effect of atmosphere on spaceborne SAR imaging, the propagation path errors should be introduced into echo generation process in every transmitted pulse. On the other hand, the multiband responses with atmospheric refraction effects are also the key topic, which can not only guide the course of spaceborne SAR system design, but also assist the in-orbit microwave imaging and analysis. Therefore, the multiband spaceborne SAR imaging simulation is carried out for atmospheric refraction error analysis and modeling.

According to classical SAR simulation process, the imaging simulation with path error involves four steps, including refractive index calculation, propagation path error calculation, raw data simulation, and imaging analysis, as shown in Figure 9. The simulation method is as follows.

- (i) According to the description of Section 2, we can calculate the different height's refractive index in ionosphere and troposphere by the general engineering model. Then we change the microwave frequency to get the different refractive index distribution along the vertical height, which can be used in actual path calculation.
- (ii) Based on the path tracing method, the microwave propagation path under Snell's law is calculated with considering the ionosphere and troposphere refraction. The specific algorithm is introduced in Section 3. On this basis, we simulate the satellite orbit and calculate the path error at each pulse transmitting time and then get the error curve along the azimuth direction. To compare the multiband characteristic, it is assumed that the multiband simulation should be executed with same orbit and radar parameters. After multifrequency replacement, the multiband path error can be simulated.
- (iii) The spaceborne SAR raw data simulation includes four steps: target deployment, orbit calculation, path error injection, and raw data calculation. In order to

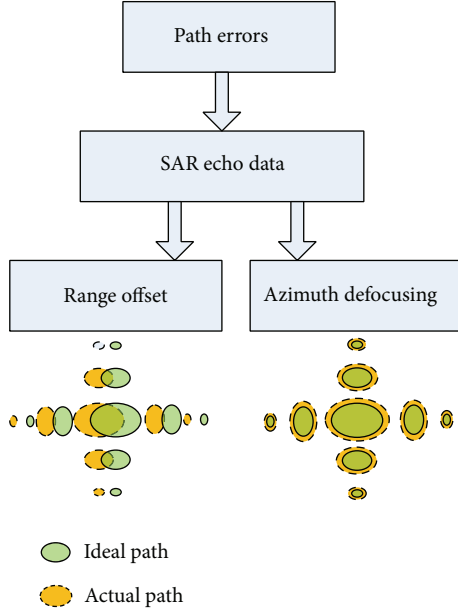


FIGURE 8: Sketch map of the offset error imaging in range section and quadratic phase error in azimuth section.

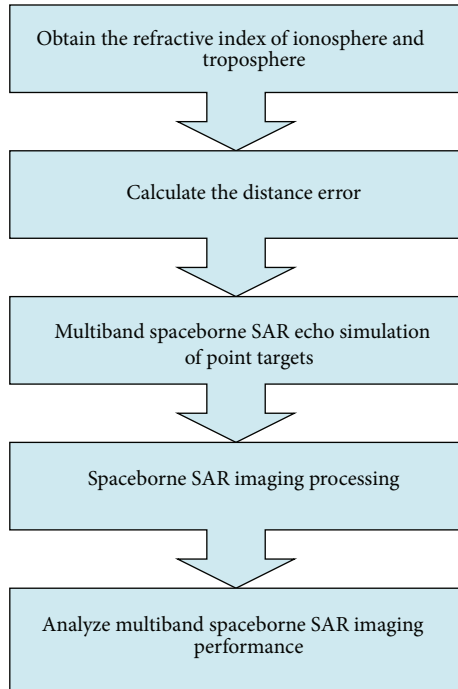


FIGURE 9: Process of the simulation.

measure the image quality, point targets are located in the simulated scene. Moreover, the time-domain algorithm that can easily introduce system errors is selected for spaceborne SAR raw data calculation. Through the simulation processing, the multiband SAR raw data can be generated for imaging analysis.

- (iv) The imaging analysis includes image processing and image quality assessment. First, the raw data should be processed by classical Chirp-Scaling imaging algorithm. Second, the point target data should be cut from SAR image for extracting the profile of range direction and azimuth direction. Finally, the SAR imaging index, such as resolution, expansion ratio, peak sidelobe ratio, and integral sidelobe ratio, can be calculated to analyze the multiband atmosphere refraction effects.

5. Simulation Result and Discussion

Simulations are carried out for *L*-band and *X*-band, which are applied for different remote sensing purpose and less discussed. The simulation parameters are shown in Table 1 and experimental conditions are described below:

- (1) point target array is placed in the middle of simulated image;
- (2) in the course of refractive index calculation, the ionosphere height is 100~1000 km, the troposphere height is 0~12 km, and the vertical divided layer scale of ionosphere and troposphere is, respectively, 0.1 km and 0.001 km;
- (3) in horizontal electron density profile model, the average peak value is set to 10^{12} el/m³ and the perturbation is set to 10%. The simulated horizontal distance of electron density profile is 10 km with sampling interval of 100 m.

Figure 10 shows the microwave propagation path errors of *L*-band and *X*-band in a synthetic aperture time. With the change of slant range, the path error also varies in quadratic curve. If we do not take the horizontal TEC into consideration, the curve will be smooth. However, the curve shows a zigzag line by considering the refraction. From the results, the path error of *L*-band is greater than *X*-band, but the two bands have the similar fluctuation. Because ionosphere is higher than troposphere, the ionosphere contributes the majority of path errors for longer propagation path. It is seen that the higher frequency band radar works with the greater the refraction effects and worse image quality. Figure 11 depicts, respectively, the point target response profile of range direction and azimuth direction in *L*-band and *X*-band. The azimuth profile in *L*-band has a serious quadratic phase error, which leads to the sidelobe uplift. The azimuth profile in *X*-band is close to the ideal curve. Otherwise, both the two range profiles are very standard. We can see that the path errors will lead to the decline in image quality indicators of azimuth section. Tables 2 and 3 provide a quantitative proof of the conclusion.

As shown in Table 2, compared with theoretical indicators, the resolution errors at *L*-band are 0.0246 m bigger than *X*-band in range direction and 1.9193 m more in azimuth section. Otherwise, the expansion ratio, the peak sidelobe ratio, and the integral sidelobe ratio are the same situations that the effects in *L*-band are worse than *X*-band, and the indicators in azimuth direction are worse than range

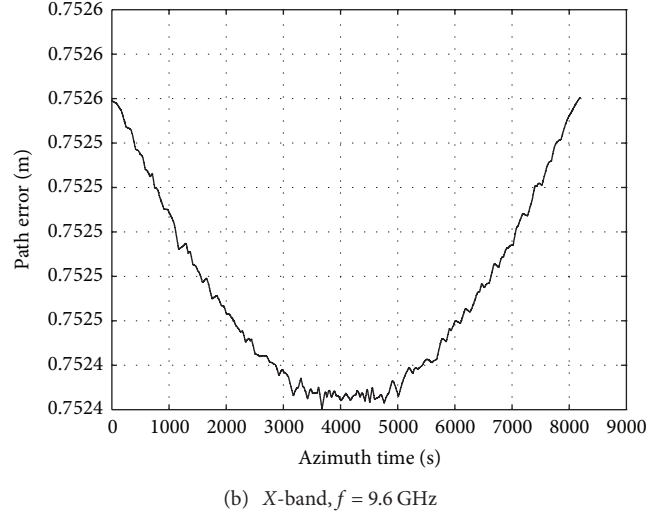
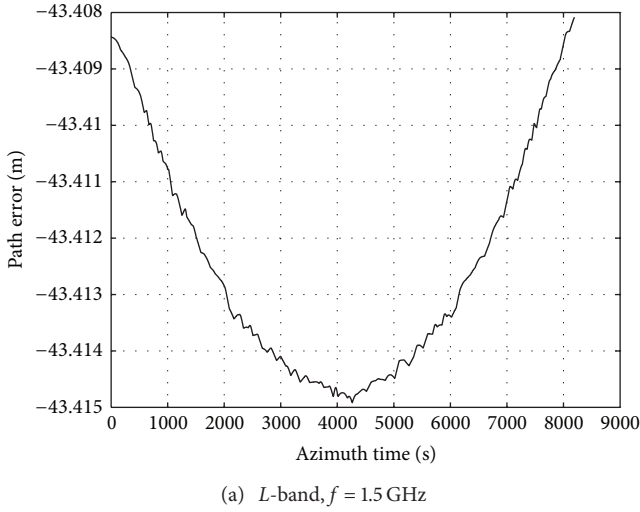
FIGURE 10: The path error of L -band and X -band.

TABLE 1: Simulation parameters.

Parameters	Value
Semimajor axis	7000 km
Eccentricity	0.0
Orbital inclination	95 degrees
RAAN	150 degrees
Argument of perigee	210 degrees
PRF	2000 Hz
Band width	60 MHz
Pulse width	30 μ s
Sampling rate	66.6 MHz

TABLE 2: Imaging indicators errors of L -band and X -band compared to the theoretical indicators in range section.

Indicators	L	X
Resolution (m)	0.0327	0.0081
Expansion ratio (dB)	0.071	0.0017
Peak sidelobe ratio (dB)	0.1072	-0.0625
Integral sidelobe ratio (dB)	0.2509	-0.1326

TABLE 3: Imaging indicators errors of L -band to X -band compared to the theoretical indicators in azimuth section.

Indicators	L	X
Resolution (m)	1.9672	0.0479
Expansion ratio (dB)	0.4837	0.0118
Peak sidelobe ratio (dB)	-1.6258	-0.8447
Integral sidelobe ratio (dB)	4.6385	-0.5886

direction. As shown in Table 4, the pixel positions of the point target at L -band and X -band are different from the theoretical position. It can be seen that the lower frequency imaging is seriously affected by the propagation.

TABLE 4: Position of the point target in range section.

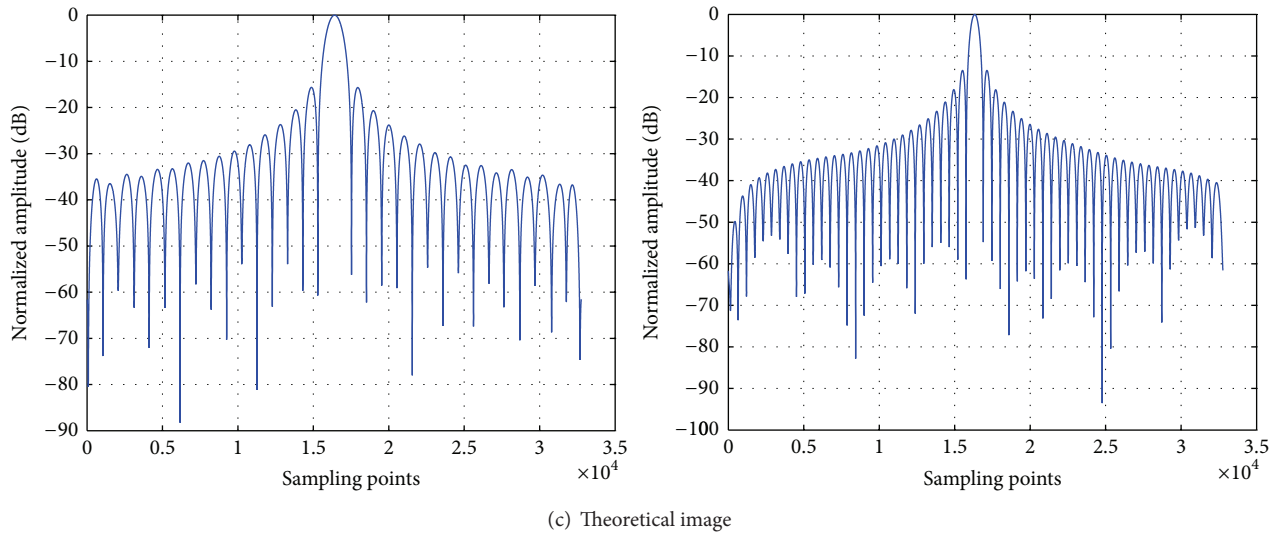
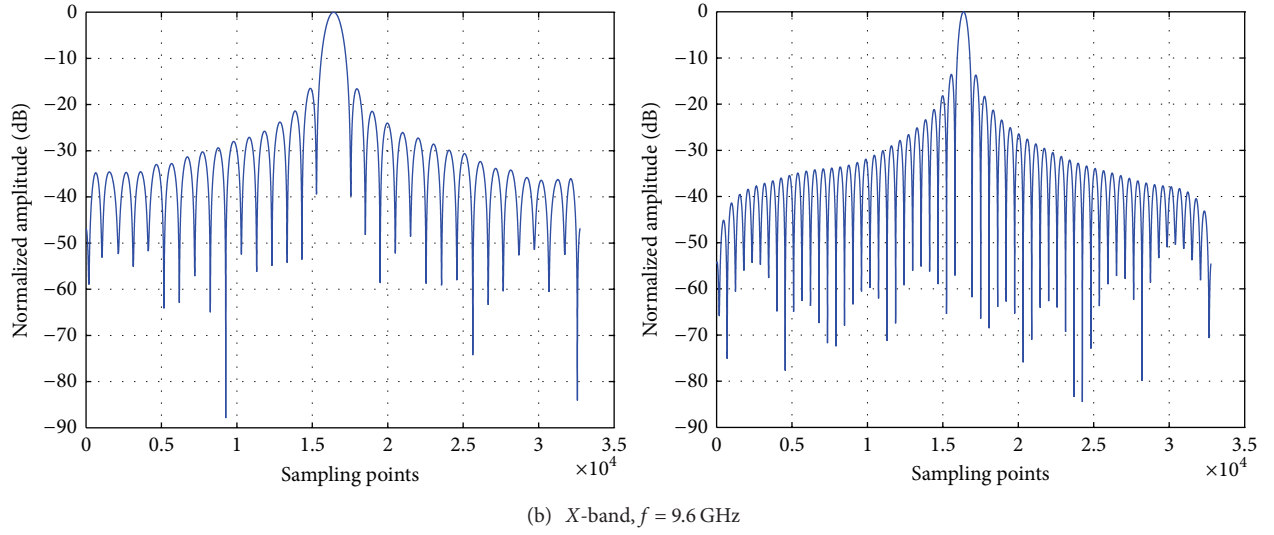
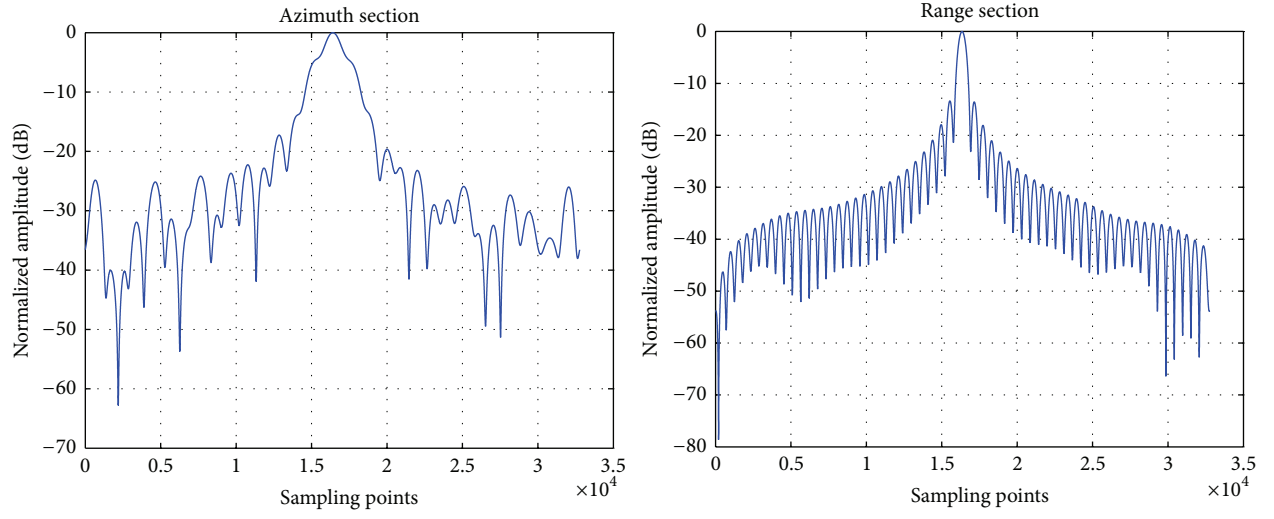
Theoretical position	L -band	X -band
(2048.00, 512.00)	(2031.00, 512.00)	(2047.00, 512.00)

According to the analysis of Section 3, the path errors also affect the position of point target. Therefore, we measure the position of two band SAR images in pixel. As can be seen from Table 4, the range direction offset is 17 pixels and 1 pixel in L -band and X -band compared with theoretical position in the image. The image offset is proportional to the path error.

The simulation results show that path error caused by ionospheric and tropospheric refraction affects both range section and azimuth section imaging indicators especially on azimuth section, such as resolution, expansion ratio, peak sidelobe ratio, and integral sidelobe ratio. And the lower the frequency is, the more serious the effects are. Table 4 shows that there is offset error imaging in range section. With the distance between the satellite and target increasing, the imaging results will get worse. The accurate estimation of ionosphere and troposphere model will assist the autofocus compensation to improve spaceborne SAR image quality and reduce the dependence on external calibration measurement.

6. Conclusions

In this paper, we use the engineering practical ionospheric electron density profile model to get the electron concentration of different heights. After that, we can get the ionospheric refractive index of different heights. As for troposphere, we use Hopfield model to get the tropospheric refractive index. The actual distance is calculated by path tracing method. Compared to the propagation path in the vacuum, the real path must be bent. The path error can lead to phase error which is the key to the spaceborne SAR imaging. After researching related literatures, we find that people care a lot about the effect of troposphere and ionosphere on SAR

FIGURE 11: Point target assessment curve at L -band and X -band.

imaging independently, but few materials considering both of them. So the study of the effects of two kinds of refractions on the spaceborne SAR imaging performance is essential. Other imaging indicators like image quality analyzing still needs to be further studied. In the future, we will analyze the correction of refractive effects on spaceborne SAR imaging.

Conflict of Interests

The authors declare that there is no conflict of interests regarding the publication of this paper.

Acknowledgments

This work was supported in part by the National Natural Science Foundation of China under Grant 61003132, 61302164, by the Beijing Higher Education Young Elite Teacher Project under Grant YETP0500, and by the Interdisciplinary Research Project in Beijing University of Chemical Technology. The authors sincerely thank the geological and geophysical data sharing platform of the Institute of Geology and Geophysics, Chinese Academy of Sciences for providing ionospheric TEC data contour maps of Chinese region.

References

- [1] D. P. Belcher and N. C. Rogers, "Theory and simulation of ionospheric effects on synthetic aperture radar," *IET Radar, Sonar & Navigation*, vol. 3, no. 5, pp. 541–551, 2009.
- [2] W. S. Zhai and Y. H. Zhang, "Simulation and correction of ionospheric effects on P-band spaceborne SAR imaging," *Journal of Test and Measurement Technology*, no. 5, pp. 459–464, 2008 (Chinese).
- [3] O. V. Goriachkin and D. D. Klovsky, "Some problems of realization spaceborne SAR in P, UHF, VHF bands," in *Proceedings of the IEEE International Geoscience and Remote Sensing Symposium (IGARSS '99)*, vol. 2, pp. 1271–1273, July 1999.
- [4] A. Danklmayer, B. J. Doring, M. Schwerdt, and M. Chandra, "Assessment of atmospheric propagation effects in SAR images," *IEEE Transactions on Geoscience and Remote Sensing*, vol. 47, no. 10, pp. 3507–3518, 2009.
- [5] M. Jehle, M. Ruegg, L. Zuberbuhler, D. Small, and E. Meier, "Measurement of ionospheric faraday rotation in simulated and real spaceborne SAR Data," *IEEE Transactions on Geoscience and Remote Sensing*, vol. 47, no. 5, pp. 1512–1523, 2009.
- [6] J. Chen, W. Liu, Y. Zhou, and C. Li, "Operation mode for topside ionospheric sounding based on space-borne high frequency synthetic aperture radar," in *Proceedings of the 1st Asian and Pacific Conference on Synthetic Aperture Radar (APSAR '07)*, pp. 1–5, November 2007.
- [7] J. Liu, Y. Kuga, A. Ishimaru, X. Pi, and A. Freeman, "Ionospheric effects on SAR imaging: a numerical study," *IEEE Transactions on Geoscience and Remote Sensing*, vol. 41, no. 5, pp. 939–947, 2003.
- [8] A. Ishimaru, Y. Kuga, J. Liu, and T. Freeman, "Ionospheric effects on synthetic aperture radar at 100 MHz to 2 GHz," *Radio Science*, vol. 34, no. 1, pp. 257–268, 1999.
- [9] C. Wang, M. Zhang, Z. W. Xu, and C. Chen, "Simulation of ionospheric effects on SAR imaging with noise at P-band," in *Proceedings of the 10th International Symposium on Antennas, Propagation & EM Theory*, pp. 419–422, October 2012.
- [10] J. P. Sun, Y. P. Wang, W. Hong, and S. Y. Mao, "Effects of atmospheric refractivity on high resolution airborne SAR performance," *Journal of Systems Engineering and Electronics*, vol. 34, no. 4, pp. 681–685, 2012 (Chinese).
- [11] P. Valtr and P. Pechac, "The influence of horizontally variable refractive index height profile on radio horizon range," *IEEE Antennas and Wireless Propagation Letters*, vol. 4, no. 1, pp. 489–491, 2005.
- [12] P. N. Jiao and Z. Z. Zhang, *Radar Environment and Transmitting Characteristic of Electric Wave*, Publishing House of Electronics Industry, Beijing, China, 2004, (Chinese).
- [13] M. Jehle, O. Frey, D. Small, and E. Meier, "Measurement of ionospheric tec in spaceborne sar data," *IEEE Transactions on Geoscience and Remote Sensing*, vol. 48, no. 6, pp. 2460–2468, 2010.
- [14] J. Liu, Y. Kuga, and A. Ishimaru, "Simulations of ionospheric effects on SAR at P-band," in *Proceedings of the IEEE International Geoscience and Remote Sensing Symposium (IGARSS '99)*, vol. 3, pp. 1842–1844, July 1999.
- [15] Z. Meng and G. Y. LIU, "Ionosphere effects on the range performance of P-band spaceborne SAR signal," *Modern Radar*, vol. 34, no. 2, pp. 8–11, 2012 (Chinese).
- [16] Z.-W. Xu, J. Wu, and Z.-S. Wu, "Potential effects of the ionosphere on space-based SAR imaging," *IEEE Transactions on Antennas and Propagation*, vol. 56, no. 7, pp. 1968–1975, 2008.
- [17] J. M. Goodman and J. Aarons, "Ionospheric effects on modern electronic systems," *Proceedings of the IEEE*, vol. 78, no. 3, pp. 512–528, 1990.
- [18] GJB/Z87-97, *Handbook of Refraction and Attenuation of Radiowave Propagation for Radar*, People's Republic of China National Military Standard, 1997, (Chinese).
- [19] D. Xia, Y. Li, W. Hong, and Y. Wu, "An approach for ionospheric effects reducing on SAR imaging," in *Proceedings of the 2nd Asia-Pacific Conference on Synthetic Aperture Radar (APSAR '09)*, pp. 1072–1075, October 2009.
- [20] D.-K. Xia, Y. Li, Y.-L. Qi, W. Hong, and Y.-R. Wu, "Investigation on ionospheric decorrelation of space-borne POL-in-SAR systems," *Acta Electronica Sinica*, vol. 20, no. 6, pp. 1309–1314, 2011 (Chinese).
- [21] J. L. Porcello, "Turbulence-induced phase errors in synthetic-aperture radars," *IEEE Transactions on Aerospace and Electronic Systems*, vol. 6, no. 5, pp. 636–644, 1970.
- [22] J. Chen, Z. Li, W. Liu, C. Li, and Y. Zhou, "Image formation algorithm for topside ionosphere sounding with spaceborne HF-SAR system," in *Proceedings of the IEEE International Geoscience and Remote Sensing Symposium (IGARSS '08)*, vol. 2, pp. II549–II552, July 2008.

Research Article

Sparse Recovery for Bistatic MIMO Radar Imaging in the Presence of Array Gain Uncertainties

Jun Li, Shengqi Zhu, Xixi Chen, Li Lv, Guisheng Liao, and Menglei Yi

National Lab of Radar Signal Processing, Xidian University, Xi'an, Shaanxi 710071, China

Correspondence should be addressed to Jun Li; junli01@mail.xidian.edu.cn

Received 18 March 2014; Accepted 22 April 2014; Published 13 May 2014

Academic Editor: Wen-Qin Wang

Copyright © 2014 Jun Li et al. This is an open access article distributed under the Creative Commons Attribution License, which permits unrestricted use, distribution, and reproduction in any medium, provided the original work is properly cited.

A sparse recovery based transmit-receive angle imaging scheme is proposed for bistatic multiple-input multiple-output (MIMO) radar. The redundancy of the transmit and receive angles in the same range cell is exploited to construct the sparse model. The imaging is then performed by compressive sensing method with consideration of both the transmit and receive array gain uncertainties. An additional constraint is imposed on the inverse of the transmit and receive array gain errors matrices to make the optimization problem of the CS solvable. The image of the targets can be reconstructed using small number of snapshots in the case of large array gain uncertainties. Simulation results confirm the effectiveness of the proposed scheme.

1. Introduction

Multiple-input multiple-output (MIMO) radar has multiple transmit channels and multiple receive channels, and the transmit channels can be separated by waveforms or time or frequencies or polarizations at each receiver. So, the transmit aperture can be exploited completely by processing receive data [1–3]. Most of the advantages of the MIMO radar come from increasing the number of channels. Two main classes of MIMO radar have been proposed, with widely separated antennas [1] and with colocated antennas [2]. The first class utilizes the different scattering properties of a target from sufficiently spaced antennas to improve the performance of the systems. The second class allows the improvement of the radar performances by coherent processing of the multiple channels.

Bistatic MIMO radar scheme has been proposed in [3], where a two-dimensional radar imaging method based on the Capon method is developed. Bistatic MIMO radar has the particular advantage of being able to obtain the target angles with respect to both the transmit and the receive arrays by processing the receive data [3–7]. So, the range information of the target is redundant in this case and the time synchronization of the bistatic radar is relaxed. Nevertheless, the errors of both the transmit array and the receive array will degrade the performances of these techniques. Many works have been

done to estimate the array errors and correct the transmit array and receive array simultaneously in bistatic MIMO radar [8, 9]. However, these methods need large number of snapshots to estimate the covariance matrix and some well-calibrated elements.

Compressive sensing (CS) has received considerable attention recently and has been applied to source localization by exploiting the spatial sparsity of the sources [10]. The CS can work even in the case of single snapshot. A CS based multitarget detection method for bistatic MIMO radar is presented in [11]. However, the range cell is not considered in this paper. Furthermore, they assume that there are no array errors in the systems. In this paper, the redundancy of the transmit and receive angles in the same range cell is exploited to construct the sparse model. CS based method is presented to image transmit-receive angle image in the presence of unknown array gain errors for bistatic MIMO radar. The image can be recovered well in the case of small snapshots and large array gain uncertainties.

This paper is organized as follows. The sparse signal model of bistatic MIMO radar with uncertain array gain is presented in Section 2. In Section 3, CS based algorithm is applied to estimate the transmit angle and receive angle of targets in the presence of array gain errors. The effectiveness of the method will be confirmed by simulations in Section 4. Finally, Section 5 concludes the paper.

2. Sparse Model of Bistatic MIMO Radar

The configuration of the bistatic MIMO radar used in this paper is illustrated in Figure 1. An M -transmit/ N -receive (M T/ N R) antenna configuration is considered, and both transmitter and receiver are uniform linear array (ULA). Let the signal transmitted by M -transmitters at every pulse period be $\mathbf{S} \in \mathbb{C}^{M \times L}$, where L is the number of the codes in one pulse period. Assume that the target is at angles (θ_t, θ_r) , where θ_t is the angle of the target with respect to the transmit array (i.e., DOD) and θ_r is the angle with respect to the receive array (DOA). λ denotes the carrier wavelength. In the case of P pixels at location (θ_t, θ_r) , the received signal during the q th pulse period can be expressed as

$$\mathbf{Y}_q = \mathbf{A}_{ur} \mathbf{D}_q \mathbf{A}_{ut}^T \mathbf{S} + \mathbf{E}_q, \quad q = 1, 2, \dots, Q, \quad (1)$$

where $(\cdot)^T$ denote transpose operator. $\mathbf{A}_{ur} = \mathbf{\Gamma}_r \mathbf{A}_r$ and $\mathbf{A}_{ut} = \mathbf{\Gamma}_t \mathbf{A}_t$ are the unknown gain steering matrices of the receive and transmit array, respectively. $\mathbf{\Gamma}_t = \text{diag}[\rho_{t1}, \dots, \rho_{tM}]$ and $\mathbf{\Gamma}_r = \text{diag}[\rho_{r1}, \dots, \rho_{rN}]$ are the diagonal matrices with array gain errors at diagonal elements. $\mathbf{A}_r = [\mathbf{a}_{rp}]_{N \times P}$ and $\mathbf{A}_t = [\mathbf{a}_{tp}]_{M \times P}$ are the receive and transmit steering matrices of P targets, respectively, where $\mathbf{a}_{rp} = [1 \ e^{j(2\pi/\lambda)d_r \sin \theta_{rp}} \ e^{j(2\pi/\lambda)2d_r \sin \theta_{rp}} \ \dots \ e^{j(2\pi/\lambda)(N-1)d_r \sin \theta_{rp}}]^T$ and $\mathbf{a}_{tp} = [1 \ e^{j(2\pi/\lambda)d_t \sin \theta_{tp}} \ e^{j(2\pi/\lambda)2d_t \sin \theta_{tp}} \ \dots \ e^{j(2\pi/\lambda)(M-1)d_t \sin \theta_{tp}}]^T$. d_t and d_r are the ideal interelement space at the transmitter and receiver. $\mathbf{D}_q = \text{diag}(d_1, \dots, d_P)$ is a diagonal matrix composed of target reflection coefficients for the q th pulse period. The noise vector \mathbf{E}_q is assumed to be independent, zero-mean complex Gaussian distribution with $\mathbf{E}_q \sim N^c(0, \sigma_n^2 \mathbf{I}_N)$.

We divide the whole area of interest in some discrete set of angular positions [10]. Let the two-dimensional grid consist of the dictionary of all potential angular position pairs $\Omega = \{(\bar{\theta}_k, \bar{\theta}_l) : (k, l) \in \{1, \dots, G\} \times \{1, \dots, G\}\}$. Then we construct the matrices composed of steering vectors corresponding to each potential source location as its columns: $\Phi_t = [\mathbf{a}_t(\bar{\theta}_1), \dots, \mathbf{a}_t(\bar{\theta}_G)]$ and $\Phi_r = [\mathbf{a}_r(\bar{\theta}_1), \dots, \mathbf{a}_r(\bar{\theta}_G)]$. Let $\mathbf{X}_q \in \mathbb{C}^{G \times G}$ be the matrix of reflection coefficients of the targets at G^2 possible grid point of interest during q th pulse period. Assume that the transmit waveforms are orthogonal to each other; that is, $\mathbf{S} \mathbf{S}^H = \mathbf{I}$. Then the receive signals in (1) after being matched by transmit waveforms can be rewritten as

$$\mathbf{Y}_q = \mathbf{\Gamma}_r \Phi_r \mathbf{X}_q \Phi_t^T \mathbf{\Gamma}_t^T + \bar{\mathbf{E}}_q, \quad q = 1, 2, \dots, Q. \quad (2)$$

$\mathbf{X}_q[k, l]$ is nonzero only if there is pixel of the target at (θ_k, θ_l) . Fortunately, we can recover the image range by range. It can be observed in Figure 1 that the grid points which are in the same range cell should be distributed on the surface of an ellipse with the focuses on receivers and transmitters, respectively. So, only surface of the ellipse has the pixels of the target and any other grid points in the Ω are zeros when we process the data of one range cell. It is clear that \mathbf{X}_q is a sparse matrix in this case. The pixels in the same range cell are virtually sparse because of the redundancy of the transmit and receive angles. This implies that we can recover the scene

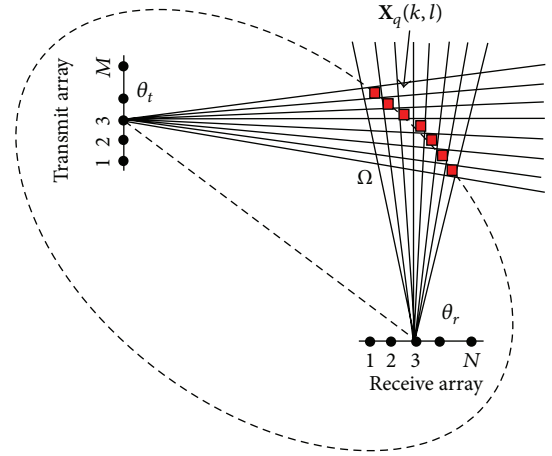


FIGURE 1: Bistatic MIMO radar configuration.

by sparse recovery method even though the actual scene is not sparse.

3. CS Based Sparse Imaging with Array Gain Uncertainties

In this section, we develop the CS based sparse imaging method in the presence of the array gain uncertainties for bistatic MIMO radar imaging.

3.1. Problem Formulation. The radar imaging is an inverse scattering problem. The spatial map of reflectivity can be reconstructed from measurements of scattered electronic fields. To transform our problem into the standard framework of the sparse recovery, we first rewrite (2) as

$$\begin{aligned} \mathbf{y}_q &= \text{vec}(\mathbf{Y}_q) = [(\mathbf{\Gamma}_t \Phi_t) \otimes (\mathbf{\Gamma}_r \Phi_r)] \text{vec}(\mathbf{X}_q) + \bar{\mathbf{e}}_q \\ &= (\mathbf{\Gamma}_t \otimes \mathbf{\Gamma}_r) (\Phi_t \otimes \Phi_r) \mathbf{x}_q + \bar{\mathbf{e}}_q \\ &= \mathbf{\Gamma} \Phi \mathbf{x}_q + \bar{\mathbf{e}}_q, \end{aligned} \quad (3)$$

where \otimes denote Kroneck product; $\mathbf{\Gamma} = \mathbf{\Gamma}_t \otimes \mathbf{\Gamma}_r$ and $\Phi = \Phi_t \otimes \Phi_r$; $\mathbf{x}_q = \text{vec}(\mathbf{X}_q)$ and $\bar{\mathbf{e}}_q = \text{vec}(\bar{\mathbf{E}}_q)$.

When Q pulse periods are transmitted, (3) can be expressed as follows:

$$\mathbf{Y} = \mathbf{\Gamma} \Phi \mathbf{X} + \bar{\mathbf{E}}, \quad (4)$$

where $\mathbf{Y} = [\mathbf{y}_1, \dots, \mathbf{y}_Q]$ and $\mathbf{X} = [\mathbf{x}_1, \dots, \mathbf{x}_Q]$. $\bar{\mathbf{E}}$ is the noise matrix composed by $\bar{\mathbf{e}}_q$; that is, $\bar{\mathbf{E}} = [\bar{\mathbf{e}}_1, \bar{\mathbf{e}}_2, \dots, \bar{\mathbf{e}}_Q]$. Here, what we need to do is to recover matrix \mathbf{X} from the given data \mathbf{Y} .

CS can be used to efficiently reconstruct a signal with a sparse representation. For a given observation matrix \mathbf{Y} and a sensing matrix Φ , $\mathbf{Y} = \Phi \mathbf{X}$. The recovery process is formulated as an l_1 -optimization problem; that is,

$$\begin{aligned} \min \quad & \|\mathbf{X}\|_1, \\ \text{s.t.} \quad & \mathbf{y} = \Phi \mathbf{X}. \end{aligned} \quad (5)$$

However, the CS method in (5) cannot resolve the the problem in model (4) directly as there is an additional unknown array gain error matrix Γ . The optimization problem will lead to a trivial solution if we add Γ directly in (5) without further constraint on Γ . Also, the Gaussian noise $\bar{\mathbf{E}}$ is not considered in the optimization problem in (5), which will degrade the performance of the recovery. What we are interested in is to construct an optimization problem that considers both the array gain uncertainties Γ and the noise $\bar{\mathbf{E}}$. We will achieve the imaging recovery of bistatic MIMO radar with array gain uncertainties by the help of the idea from [12] later.

3.2. Direct CS Method. The problem of recovering the sparse \mathbf{X} from the measurement data \mathbf{Y} is commonly known as multiple measurement vector (MMV) problem in CS [13]. Many sparse recovery methods of this problem have considered effect of the noise. Considering the effect of the noise, the MMV problem can be formulated as

$$(\hat{\mathbf{X}}) = \arg \min \left(\|\mathbf{X}\|_1 + \frac{\mu}{2} \|\mathbf{Y} - \Phi \mathbf{X}\|_F^2 \right), \quad (6)$$

where μ is a balance constant related to the noise.

We rewrite model (4) as

$$\mathbf{Y} = \Phi \mathbf{X} + (\Gamma - \mathbf{I}) \Phi \mathbf{X} + \bar{\mathbf{E}}, \quad (7)$$

where $(\Gamma - \mathbf{I})\Phi \mathbf{X}$ is the error from the array gain uncertainties which can be combined with the noise $\bar{\mathbf{E}}$. So, (7) can be expressed as

$$\mathbf{Y} = \Phi \mathbf{X} + \tilde{\mathbf{E}}, \quad (8)$$

where $\tilde{\mathbf{E}} = (\Gamma - \mathbf{I})\Phi \mathbf{X} + \bar{\mathbf{E}}$. The revised model (8) can be resolved directly by using the optimization problem of CS in (6).

As was known to all, CS methods are sensitive to the noise. So the performance of imaging recovery will degrade when the noise is large even though (6) considers the noise. So, this direct CS method can only be used well with small array gain uncertainties. We will evaluate the performance of this method in Section 4.

3.3. CS Method with Constraint of the Array Gain Uncertain. As the method above regards the array gain uncertainties as noise, the performance will degrade with large array gain errors. In fact, we can regard both the image matrix \mathbf{X} and the array gain uncertain Γ as the estimated value. Considering the CS method, it seems natural to consider the following optimization problem:

$$(\hat{\mathbf{X}}, \hat{\Gamma}) = \arg \min \left(\|\mathbf{X}\|_1 + \frac{\mu}{2} \|\mathbf{Y} - \Gamma \Phi \mathbf{X}\|_F^2 \right). \quad (9)$$

However, the optimization problem in (10) will lead a trivial solution without further constraint on Γ or \mathbf{X} [12]. In order to construct a solvable optimization problem of the CS, the constraint on trace of Γ should be considered.

Considering the noise reduction, we construct the following optimization problem:

$$\begin{aligned} (\hat{\mathbf{X}}, \hat{\Gamma}) &= \arg \min \left(\|\mathbf{X}\|_1 + \frac{\mu}{2} \|\Gamma^{-1} \mathbf{Y} - \Phi \mathbf{X}\|_F^2 \right) \\ \text{s.t. } \text{tr}(\Gamma^{-1}) &= MN, \end{aligned} \quad (10)$$

where μ is a balance coefficient which is selected according to the noise level. The trace of the unknown gain matrix can be derived as

$$\text{tr}(\Gamma^{-1}) = \text{tr}(\Gamma_t^{-1} \otimes \Gamma_r^{-1}) = \text{tr}(\Gamma_t^{-1}) \text{tr}(\Gamma_r^{-1}). \quad (11)$$

The estimate of \mathbf{X} can be obtained by resolving the optimization problem (11) and image of bistatic MIMO radar is then reconstructed.

4. Simulation Results

In this section, we evaluate the performance of the proposed bistatic MIMO radar sparse imaging methods and compare them with the robust Capon beamforming method (RCB) [14]. We consider bistatic MIMO radar with 20 transmit elements and 20 receive elements. Both the transmit and the receive antennas are uniform linear array with half-wavelength space between adjacent elements. The radar will be scanned across a transmit angular region range from 1° to 10° and a receive angular from 1° to 10° . We place two targets in the scene. Assume that two targets are located at angles $[\theta_{t1}, \theta_{r1}] = [8^\circ, 3^\circ]$ and $[\theta_{t2}, \theta_{r2}] = [3^\circ, 8^\circ]$. The number of snapshots is 20 for the sparse recovery methods and 500 for the RCB. The transmit array and receive array gain uncertainties are generated by $\Gamma_t = \text{diag}\{\exp[N(0, \sigma_t^2)]\}$ and $\Gamma_r = \text{diag}\{\exp[N(0, \sigma_r^2)]\}$, where σ_t and σ_r are the parameter governing the array gain. $N(0, \sigma_t^2)$ denotes the Gaussian distribution. We select the balance coefficients $\mu = 1$ in both the direct CS and the constraint CS methods.

Figure 2 shows the results of the image recovery using the proposed method with small array gain uncertainties; that is, $\sigma_t = \sigma_r = 0.1$. It can be observed that both the proposed methods and RCB method can recover the image. The direct CS and constraint CS obtain almost equal performance and the performance of RCB is better than the one of proposed method. However, RCB needs very large amount of samples to enable the algorithm to work. The results of the image recovery with large array gain uncertainties are plotted in Figure 3. It is shown that the recovery performance of constraint CS method is better than that of direct CS. The reason had been discussed in Section 3.2. The performance of both of the CS methods is better than that of RCB method even though the RCB method uses 500 samples compared to 20 samples of the CS method. It implies that the direct CS method is suitable to imaging recovery for bistatic MIMO radar with large array gain errors in the case of small samples.

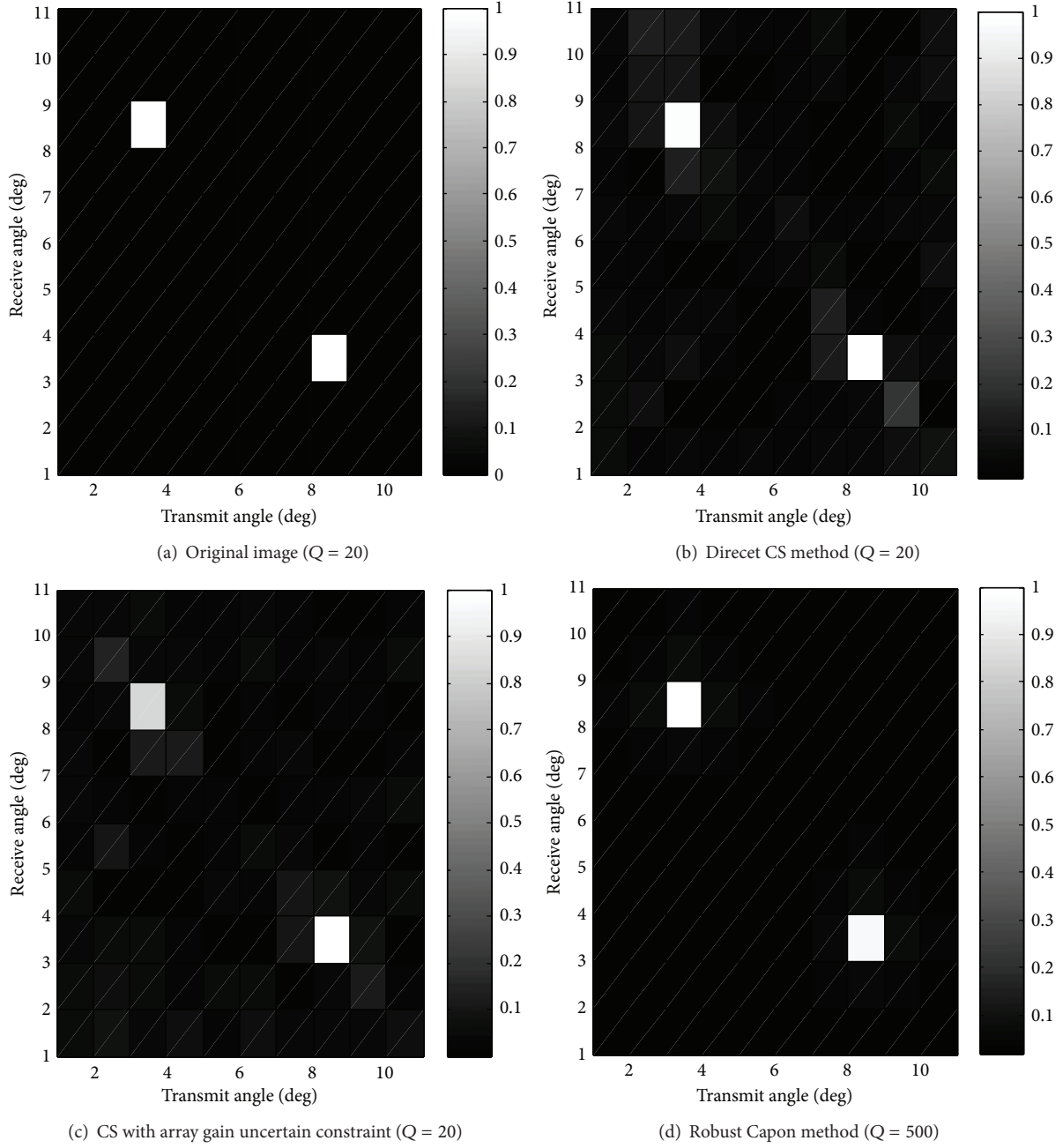


FIGURE 2: The performance of the proposed method with small array gain uncertain ($M = N = 20$, $[\theta_{t1}, \theta_{r1}] = [8^\circ, 3^\circ]$, $[\theta_{t1}, \theta_{r1}] = [3^\circ, 8^\circ]$, $Q = 20$, SNR = 10 dB, $\sigma_t = \sigma_r = 0.1$).

We defined the performance recovery coefficient (RPC) γ to evaluate the performance of the imaging. The RPC is defined as

$$\gamma = \frac{|x'_1 x_2|}{\|x_1\|_2 \|x_2\|_2}, \quad (12)$$

where x_1 represents the estimated target coefficient and x_2 represents the true target coefficient. RPC describes the similarity of the true image and the recovering one.

Figure 4 plots the variation of the RPC of the CS with array gain uncertain constraint, direct CS, and the RCB method with array gain errors. It is shown that the performance of RCB is better than that of the CS with array gain uncertain constraint and direct CS methods in small array gain error case. The performance of direct CS is better than that of CS with array gain uncertain constraint in the case of small errors. However, the performance of the CS with array gain uncertain constraint method is stable in all of array errors. When the array gain errors are large, the performance of

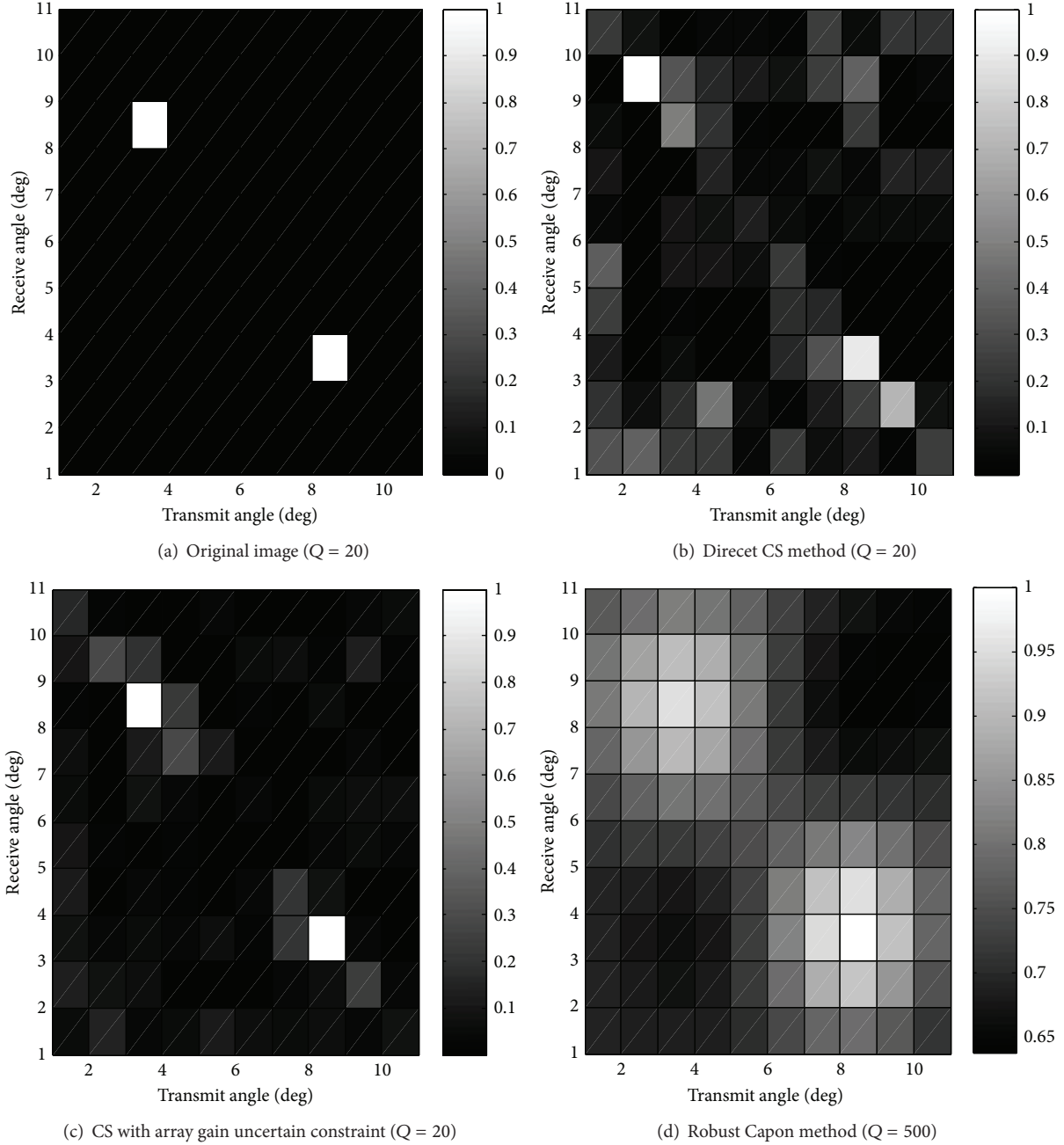


FIGURE 3: The performance of the proposed method with large array gain uncertain ($M = N = 20$, $[\theta_{t1}, \theta_{r1}] = [8^\circ, 3^\circ]$, $[\theta_{t1}, \theta_{r1}] = [3^\circ, 8^\circ]$, $Q = 20$, $\text{SNR} = 10$ dB, $\sigma_t = \sigma_r = 0.8$).

the error constraint CS is the best. The results confirm that the CS with array gain uncertain constraint method is suitable to imaging recovery for bistatic MIMO radar with large array gain errors in the case of small samples.

5. Conclusions

Sparse recovery based transmit-receive angle imaging scheme is proposed for bistatic MIMO with array gain uncertainties in this paper. The redundancy of the transmit

and receive angles in the same range cell is exploited to construct the sparse model. CS based algorithm with consideration of both transmit and receive array gain errors is presented for image recovery. Simulation results show that the transmit-receive angle image can be recovered well in bistatic MIMO radar with small number of snapshots in the case of large array gain errors by using sparse recovery based method. Further works should be done to develop sparse recovery based imaging method for bistatic MIMO radar when both array gain and phase errors exist.

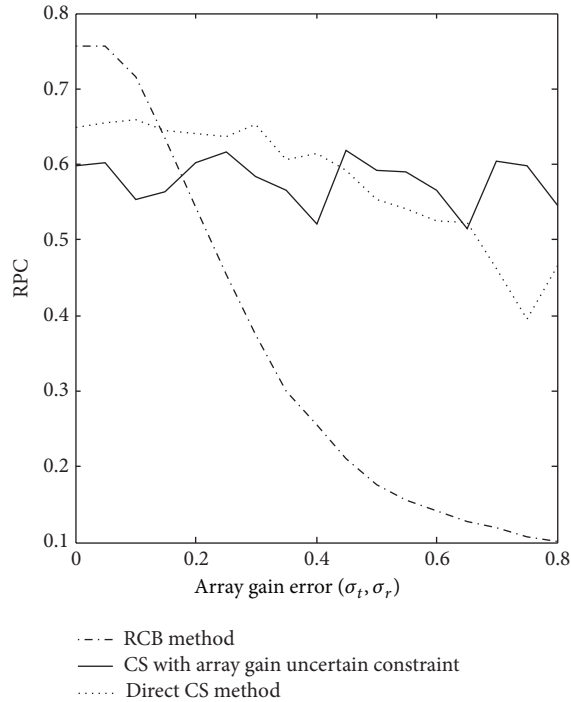


FIGURE 4: Comparison of the performance of sparse recovery method with the RCB.

Conflict of Interests

The authors declare that they have no competing interests.

Acknowledgments

This study has been supported by the National Natural Science Foundation of China under Contract no. 61271292. The authors are grateful to the anonymous referees for their constructive comments and suggestions in improving the quality of this paper.

References

- [1] A. M. Haimovich, R. S. Blum, and L. J. Cimini, "MIMO radar with widely separated antennas," *IEEE Signal Processing Magazine*, vol. 25, no. 1, pp. 116–129, 2008.
- [2] J. Li and P. Stoica, "MIMO radar with colocated antennas," *IEEE Signal Processing Magazine*, vol. 24, no. 5, pp. 106–114, 2007.
- [3] H. Yan, J. Li, and G. Liao, "Multitarget identification and localization using bistatic MIMO radar systems," *EURASIP Journal on Advances in Signal Processing*, vol. 2008, Article ID 283483, 8 pages, 2008.
- [4] M. Jin, G. Liao, and J. Li, "Joint DOD and DOA estimation for bistatic MIMO radar," *Signal Processing*, vol. 89, no. 2, pp. 244–251, 2009.
- [5] D. Nion and N. D. Sidiropoulos, "Adaptive algorithms to track the PARAFAC decomposition of a third-order tensor," *IEEE Transactions on Signal Processing*, vol. 57, no. 6, pp. 2299–2310, 2009.
- [6] M. L. Bencheikh, Y. Wang, and H. He, "Polynomial root finding technique for joint DOA DOD estimation in bistatic MIMO radar," *Signal Processing*, vol. 90, no. 9, pp. 2723–2730, 2010.
- [7] X. Zhang, Z. Xu, L. Xu, and D. Xu, "Trilinear decomposition-based transmit angle and receive angle estimation for multiple-input multiple-output radar," *IET Radar, Sonar, Navigation*, vol. 5, no. 6, pp. 626–631, 2011.
- [8] Y. D. Guo, Y. S. Zhang, and N. N. Tong, "ESPRIT-like angle estimation for bistatic MIMO radar with gain and phase uncertainties," *Electronics Letters*, vol. 47, no. 17, pp. 996–997, 2011.
- [9] J. Li, X. Zhang, R. Cao, and M. Zhou, "Reduced-dimension music for angle and array gain-phase error estimation in bistatic MIMO radar," *IEEE Communication Letters*, vol. 17, no. 3, pp. 443–446, 2013.
- [10] D. Malioutov, M. Çetin, and A. S. Willsky, "A sparse signal reconstruction perspective for source localization with sensor arrays," *IEEE Transactions on Signal Processing*, vol. 53, no. 8, pp. 3010–3022, 2005.
- [11] M. M. Hyder and K. Mahata, "A joint sparse signal representation perspective for target detection using bistatic MIMO radar system," in *Proceedings of the 17th International Conference on Digital Signal Processing (DSP '11)*, pp. 1–5, Corfu, Greece, July 2011.
- [12] R. Gribonval, G. Chardon, and L. Daudet, "Blind calibration for compressed sensing by convex optimization," in *Proceedings of the IEEE Conference on Acoustic, Speech and Signal Processing (ICASSP '12)*, pp. 2713–2716, Kyoto, Japan, March 2012.
- [13] S. F. Cotter, B. D. Rao, K. Engan, and K. Kreutz-Delgado, "Sparse solutions to linear inverse problems with multiple measurement vectors," *IEEE Transactions on Signal Processing*, vol. 53, no. 7, pp. 2477–2488, 2005.
- [14] J. Li and P. Stoica, *Robust Adaptive Beamforming*, John Wiley & Sons, Hoboken, NJ, USA, 2006.

Research Article

3D Imaging Algorithm for Down-Looking MIMO Array SAR Based on Bayesian Compressive Sensing

Xiaozhen Ren,¹ Lina Chen,² and Jing Yang¹

¹ College of Information Science and Engineering, Henan University of Technology, Zhengzhou 450001, China

² Textile College, Henan Institute of Engineering, Zhengzhou 451191, China

Correspondence should be addressed to Xiaozhen Ren; rxz235@163.com

Received 21 February 2014; Accepted 17 April 2014; Published 11 May 2014

Academic Editor: Wei Xu

Copyright © 2014 Xiaozhen Ren et al. This is an open access article distributed under the Creative Commons Attribution License, which permits unrestricted use, distribution, and reproduction in any medium, provided the original work is properly cited.

Down-looking MIMO array SAR can reconstruct 3D images of the observed area in the inferior of the platform of the SAR and has wide application prospects. In this paper, a new strategy based on Bayesian compressive sensing theory is proposed for down-looking MIMO array SAR imaging, which transforms the cross-track imaging process of down-looking MIMO array SAR into the problem of sparse signal reconstruction from noisy measurements. Due to account for additive noise encountered in the measurement process, high quality image can be achieved. Simulation results indicate that the proposed method can provide better resolution and lower sidelobes compared to the conventional method.

1. Introduction

Traditional synthetic aperture radar (SAR) is a microwave sensor which can reconstruct two-dimensional (2D) images of the observed area with weather independence and all-day operation capabilities [1, 2]. However, traditional 2D SAR works in side-looking mode and often meets with shading and lay over effects in urban and mountain areas. Compared with 2D SAR, 3D SAR has distinct advantage in estimation of forest height, 3D digital maps, complex terrain mapping, and so on. Multibaseline SAR tomography is an advanced 3D SAR imaging mode, which forms an additional synthetic aperture in the height direction. Therefore, it has resolving capability along this dimension. Unfortunately, for the current SAR tomography, it is almost impossible to avoid an uneven track distribution in repeat-pass data acquisition, which is just the main reason for the strong ambiguity in height [3, 4].

Down-looking array SAR is an innovative imaging mode, which obtains range resolution by pulse compression, azimuth resolution by virtual aperture synthesis with platform movement, and cross-track resolution by a linear array antenna [5–7]. Down-looking array SAR can overcome restrictions of shading and lay over effects in side-looking SAR and also avoid the height ambiguity problem in SAR

tomography caused by the uneven track distribution. However, in order to avoid the grating lobe effect in the cross-track direction, a large number of antenna elements are required, which increase the cost and complexity of the equipment. Therefore, multiple-input-multiple-output (MIMO) antenna array is often used in down-looking array SAR, which can reduce the number of real antenna elements largely for a given size of antenna array [8–10]. The common methods used for down-looking MIMO array SAR imaging are usually based on matched filter, which often suffer from low resolution and high sidelobe interference in the images [7, 8]. Moreover, the cross-track resolution is limited by the length of linear array. Hence, high resolution imaging algorithms are desired.

In recent years, Bayesian compressive sensing (BCS) has caused widespread concern, showing significant advantages to sparse signal reconstruction [11]. BCS methods provide certain improvements compared with norm-based CS methods in low noise level, by exploiting the sparseness prior distribution of the image scene. In addition, the Bayesian framework takes into account the additive noise encountered when implementing compressed sampling. Therefore, some BCS based methods for SAR applications have been concerned about recently [12, 13]. As the 3D illuminated scene contains only a very small strong scattering centers compared

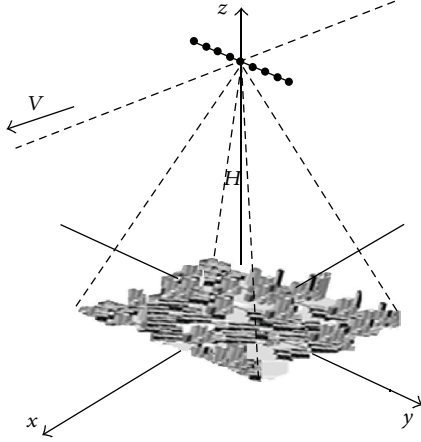


FIGURE 1: Geometry of down-looking MIMO array SAR.

with the total space cells, representing strong spatial sparsity in high frequency radar application, we propose a new 3D imaging algorithm for down-looking MIMO array SAR based on BCS.

The rest of the paper is organized as follows. Section 2 presents the geometry and principle of down-looking MIMO array SAR system. In Section 3, a new 3D imaging algorithm for down-looking MIMO array SAR is described in detail. The performance of the method is investigated in Section 4. Finally, Section 5 gives a brief conclusion.

2. Down-Looking MIMO Array SAR

2.1. Geometrical Model. The geometry of down-looking MIMO array SAR is shown in Figure 1. x , y , and r denote the azimuth, cross-track, and slant range direction, respectively. The radar platform flies along the x -axis corresponding to azimuth direction, with velocity v at height H . The thinned linear antenna array, which contains M transmitting antenna elements and N receiving antenna elements, is mounted in the cross-track direction along the wings. The transmitting antenna elements are located at the tips with the distance d , the receiving antenna elements are centered at the y -axis with spacing $Md/2$, and the distance between the transmitting and receiving antenna elements is $d/2$. The thinned linear antenna array works in the time division mode. Each time, only one transmitting antenna element transmits signal and all the receiving antenna elements receive echo simultaneously. The transmitting antenna elements work sequentially and an aperture synthesis period is acquired until all the transmitting antenna elements have worked once. According to the principle of equivalent phase center, the thinned linear array formed by the above positions and work mode is equal to a fully distributed virtual uniform linear array [5, 10]. The virtual antenna array is composed of MN virtual elements and works in self-transmitting and receiving mode. That is to say, each virtual antenna element transmits and receives signal by itself. These virtual antenna elements are uniform distributed along the wings and centered at the y -axis. Each virtual antenna element is located at the mean position of a

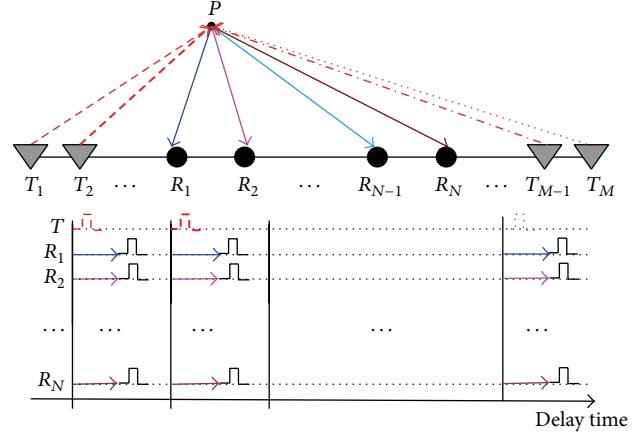


FIGURE 2: Transmitting and receiving order of down-looking MIMO array SAR.

real single transmitting element and a real single receiving element, and the distance between individual virtual antenna elements is $d/2$. Figure 2 shows the transmitting and the receiving order of each antenna element for a down-looking MIMO array SAR.

2.2. Equivalent Phase Error Compensation. Consider the data acquisition shown in Figure 1. At the slow time t_m , the position of the i th transmitting antenna element is given by (x, y_{Ti}, H) , where $x = vt_m$ is the azimuth position, and y_{Ti} is the cross-track position of the i th transmitting antenna element. The position of the j th receiving antenna element is given by (x, y_{Rj}, H) , where y_{Rj} is the cross-track position of the j th receiving antenna element. For a point scatterer P positioned at (x_p, y_p, z_p) , the transmitting and receiving paths R_{Ti} and R_{Rj} are given by

$$\begin{aligned} R_{Ti} &= \sqrt{(x - x_p)^2 + (y_{Ti} - y_p)^2 + (H - z_p)^2} \\ &= \sqrt{(y_{Ti} - y_p)^2 + R_p^2}, \\ R_{Rj} &= \sqrt{(x - x_p)^2 + (y_{Rj} - y_p)^2 + (H - z_p)^2} \\ &= \sqrt{(y_{Rj} - y_p)^2 + R_p^2}, \end{aligned} \quad (1)$$

where

$$R_p = \sqrt{(x - x_p)^2 + (H - z_p)^2}. \quad (2)$$

Then the complete travelling path of the wave from the i th transmitting antenna element to point scatterer P to the j th receiving antenna element is given by

$$R_{i,j} = R_{Ti} + R_{Rj} = \sqrt{(y_{Ti} - y_p)^2 + R_p^2} + \sqrt{(y_{Rj} - y_p)^2 + R_p^2}. \quad (3)$$

From (2) we can get that the complete travelling path contains two square roots, which will lead to complex computation for the following imaging process. According to the principle of equivalent phase center, the above complete travelling path can be equal to the dual echo paths from the virtual antenna element located at $y = (y_{Ti} + y_{Rj})/2$ to point scatterer P [5]. And the equivalent echo path can be written as

$$R = \sqrt{(x - x_p)^2 + (y - y_p)^2 + (H - z_p)^2} \\ = \sqrt{(y - y_p)^2 + R_p^2}. \quad (4)$$

Then, the phase difference between the virtual antenna element and the reality antenna element is given by

$$\Delta\varphi = \frac{2\pi}{\lambda} (R_{i,j} - 2R) \\ = \frac{2\pi}{\lambda} \left(\sqrt{(y_{Ti} - y_p)^2 + R_p^2} + \sqrt{(y_{Rj} - y_p)^2 + R_p^2} \right. \\ \left. - 2\sqrt{(y - y_p)^2 + R_p^2} \right) \\ \approx \frac{\pi(y_{Ti} - y_{Rj})^2}{2\lambda R_p}. \quad (5)$$

When the scatterers are located at the far field, the phase difference $\Delta\varphi$ is approximate to zero. Otherwise, the phase compensation should be implemented before the image processing. From (5) it can be seen that the compensated phase varies with R_p ; in practice we use the center of view field as reference point to compensate the whole view field.

Furthermore, the down-looking MIMO array SAR works in the time division mode and the virtual antenna elements obtained from different pulse repetition period are not in a straight line with the movement of the platform. Therefore, in order to obtain a fully distributed virtual uniform linear array, the motion compensation should be implemented. The compensated phase caused by the overtake or lag phases owing to the position difference of the antenna elements is given by

$$\Delta\varphi_{l,k} = \frac{4\pi}{\lambda} \left(\left(\left(\frac{Mv}{\text{PRF}} \left(l - \frac{L}{2} \right) + \Delta x_k - x_p \right)^2 \right. \right. \\ \left. \left. + (y - y_p)^2 + (H - z_p)^2 \right)^{1/2} \right. \\ \left. - \left(\left(\frac{Mv}{\text{PRF}} \left(l - \frac{L}{2} \right) - x_p \right)^2 \right. \right. \\ \left. \left. + (y - y_p)^2 + (H - z_p)^2 \right)^{1/2} \right), \\ l = 1, 2, \dots, L; k = 1, 2, \dots, M, \quad (6)$$

where L is the azimuth sample number and Δx_k is the move spacing between the k th and the first transmitting antenna element in the azimuth direction. v is the velocity of the platform and PRF is the pulse repetition frequency.

After the process above, the collected data of down-looking MIMO array SAR can be regarded as received by the fully distributed virtual linear array.

3. Three-Dimensional Imaging Algorithm for Down-Looking MIMO Array SAR

Based on the principle of equivalent phase center, the thinned linear array formed by the time division mode can be equal to a virtual linear array, and each virtual antenna element transmits and receives signal by itself. The linear frequency modulated pulse signal transmitted by the m th virtual antenna element is given by

$$s(\hat{t}) = \text{rect}\left(\frac{\hat{t}}{T_r}\right) \exp\left[j2\pi\left(f_c\hat{t} + \frac{1}{2}\gamma\hat{t}^2\right)\right], \quad (7)$$

where \hat{t} denotes the fast time, T_r denotes the pulse width, f_c is the carrier frequency, γ is the chirp rate, and $\text{rect}(\cdot)$ is the unit rectangular function.

For an arbitrary point scatterer positioned at $P(x_p, y_p, z_p)$, the echo signal received by the m th virtual antenna element can be expressed as

$$s_1(\hat{t}, \tau, y_m) = \text{rect}\left(\frac{\hat{t} - 2R/c}{T_r}\right) \text{rect}\left(\frac{\tau - \tau_p}{T_a}\right) \\ \times \exp\left[j\pi\gamma\left(\hat{t} - \frac{2R}{c}\right)^2 - j\frac{4\pi}{\lambda}R\right], \quad (8)$$

where τ denotes the azimuth time, $\tau_p = x_p/v$ is the azimuth time of the point scatterer P , c is the light velocity, T_a is the observing duration, λ is the wavelength, and R is the instantaneous distance between the m th virtual antenna element and the point scatterer

$$R = \sqrt{(v\tau - x_p)^2 + (y_m - y_p)^2 + (H - z_p)^2} \\ \approx R_p + \frac{(v\tau - x_p)^2}{2R_p} + \frac{y_m^2 - 2y_m y_p}{2R_p}, \quad (9)$$

where $R_p = \sqrt{(H - z_p)^2 + y_p^2}$ and y_m is the cross-track position of the m th virtual antenna element.

3.1. Range Compression. Transform the signal expressed in (8) into the range frequency domain

$$S_1(f_r, \tau, y_m) \\ = \text{rect}\left(\frac{f_r}{T_r\gamma}\right) \text{rect}\left(\frac{\tau - \tau_p}{T_a}\right) \\ \times \exp\left(-j\frac{\pi f_r^2}{\gamma}\right) \exp\left(-j\frac{4\pi f_r}{c}R\right) \exp\left(-j\frac{4\pi}{\lambda}R\right), \quad (10)$$

where f_r is range frequency.

The matched filter function for the range compression is given by

$$H_1(f_r) = \text{rect}\left(\frac{f_r}{T_r\gamma}\right) \exp\left(j\frac{\pi f_r^2}{\gamma}\right). \quad (11)$$

After the range compression, the received signal can be written as

$$s_2(\hat{t}, \tau, y_m) = \text{rect}\left(\frac{\tau - \tau_p}{T_a}\right) \text{sinc}\left[T_r\gamma\left(\hat{t} - \frac{2R_c}{c}\right)\right] \times \exp\left(-j\frac{4\pi R}{\lambda}\right). \quad (12)$$

3.2. Azimuth Compression. From (9) and (12) we get that the distance between the antenna element and the scatterer varies with the azimuth position of the radar platform, which leads to the coupling of the envelope in the range-azimuth plane. Therefore, the range migration in the azimuth direction should be removed first before the azimuth compression. And the correction function for the range migration can be derived from (9)

$$H_2(f_r, \tau) = \exp\left(j\frac{2\pi(v\tau - x_p)^2}{cR_p}f_r\right). \quad (13)$$

Transform the signal expressed in (12) to the range frequency domain and correct the range migration using $H_2(f_r, \tau)$. Then, after the range inverse Fourier transform, the signal becomes

$$s_3(\hat{t}, \tau, y_m) = \text{rect}\left(\frac{\tau - \tau_p}{T_a}\right) \text{sinc}\left[T_r\gamma\left(\hat{t} - \frac{2R_c}{c}\right)\right] \times \exp\left(-j\frac{4\pi R_p}{\lambda}\right) \cdot \exp\left[-j\frac{2\pi v^2(\tau - \tau_p)^2}{\lambda R_p}\right] \times \exp\left[-j\frac{2\pi(y_m^2 - 2y_m y_p)}{\lambda R_p}\right], \quad (14)$$

where $R_c = R_p + (y_m^2 - 2y_m y_p)/2R_p$.

An azimuth Fourier transform is then performed on each range gate to transform the data into the range time-azimuth frequency domain, and the signal becomes

$$S_3(\hat{t}, f_a, y_m) = \text{rect}\left(\frac{f_a}{\gamma_a T_a}\right) \text{sinc}\left[T_r\gamma\left(\hat{t} - \frac{2R_c}{c}\right)\right] \times \exp\left[-j\frac{2\pi(y_m^2 - 2y_m y_p)}{\lambda R_p}\right] \cdot \exp\left(-j\frac{4\pi R_p}{\lambda}\right) \times \exp\left[j\frac{\pi f_a^2}{\gamma_a}\right] \exp(-j2\pi\tau_p f_a), \quad (15)$$

where $\gamma_a = 2v^2/\lambda R_p$. Then a multiplication of the signal with the azimuth matched filter function $H_3(f_a)$ is performed, where

$$H_3(f_a) = \exp\left(-j\frac{\pi f_a^2}{\gamma_a}\right). \quad (16)$$

Then, we get the azimuth compressed signal by performing inverse Fourier transform in the azimuth direction

$$s_4(\hat{t}, \tau, y_m) = \text{sinc}\left[T_r\gamma\left(\hat{t} - \frac{2R_c}{c}\right)\right] \text{sinc}\left[T_a\gamma_a(\tau - \tau_p)\right] \cdot \exp\left[-j\frac{2\pi(y_m^2 - 2y_m y_p)}{\lambda R_p}\right] \exp\left(-j\frac{4\pi R_p}{\lambda}\right). \quad (17)$$

3.3. Cross-Track Compression. From (17) it can be seen that the distance between the antenna element and the scatterer also varies with the cross-track position of the antenna element. Therefore, the range migration in the cross-track direction should be removed before the cross-track compression. And the amount of the range migration to be corrected can be given by (9)

$$\Delta R_c = \frac{y_m^2 - 2y_m y_p}{2R_p}. \quad (18)$$

Transform the signal expressed in (17) into the range frequency domain, and correct the range migration in the range frequency domain. Then the signal becomes

$$s_4(\hat{t}, \tau, y_m) = \text{sinc}\left[T_r\gamma\left(\hat{t} - \frac{2R_p}{c}\right)\right] \text{sinc}\left[T_a\gamma_a(\tau - \tau_p)\right] \cdot \exp\left(-j\frac{2\pi y_m^2}{\lambda R_p}\right) \exp\left(j\frac{4\pi y_m y_p}{\lambda R_p}\right) \exp\left(-j\frac{4\pi R_p}{\lambda}\right). \quad (19)$$

The first phase term in (19) represents a quadratic distortion, which can be compensated by

$$H_4(y_m) = \exp\left(j\frac{2\pi y_m^2}{\lambda R_p}\right). \quad (20)$$

In high frequency radar application, the interest scene can be modeled by a limited number of strong scattering centers reflecting impinging electromagnetic waves isotropically to all receivers, representing strong spatial sparsity [14]. Therefore, the cross-track imaging process of down-looking MIMO array SAR can be transformed into the problem of sparse signal reconstruction from noisy measurements. After the 2D imaging process in the range and azimuth directions, the signal in the range-azimuth cell corresponding to $(\hat{t} = 2R_p/c, \tau = \tau_p)$ by neglecting the constant phase term of (19) can be written as

$$s_5(\hat{t}, \tau, y_m) = \sum_{p=1}^P \sigma_p(\hat{t}, \tau) \exp(j2\pi f_p y_m), \quad (21)$$

where $\sigma_p(\hat{t}, \tau)$ and $f_p = 2y_p/\lambda R_p$ denote the backward scattering coefficient and the frequency of the p th point scatterer, respectively.

For numerical analysis, (21) can be described by discrete system model

$$\mathbf{s} = \Phi \boldsymbol{\sigma}, \quad (22)$$

where $\mathbf{s} = [s_5(\hat{t}, \tau, y_1), s_5(\hat{t}, \tau, y_2), \dots, s_5(\hat{t}, \tau, y_{MN})]^T$ is the signal vector corresponding to the MN virtual antenna elements, $\boldsymbol{\sigma} = [\sigma_1(\hat{t}, \tau), \sigma_2(\hat{t}, \tau), \dots, \sigma_P(\hat{t}, \tau)]^T$ is the complex-valued scatter coefficient vector in the cross-track direction, and the matrix Φ can be constructed as

$$\Phi = [\phi_1, \phi_2, \dots, \phi_P, \dots, \phi_P], \quad (23)$$

where

$$\phi_p = [\exp(j2\pi f_p y_1), \exp(j2\pi f_p y_2), \dots, \exp(j2\pi f_p y_{MN})]^T, \quad (24)$$

where $(\cdot)^T$ represents the transpose operation.

In the more realistic case some noise is added on the measurements

$$\mathbf{s} = \Phi \boldsymbol{\sigma} + \mathbf{n} \quad (25)$$

with \mathbf{n} a complex Gaussian vector with zero mean and power σ_n^2 .

Then, the Bayesian compressive sensing method is employed to estimate the $\boldsymbol{\sigma}$. From the aspect of denoising, Laplace distribution is often used as the sparseness prior [15]. Hence, the probability distribution function of $\boldsymbol{\sigma}$ can be given by

$$\begin{aligned} p(\boldsymbol{\sigma} | \sigma_\delta) &= \prod_{i=1}^P p(\sigma_i | \sigma_\delta) \\ &= \prod_{i=1}^P \frac{1}{\sqrt{2}\sigma_\delta} \exp\left(-\frac{\sqrt{2}\sigma_i}{\sigma_\delta}\right), \end{aligned} \quad (26)$$

where σ_δ is the scale parameter of the Laplace distribution.

And the probability density function of Gaussian noise \mathbf{n} is given by

$$p(\mathbf{n} | \sigma_n^2) = \left(\frac{1}{2\pi\sigma_n^2}\right)^{MN} \exp\left(-\frac{\|\mathbf{n}\|_2^2}{2\sigma_n^2}\right), \quad (27)$$

where $\|\cdot\|_2$ denotes the l_2 norm.

Therefore, the likelihood function of the received data \mathbf{s} is

$$p(\mathbf{s} | \boldsymbol{\sigma}, \sigma_n^2) = \left(\frac{1}{2\pi\sigma_n^2}\right)^{MN} \exp\left\{-\frac{\|\mathbf{s} - \Phi \boldsymbol{\sigma}\|_2^2}{2\sigma_n^2}\right\}. \quad (28)$$

Based on Bayesian theory, the maximum a posteriori (MAP) estimator is used to estimate $\boldsymbol{\sigma}$ as

$$\begin{aligned} \hat{\boldsymbol{\sigma}} &= \arg \max [p(\boldsymbol{\sigma} | \mathbf{s})] \\ &= \arg \max [p(\mathbf{s} | \boldsymbol{\sigma}, \sigma_n^2) \cdot p(\boldsymbol{\sigma} | \sigma_\delta)]. \end{aligned} \quad (29)$$

Apparently, the MAP solution of $\boldsymbol{\sigma}$ can be estimated by maximizing the log posterior of $\boldsymbol{\sigma}$ as

$$\begin{aligned} \hat{\boldsymbol{\sigma}} &= \arg \max J(\boldsymbol{\sigma}) \\ &= \arg \max [\ln p(\mathbf{s} | \boldsymbol{\sigma}, \sigma_n^2) + \ln p(\boldsymbol{\sigma} | \sigma_\delta)] \\ &= \arg \max \left[-\frac{1}{2\sigma_n^2} \|\mathbf{s} - \Phi \boldsymbol{\sigma}\|_2^2 - \frac{\sqrt{2}}{\sigma_\delta} \sum_{i=1}^P \sigma_i \right] \\ &= \arg \min [\|\mathbf{s} - \Phi \boldsymbol{\sigma}\|_2^2 + \mu \|\boldsymbol{\sigma}\|_1], \end{aligned} \quad (30)$$

where $\mu = 2\sqrt{2}\sigma_n^2/\sigma_\delta$.

Then, the quasi-Newton iterative method with Hessian update scheme is used to solve the optimization problem [16]. The gradient of the objective function $J(\boldsymbol{\sigma})$ with respect to $\boldsymbol{\sigma}$ is given by

$$\nabla J(\boldsymbol{\sigma}) = \tilde{H}(\boldsymbol{\sigma}) \boldsymbol{\sigma} - 2\Phi^H \mathbf{s}, \quad (31)$$

where

$$\begin{aligned} \tilde{H}(\boldsymbol{\sigma}) &= 2\Phi^H \Phi + \mu \Lambda(\boldsymbol{\sigma}), \\ \Lambda(\boldsymbol{\sigma}) &= \text{diag} \left\{ (|\langle \boldsymbol{\sigma} \rangle_i|^2 + \varepsilon)^{-1/2} \right\}. \end{aligned} \quad (32)$$

Here $\tilde{H}(\boldsymbol{\sigma})$ is used as an approximation to the Hessian, and $\boldsymbol{\sigma}$ can be obtained from the following quasi-Newton iteration:

$$\hat{\boldsymbol{\sigma}}^{(n+1)} = \hat{\boldsymbol{\sigma}}^{(n)} - \gamma [\tilde{H}(\hat{\boldsymbol{\sigma}}^{(n)})]^{-1} \nabla J(\hat{\boldsymbol{\sigma}}^{(n)}), \quad (33)$$

where γ is the step size. After substituting (31) into (33), we obtain the following iterative algorithm:

$$\tilde{H}(\hat{\boldsymbol{\sigma}}^{(n)}) \hat{\boldsymbol{\sigma}}^{(n+1)} = (1 - \gamma) \tilde{H}(\hat{\boldsymbol{\sigma}}^{(n)}) \hat{\boldsymbol{\sigma}}^{(n)} + 2\gamma \Phi^H \mathbf{s}. \quad (34)$$

The iteration is stopped when $\|\hat{\boldsymbol{\sigma}}^{(n+1)} - \hat{\boldsymbol{\sigma}}^{(n)}\|_2 < \zeta$, where ζ is a small positive constant.

Then, the 3D image of down-looking MIMO array SAR can be obtained until all the range-azimuth cells have been processed using the same procedure.

In conclusion, the 3D imaging processing flow of the proposed method for down-looking MIMO array SAR can be shown in Figure 3.

3.4. Estimation of the Parameters σ_n^2 and σ_δ . It is clear that the imaging performance of the proposed method is related to the correct selection of the noise level σ_n^2 . Therefore, the noise level must be estimated accurately. Because the noise always distributes evenly and there are many range cells containing noise only in down-looking SAR imaging, the noise level estimation is available by setting an energy-based threshold to select the noise cells [17]. The threshold is given by

$$\text{thres} = E_m + \left[\sum_{i=1}^{PQ} \frac{(E_i - E_m)^2}{PQ} \right]^{1/2}, \quad (35)$$

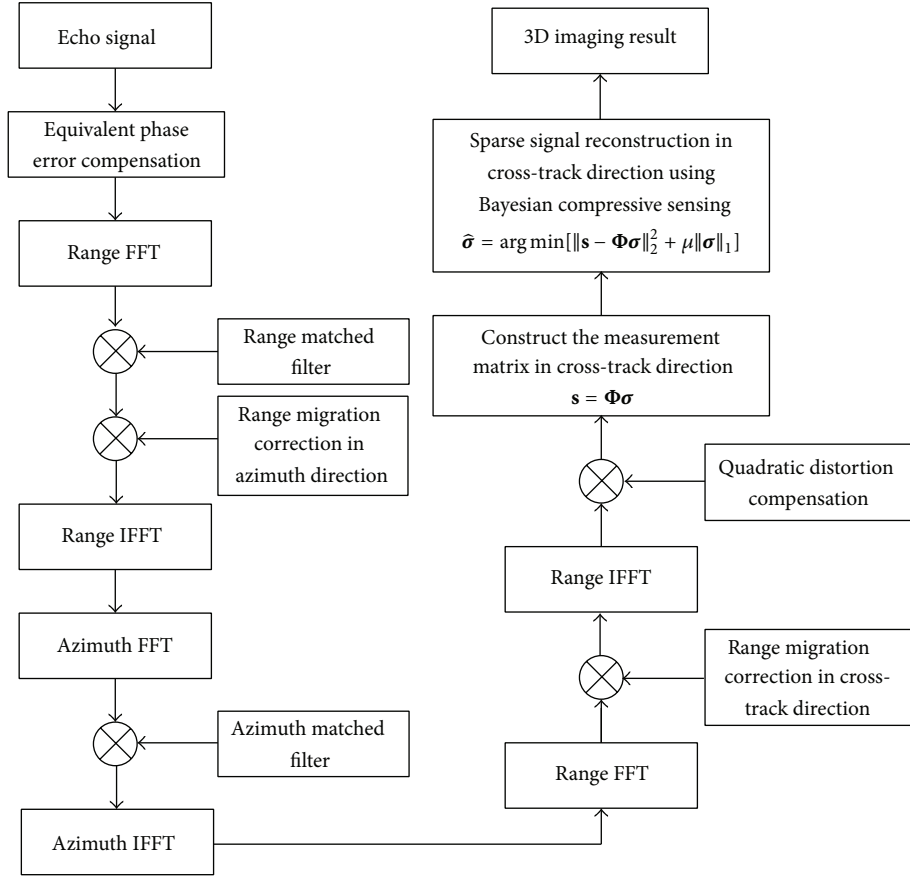


FIGURE 3: The flowchart of proposed method for down-looking MIMO array SAR imaging.

where E_i is the energy of the i th range cell and E_m denotes the mean energy of all range cells. If the energy of a range cell is below the threshold, this range cell is selected as noise cell. Then, the energy of all the selected cells can be used as the noise level σ_n^2 .

In addition, the maximum likelihood estimate method is used to choose the objective statistical parameter σ_δ . According to (26), the log-likelihood function for the Laplace distribution can be written as

$$\ell(\sigma_\delta | \sigma_1, \sigma_2, \dots, \sigma_P) = -P \ln \sqrt{2}\sigma_\delta - \sum_{i=1}^P \frac{\sqrt{2}\sigma_i}{\sigma_\delta}. \quad (36)$$

Maximizing the log likelihood function (36) with respect to σ_δ produces the following equation:

$$\hat{\sigma}_\delta = \frac{1}{P} \sum_{i=1}^P \sqrt{2}\sigma_i. \quad (37)$$

From (37) it is clear that we can average the estimates of all pixel values to obtain the estimation of the statistical parameter σ_δ .

TABLE 1: Parameters used for simulation.

Parameter	Value
Carrier frequency	37.5 GHz
Pulse bandwidth	300 MHz
Pulse repetition frequency	1024 Hz
Chirp duration	1.0 μ s
Radar height	500 m
Radar velocity	50 m/s
Number of transmitting antenna elements	4
Number of receiving antenna elements	32
Azimuth resolution	0.4 m
Range resolution	0.5 m
Cross-track resolution	0.4 m

4. Simulation Results

In this section, point target simulation is carried out to verify the validity of the proposed imaging algorithm. The main parameters used for simulation are listed in Table 1.

Suppose that there are five point targets located at the scene with the azimuth-range-cross track values equal to (0, 485, 0), (8, 495, 20), (8, 495, -20), (-8, 495, 20), and (-8, 495, -20), respectively. The distributions of the five point targets are shown in Figure 4(a). After raw data generation

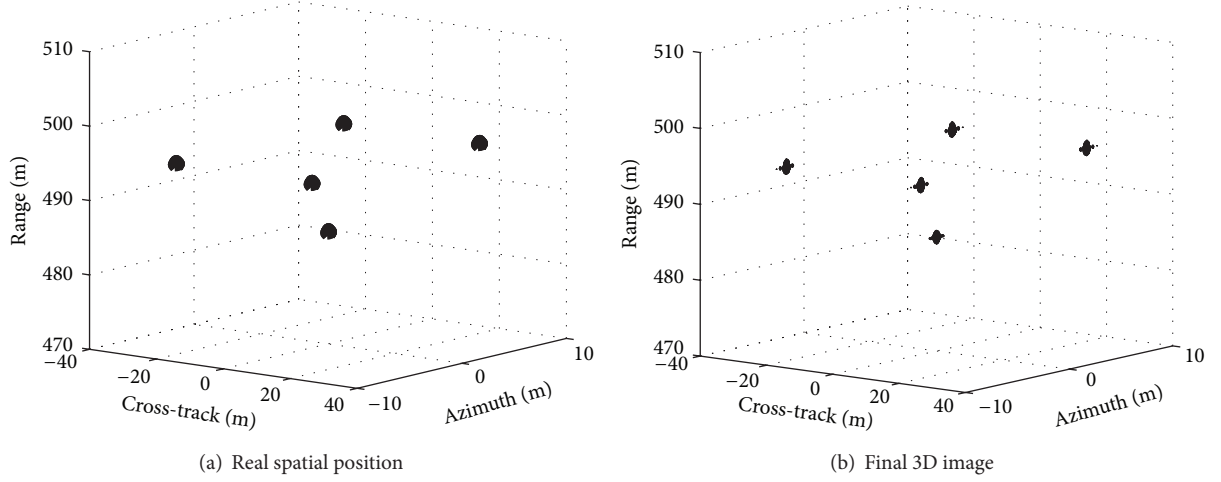


FIGURE 4: Real spatial position and final 3D image.

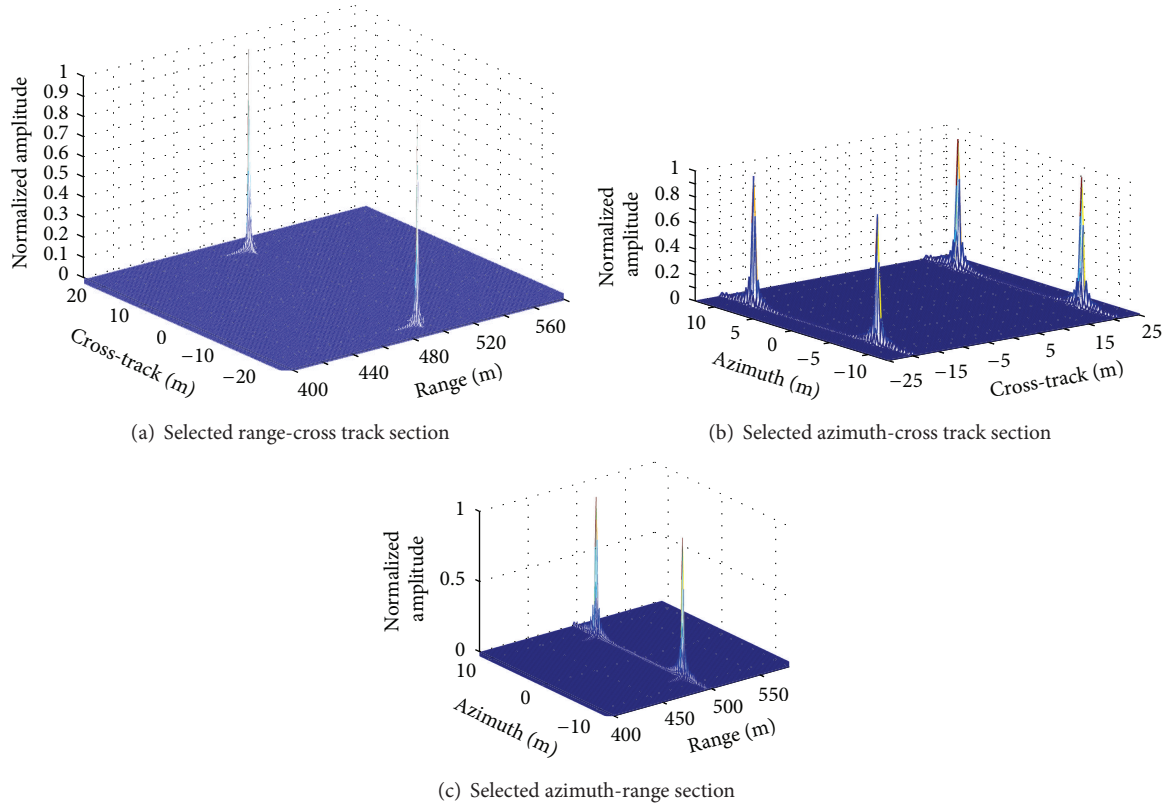


FIGURE 5: 2D image of selected sections.

and 3D imaging processing by using the proposed algorithm, the surfaces of the final 3D image are plotted at -20 dB in Figure 4(b). As expected, the image is reconstructed in 3D space, and the whole space structure is very consistent with the real situation in Figure 4(a). Figure 5 shows three selected sections of the final 3D image of down-looking MIMO array SAR. Figure 5(a) shows the 2D image of the selected range-cross track section corresponding to azimuth position 8 m. Figure 5(b) shows the 2D image of the selected azimuth-cross track section corresponding to range position 495 m.

Figure 5(c) shows the 2D image of the selected azimuth-range section corresponding to cross-track position -20 m. The below imaging results show that the point scatterers are well focused in three directions, confirming the validity of the proposed algorithm.

In order to analyze the performance of the proposed method, the imaging result obtained by Fourier transform is given for comparison. Supposed that there are two targets located at the azimuth-range-cross track unit of $(8, 0.18, 495)$ and $(8, -0.18, 495)$. Figure 6(a) shows the range-cross track

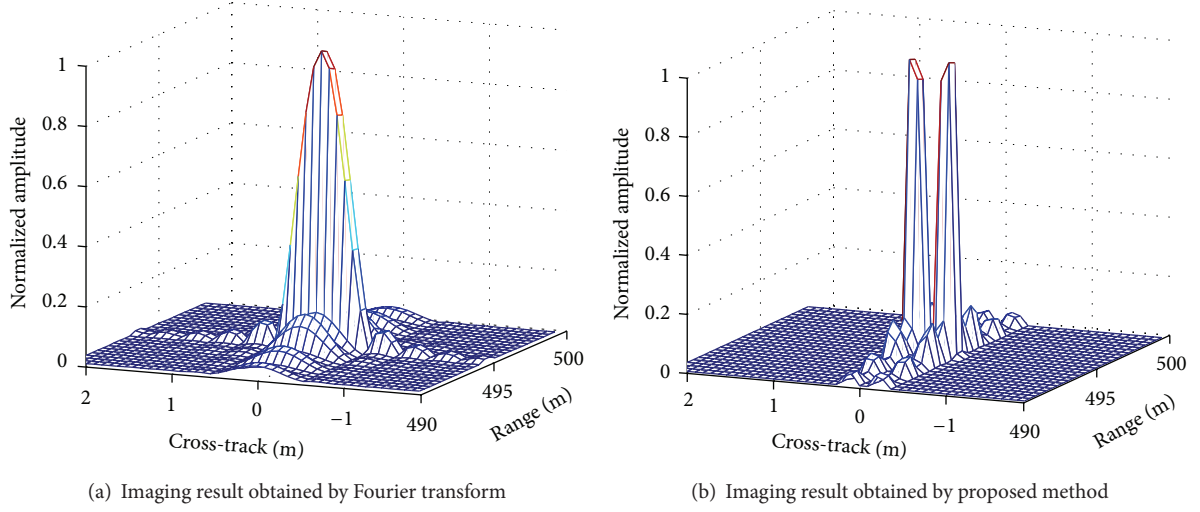


FIGURE 6: Comparison of the range-cross track imaging results of down-looking MIMO array SAR.

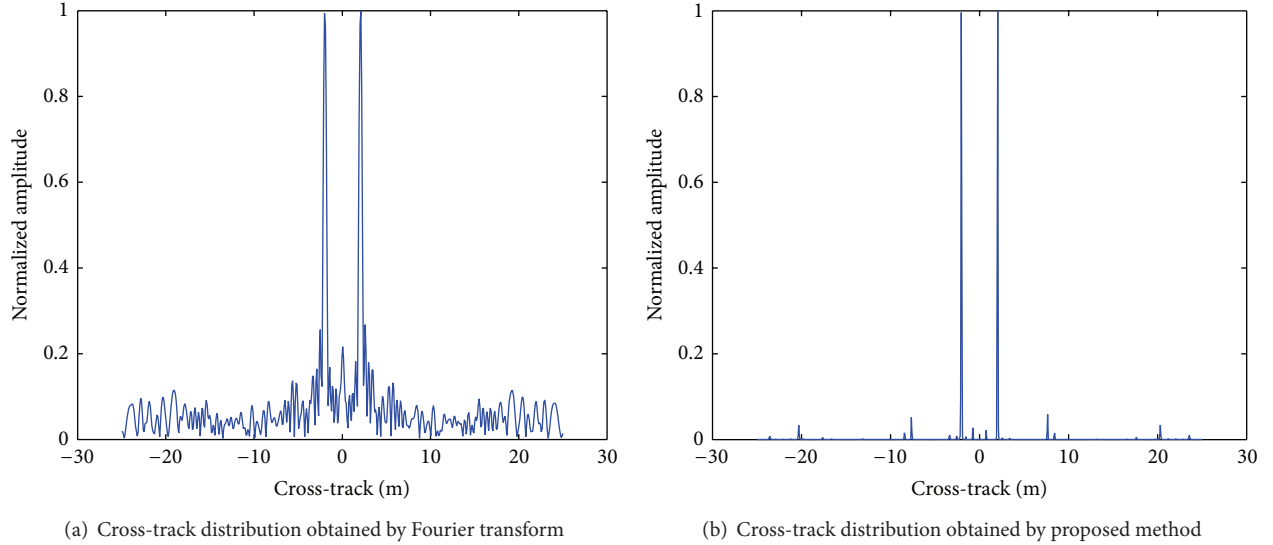


FIGURE 7: Comparison of the cross-track distribution obtained by Fourier transform and the proposed method.

reconstruction result obtained by Fourier transform, and Figure 6(b) shows the range-cross track reconstruction result obtained by the proposed method. As the cross-track distance of the two targets is 0.36 m, which is less than the cross-track resolution of 0.4 m, the two targets can not be distinguished in the image obtained by Fourier based method. However, the proposed method can improve the spatial resolution and distinguish the two targets clearly.

In the following experiment, we take into account two targets located at the same azimuth and range positions and with the cross-track values equal to -2 m and 2 m, respectively. Moreover, additional Gaussian distributed complex noise is added to generate measurements with SNR of 5 dB. Figures 7(a) and 7(b) show the cross-track distribution of the two targets obtained by Fourier transform and the proposed method, respectively. By comparing the imaging results, it can be seen that the proposed method is more robust to noise and

it recovers target image together with suppressing the noise components.

5. Conclusions

Down-looking MIMO array SAR can reconstruct 3D images of the observed area and overcome restrictions of shading and lay over effects in side-looking SAR. Therefore, down-looking MIMO array SAR has challenging potential for 3D digital maps, complex terrain mapping, and so on. However, the cross-track resolution of down-looking MIMO array SAR is limited by the length of linear array. In this paper, a novel 3D imaging strategy is proposed for down-looking MIMO array SAR. Exploiting the spatial sparsity of the interest scene, we transform the cross-track imaging process of down-looking MIMO array SAR into the problem of sparse signal

reconstruction from noisy measurements. Raw data of down-looking MIMO array SAR in Ka-band is simulated and the 3D image is achieved. The results of the simulated data confirm the effectiveness of the proposed method.

Conflict of Interests

The authors declare that there is no conflict of interests regarding the publication of this paper.

Acknowledgments

This work was supported by the National Natural Science Foundation of China under Grant 61201390, Grant 61201389 and Grant 11201120, and the Natural Science Foundation for Education Department of Henan Province under Grant 13A510184.

References

- [1] D. L. Mensa, *High Resolution Radar Imaging*, Artech House, Dedham, Mass, USA, 1981.
- [2] W. G. Carrara, R. S. Goodman, and R. M. Majewski, *Spotlight Synthetic Aperture Radar: Signal Processing and Algorithms*, Artech House, Boston, Mass, USA, 1995.
- [3] X. Ren, J. Sun, and R. Yang, "A new three-dimensional imaging algorithm for airborne forward-looking SAR," *IEEE Geoscience and Remote Sensing Letters*, vol. 8, no. 1, pp. 153–157, 2011.
- [4] B. Pang, D. Dai, Y. Z. Li et al., "Research on forward-looking synthetic aperture radar imaging algorithm of high velocity platform," in *Proceedings of the IET International Radar Conference*, 2013.
- [5] J. Klare, "A new airborne radar for 3D imaging simulation study of ARTINO," in *Proceedings of the 6th European Conference on Synthetic Aperture Radar (EUSAR '06)*, Dresden, Germany, May 2006.
- [6] Y. Wang, L. Du, W. Hong, W. Tan, and Y. Wu, "A three-dimensional range migration algorithm for downward-looking 3D-SAR with single-transmitting and multiple-receiving linear array antennas," *EURASIP Journal on Advances in Signal Processing*, vol. 2010, Article ID 957916, 2010.
- [7] X. M. Peng, Y. P. Wang, W. X. Tan et al., "Fast wavenumber domain imaging algorithm for airborne downward-looking array 3d-SAR based on region of interest pick," *Journal of Electronics & Information Technology*, vol. 35, no. 7, pp. 1525–1531, 2013.
- [8] J. Klare, "Digital beamforming for a 3D mimo sar—improvements through frequency and waveform diversity," in *Proceedings of the IEEE International Geoscience and Remote Sensing Symposium (IGARSS '08)*, pp. V17–V20, Boston, Mass, USA, July 2008.
- [9] W. Q. Wang, "MIMO SAR imaging: potential and challenges," *IEEE Aerospace and Electronic Systems Magazine*, vol. 28, no. 8, pp. 18–23, 2013.
- [10] Y. N. Hou, *Study of radar imaging technology based on sparse array antenna [Ph.D. thesis]*, Institute of Electronics, Chinese Academy of Sciences, 2010.
- [11] S. Ji, Y. Xue, and L. Carin, "Bayesian compressive sensing," *IEEE Transactions on Signal Processing*, vol. 56, no. 6, pp. 2346–2356, 2008.
- [12] X. Z. Zhang, J. H. Qin, and G. J. Li, "SAR target classification using bayesian compressive sensing with scattering centers features," *Progress in Electromagnetics Research*, vol. 136, pp. 385–407, 2013.
- [13] J. Xu, Y. Pi, and Z. Cao, "Bayesian compressive sensing in synthetic aperture radar imaging," *IET Radar, Sonar & Navigation*, vol. 6, no. 1, pp. 2–8, 2012.
- [14] M. A. Herman and T. Strohmer, "High-resolution radar via compressed sensing," *IEEE Transactions on Signal Processing*, vol. 57, no. 6, pp. 2275–2284, 2009.
- [15] S. D. Babacan, R. Molina, and A. K. Katsaggelos, "Bayesian compressive sensing using laplace priors," *IEEE Transactions on Image Processing*, vol. 19, no. 1, pp. 53–63, 2010.
- [16] M. Çetin and W. C. Karl, "Feature-enhanced synthetic aperture radar image formation based on nonquadratic regularization," *IEEE Transactions on Image Processing*, vol. 10, no. 4, pp. 623–631, 2001.
- [17] L. Zhang, Z.-J. Qiao, M. Xing, Y. Li, and Z. Bao, "High-resolution ISAR imaging with sparse stepped-frequency waveforms," *IEEE Transactions on Geoscience and Remote Sensing*, vol. 49, no. 11, pp. 4630–4651, 2011.

Research Article

“Three Crossings” Compensations of the High Speed Moving MIMO Radar

Cheng Luo and Zishu He

School of Electronic Engineering, University of Electronic Science and Technology of China, Chengdu 611731, China

Correspondence should be addressed to Cheng Luo; genielc@aliyun.com

Received 15 November 2013; Revised 1 February 2014; Accepted 12 February 2014; Published 10 April 2014

Academic Editor: Wen-Qin Wang

Copyright © 2014 C. Luo and Z. He. This is an open access article distributed under the Creative Commons Attribution License, which permits unrestricted use, distribution, and reproduction in any medium, provided the original work is properly cited.

The problems of the “Three Crossings” motions and compensations for the moving target of the high speed moving MIMO radar are studied. Firstly, the space model is established to describe the problems by educing the equations of delay and transmitting pattern, which are changing with time. The echo characteristics are analyzed and the formulas of the “Three Crossings” are given. Secondly, a compensation method, which uses the fractional Fourier transform (FrFT) to compensate the crossing Doppler-cell and the preprocess to compensate the crossing range-cell and crossing-beam, is proposed. This method could compensate the “Three Crossings” simultaneously with little complexity of calculation because the preprocess deals only with the transmitting signals. Lastly, the phantom antenna array is employed in the simulations, the working model of “sparse transmitting dense receiving” is applied to the simulation of crossing-beam, and the results of simulations demonstrate the validity and the practicability of the method of combining the preprocess and the FrFT to compensate “Three Crossings.”

1. Introduction

The aircrafts are moving faster and faster as the development of the aviation technology, some of them could attain a velocity more than mach 10, and the maneuverability is becoming stronger too, which make the moving targets much more difficult to be searched, detected, and tracked by radar. Long time accumulation could increase the SNR output and the performance of detection, but adding accumulation time may cause “Three Crossings”, which means crossing Doppler-cell, crossing range-cell, and crossing-beam. The “Three Crossings” ruin the coherence of the echo. In order to accumulate coherently to get the best detection ability, the “Three Crossings” must be compensated before the accumulation.

Some valuable studies have been proposed for the crossing Doppler-cell and crossing range-cell [1–8], but most of them could compensate only one of these crossings. The narrow beam of the phase array (PA) radar limited the study about the crossing-beam, for PA radar cannot compensate the crossing-beam; so far there is no reference for this study. The MIMO radar transmits orthogonal signals to form a low amplitude but wide beam to cover the whole surveillance

area [9–11]. Even though the “Three Crossings” happen simultaneously, the MIMO radar can receive all the echoes without any energy loss. So, the MIMO radar produces the qualification for the study of the “Three Crossings,” especially the crossing-beam.

In this paper, the “Three Crossings” of the target detected by a high-speed moving MIMO radar are studied. A space model is established firstly to educe the equations about how the delay and the transmitting pattern change with the time. Secondly, an analysis of the echo is proposed to show the “Three Crossings” of the target. Thirdly, the preprocessing method [12] is employed to compensate the crossing range-cell and the crossing-beam, while the fractional Fourier transform (FrFT) [13] is employed to compensate the crossing Doppler-cell. A performance brief analysis about the compensation mismatching is proposed after all this, and the simulation results are produced at last.

2. Space Model

At time t , the radar lies at point P with the height of H and moves along the Y -axis with a high speed v_r , while the target

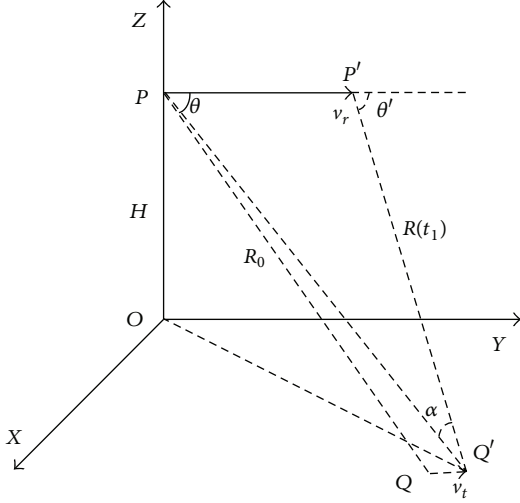


FIGURE 1: The space geometry relationship of the MIMO radar and the detected target.

lies at point Q and moves with a low speed v_t , assuming that v_r is much larger than v_t . Let the distance of the radar and the target $PQ = R_0$; the angle between the direction of the radar and PQ is θ . After t_1 , the transmitting signal propagates to the point where the target lies; assume that the point is Q' , the radar moves to point P' , and the distance becomes $R(t_1)$. Because the target moves very slowly, the range QQ' is very small, PQ and PQ' are nearly the same, and angle $\angle P'PQ$ and angle $\angle P'PQ'$ are almost equal to each other, then we can assume that $PQ' = PQ = R_0$ and $\angle P'PQ' = \angle P'PQ = \theta$. The space geometry relationship of the MIMO radar and the detected target is shown in Figure 1.

According to the cosine theorem, $R(t_1)$ can be calculated; after Taylor expandedness, the delay of the echo should be

$$\tau(t) = \frac{2R_0}{c} + \frac{-2v}{c-v} \left(t - \frac{R_0}{c} \right) + \frac{ac^2}{(c-v)^3} \left(t - \frac{R_0}{c} \right)^2, \quad (1)$$

where v is the relative velocity, c is the velocity of light, and a is the acceleration. Educe a further step; (2) can be gotten as follows:

$$\begin{aligned} t - \tau(t) &= t - \frac{2R_0}{c} + \frac{2v}{c-v} \left(t - \frac{R_0}{c} \right) - \frac{ac^2}{(c-v)^3} \left(t - \frac{R_0}{c} \right)^2 \\ &= \frac{c+v}{c-v} t - \frac{c+v}{c-v} \frac{2R_0}{c} - \frac{ac^2}{(c-v)^3} t^2 \\ &= kt - kt_0 - pt^2, \end{aligned} \quad (2)$$

where

$$k = \frac{c+v}{c-v}, \quad t_0 = \frac{2R_0}{c+v}, \quad p = \frac{ac^2}{(c-v)^3}. \quad (3)$$

Extracting the triangle $PP'Q'$, in the whole surveillance period, the changing angle from the target to the radar is equal to α , as is shown in Figure 2.

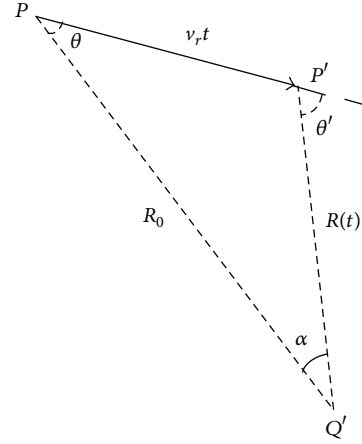


FIGURE 2: The changing angle.

Assuming that α is constant in one pulse repeat interval (PRI) and variable between each PRI, the MIMO radar has an M elements transmitting uniform linear array (ULA) and an N elements receiving ULA; L pulses are transmitted in the accumulation period. So, the phase matrixes of the steering vectors of the transmitting and receiving arrays are

$$\begin{aligned} \Psi_T &= [\psi(t_1), \psi(t_2), \dots, \psi(t_L)]^T \\ &= \begin{bmatrix} \psi_1(t_1) & \psi_1(t_2) & \cdots & \psi_1(t_L) \\ \psi_2(t_1) & \psi_2(t_2) & \cdots & \psi_2(t_L) \\ \vdots & \vdots & \ddots & \vdots \\ \psi_M(t_1) & \psi_M(t_2) & \cdots & \psi_M(t_L) \end{bmatrix}^T, \end{aligned} \quad (4)$$

$$\begin{aligned} \Psi_R &= [\Phi(t_1), \Phi(t_2), \dots, \Phi(t_L)]^T \\ &= \begin{bmatrix} \phi_1(t_1) & \phi_1(t_2) & \cdots & \phi_1(t_L) \\ \phi_2(t_1) & \phi_2(t_2) & \cdots & \phi_2(t_L) \\ \vdots & \vdots & \ddots & \vdots \\ \phi_N(t_1) & \phi_N(t_2) & \cdots & \phi_N(t_L) \end{bmatrix}^T, \end{aligned} \quad (5)$$

where the phase of the m th transmitting channel is

$$\begin{aligned} \psi_m(t_l) &= \frac{2\pi(m-1)d_t}{\lambda} \sin[\alpha_1(t_l)], \\ m &= 1 \sim M, \quad l = 1 \sim L \end{aligned} \quad (6)$$

and the phase of the n th receiving channel is

$$\begin{aligned} \phi_n(t_l) &= \frac{2\pi(n-1)d_r}{\lambda} \sin[\alpha_2(t_l)], \\ n &= 1 \sim N, \quad l = 1 \sim L. \end{aligned} \quad (7)$$

The angles α_1 and α_2 are the α in Figure 2. Assume that, after b PRI, the angle changes, so t_l should be

$$t_l = \left\lceil \frac{l}{b} \right\rceil T, \quad l = 1 \sim L, \quad (8)$$

where T could be any moment in the radar period T_r . According to the cosine theorem, the $\sin \alpha$ can be calculated in the triangle $PP'Q'$; put $\sin \alpha$ into (6); then we can get

$$\begin{aligned} \psi_m(t_l) &= \left(1 + \frac{v_r}{R_0} \left\lceil \frac{l}{b} \right\rceil T \cos \theta \right) \frac{v_r}{R_0} \left\lceil \frac{l}{b} \right\rceil T \\ &\quad \cdot \frac{2\pi(m-1)d \sin \theta}{\lambda}, \\ m &= 1 \sim M, \\ l &= 1 \sim L. \end{aligned} \quad (9)$$

If the transmitting array and the receiving array are the same, $\sin[\alpha_2(t_l)]$ would have the same formula with $\sin[\alpha_1(t_l)]$, so (9) can be used for $\phi_n(t_l)$ too.

3. Echo Analysis

The transmitting signal can be expressed as

$$\mathbf{S} = [\mathbf{s}_1(t), \dots, \mathbf{s}_L(t)] = \begin{bmatrix} s_{11}(t), \dots, s_{1M}(t) \\ s_{21}(t), \dots, s_{2M}(t) \\ \vdots \\ s_{L1}(t), \dots, s_{LM}(t) \end{bmatrix}^T, \quad (10)$$

where the signal transmitted by the m th element at the l th period is

$$s_{lm}(t) = \text{rect}\left(\frac{t - lT_r}{T_p}\right) s_{bm}(t - lT_r) e^{j2\pi f_c t}, \quad (11)$$

where $s_{bm}(t)$ denotes the transmitted baseband signal. The echo received by the n th channel after mixing should be

$$\begin{aligned} s_{r,n}(t) &= \sum_{m=1}^M \text{rect}\left[\frac{t - \tau(t) - lT_r}{T_p}\right] s_{bm}[t - \tau(t) - lT_r] \\ &\quad \times e^{-j2\pi f_c \tau(t)} e^{j\psi_m(t_l)} \cdot e^{j\phi_n(t_l)} + v_n(t). \end{aligned} \quad (12)$$

In this paper, the clutter is ignored to focus on the “Three Crossings” and their compensations; the clutter compression in this case of the airborne MIMO radar, including the clutter diffusing and agglomerating, will be discussed in another paper, so $v_n(t)$ in (12) only stands for the noise.

Name the rectangle function in (12) as $f(t)$, so

$$f(t) = \text{rect}\left[\frac{t - \tau(t) - lT_r}{T_p}\right] = \text{rect}\left(\frac{kt - kt_0 - pt^2 - lT_r}{T_p}\right). \quad (13)$$

Let the numerator in (13) be 0; the front edge in the fast-slow time domain of the echo can be calculated as

$$\hat{t}(l) = \frac{pT_r^2}{k^3} l^2 + \left(\frac{1}{k} - 1 - \frac{2pT_r t_0}{k^2}\right) lT_r + (2k-1)t_0 + \frac{pt_0^2}{k}. \quad (14)$$

The echo envelope will move in the fast-slow time domain as the number of the pulse increases, according to (14), so the range migration would happen in this case.

Name the baseband signal and the first exponential function in (12) as $g(t)$, so

$$g(t) = \sum_{m=1}^M s_{bm}[t - \tau(t) - lT_r] e^{-j2\pi f_c \tau(t)}. \quad (15)$$

Here, the delay $\tau(t)$ is a quadric polynomial and the Doppler-frequency of the echo $f_d(t)$ would be a function of time, which would make the coherence of the echo be destroyed; that is to say, the Doppler migration would happen in this case.

Name the last two exponential functions in (12) as $h(t)$, so

$$h(t) = \sum_{m=1}^M e^{j\psi_m(t_l)} \cdot e^{j\phi_n(t_l)}. \quad (16)$$

According to (4)~(9), we have

$$\psi_m(t_{l_1}) \neq \psi_m(t_{l_{1+b}}), \quad \phi_n(t_{l_1}) \neq \phi_n(t_{l_{1+b}}). \quad (17)$$

That is to say, after b PRI, the target moves into the next beam and the crossing-beam would happen in this case.

4. Compensation Methods

In this paper, the preprocess method and the FrFT are employed to compensate the “Three Crossings.” The preprocess method compensates the range migration by combining the direct digital synthesis (DDS) technology to control the transmit signal elaborately, that is, to regulate the pulse width of the transmitting signal to make the echo envelopes be aligned automatically in the fast-slow time domain. The beam-crossing is compensated by preprocessing the transmitting signal too. Based on the algorithm of the preprocess, the conjugate of the transmitting pattern is added in the transmitting signals to make the transmitting angles be compensated at the target.

From $p = ac^2/(c-v)^3 \approx a/c$, p provides little effect on the range migration, so $f(t)$ can be approximated as

$$f(t) = \text{rect}\left(\frac{kt - kt_0 - lT_r}{T_p}\right). \quad (18)$$

So, the new transmitting signal can be written as

$$\begin{aligned} s_{lm}(t) &= \text{rect}\left(\frac{t/k - lT_r}{T_p}\right) s_{bm}\left(\frac{t}{k} - lT_r\right) e^{-j\psi_m(t_l)} e^{j2\pi f_c t}, \\ m &= 1 \sim M. \end{aligned} \quad (19)$$

Then, the added signal at the target should be

$$s_{T,Im}(t) = \sum_{m=1}^M \text{rect} \left[\frac{(t - t_1)/k - lT_r}{T_p} \right] s_{bm} \times \left[\frac{(t - t_1)}{k} - lT_r \right] e^{j2\pi f_c(t-t_1)}, \quad (20)$$

where t_1 is the transmitting delay from radar to the target. So, the echo after mixing should be

$$s_{r,In}(t) = \sum_{m=1}^M \text{rect} \left(\frac{\hat{t} - t_0}{T_p} \right) s_{bm} \left[\frac{t - \tau(t)}{k} - lT_r \right] \times e^{-j2\pi f_c \tau(t)} e^{j\phi_n(t_1)} + v_n(t). \quad (21)$$

The front edge of the echo envelopes in the fast-slow time domain is a constant t_0 , which means the echo envelopes are aligned, so the range-cell crossing is compensated.

After the receiving beam forming, we have

$$s_{r,I}(t) = \sum_{n=1}^N s_{r,In}(t) e^{-j\phi_n(t_1)} = \sum_{n=1}^N \sum_{m=1}^M \text{rect} \left(\frac{\hat{t} - t_0}{T_p} \right) s_{bm} \left[\frac{t - \tau(t)}{k} - lT_r \right] e^{-j2\pi f_c \tau(t)} + \sum_{n=1}^N v_n(t). \quad (22)$$

In (22), the transmitting pattern is canceled by the receiving pattern, so the beam-crossing is compensated. Next, the FrFT is employed to compensate the Doppler-cell crossing, which would make the phases of the echo contain only constant and one-order polynomial; the result should be

$$s_{r,I}(t) = \sum_{n=1}^N \sum_{m=1}^M \text{rect} \left(\frac{\hat{t} - t_0}{T_p} \right) s_{bm} (\lambda_1 t + \lambda_0) \times e^{-j2\pi f_c (\xi_1 t + \xi_0)} + \sum_{n=1}^N v_n(t), \quad (23)$$

where λ_1 and ξ_1 are the coefficients of the one-order polynomial of t and λ_0 and ξ_0 are constants.

In (23), the echo envelopes are aligned in the fast-slow time domain, the orders of the echo phases are less than 2, and the pattern is constant, so after the processes of the preprocess and the FrFT, the ‘‘Three Crossings’’ are corrected, echo pulses are coherent, and the highest accumulation output can be gotten after the matched filter and FFT.

5. Simulations

The LFM signal is employed in the simulations. The conditions are as follows: the PRI is 1 ms, the pulse width is

0.1 ms, the original range between the radar and the target is 100 km, the velocity of the radar platform is 1 km/s, $\theta = \pi/6$, the number of the transmitting antennas is 2, the bandwidth is 0.2 MHz, the frequency interval of the channels is 0.2 MHz, the number of the pulses is 500, the sample frequency is 1 MHz, the carrier frequency is 2 GHz, and the zero intermediate frequency is 0.2 MHz. After a little simple calculation, the original relative velocity is $v_r \approx 866$ m/s, the acceleration is 5 m/s^2 , during the accumulation period, and the range between the radar and the target shifts $\Delta R \approx 433.6$ m.

The relative range shifts about 450 m in Figure 3(a); it is quite close to the number calculated by equation. The MTD result expands in the velocity dimension because of the Doppler shift.

After the range compensation, the peaks of the MF results are superposition, but the MTD result is still expanding. From Figure 4, the range-cell crossing has been compensated, but the Doppler-cell crossing still exists.

After the range and Doppler compensations are done, the MF results are totally superposition and the MTD result is an ideal thumb pin; then we can gain the highest accumulation output (see Figure 5).

When the beam-crossing happens, three conditions are satisfied generally; those are as follows: (1) the number of the transmitting elements is large, (2) the relative range between the radar and the target is not too far away, and (3) the vertical velocity is high. So, the relative range is reset as 20 km, the velocity of the radar is reset as 3000 m/s, the number of the transmitting elements is 10, and the PRI changes into 2 ms. The phantom element [14] is employed in the transmitting array and the interval distance is equal to the product of the number of the transmitting elements and the half of the wavelength, which could expand the transmitting caliber to 100 transmitting elements to decrease the width of the transmitting main lobe. It can be calculated that the width of the main lobe is about 0.731° , the shift of the angle in one PRI is 0.0744° , after 100 PRI, and the target moves across 2.0362 beams.

The accumulations before and after compensating the beam-crossing, on condition that the range-cell crossing and the Doppler-cell crossing have been compensated, are shown in Figure 6, and the accumulations are normalized by the accumulation result before compensating the beam-crossing. It is obvious to see that the peak after compensation is twice higher than that before, which is consistent with the case that the target moves across about 2 beams.

To prove the validity of the precompensation method, simulations are taken under the main conditions that the numbers of the transmitting and receiving channels are $M = N = 4$, the number of the transmitting pulses is $L = 200$, the radar PRI is $T_r = 1$ ms, the pulse width is $T_p = 50 \mu\text{s}$, the original distance of the radar and the target is $R_0 = 100$ km, and the real relative velocity is $v_0 = 4$ km/s. Consider that it is difficult to know the real relative velocity in practice, so in order to check the performance of the precompensation when $v \neq v_0$, four different possible relative velocities are selected as the compensation velocities and $v = 4, 5, 6, 7$ km/s; for the

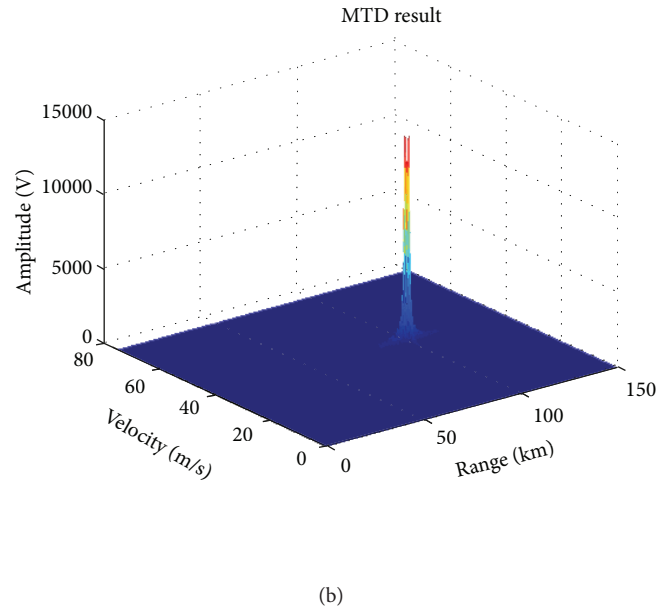
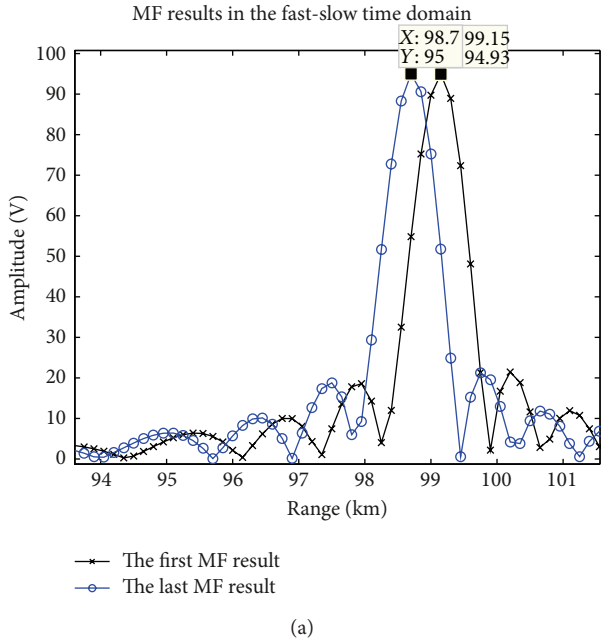


FIGURE 3: The matched filter (MF) and MTD results without any compensation.

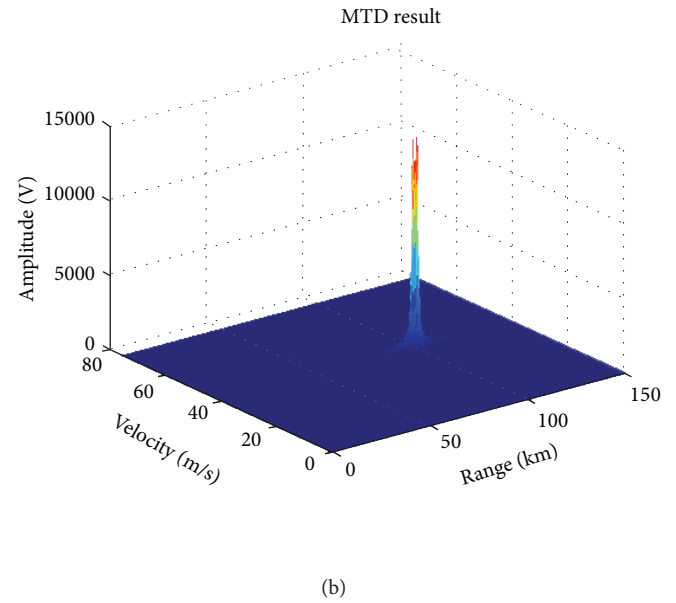
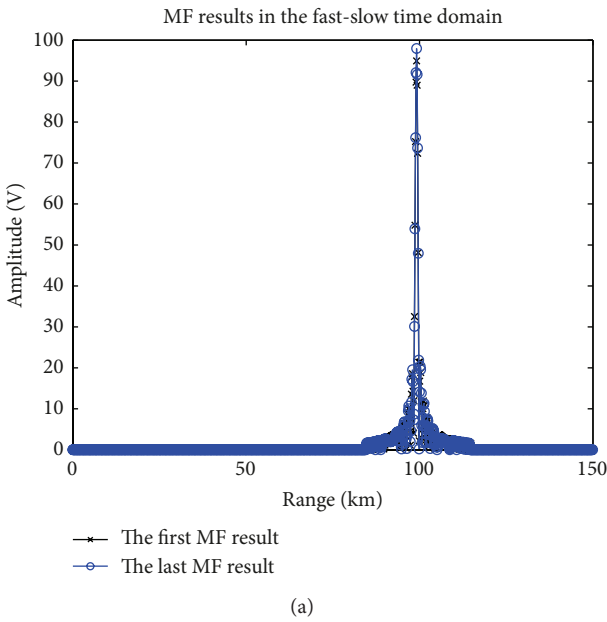


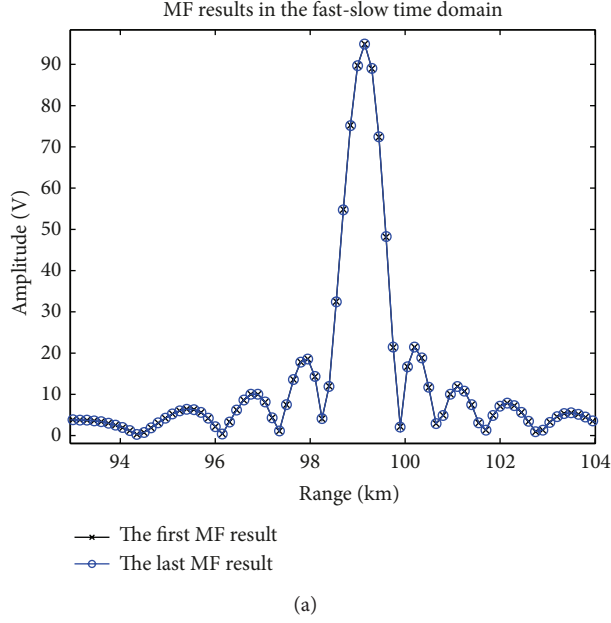
FIGURE 4: The matched filter and MTD results after range compensation.

symmetry, the performances of these velocities should be the same, respectively, to $v = 4, 3, 2, 1$ km/s.

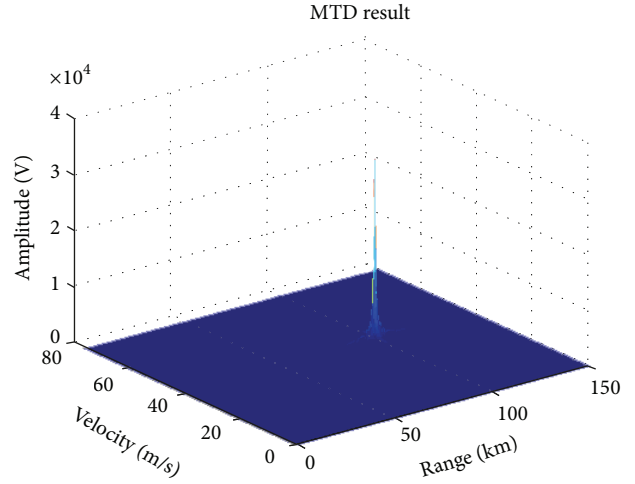
Firstly, the accumulation results of different compensation velocities are shown in Figure 7. It is easy to see that when the compensation velocity is more different from the real relative velocity, the accumulation result is wider and the peak is lower, which means the compensation performance is worse. When the compensation velocity is 7 km/s, the peak of the accumulation is nearly 3 dB less than the accumulation of

$v = 4$ km/s. So, when the difference between the real relative velocity and the compensation velocity is less than 3 km/s, the accumulation performance is acceptable. At the same time, one could see that there is a good velocity difference tolerance.

Secondly, the detection probabilities of the four different compensation velocities are shown in Figure 8. Corresponding to the results in Figure 7, at the same SNR value, when the compensation velocity is more different from the real relative velocity, the detection probability is lower. If there is



(a)



(b)

FIGURE 5: The matched filter and MTD results after range and Doppler compensations.

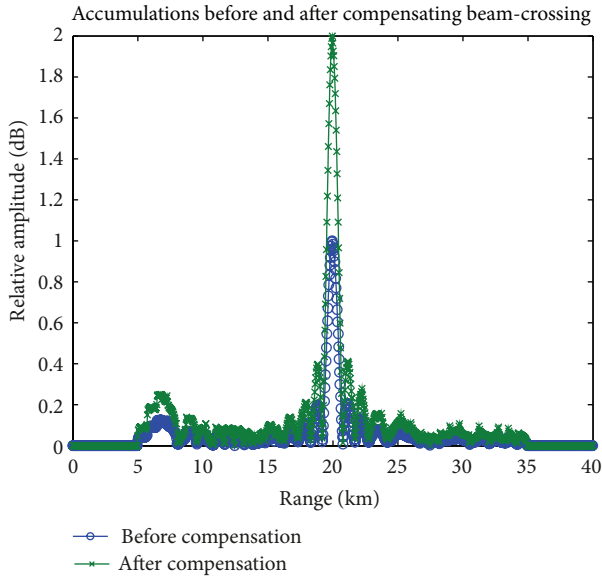


FIGURE 6: Accumulation results before and after the beam-crossing compensations.

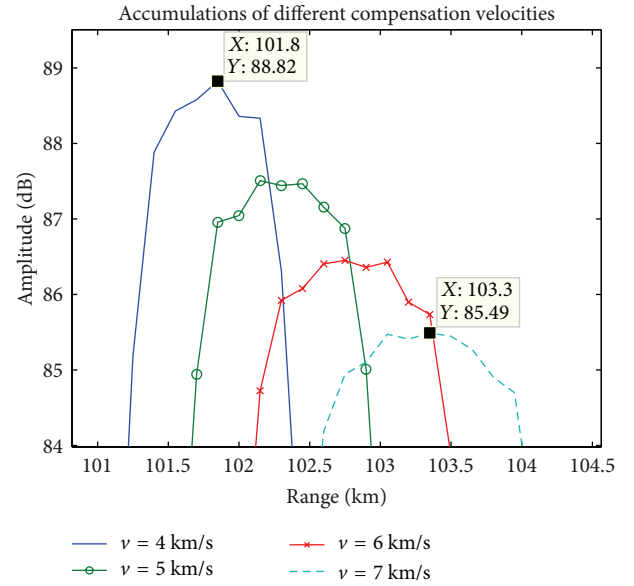


FIGURE 7: Accumulations of four different compensation velocities.

no compensation, the scenario is the same to the $v = 8$ km/s or $v = 0$ km/s and the detection performance would be even worse than the one when $v = 7$ km/s.

From these two groups of simulation results, one can figure out that the precompensation can compensate the range migration valid in a tolerance of the difference between the real relative velocity and the compensation velocity. The detection probability at 90% after compensation when $v = v_0$ is about 7 dB or 8 dB better than the one when these two velocities are 3 km/s different.

6. Conclusion

As the developments of the velocity and the maneuverability of aircrafts, the “Three Crossings” are becoming bigger problems for the MTD. Traditional radars cannot compensate the beam-crossing, so no article discussed this problem. MIMO radar, which transmits a wide beam, provides the probability to achieve the compensation of the beam-crossing. In this paper, the “Three Crossings” are discussed simultaneously based on the airborne MIMO radar system. To detect the moving target, the characteristic of the echo is analyzed, the

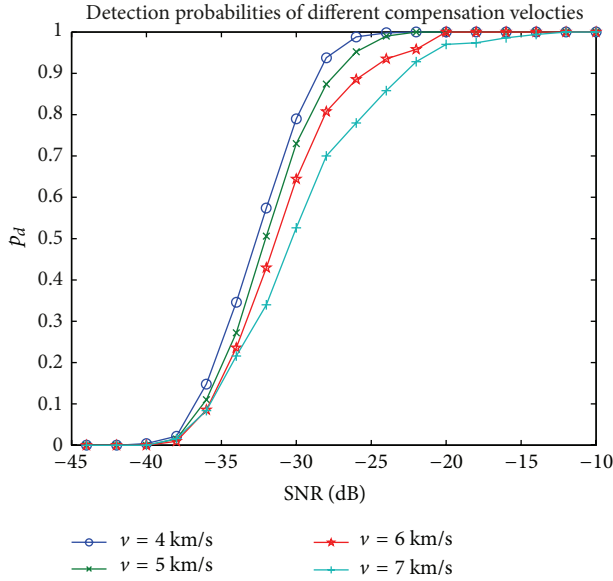


FIGURE 8: Detection probabilities of four different compensation velocities.

“Three Crossings” model is proposed, and then the preprocessing method and the FrFT are employed to compensate the “Three Crossings.” The simulation results show that these two methods can compensate the “Three Crossings” validly; the accumulation peak is significantly higher after the compensations. Even when the compensation velocity is not exactly the same with the real one, the compensation performance is also acceptable within a large velocity tolerance.

Conflict of Interests

The authors declare that there is no conflict of interests regarding the publication of this paper.

Acknowledgments

The authors would like to thank all the editors and referees for their suggestions and advices. This work is supported by the National Natural Science Foundation of China (no. 11076006, no. 61032010, and no. 61101173).

References

- [1] R. P. Perry, R. C. Dipietro, and R. L. Fante, “SAR imaging of moving targets,” *IEEE Trans on AES*, vol. 32, no. 1, pp. 188–200, 1999.
- [2] Y. Liu, H. Meng, G. Li, and X. Wang, “Velocity estimation and range shift compensation for high range resolution profiling in stepped-frequency radar,” *IEEE Geoscience and Remote Sensing Letters*, vol. 7, no. 4, pp. 791–795, 2010.
- [3] Y. Boers and J. N. Driessen, “Multi-target particle filter track before detect application,” *IET Proceeding of Radar Sonar Navigation*, vol. 151, no. 6, pp. 351–357, 2004.
- [4] J. Su, M. Xing, G. Wang, and Z. Bao, “High-speed multi-target detection with narrowband radar,” *IET Radar, Sonar and Navigation*, vol. 4, no. 4, pp. 595–603, 2010.
- [5] Y. Liu, H. Meng, G. Li, and X. Wang, “Velocity estimation and range shift compensation for high range resolution profiling in stepped-frequency radar,” *IEEE Geoscience and Remote Sensing Letters*, vol. 7, no. 4, pp. 791–795, 2010.
- [6] Y. Boers and J. N. Driessen, “Multi-target particle filter track before detect application,” *IEEE Proceedings of Radar Sonar Navig.*, vol. 151, no. 6, pp. 351–357, 2004.
- [7] F. G. Geroleo and M. Brandt-Pearce, “Detection and estimation of LFM CW radar signals,” *IEEE Transactions on Aerospace and Electronic Systems*, vol. 48, no. 1, pp. 405–418, 2012.
- [8] J. Guan, X. -L. Chen, Y. Huang, and Y. He, “Adaptive fractional Fourier transform-based detection algorithm for moving target in heavy sea clutter,” *IET Radar, Sonar and Navigation*, vol. 6, no. 5, pp. 389–401, 2012.
- [9] D. J. Rabideau and P. Parker, “Ubiquitous MIMO multifunction digital array radar,” in *Conference Record of the 37th Asilomar Conference on Signals, Systems and Computers*, vol. 1, pp. 1057–1064, November 2003.
- [10] P. W. Moo, “Multiple-input multiple-output radar search strategies for high-velocity targets,” *IET Radar, Sonar and Navigation*, vol. 5, no. 3, pp. 256–265, 2011.
- [11] A. Hassanien, S. A. Vorobyov, and A. B. Gershman, “Moving target parameters estimation in noncoherent MIMO radar systems,” *IEEE Transactions on Signal Processing*, vol. 60, no. 5, pp. 2354–2361, 2012.
- [12] C. Luo, J. Li, H. M. Liu, and Z. S. He, “Compensation method for envelop migration of MIMO radar high speed moving target based on transmit signal pre-process,” in *International Workshop on Microwave and Millimeter Wave Circuits and System Technology (MMWCST '12)*, pp. 1–4, Cheng Du, China, 2012.
- [13] H.-B. Sun, G.-S. Liu, H. Gu, and W.-M. Su, “Application of the fractional Fourier transform to moving target detection in airborne SAR,” *IEEE Transactions on Aerospace and Electronic Systems*, vol. 38, no. 4, pp. 1416–1424, 2002.
- [14] B. J. Donnet and I. D. Longstaff, “MIMO radar, techniques and opportunities,” in *Proceedings of the 3rd European Radar Conference*, pp. 112–115, Manchester, UK, September 2006.

Research Article

Low Complexity Direction and Doppler Frequency Estimation for Bistatic MIMO Radar in Spatial Colored Noise

Lingyun Xu,^{1,2} Guangbin Zhang,¹ Xiaofei Zhang,¹ and Zongze Xu¹

¹ College of Science, Nanjing University of Aeronautics and Astronautics, Nanjing 210016, China

² Nanjing Telecommunication Technology Institute, Nanjing 210007, China

Correspondence should be addressed to Guangbin Zhang; zhgb2007@nuaa.edu.cn

Received 5 November 2013; Revised 18 February 2014; Accepted 20 February 2014; Published 6 April 2014

Academic Editor: Shengqi Zhu

Copyright © 2014 Lingyun Xu et al. This is an open access article distributed under the Creative Commons Attribution License, which permits unrestricted use, distribution, and reproduction in any medium, provided the original work is properly cited.

We investigate the algorithm of direction and Doppler frequency estimation for bistatic multiple-input multiple-output (MIMO) radar in spatial colored noise. A novel method of joint estimation of direction and Doppler frequency in spatial colored noise based on propagator method (PM) for bistatic MIMO radar is discussed. Utilizing the cross-correlation matrix which is formed by the adjacent outputs of match filter in the time domain, the special matrix is constructed to eliminate the influence of spatial colored noise. The proposed algorithm provides lower computational complexity and has very close parameters estimation compared to estimation of signal parameters via rotational invariance technique (ESPRIT) algorithm in high signal-to-noise ratio (SNR). It is applicable even if the transmitted waveforms are not orthogonal. The estimated parameters can be paired automatically and the Cramér-Rao Bound (CRB) is given in spatial colored noise. Simulation results confirm the effectiveness of the proposed method.

1. Introduction

Since multiple-input multiple-output (MIMO) radars use multiple antennas to simultaneously transmit diverse waveforms and utilize multiple antennas to receive the reflected signals, they have many potential advantages over conventional phased-array radars [1–4]. According to the array configuration, MIMO radar can be divided into two categories: the statistical MIMO radar and colocated MIMO radar [5–15]. The advantages of MIMO radar with colocated antennas have been studied extensively, which include improved direction performance and higher resolution [16], higher sensitivity or detection of moving targets, and increased degrees of freedom for transmit beamforming [17]. MIMO radar with widely separated antennas can capture the spatial diversity of the target's radar cross-section (RCS) [18]. This spatial diversity provides radar system with the ability to improve target parameter estimation [19–22], high resolution target localization, and tracking performance [23, 24].

Target direction estimation is a basic function of a radar system. Many advanced direction estimation algorithms for MIMO radar have been extensively discussed in the current

literature which include ESPRIT algorithm, Capon algorithm, parallel factor (PARAFAC) algorithm, multiple signal classification (MUSIC) algorithm, and PM algorithm [25–33]. In [25, 29], ESPRIT algorithm exploited the invariance property of both the transmit array and the receive array for direction estimation in MIMO radar systems. Reference [30] derived a reduced-dimension multiple signal classification (MUSIC) algorithm for direction of departure (DOD) and direction of arrival (DOA) estimation. The algorithm, which only requires one-dimensional search, can avoid the high computational cost of the two-dimensional MUSIC algorithm. However, the mentioned algorithm above did not consider the Doppler frequency estimation, and the noises were assumed to be the Gaussian white noise. In [31], the ESPRIT method was used for DOD-DOA and Doppler frequency estimation which necessitates eigen decomposition of the sample covariance matrix. Huge computation will be involved where the large array size is required in applications. Yunhe [32] proposed the DOA matrix algorithm to estimate the DOD-DOA and Doppler frequency, but it cannot eliminate the influence of spatial colored noise. In this paper, we propose a low-complexity angle and Doppler frequency

estimation algorithm which can reduce computational cost. It has very close parameters estimation performance compared to ESRPIT and DOA matrix algorithm in high SNR. And the proposed algorithm pairs the parameters automatically and eliminates the influence of the spatial colored noise. Simulation results illustrate performance of the proposed algorithm.

The remainder of this paper is structured as follows. Section 2 develops the data model for a bistatic MIMO radar system, and Section 3 proposes the proposed algorithm for angle and Doppler frequency estimation in MIMO radar. In Section 4, simulation results are presented to verify improvement for the proposed algorithm, while the conclusions are shown in Section 5.

Notation. $(\cdot)^*$, $(\cdot)^T$, $(\cdot)^H$, $(\cdot)^{-1}$, $(\cdot)^\dagger$, and $\text{vec}[\cdot]$ denote complex conjugation, transpose, conjugate-transpose, inverse, Moore-Penrose inverse (pseudoinverse), and vectorization operator, respectively. $\|\cdot\|_F$ presents Frobenius norm; \mathbf{I}_K is a $K \times K$ identity matrix; \otimes represents Kronecker product; $\min(\cdot)$ is to get minimum elements of an array; $\angle(\cdot)$ denotes the phase of a complex; $\text{row}(\cdot)$ denotes the operator that stacks the rows of a matrix in a column vector. $D_n(\cdot)$ is to take the n th row of the matrix to construct a diagonal matrix. $E[\cdot]$ is expectation operator.

2. Data Model

We consider a narrowband bistatic MIMO radar system with M -element transmit antennas and N -element receive antennas, both of which are half-wavelength spaced uniform linear arrays. The transmit antennas transmit M orthogonal coded signals. $\mathbf{s}_m = [s_m(1), s_m(2), \dots, s_m(P)]^T \in \mathbb{C}^{P \times 1}$, $m = 1, 2, \dots, M$ denotes the sampled baseband coded signal of the m th transmit antenna with one repetition interval with P being the length of the transmitted code sequence, so the transmit signals can be expressed as $\mathbf{S} = [\mathbf{s}_1, \mathbf{s}_2, \dots, \mathbf{s}_M]^T$. We also assume that there are a number of K far-field independent targets; $\mathbf{a}_r(\theta_k)$ and $\mathbf{a}_t(\phi_k)$ are the receive steering vector and transmit steering vector for θ_k (DOA) and ϕ_k (DOD) of the k th target, so the arrival signal of the k th target is $\mathbf{a}_t^T(\phi_k)\mathbf{S}$. The received array through reflections of the target can be expressed as

$$\mathbf{Y}(t) = \sum_{k=1}^K \beta_k e^{j2\pi f_{dk}(t-1)/f_s} \mathbf{a}_r(\theta_k) \mathbf{a}_t^T(\phi_k) \mathbf{S} + \mathbf{W}(t), \quad (1)$$

where β_k and f_{dk} denote the radar cross-section (RCS) fading coefficient and Doppler frequency of the k th target. f_s is the pulse repeat frequency. Due to the steering vector of ULA, we have $\mathbf{a}_r(\theta_k) = [1, e^{-j\pi \sin \theta_k}, \dots, e^{-j\pi(N-1) \sin \theta_k}]^T$, $\mathbf{a}_t(\phi_k) = [1, e^{-j\pi \sin \phi_k}, \dots, e^{-j\pi(M-1) \sin \phi_k}]^T$.

$\mathbf{w}(t) \in \mathbb{C}^{N \times P}$ denotes a Gaussian noise of zeros mean with unknown covariance matrix \mathbf{Q}_w . Matching the received data with the signal $(1/\sqrt{P})\mathbf{S}^H$, we obtain

$$\mathbf{x}(t) = \mathbf{A}\boldsymbol{\eta}(t) + \mathbf{n}(t), \quad (2)$$

where $\mathbf{A} = [\bar{\mathbf{a}}_1, \bar{\mathbf{a}}_2, \dots, \bar{\mathbf{a}}_K]$ is an $MN \times K$ matrix composed of the K steering vectors, and $\bar{\mathbf{a}}_k = \mathbf{a}_r(\theta_k) \otimes \mathbf{a}_t(\phi_k)$ is the Kronecker product of the receive and the transmit steering vectors for the k th target. $\bar{\mathbf{a}}_t(\phi_k) = \mathbf{R}_s^T \mathbf{a}_t(\phi_k)$, owing to $\mathbf{R}_s = E[\mathbf{S}\mathbf{S}^H/P] = \mathbf{I}_M$; then $\bar{\mathbf{a}}_t(\phi_k) = \mathbf{a}_t(\phi_k)$. $\boldsymbol{\eta}(t) = [\eta_1(t), \eta_2(t), \dots, \eta_K(t)]^T$, $\eta_k(t) = \sqrt{P}\beta_k e^{j2\pi f_{dk}(t-1)/f_s}$, $k = 1, 2, \dots, K$. $\mathbf{n}(t) = \text{vec}[\mathbf{W}(t)\mathbf{S}^H/\sqrt{P}]$.

The covariance matrix of $\mathbf{n}(t)$ is as follows:

$$\begin{aligned} E[\mathbf{n}(i) \mathbf{n}^H(j)] &= \frac{E\{\text{vec}[\mathbf{W}(i)\mathbf{S}^H] \text{vec}^H[\mathbf{W}(j)\mathbf{S}^H]\}}{P} \\ &= \frac{E\{[\mathbf{S}^* \otimes \mathbf{I}_N] [\text{vec}(\mathbf{W}(i)) \text{vec}^H(\mathbf{W}(j))] [\mathbf{S}^T \otimes \mathbf{I}_N]\}}{P} \\ &= \begin{cases} \mathbf{I}_M \otimes \mathbf{Q}_w, & i = j \\ \mathbf{0}, & i \neq j. \end{cases} \end{aligned} \quad (3)$$

3. Direction and Doppler Frequency Estimation Algorithm for MIMO Radar

3.1. The Proposed Algorithm Description. We assume that $\mathbf{a}_t(\phi_k)$ and $\mathbf{a}_r(\theta_k)$ are constant for L samples and define \mathbf{X} as $\mathbf{X} = [\mathbf{x}(1), \mathbf{x}(2), \dots, \mathbf{x}(L)]$, and we assume that the number of snapshots is L . Let

$$\begin{aligned} \mathbf{X}_1 &= [\mathbf{x}(1), \mathbf{x}(2), \dots, \mathbf{x}(L-1)] = \mathbf{A}\boldsymbol{\eta}_1 + \mathbf{N}_1, \\ \mathbf{X}_2 &= [\mathbf{x}(2), \mathbf{x}(3), \dots, \mathbf{x}(L)] = \mathbf{A}\boldsymbol{\eta}_2 + \mathbf{N}_2, \end{aligned} \quad (4)$$

where $\boldsymbol{\eta}_1 = [\boldsymbol{\eta}(1), \boldsymbol{\eta}(2), \dots, \boldsymbol{\eta}(L-1)]$, $\boldsymbol{\eta}_2 = [\boldsymbol{\eta}(2), \boldsymbol{\eta}(3), \dots, \boldsymbol{\eta}(L)]$, $\mathbf{N}_1 = [\mathbf{n}(1), \mathbf{n}(2), \dots, \mathbf{n}(L-1)]$, and $\mathbf{N}_2 = [\mathbf{n}(2), \mathbf{n}(3), \dots, \mathbf{n}(L)]$. Equation (3) shows that the cross-covariance matrix of noises is $\mathbf{0}$. This characteristic will be utilized in this paper to improve the estimate performance.

Note that $E[\mathbf{N}_2 \mathbf{N}_1^H] = \mathbf{0}$, $\boldsymbol{\eta}_2 = \boldsymbol{\Phi} \boldsymbol{\eta}_1$, $\boldsymbol{\Phi} = \text{diag}[e^{j2\pi f_{d1}/f_s}, e^{j2\pi f_{d2}/f_s}, \dots, e^{j2\pi f_{dK}/f_s}]$. This indicates that the rotation factor $\boldsymbol{\Phi}$ is generated by adjacent outputs of match filters.

The covariance matrix of \mathbf{X}_1 and \mathbf{X}_2 can be written as follows:

$$\mathbf{R}_x = E[\mathbf{X}_2 \mathbf{X}_1^H] = \mathbf{A} \boldsymbol{\Phi} \mathbf{R}_{\boldsymbol{\eta}} \mathbf{A}^H + E[\mathbf{N}_2 \mathbf{N}_1^H] = \mathbf{A} \boldsymbol{\Phi} \mathbf{R}_{\boldsymbol{\eta}} \mathbf{A}^H, \quad (5)$$

where $\mathbf{R}_{\boldsymbol{\eta}} = E[\boldsymbol{\eta}_1 \boldsymbol{\eta}_1^H]$. For the independent targets, $\mathbf{R}_{\boldsymbol{\eta}}$ should be a diagonal matrix; then we have the relationship $\mathbf{R}_{\boldsymbol{\eta}} \boldsymbol{\Phi}^H = \boldsymbol{\Phi}^H \mathbf{R}_{\boldsymbol{\eta}}$. Owing to $E[\mathbf{N}_2 \mathbf{N}_1^H] = \mathbf{0}$, \mathbf{R}_x can eliminate the influence of spatial colored noise. A new matrix \mathbf{R} is constructed by utilizing (5):

$$\mathbf{R} = \begin{bmatrix} \mathbf{R}_x^H \\ \mathbf{R}_x \end{bmatrix} = \begin{bmatrix} \mathbf{A} \boldsymbol{\Phi}^H \\ \mathbf{A} \boldsymbol{\Phi} \end{bmatrix} \mathbf{R}_{\boldsymbol{\eta}} \mathbf{A}^H = \underbrace{\begin{bmatrix} \mathbf{A} \boldsymbol{\Phi}^H \\ \mathbf{A} \boldsymbol{\Phi} \end{bmatrix}}_{\mathbf{B}} \mathbf{R}_{\boldsymbol{\eta}} \mathbf{A}^H = \mathbf{B} \mathbf{R}_{\boldsymbol{\eta}} \mathbf{A}^H. \quad (6)$$

The propagator method relies on the partition of the matrix \mathbf{B} [34]. \mathbf{B} can be denoted by $\mathbf{B} = \begin{bmatrix} \mathbf{B}_1 \\ \mathbf{B}_2 \end{bmatrix}$, where $\mathbf{B}_1 \in \mathbb{C}^{K \times K}$

is the full rank matrix; $\mathbf{B}_2 \in \mathbb{C}^{(2MN-K) \times K}$. The propagator \mathbf{V} is a unique linear operator which can be written as $\mathbf{V}^H \mathbf{B}_1 = \mathbf{B}_2$. Similarly partitioning received data matrix \mathbf{R} into two submatrices \mathbf{R}_1 and \mathbf{R}_2 with dimensions $K \times MN$ and $(2MN - K) \times MN$, respectively. Then the unique linear operation holds between \mathbf{R}_1 and \mathbf{R}_2 :

$$\mathbf{V}^H \mathbf{R}_1 = \mathbf{R}_2. \quad (7)$$

An estimation matrix \mathbf{V} can be obtained by minimizing the cost function: $J(\mathbf{V}) = \min \|\mathbf{R}_2 - \mathbf{V}^H \mathbf{R}_1\|_F^2$. The optimal solution is given by $\mathbf{V} = (\mathbf{R}_1 \mathbf{R}_1^H)^{-1} \mathbf{R}_1 \mathbf{R}_2^H$. Define a new matrix $\tilde{\mathbf{V}}^H = \begin{bmatrix} \mathbf{I}_K \\ \mathbf{V}^H \end{bmatrix}$, where \mathbf{I}_K is the identity matrix. Combining $\tilde{\mathbf{V}}$ and (7), we obtain

$$\tilde{\mathbf{V}}^H \mathbf{R}_1 = \begin{bmatrix} \mathbf{R}_1 \\ \mathbf{R}_2 \end{bmatrix} = \begin{bmatrix} \mathbf{B}_1 \\ \mathbf{B}_2 \end{bmatrix} \mathbf{R}_\eta \mathbf{A}^H = \begin{bmatrix} \mathbf{A} \Phi^{-1} \\ \mathbf{A} \Phi \end{bmatrix} \mathbf{R}_\eta \mathbf{A}^H = \mathbf{B} \mathbf{R}_\eta \mathbf{A}^H. \quad (8)$$

Rewrite (8) as

$$\tilde{\mathbf{V}}^H = \underbrace{\mathbf{B} \mathbf{R}_\eta \mathbf{A}^H \mathbf{R}_1^\dagger}_{\mathbf{T}} = \mathbf{B} \mathbf{T}, \quad (9)$$

where \mathbf{R}_1^\dagger is the pseudoinverse of \mathbf{R}_1 and \mathbf{T} is a nonsingular matrix. From (9), the columns in $\tilde{\mathbf{V}}$ span the same signal subspace as the column vectors in \mathbf{B} . So the signal subspace can be obtained by avoiding the estimation and eigen decomposition of the sample covariance matrix. The matrix $\tilde{\mathbf{V}}^H$ can be partitioned into two submatrices $\tilde{\mathbf{V}}^H = \begin{bmatrix} \tilde{\mathbf{V}}_1 \\ \tilde{\mathbf{V}}_2 \end{bmatrix}$. According to (9), we can get

$$\begin{bmatrix} \tilde{\mathbf{V}}_1 \\ \tilde{\mathbf{V}}_2 \end{bmatrix} = \underbrace{\begin{bmatrix} \mathbf{A} \Phi^{-1} \\ \mathbf{A} \Phi \end{bmatrix}}_{\mathbf{B}} \mathbf{T}. \quad (10)$$

Notice that $\Phi = \Phi^{-1} \Phi^2$; from (10) we can obtain

$$\Phi^2 = \mathbf{T} \tilde{\mathbf{V}}_1^\dagger \tilde{\mathbf{V}}_2 \mathbf{T}^{-1}, \quad (11)$$

$$\mathbf{A} \Phi = \tilde{\mathbf{V}}_2 \mathbf{T}^{-1}. \quad (12)$$

Equation (11) shows that the main diagonal elements of Φ^2 are equal to the eigen values obtained via the eigen decomposition of $\tilde{\mathbf{V}}_1^\dagger \tilde{\mathbf{V}}_2$ with \mathbf{T} the corresponding eigenvectors. Thus the Doppler frequency of the k th target can be calculated as

$$\hat{f}_k = \frac{\text{angle}(\varphi_k) f_s}{4\pi}, \quad (13)$$

where φ_k is the k th diagonal element of Φ^2 . The $\hat{\mathbf{A}}$ can be calculated from (12), because the Φ is the diagonal matrix, and it cannot affect the estimation of DOD and DOA using the least square method from the matrix $\hat{\mathbf{A}}$. We note that the pairing is automatically obtained because the DOA-DODs and Doppler frequencies are given through

the corresponding eigenvectors. The matrix $\hat{\mathbf{A}}$ can be also denoted by

$$\hat{\mathbf{A}} = \hat{\mathbf{A}}_R \circ \hat{\mathbf{A}}_T = \begin{bmatrix} \hat{\mathbf{A}}_T D_1(\hat{\mathbf{A}}_R) \\ \hat{\mathbf{A}}_T D_2(\hat{\mathbf{A}}_R) \\ \vdots \\ \hat{\mathbf{A}}_T D_N(\hat{\mathbf{A}}_R) \end{bmatrix} = \begin{bmatrix} \hat{\mathbf{A}}_T \\ \hat{\mathbf{A}}_T \hat{\Phi}_r \\ \vdots \\ \hat{\mathbf{A}}_T \hat{\Phi}_r^{N-1} \end{bmatrix}, \quad (14)$$

where $\hat{\mathbf{A}}_T = [\hat{\mathbf{a}}_t(\phi_1), \hat{\mathbf{a}}_t(\phi_2), \dots, \hat{\mathbf{a}}_t(\phi_K)]$ and $\hat{\mathbf{A}}_R = [\hat{\mathbf{a}}_r(\theta_1), \hat{\mathbf{a}}_r(\theta_2), \dots, \hat{\mathbf{a}}_r(\theta_K)]$ are the transmit and receive direction matrices, respectively:

$$\hat{\Phi}_r = \text{diag} \left[\exp(-j\pi \sin \hat{\theta}_1), \exp(-j\pi \sin \hat{\theta}_2), \dots, \exp(-j\pi \sin \hat{\theta}_K) \right]. \quad (15)$$

There exists an $MN \times MN$ transformation matrix \mathbf{C} corresponding to the finite number of row interchanged operations such that

$$\hat{\mathbf{F}} = \mathbf{C} \hat{\mathbf{A}} = \hat{\mathbf{A}}_T \circ \hat{\mathbf{A}}_R = \begin{bmatrix} \hat{\mathbf{A}}_R D_1(\hat{\mathbf{A}}_T) \\ \hat{\mathbf{A}}_R D_2(\hat{\mathbf{A}}_T) \\ \vdots \\ \hat{\mathbf{A}}_R D_M(\hat{\mathbf{A}}_T) \end{bmatrix} = \begin{bmatrix} \hat{\mathbf{A}}_R \\ \hat{\mathbf{A}}_R \hat{\Phi}_t \\ \vdots \\ \hat{\mathbf{A}}_R \hat{\Phi}_t^{M-1} \end{bmatrix}, \quad (16)$$

where

$$\hat{\Phi}_t = \text{diag} \left[\exp(-j\pi \sin \hat{\phi}_1), \exp(-j\pi \sin \hat{\phi}_2), \dots, \exp(-j\pi \sin \hat{\phi}_K) \right]. \quad (17)$$

We define

$$\mathbf{P}_b = \left[(\hat{\mathbf{A}}_T \hat{\Phi}_r)^T, (\hat{\mathbf{A}}_T \hat{\Phi}_r^2)^T, \dots, (\hat{\mathbf{A}}_T \hat{\Phi}_r^{N-1})^T \right]^T, \quad (18)$$

$$\mathbf{P}_a = \left[(\hat{\mathbf{A}}_T)^T, (\hat{\mathbf{A}}_T \hat{\Phi}_r)^T, \dots, (\hat{\mathbf{A}}_T \hat{\Phi}_r^{N-2})^T \right]^T.$$

Owing to $\mathbf{P}_a \hat{\Phi}_r = \mathbf{P}_b$, $\hat{\Phi}_r = \mathbf{P}_a^\dagger \mathbf{P}_b$, then we get the estimation of DOA:

$$\hat{\theta}_k = \sin^{-1} \left(\frac{\text{angle}(p_k)}{\pi} \right), \quad (19)$$

where p_k is the k th diagonal element of the matrix $\hat{\Phi}_r$.

We also define

$$\mathbf{B}_b = \left[(\hat{\mathbf{A}}_R \hat{\Phi}_t)^T, (\hat{\mathbf{A}}_R \hat{\Phi}_t^2)^T, \dots, (\hat{\mathbf{A}}_R \hat{\Phi}_t^{N-1})^T \right]^T, \quad (20)$$

$$\mathbf{B}_a = \left[(\hat{\mathbf{A}}_R)^T, (\hat{\mathbf{A}}_R \hat{\Phi}_t)^T, \dots, (\hat{\mathbf{A}}_R \hat{\Phi}_t^{N-2})^T \right]^T,$$

Owing to $\mathbf{B}_a \hat{\Phi}_t = \mathbf{B}_b$, $\hat{\Phi}_t = \mathbf{B}_a^\dagger \mathbf{B}_b$, we can also get the estimation of DOD:

$$\hat{\phi}_k = \sin^{-1} \left(\frac{\text{angle}(\lambda_k)}{\pi} \right). \quad (21)$$

where λ_k is the k th diagonal element of the matrix $\hat{\Phi}_t$.

Now we show the major steps of the proposed algorithm as follows.

- (1) Compute the covariance matrix of the received data through (5).
- (2) Estimate the propagator \mathbf{V} from (7).
- (3) Compute the Doppler frequency according to (10), (11), and (13).
- (4) Estimate matrix $\hat{\mathbf{A}}$ from (12); then use the least square method to estimate the DOD and DOA according to (14)~(21).

Remark 1. In fact completely orthogonal signals cannot be found in reality, if we consider the transmitted nonorthogonal signals; that is, $\tilde{\mathbf{a}}_t(\phi_k) \neq \mathbf{a}_t(\phi_k)$, and the output signal can be expressed as $\mathbf{x}(t) = \tilde{\mathbf{A}}\boldsymbol{\eta}(t) + \mathbf{n}(t)$, where $\tilde{\mathbf{A}} = [\tilde{\mathbf{a}}_1, \tilde{\mathbf{a}}_2, \dots, \tilde{\mathbf{a}}_K]$ and $\tilde{\mathbf{a}}_k = \mathbf{a}_r(\theta_k) \otimes \tilde{\mathbf{a}}_t(\phi_k)$. Define $\tilde{\mathbf{A}}_T = [\tilde{\mathbf{a}}_t(\phi_1), \tilde{\mathbf{a}}_t(\phi_2), \dots, \tilde{\mathbf{a}}_t(\phi_K)]$, $\tilde{\mathbf{A}}_T = \mathbf{R}_s \mathbf{A}_T$, $\tilde{\mathbf{A}} = \mathbf{A}_R \circ \tilde{\mathbf{A}}_T = \tilde{\mathbf{R}}_s [\mathbf{A}_T^T, (\mathbf{A}_T \Phi_r)^T, \dots, (\mathbf{A}_T \Phi_r^{N-1})^T]^T$, where $\tilde{\mathbf{R}}_s = \text{diag}[\mathbf{R}_s, \mathbf{R}_s, \dots, \mathbf{R}_s]$. The estimation of $\tilde{\mathbf{A}}$ can be denoted as $\hat{\mathbf{A}} = \tilde{\mathbf{A}}\boldsymbol{\Pi} = \tilde{\mathbf{R}}_s \mathbf{A}\boldsymbol{\Pi}$, $\boldsymbol{\Pi}^{-1} = \boldsymbol{\Pi}$. Estimating the matrix $\tilde{\mathbf{A}}$ from (12), then multiplying $(\tilde{\mathbf{R}}_s)^{-1}$, we get $\hat{\mathbf{A}} = \mathbf{A}\boldsymbol{\Pi}$, using the least square method to estimate the DOD and DOA according to (14)~(21).

3.2. Complexity Analysis. In contrast to ESPRIT algorithm [31], our algorithm has a low computational load; the main computational cost of our algorithm is the estimation of the matrix $\tilde{\mathbf{V}}^H$, which takes $O(2M^2N^2K + MNK^2 + K^3)$; the total computational complexity of our algorithm is $O[M^2N^2(L-1) + 2M^2N^2K + 2MNK^2 + 2K^3 + M(N-1)K^2 + N(M-1)K^2]$, while ESPRIT requires $O(4(L-1)M^2N^2 + 8M^3N^3 + 2K^3 + M(N-1)K^2 + N(M-1)K^2)$ in the eigen decomposition of the covariance matrices. DOA matrix algorithm [32] requires $O(2(L-1)M^2N^2 + 2M^3N^3 + M(N-1)K^2 + N(M-1)K^2)$. Figure 1 shows the complexity comparison with $M = 9$, $N = 9$, $K = 3$, and different L . From Figure 1 we find that our algorithm has much lower computational load than ESPRIT algorithm and DOA matrix algorithm. The computational cost (CPU time) of the proposed algorithm is 0.053029 s, while ESPRIT algorithm and DOA matrix algorithm need 0.210587 s and 0.121686 s, respectively, at $M = 9$, $N = 9$, $K = 3$, and $L = 100$ with CPU frequency 2.20 GHz.

3.3. Discussion

- (1) From Figure 1 we find that our algorithm has much lower computational load than ESPRIT algorithm and DOA matrix algorithm. ESPRIT algorithm employs either eigen-value decomposition (EVD) of cross-correlation matrix or singular value. Using the techniques, the computational complexity is very high. Reference [34] has shown the propagator method (PM) for array signal processing to estimate DOA of incident signals without eigen-value decomposition of cross-correlation matrix of the received data. In our proposed algorithm, propagator \mathbf{V} is a linear operator which can easily be extracted from the data matrix \mathbf{R} . But the construction of matrix $\tilde{\mathbf{V}}$ leads

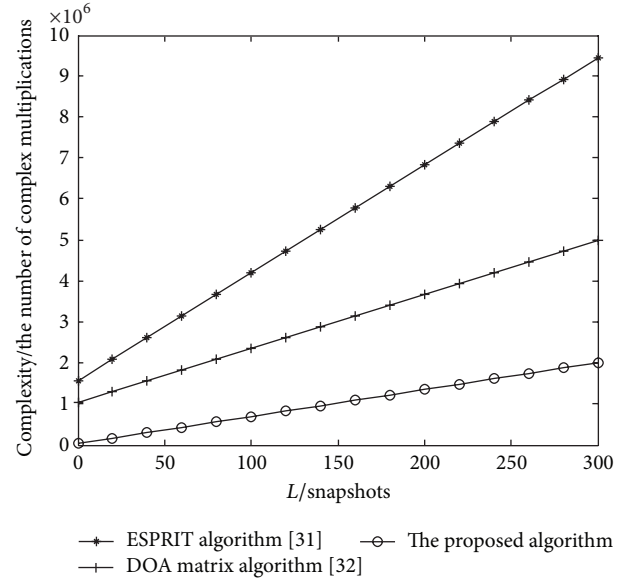


FIGURE 1: Complexity comparison with $M = 9$, $N = 9$, $K = 3$, and different L .

the proposed algorithm's performance to degrade in low SNR. So the proposed algorithm has very close parameters estimation to ESPRIT algorithm and DOA matrix algorithm in high SNR.

- (2) Since the DOA-DODs and Doppler frequencies are given through the corresponding eigenvectors, it can achieve automatically paired estimation of angles and Doppler frequencies.
- (3) The proposed algorithm can eliminate the effect of the spatial colored noise since the new matrix is constructed by (5) and (6).

3.4. The Cramér-Rao Bound (CRB). In this section, we derive CRB of parameter estimation for MIMO radar and rewrite the received data as

$$\mathbf{Z} = \text{row}(\mathbf{X}) = \mathbf{K}(f_d, \phi, \theta) \boldsymbol{\beta} + \mathbf{W}, \quad (22)$$

where $\mathbf{K}(f_d, \phi, \theta) = [\mathbf{K}_1, \mathbf{K}_2, \dots, \mathbf{K}_K]$, $\mathbf{K}_k = \mathbf{a}_f(f_{dk}) \otimes \mathbf{a}_k$, $\mathbf{a}_f(f_{dk}) = [1, e^{j2\pi f_{dk}/f_s}, \dots, e^{j2\pi f_{dk}(L-1)/f_s}]^T$, $\boldsymbol{\beta} = [\sqrt{P}\beta_1, \dots, \sqrt{P}\beta_K]^T$, and \mathbf{W} represents the noise vector. The fisher information matrix (FIM) with respect to $\phi = [\phi_1, \phi_2, \dots, \phi_K]$, $\theta = [\theta_1, \theta_2, \dots, \theta_K]$, and $f_d = [f_{d1}, f_{d2}, \dots, f_{dK}]$ can be calculated as follows [31, 35]:

$$\mathbf{F} = \begin{bmatrix} \mathbf{F}_{11} & \mathbf{F}_{12} & \mathbf{F}_{13} \\ \mathbf{F}_{21} & \mathbf{F}_{22} & \mathbf{F}_{23} \\ \mathbf{F}_{31} & \mathbf{F}_{32} & \mathbf{F}_{33} \end{bmatrix}, \quad (23)$$

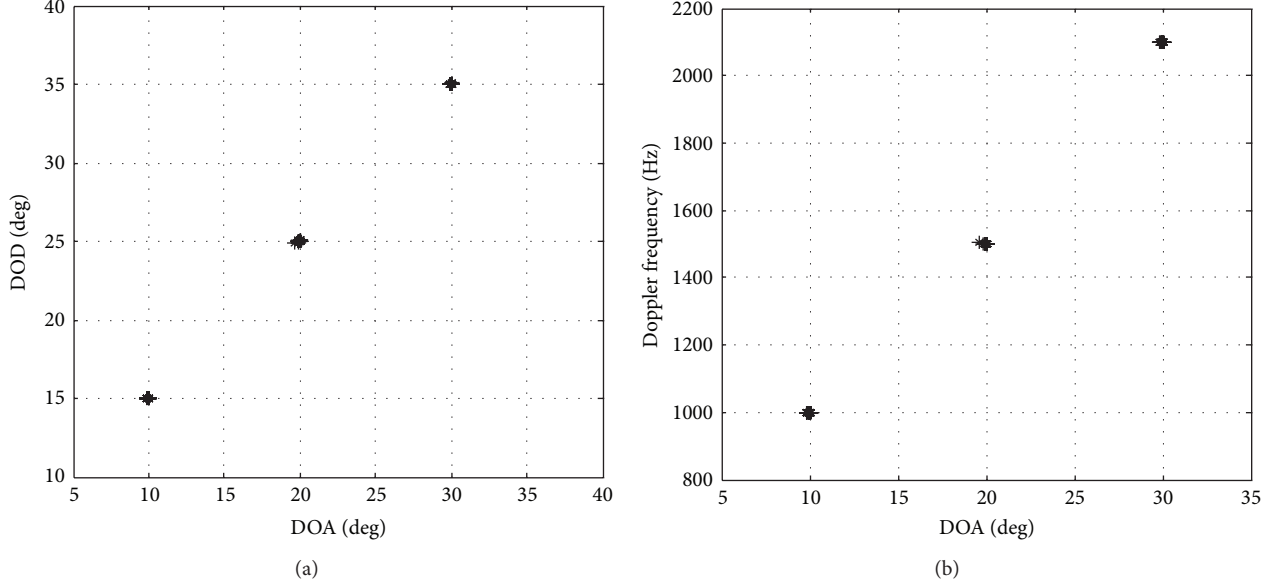


FIGURE 2: Angle and Doppler frequency estimation at SNR = 10 dB.

where

$$\begin{aligned}
 \mathbf{F}_{11} &= 2 \operatorname{Re} \left[\mathbf{\Gamma}^H (\mathbf{K}'_{\theta})^H \mathbf{\Pi}^H \mathbf{Q}^{-1} \mathbf{\Pi} \mathbf{K}'_{\theta} \mathbf{\Gamma} \right], \\
 \mathbf{F}_{12} &= 2 \operatorname{Re} \left[\mathbf{\Gamma}^H (\mathbf{K}'_{\theta})^H \mathbf{\Pi}^H \mathbf{Q}^{-1} \mathbf{\Pi} \mathbf{K}'_{\phi} \mathbf{\Gamma} \right], \\
 \mathbf{F}_{13} &= 2 \operatorname{Re} \left[\mathbf{\Gamma}^H (\mathbf{K}'_{\theta})^H \mathbf{\Pi}^H \mathbf{Q}^{-1} \mathbf{\Pi} \mathbf{K}'_f \mathbf{\Gamma} \right], \\
 \mathbf{F}_{21} &= 2 \operatorname{Re} \left[\mathbf{\Gamma}^H (\mathbf{K}'_{\phi})^H \mathbf{\Pi}^H \mathbf{Q}^{-1} \mathbf{\Pi} \mathbf{K}'_{\theta} \mathbf{\Gamma} \right], \\
 \mathbf{F}_{22} &= 2 \operatorname{Re} \left[\mathbf{\Gamma}^H (\mathbf{K}'_{\phi})^H \mathbf{\Pi}^H \mathbf{Q}^{-1} \mathbf{\Pi} \mathbf{K}'_{\phi} \mathbf{\Gamma} \right], \\
 \mathbf{F}_{23} &= 2 \operatorname{Re} \left[\mathbf{\Gamma}^H (\mathbf{K}'_{\phi})^H \mathbf{\Pi}^H \mathbf{Q}^{-1} \mathbf{\Pi} \mathbf{K}'_f \mathbf{\Gamma} \right], \\
 \mathbf{F}_{31} &= 2 \operatorname{Re} \left[\mathbf{\Gamma}^H (\mathbf{K}'_f)^H \mathbf{\Pi}^H \mathbf{Q}^{-1} \mathbf{\Pi} \mathbf{K}'_{\theta} \mathbf{\Gamma} \right], \\
 \mathbf{F}_{32} &= 2 \operatorname{Re} \left[\mathbf{\Gamma}^H (\mathbf{K}'_f)^H \mathbf{\Pi}^H \mathbf{Q}^{-1} \mathbf{\Pi} \mathbf{K}'_{\phi} \mathbf{\Gamma} \right], \\
 \mathbf{F}_{33} &= 2 \operatorname{Re} \left[\mathbf{\Gamma}^H (\mathbf{K}'_f)^H \mathbf{\Pi}^H \mathbf{Q}^{-1} \mathbf{\Pi} \mathbf{K}'_f \mathbf{\Gamma} \right],
 \end{aligned} \tag{24}$$

and $\mathbf{\Gamma} = \operatorname{diag}(\boldsymbol{\beta})$ denotes the diagonal matrix constructed by the vector $\boldsymbol{\beta}$:

$$\begin{aligned}
 \mathbf{Q} &= \mathbf{I}_{ML} \otimes \mathbf{Q}_w, \quad \mathbf{\Pi} = \mathbf{I}_{MN} - \mathbf{K}(\mathbf{K}^H \mathbf{Q}^{-1} \mathbf{K})^{-1} \mathbf{K}^H \mathbf{Q}^{-1}, \\
 \mathbf{K}'_{\theta} &= \left[\mathbf{a}_f(f_{d1}) \otimes \left[\mathbf{a}_t(\phi_1) \otimes \frac{\partial \mathbf{a}_r(\theta_1)}{\partial \theta_1} \right], \dots, \right. \\
 &\quad \left. \mathbf{a}_f(f_{dK}) \otimes \left[\mathbf{a}_t(\phi_K) \otimes \frac{\partial \mathbf{a}_r(\theta_K)}{\partial \theta_K} \right] \right],
 \end{aligned}$$

$$\begin{aligned}
 \mathbf{K}'_{\phi} &= \left[\mathbf{a}_f(f_{d1}) \otimes \left[\frac{\partial \mathbf{a}_t(\phi_1)}{\partial \phi_1} \otimes \mathbf{a}_r(\theta_1) \right], \dots, \right. \\
 &\quad \left. \mathbf{a}_f(f_{dK}) \otimes \left[\frac{\partial \mathbf{a}_t(\phi_K)}{\partial \phi_K} \otimes \mathbf{a}_r(\theta_K) \right] \right] \\
 \mathbf{K}'_f &= \left[\frac{\partial \mathbf{a}_f(f_{d1})}{\partial f_{d1}} \otimes [\mathbf{a}_t(\phi_1) \otimes \mathbf{a}_r(\theta_1)], \dots, \right. \\
 &\quad \left. \frac{\partial \mathbf{a}_f(f_{dK})}{\partial f_{dK}} \otimes [\mathbf{a}_t(\phi_K) \otimes \mathbf{a}_r(\theta_K)] \right]
 \end{aligned} \tag{25}$$

Then the CRB matrix is

$$\mathbf{CRB} = \mathbf{F}^{-1}. \tag{26}$$

4. Simulation Results

We present the Monte Carlo simulations to assess the parameter estimation performance of our algorithm. Define root mean squared error (RMSE) as $(1/K) \sum_{k=1}^K \sqrt{(1/1000) \sum_{n=1}^{1000} [(\hat{\phi}_{k,n} - \phi_k)^2 + (\hat{\theta}_{k,n} - \theta_k)^2]}$, where $\hat{\theta}_{k,n}$ is the estimate of DOA θ_k of the n th Monte Carlo trial and $\hat{\phi}_{k,n}$ is the estimate of DOD ϕ_k of the n th Monte Carlo trial. Define RMSE of Doppler frequency as $(1/K) \sum_{k=1}^K \sqrt{(1/1000) \sum_{n=1}^{1000} (\hat{f}_{k,n} - f_k)^2}$, where $\hat{f}_{k,n}$ is the estimate of Doppler frequency f_k of the n th Monte Carlo trial. Note that M , N , L , and K are the number of transmit antennas, the receive antennas, the snapshots of the targets, and the number of the targets, respectively. We assume that

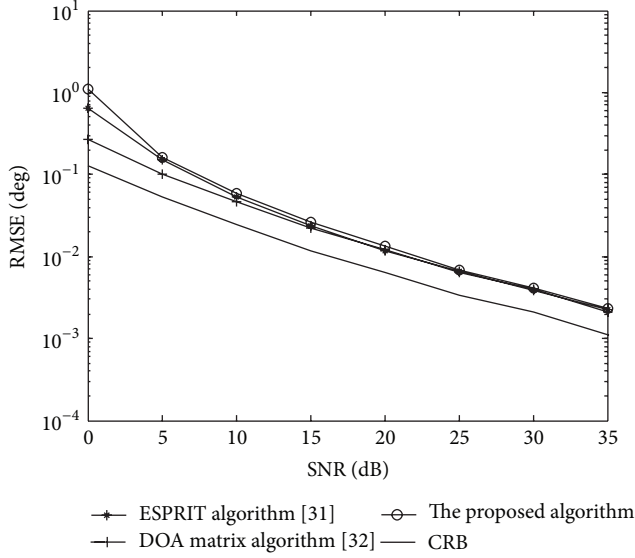


FIGURE 3: Angle estimation comparison performance.

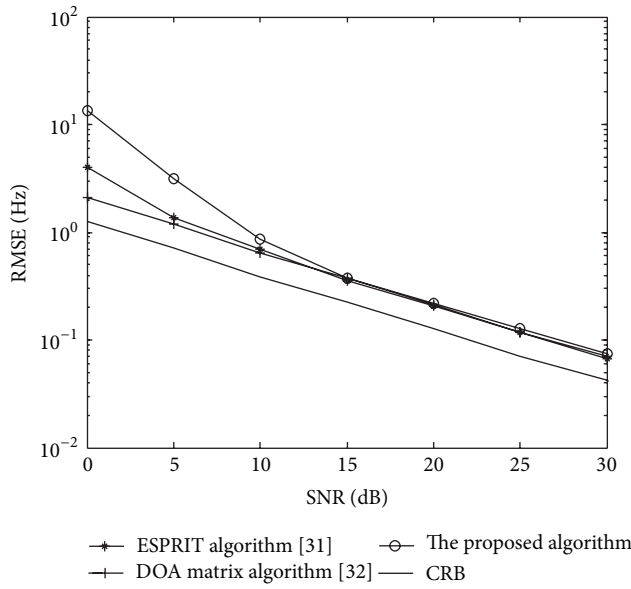
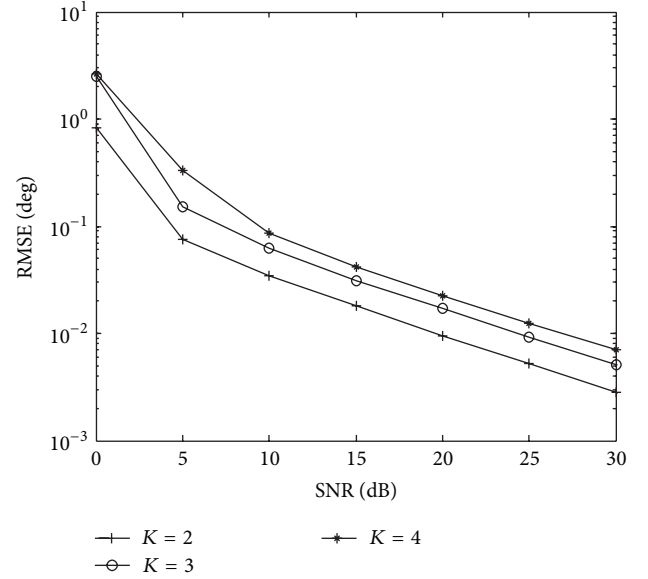
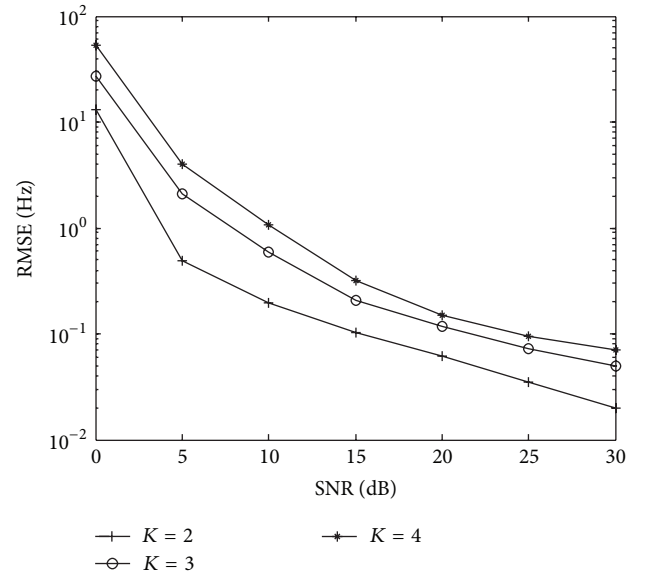


FIGURE 4: Doppler frequency estimation comparison.

there are $K = 3$ independent targets, which are located at angles $(\theta_1, \phi_1) = (10^\circ, 15^\circ)$, $(\theta_2, \phi_2) = (20^\circ, 25^\circ)$, and $(\theta_3, \phi_3) = (30^\circ, 35^\circ)$, respectively. The Doppler frequencies of the three targets are 1000 Hz, 1500 Hz, and 2100 Hz, respectively, and their RCS are given by $\beta_1 = \beta_2 = \beta_3 = 1$. The pulse repeat frequency f_s is 10 KHz for a $M = 9$ and $N = 9$ bistatic MIMO radar. The (m, n) th element of the unknown noise covariance matrix \mathbf{Q}_w is $0.9^{|m-n|} e^{j\pi(m-n)/2}$. Figure 2 shows the estimation results with 100 Monte Carlo trials at $L = 100$. As seen in Figure 2, the DODs, DOAs, and Doppler frequencies of all three targets are correctly paired and well localised.

Figures 3 and 4 show the angle and Doppler frequency estimation performance comparison with $M = 9$, $N = 9$,

FIGURE 5: Angle estimation with different values of K .FIGURE 6: Doppler frequency estimation with different values of K .

$K = 3$, and $L = 100$, where we compare our algorithm with ESPRIT algorithm [31], DOA matrix algorithm [32], and CRB. It is indicated in Figures 3 and 4 that our algorithm has very close parameter estimation performance to ESPRIT algorithm and DOA matrix algorithm in high SNR condition.

The simulation of Figures 5 and 6 investigates the performance of our proposed algorithm under different number of targets K . The number of targets is set as 2 and 4. Our proposed algorithm has the different performance under different K , as shown in Figures 5 and 6 where $M = 9$, $N = 9$, and $L = 100$ are considered. From Figures 5 and 6 we find that angle estimation performance of our proposed algorithm degrades with K increasing.

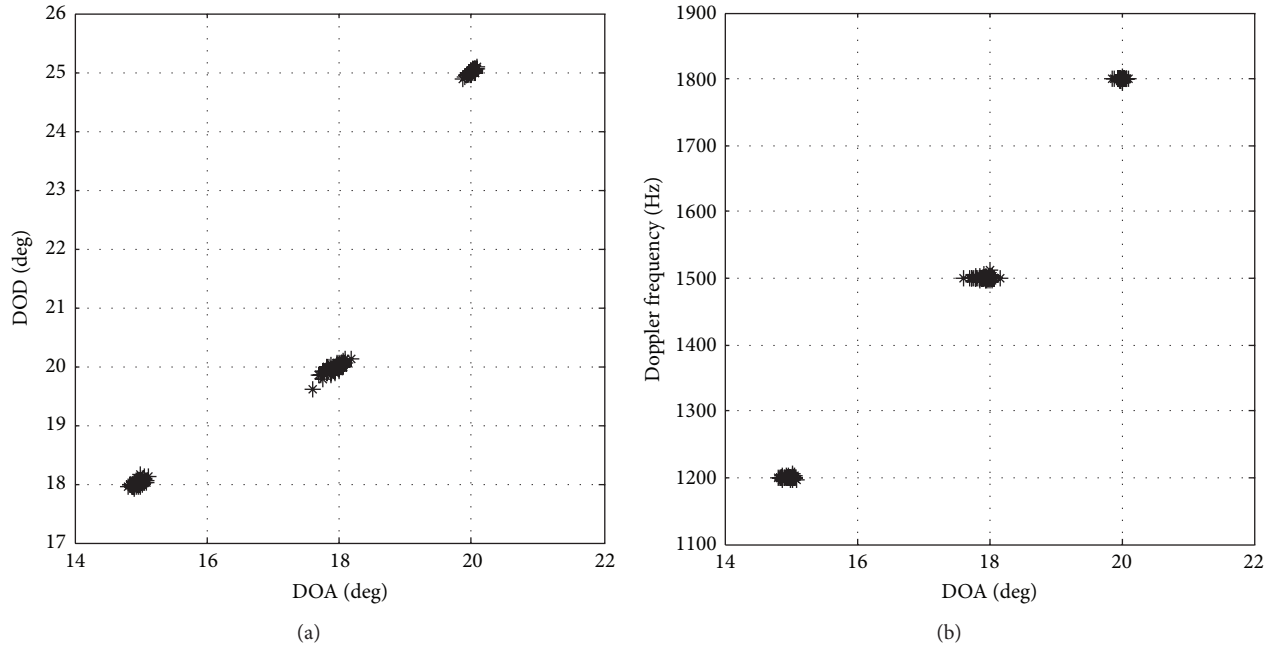


FIGURE 7: Angle and Doppler frequency estimation at SNR = 12 dB.

Figure 7 presents parameter estimation performance with three closely spaced targets, where $M = 8$, $N = 8$, and $L = 100$ are considered. The closely spaced targets are located at angles $(\theta_1, \phi_1) = (15^\circ, 18^\circ)$, $(\theta_2, \phi_2) = (18^\circ, 20^\circ)$, and $(\theta_3, \phi_3) = (20^\circ, 25^\circ)$. The Doppler frequencies of the three targets are 1200 Hz, 1500 Hz, and 1800 Hz, respectively. From Figure 7, we find that our algorithm works well in the case of closely spaced targets.

5. Conclusion

We have presented a low-complexity angle and Doppler frequency estimation based on propagator method for MIMO radar in spatial colored noise. The proposed algorithm can obtain automatically paired transmit and receive angle estimations in the MIMO radar and eliminate the influence of the spatial colored noise. Furthermore, it provides lower computational complexity and has close parameters estimation compared to ESPRIT algorithm and DOA matrix algorithm in high SNR. It is applicable even if the transmitted waveforms are not orthogonal.

Conflict of Interests

The authors declare that there is no conflict of interests regarding the publication of this paper.

Acknowledgments

This work is supported by Nanjing University of Aeronautics and Astronautics Research Funding (NZ2013208). The authors are grateful to the anonymous referees for their

constructive comments and suggestions in improving the quality of this paper.

References

- [1] E. Fishler, A. Haimovich, R. Blum, D. Chizhik, L. Cimini, and R. Valenzuela, "MIMO radar: an idea whose time has come," in *Proceedings of the IEEE Radar Conference*, pp. 71–78, April 2004.
- [2] J. Li and P. Stoica, "MIMO radar-diversity means superiority," in *Proceedings of the 14th Adaptive Sensor Array Process Workshop (ASAP '06)*, Lincoln Lab, Lexington, Mass, USA, December 2006.
- [3] E. Fishler, A. Haimovich, R. S. Blum, L. J. Cimini Jr., D. Chizhik, and R. A. Valenzuela, "Spatial diversity in radars—models and detection performance," *IEEE Transactions on Signal Processing*, vol. 54, no. 3, pp. 823–838, 2006.
- [4] D. R. Fuhrmann and G. S. Antonio, "Transmit beamforming for MIMO radar systems using partial signal correlation," in *Proceedings of the 38th Asilomar Conference on Signals, Systems and Computers*, vol. 1, no. 12, pp. 295–299, November 2004.
- [5] J. Li and P. Stoica, "MIMO radar with colocated antennas," *IEEE Signal Processing Magazine*, vol. 24, no. 5, pp. 106–114, 2007.
- [6] A. M. Haimovich, R. S. Blum, and L. J. Cimini, "MIMO radar with widely separated antennas," *IEEE Signal Processing Magazine*, vol. 25, no. 1, pp. 116–129, 2008.
- [7] M. Jin, G. S. Liao, and J. Li, "Joint DOD and DOA estimation for bistatic MIMO radar," *Signal Processing*, vol. 89, no. 2, pp. 244–251, 2009.
- [8] M. Yang and G. Zhang, "Compressive sensing based parameter estimation for monostatic MIMO noise radar," *Progress in Electromagnetics Research Letters*, vol. 30, pp. 133–143, 2012.
- [9] H. Jiang, Y. Zhang, J. Li, and H. Cui, "A parafac-based algorithm for multidimensional parameter estimation in polarimetric bistatic MIMO radar," *EURASIP Journal on Advances in Signal Processing*, vol. 2013, article 133, 2013.

- [10] M. L. Bencheikh, Y. Wang, and H. Y. He, "Polynomial root finding technique for joint DOA DOD estimation in bistatic MIMO radar," *Signal Processing*, vol. 90, no. 9, pp. 2723–2730, 2010.
- [11] M. Hatam, A. Sheikhi, and M. A. Masnadi-Shirazi, "Target detection in pulse-train mimo radars applying ICA algorithms," *Progress in Electromagnetics Research*, vol. 122, pp. 413–435, 2012.
- [12] J. C. Ding, H. W. Chen, H. Q. Wang, X. Li, and Z. W. Zhuang, "Low-grazing angle target detection and system conguration of MIMO radar," *Progress in Electromagnetics Research B*, vol. 48, pp. 23–42, 2013.
- [13] M. Yang and G. Zhang, "Parameter identifiability of monostatic MIMO chaotic radar using compressed sensing," *Progress in Electromagnetics Research B*, vol. 44, pp. 367–382, 2012.
- [14] C. Chen and X. Zhang, "A low-complexity joint 2D-DOD and 2D-DOA estimation algorithm for MIMO radar with arbitrary arrays," *International Journal of Electronics*, vol. 100, no. 10, pp. 1455–1469, 2013.
- [15] H. Lv, D.-Z. Feng, H.-W. Liu, J. He, and C. Xiang, "Tri-iterative least-square method for bearing estimation in MIMO radar," *Signal Processing*, vol. 89, no. 12, pp. 2686–2691, 2009.
- [16] I. Bekkerman and J. Tabrikian, "Target detection and localization using MIMO radars and sonars," *IEEE Transactions on Signal Processing*, vol. 54, no. 10, pp. 3873–3883, 2006.
- [17] P. Stoica, J. Li, and Y. Xie, "On probing signal design for MIMO radar," *IEEE Transactions on Signal Processing*, vol. 55, no. 8, pp. 4151–4161, 2007.
- [18] J. Li and P. Stoica, *MIMO Radar Signal Processing*, Wiley-IEEE Press, New York, NY, USA, 2008.
- [19] Q. He, R. S. Blum, H. Godrich, and A. M. Haimovich, "Target velocity estimation and antenna placement for MIMO radar with widely separated antennas," *IEEE Journal on Selected Topics in Signal Processing*, vol. 4, no. 1, pp. 79–100, 2010.
- [20] H. W. Chen, Y. P. Chen, X. Li, and Z. W. Zhuang, "Extended ambiguity function for bistatic MIMO radar," *Journal of Systems Engineering and Electronics*, vol. 23, no. 2, pp. 109–114, 2012.
- [21] L. Xu, J. Li, and P. Stoica, "Target detection and parameter estimation for MIMO radar systems," *IEEE Transactions on Aerospace and Electronic Systems*, vol. 44, no. 3, pp. 927–939, 2008.
- [22] J. Li, P. Stoica, L. Xu, and W. Roberts, "On parameter identifiability of MIMO radar," *IEEE Signal Processing Letters*, vol. 14, no. 12, pp. 968–971, 2007.
- [23] L. Xu, J. Li, and P. Stoica, "Adaptive techniques for mimo radar," in *Proceedings of the 4th IEEE Sensor Array and Multichannel Signal Processing (SAM '06)*, pp. 258–262, July 2006.
- [24] F. C. Robey, S. Coutts, D. Weikle, J. C. McHarg, and K. Cuomo, "MIMO radar theory and experimental results," in *Proceedings of the 38th Asilomar Conference on Signals, Systems and Computers*, vol. 1, no. 12, pp. 300–304, November 2004.
- [25] C. Duofang, C. Baixiao, and Q. Guodong, "Angle estimation using ESPRIT in MIMO radar," *Electronics Letters*, vol. 44, no. 12, pp. 770–771, 2008.
- [26] Z. Zheng, J. Zhang, and J. Y. Zhang, "Joint DOD and DOA estimation of bistatic MIMO radar in the presence of unknown mutual coupling," *Signal Processing*, vol. 92, no. 12, pp. 3039–3048, 2012.
- [27] R. Xie, Z. Liu, and J.-X. Wu, "Direction finding with automatic pairing for bistatic MIMO radar," *Signal Processing*, vol. 92, no. 1, pp. 198–203, 2012.
- [28] X. Zhang, H. Wu, J. Li, and D. Xu, "Computationally efficient DOD and DOA estimation for bistatic MIMO radar with propagator method," *International Journal of Electronics*, vol. 99, no. 9, pp. 1207–1221, 2012.
- [29] C. Jinli, G. Hong, and S. Weimin, "Angle estimation using ESPRIT without pairing in MIMO radar," *Electronics Letters*, vol. 44, no. 24, pp. 1422–1423, 2008.
- [30] X. Zhang, L. Xu, L. Xu, and D. Xu, "Direction of departure (DOD) and direction of arrival (DOA) estimation in MIMO radar with reduced-dimension mUSIC," *IEEE Communications Letters*, vol. 14, no. 12, pp. 1161–1163, 2010.
- [31] W.-B. Fu, T. Su, Y.-B. Zhao, and X.-H. He, "Joint estimation of angle and Doppler frequency for bistatic MIMO radar in spatial colored noise," *Journal of Electronics & Information Technology*, vol. 33, no. 12, pp. 2858–2862, 2011.
- [32] C. Yunhe, "Joint estimation of angle and Doppler frequency for bistatic MIMO radar," *Electronics Letters*, vol. 46, no. 2, pp. 170–172, 2010.
- [33] M. L. Bencheikh, Y. Wang, and H. He, "Polynomial root finding technique for joint DOA DOD estimation in bistatic MIMO radar," *Signal Processing*, vol. 90, no. 9, pp. 2723–2730, 2010.
- [34] S. Marcos, A. Marsal, and M. Benidir, "The propagator method for source bearing estimation," *Signal Processing*, vol. 42, no. 2, pp. 121–138, 1995.
- [35] P. Stoica and R. L. Moses, *Spectral Analysis of Signals*, Prentice Hall, Upper Saddle River, NJ, USA, 2005.

Research Article

Correction of Channel Imbalance for MIMO SAR Using Stepped-Frequency Chirps

Xiulian Luo,^{1,2} Yunkai Deng,¹ Robert Wang,¹ Lei Guo,^{1,2} and Mingjiang Wang^{1,2}

¹ Institute of Electronics, Chinese Academy of Sciences, Beijing 100190, China

² Graduate University of the Chinese Academy of Sciences, Beijing 100080, China

Correspondence should be addressed to Xiulian Luo; xiaoluo6070@126.com

Received 20 December 2013; Accepted 19 February 2014; Published 3 April 2014

Academic Editor: Wei Xu

Copyright © 2014 Xiulian Luo et al. This is an open access article distributed under the Creative Commons Attribution License, which permits unrestricted use, distribution, and reproduction in any medium, provided the original work is properly cited.

To simultaneously achieve two-dimensional high resolution and wide swath in synthetic aperture radar (SAR), azimuth MIMO structure combined with stepped-frequency chirp signals was developed via splitting the antenna into N subapertures. During transmitting each subaperture transmits a chirp pulse at a different carrier frequency, while during receiving every subaperture receives the N scattered pulses at the same time. Separating the N scattered pulses received by each subaperture and downlinking them to the ground yield N^2 different signal paths. Due to the dedicated network in the SAR system, the channel imbalance is inevitable. To correct the channel imbalance, this paper presents an external calibration method, where the channel characteristics are estimated from the peak value of a strong point target for each channel. Simulation and real raw data experiments are performed to validate the proposed method.

1. Introduction

Resolution and swath width are two key specifications for the spaceborne stripmap SAR. However, high azimuth resolution and wide range swath imaging pose contradicting requirement on conventional SAR system design. In order to overcome this inherent contradiction, the displaced phase center antenna (DPCA) techniques [1–3] and the multiple-input and multiple-output (MIMO) antenna techniques [4–7] are introduced to acquire additional spatial sampled information. On the other hand, the range resolution, determined by the pulse bandwidth, has to be increased to match the azimuth resolution. However, transmitting and receiving wideband signals burden the active electronically steered array (AESA) antenna and the echo sampled equipment [8, 9], thus confining the range resolution. Fortunately, a wideband chirp signal can be synthesized by a group of narrowband subchirps centered at stepped frequencies, which requires the synthetic bandwidth technique [8–10].

As the synthetic bandwidth technique will reduce the number of equivalent phase centers (EPCs), the additional sampled information in DPCA SAR is actually used to

increase the range bandwidth other than the equivalent PRF [11]. Therefore, this paper focuses on the MIMO SAR using stepped-frequency chirps (STFC) [4, 5], where both the equivalent PRF and the range bandwidth can be N times increased. However, as this MIMO system yields N^2 different signal paths, the channel imbalance is inevitable. For each subband, the collected data is from a DPCA system, where the channel imbalance can be regarded as the inner-band imbalance which results in azimuth ambiguities [12]. The imbalance among different subbands can be regarded as the interband imbalance which leads to degradation of the range performance after synthetic bandwidth [13].

Therefore, in order to acquire high quality images, effective correction of the channel imbalance is indispensable. The available correction methods can be classified as two categories: methods on internal calibration [14] and methods on raw data [15, 16]. However, all these correction methods only either handled the inner-band imbalance in the DPCA system with single subband [15, 16] or concerned the multiple subbands system with single subaperture [14]. In [14], Deng et al. gave the internal calibration approach, where the imbalance information is obtained from the internal calibration

data acquired from the calibration subsystem. This method can be extended to the MIMO system using STFC. Nevertheless, N^2 internal calibration subsystems are required, which dramatically increases the complexity of the SAR systems. In addition, it cannot correct imbalance introduced by the antennas. The subspace projection method proposed in [16] and the azimuth cross-correlation method presented in [15] do not require additional subsystem. However, they cannot correct the interband imbalance, as the phase difference caused by different carrier frequencies is range dependent and hard to compensate.

Usually, the channel imbalance information (phase and amplitude) does not change within a certain illumination time [15]. Moreover, many artificial corner reflectors have been distributed here and there for radiometric calibration [17]. Therefore, this paper proposes an external calibration method where the channel imbalance information is estimated from the peak value of a corner reflector or a strong point target in N^2 small complex images. Afterwards, the estimated channel errors are used to correct the channel imbalance when imaging for much larger data.

Succeeding sections are organized as follows. In Section 2, the MIMO SAR using STFC is conceptually designed and the corresponding image formation processing is briefly summarized. In Section 3, the external correction method is presented, followed by the simulation and real raw data experiments in Section 4 to validate the proposed method. Finally, the conclusion is drawn in Section 5.

2. MIMO SAR Using Stepped-Frequency Chirps

2.1. Conceptual Design. The MIMO SAR simultaneously transmits a set of stepped-frequency chirps, regarded as subbands, via multiple subapertures. During receiving, every subaperture receives all the N subbands in one PRI. The schematic diagram and the corresponding timeline of transmitted pulses and received echoes are illustrated in Figure 1, where the circles represent the location of the equivalent phase centers (EPCs) of the subbands, and the number inside the circles represents the sequence number of the subbands.

In order to separate two frequency-adjacent subbands and absent gaps from the connection of subbands at the same time, the subband bandwidth B_s is required to be equal to the frequency step Δf . The relationship of the time frequency for the transmitted pulses is illustrated in Figure 2, where f_m ($m = 1, 2, \dots, N$) is the carrier frequency of the m th subband.

The baseband echo of the m th subband for each subaperture is acquired as follows. Demodulate the radio frequency (RF) pulses with the carrier frequency f_m . Then filter the demodulated signal with an analog low pass filter (LPF) whose bandwidth is greater than B_s . Afterwards, convert the analog signal to a digital signal via an AD convertor with a sampling rate greater than the cutoff frequency of the LPF. As illustrated in Figure 3, due to the imperfect filtering and the Gibbs phenomenon of the signal spectrum, some spectral component of one subband is leaked into the adjacent subband, thus resulting in subband interference. In

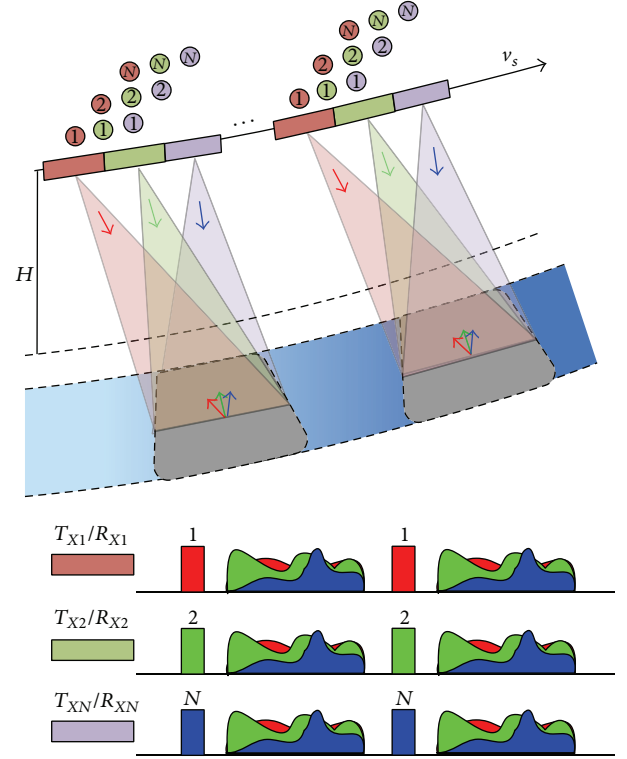


FIGURE 1: Schematic diagram of the MIMO SAR using STFC.

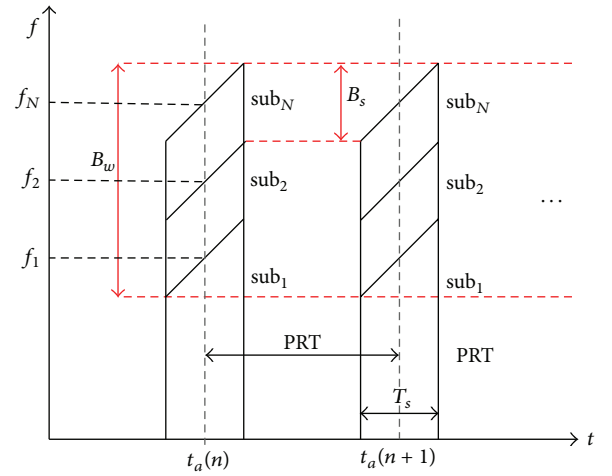


FIGURE 2: Relationship of time frequency of transmitted pulses.

order to reduce the interference, a digital rectangular window can be applied to the sampled data before imaging. Then, the interference only results from the spectral component outside the spectrum bandwidth, as illustrated by the blue-shaded region in Figure 3. As stated in [13], the influence of the subband interference under this situation can be ignored because it results in -47 dB ambiguities in range. In fact, when the subband bandwidth is larger, the ambiguities in range will be reduced further. This is because the relative amplitude of the ambiguities is determined by relating the leakage energy

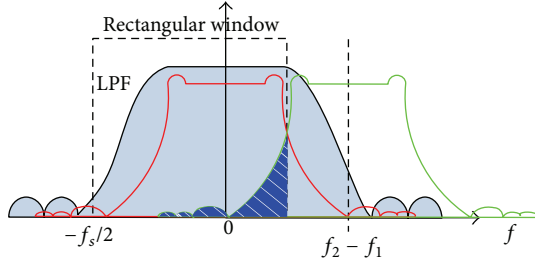


FIGURE 3: Separation of two frequency-adjacent subbands.

to the whole energy [13]. Moreover, the leakage energy is inversely proportional to the bandwidth-time product.

Therefore, in this paper, for each subaperture, adjacent subbands are assumed to be completely separated; that is, the subband interference is not considered.

2.2. Image Formation Processing. When the uniform sampling condition

$$\frac{1}{\text{PRF}} = \frac{l_{az}}{2v_s} \cdot N, \quad (1)$$

with PRF the system pulse repetition frequency, l_{az} the length of the subaperture, and v_s the velocity of the sensor, is not satisfied, multichannel reconstruction [1] is required. The reference position during the multichannel reconstruction should be the center of the whole antenna to make the EPCs to be synthesized coincide spatially. Afterwards, the frequency domain bandwidth synthesis method [9, 10] is applied to acquire a large bandwidth pulse, followed by the conventional imaging. It should be noted that the synthesized signal should be firstly converted to the original echo domain if the CS imaging algorithm is adopted. The block diagram of the image formation processing for this MIMO SAR system is presented in Figure 4. Assume that $N = 2$, and then the variation of the distribution of EPCs introduced by multichannel reconstruction and bandwidth synthesis is shown in Figure 5 (ignore the first row and the dashed circles, which will be used in Section 4).

3. Correction of the Channel Imbalance

In this section, the correction of both amplitude and phase imbalance among channels will be presented. As this correction method is based on a focused strong point target in N^2 small complex images, separating imaging for each subband and each subaperture is required.

The base-band echo for the m th subband (transmitted by the m th subaperture) received by the n th subaperture is

$$S_{m,n}(\tau, \eta) = N_{m,n}(\tau, \eta) + A_{m,n} \cdot \exp(j\varphi_{m,n}) \cdot \text{rect}\left(\frac{\tau - R_{m,n}(\eta)/c}{T_r}\right)$$

$$\begin{aligned} & \times \exp\left\{-j2\pi f_m \cdot \left(\frac{R_{m,n}(\eta)}{c}\right)\right\} \\ & \cdot \exp\left\{j\pi k_r \left(\tau - \frac{R_{m,n}(\eta)}{c}\right)^2\right\}, \end{aligned} \quad (2)$$

with τ the range time, η the azimuth time, k_r the chirp rate, c the light velocity, T_r the pulse duration, $A_{m,n}$ the amplitude characteristic, $\varphi_{m,n}$ the phase characteristic, $N_{m,n}(\tau, \eta)$ the system noise and the echo of other targets, and $R_{m,n}(\eta)$ the instantaneous distance in propagation between the transmitter and the receiver for the corner reflector (point target). Applying the Taylor series expansion and ignoring the quadratic phase term quadratic term error during the equivalence of the two-way slant ranges, $R_{m,n}(\eta)$ can be approximated as

$$R_{m,n}(\eta) = R(\eta - \Delta\eta_{m,n}), \quad (3)$$

where

$$\Delta\eta_{m,n} = \frac{(m + n - N - 1)l_{az}}{2v_s}, \quad (4)$$

is the azimuth time interval between the corresponding EPC and the center of the whole antenna, and

$$R(\eta) = 2\sqrt{R_0^2 + (v_s\eta - x_0)^2}, \quad (5)$$

represents the two-way slant range from the center of the whole antenna to the point target. In (5), R_0 and x_0 indicate the slant range and azimuth coordinates of the point target, respectively.

First, the imaging for the N^2 echoes is independently performed. Due to lower PRF than Nyquist sampling rate, strong azimuth ambiguities of the point target appear in the N^2 images. However, the ambiguities are far away from the real point target, thus scarcely impacting the estimation. The imaging result can be approximated as [18]

$$\begin{aligned} S_{m,n}(\tau, \eta) &= N'_{m,n}(\tau, \eta) + N'_{m,n,\text{amb}}(\tau, \eta) \\ &+ A_k \cdot \exp(j\varphi_k) \cdot G \cdot p_r \left(\tau - \frac{2R_0}{c}\right) \\ &\cdot \exp\left\{-j2\pi f_m \cdot \left(\frac{2R_0}{c}\right)\right\} \cdot p_{a,m,n} \left(\eta - \frac{x_0}{v_s}\right) \\ &+ A_k \cdot \exp(j\varphi_k) \cdot p_r \left(\tau - \frac{2R_0}{c}\right) \end{aligned}$$

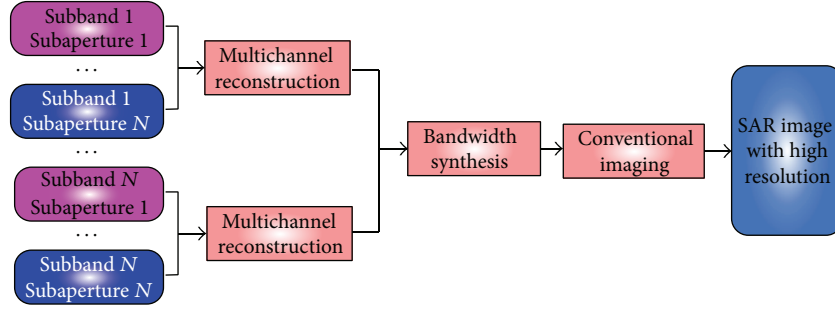


FIGURE 4: Block diagram of the image formation processing.

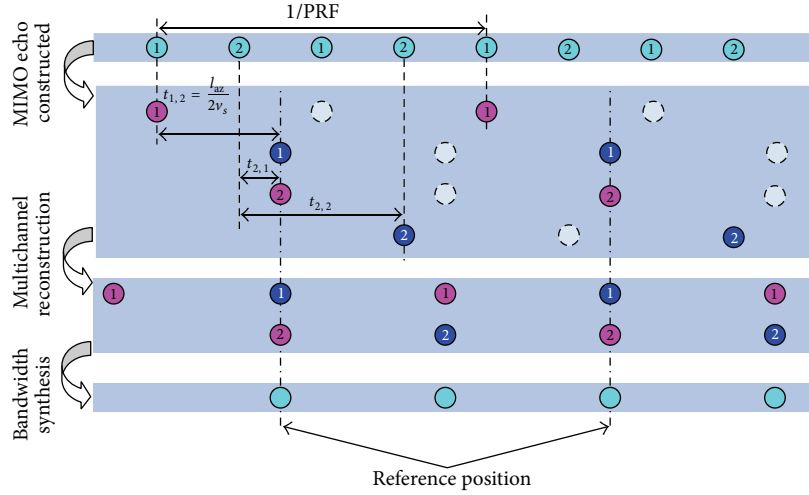


FIGURE 5: Distribution of the EPCs.

$$\begin{aligned}
 & \cdot \exp \left\{ -j2\pi f_m \cdot \left(\frac{2R_0}{c} \right) \right\} \\
 & \times \sum_{i=-N+1, i \neq 0}^{N-1} G_{\text{amb},i} \\
 & \cdot p_{a,m,n} \left(\eta - \frac{x_0}{v_s} + i \cdot \frac{\text{PRF}}{k_a} \right), \quad (6)
 \end{aligned}$$

where k_a is the azimuth chirp rate, G and $G_{\text{amb},i}$ are the gain resulting from the imaging of the “real” part and the ambiguous part of the point target, respectively, $N'_{m,n}(\tau, \eta)$ and $N'_{m,n,\text{amb}}(\tau, \eta)$ are the “real” and ambiguous response of other targets and noise, and $p_{a,m,n}$ and p_r are the amplitude of the azimuth and range impulse responses, two sinc-like functions [18]. According to (3), $p_{a,m,n}(\eta)$ can be rewritten as

$$p_{a,m,n}(\eta) = p_a(\eta - \Delta\eta_{m,n}), \quad (7)$$

where p_a is also a sinc-like function.

Considering that the peak of the corner reflector is generally much greater than other terms at position (R_0, x_0) ,

only the “real” response of the corner reflector is taken into account when deriving the correction method, which is

$$\begin{aligned}
 S_{m,n}(\tau, \eta) &= A_{m,n} \cdot \exp(j\varphi_{m,n}) \cdot G \cdot p_r \left(\tau - \frac{2R_0}{c} \right) \\
 &\times \exp \left\{ -j2\pi f_m \cdot \left(\frac{2R_0}{c} \right) \right\} \\
 &\cdot p_a \left(\eta - \frac{x_0}{v_s} - \Delta\eta_{m,n} \right). \quad (8)
 \end{aligned}$$

Second, the peak position and value of the corner reflector are estimated from these N^2 small complex images. In order to make the estimation more accurate, the 2D-interpolation over the peak point and its surrounding points is performed. Consequently, the peak position of the corner reflector is acquired to be $\bar{\tau}_{m,n} \approx 2R_0/c$. The amplitude of the peak is $\bar{A}_{m,n} \approx A_{m,n}$, and the phase of the peak is

$$\bar{\phi}_{b,m,n} \approx \varphi_{m,n} - 2\pi f_m \cdot \bar{\tau}_{m,n}. \quad (9)$$

In fact, in order to reduce the influence of the noise, \bar{A}_k and $\bar{\phi}_{b,k}$ are obtained by averaging the values of the points within the two-dimensional 1 dB main lobe. The first channel

(subband 1 and subaperture 1) is set as the reference channel. Then the estimated amplitude error matrix is

$$\overline{\mathbf{A}}_{\mathbf{E}} = \text{diag} \frac{\{\overline{A}_{1,1}, \overline{A}_{1,2}, \dots, \overline{A}_{1,N}, \dots, \overline{A}_{N,1}, \overline{A}_{N,2}, \dots, \overline{A}_{N,N}\}}{\overline{A}_{1,1}}. \quad (10)$$

Third, compensate the inherent phase caused by the offset of the carrier frequencies f_m from the center frequency of the synthesized wideband signal, f_c . After this, the phase of the peak value is changed as

$$\overline{\phi}_{m,n} = \overline{\phi}_{b,m,n} + 2\pi\Delta f_m \cdot \overline{\tau}_{m,n} \approx \varphi_{m,n} - 2\pi f_c \cdot \left(\frac{2R_0}{c}\right), \quad (11)$$

where

$$\Delta f_m = \left(m - \frac{1+N}{2}\right) \Delta f, \quad m = 1, \dots, N. \quad (12)$$

Therefore, the estimated phase error matrix can be expressed as

$$\begin{aligned} \overline{\Phi}_{\mathbf{E}} = & \left(\text{diag} \left\{ \exp(j\overline{\phi}_{1,1}), \dots, \exp(j\overline{\phi}_{1,N}), \dots, \right. \right. \\ & \left. \left. \exp(j\overline{\phi}_{N,1}), \dots, \exp(j\overline{\phi}_{N,N}) \right\} \right) \\ & \times \left(\exp(j\overline{\phi}_{1,1}) \right)^{-1}. \end{aligned} \quad (13)$$

Finally, correct the channel imbalance according to (10) and (13). The correction matrix is

$$\mathbf{C} = \left(\overline{\mathbf{A}}_{\mathbf{E}} \overline{\Phi}_{\mathbf{E}} \right)^{-1}. \quad (14)$$

Therefore, the correction is implemented as

$$\begin{aligned} \mathbf{S}_c = & \mathbf{C} \cdot [S_{1,1}(\tau, \eta), \dots, S_{1,N}(\tau, \eta), \dots, \\ & S_{N,1}(\tau, \eta), \dots, S_{N,N}(\tau, \eta)]^T. \end{aligned} \quad (15)$$

It should be noted that the data size of $S_{m,n}(\tau, \eta)$ in (2) can be much smaller than that in (15) to improve the processing efficiency. After correction, the balanced data \mathbf{S}_c is used to form the final image with high resolution. The whole processing is shown in Figure 6, where the image formation processing strategy is presented in Figure 4.

4. Experimental Results

4.1. Simulation Experiment. In the simulation, the 2D imaging of a plane scene containing a letter “A” and a 4-time (6 dB) brighter point target is performed, and this point target is inside the letter “A.” The simulation parameters are specified in Table 1.

TABLE 1: System parameters.

Parameter	Symbol	Value
Center frequency (GHz)	f_c	9.685
Slant range of scene center (km)	R_0	30
Sensor velocity (m/s)	v_s	215
Subaperture length (m)	l_{az}	2.5
System PRF (Hz)	PRF	140
Transmit pulse length (us)	T_p	10
Number of subbands/subapertures	N	2
Transmitted pulse bandwidth (MHz)	B_s	60
Sampling rate in range (MHz)	F_r	72
SNR (dB)	SNR	6

The accurate amplitude and phase errors are given in the 2nd and 3rd columns of Table 2, respectively. The first channel is set as the reference channel. According to the estimation method proposed in the last section, the amplitude and phase errors are estimated and then presented in the 4th and 5th columns of Table 2, respectively. The imaging results without and with correction of the channel imbalance are shown in Figures 7(a) and 7(b), respectively. The range comparison of the point target and its surroundings is shown in Figure 7(c). From Figure 7, one can observe that the ambiguities in azimuth (caused by the inner-band imbalance) and the raising of the side-lobes in range (stemming from the interband imbalance) are removed by the correction of channel imbalance.

From the simulation experiment, it is concluded that the proposed correction (compensation) method can correct both the inner-band and the interband imbalance for the simulated MIMO SAR data.

4.2. Real Raw Data Experiment. For the real raw data, the imaging scene is much more complicated than the simulated data, thus possibly affecting the estimation accuracy. As the real raw data collected by a MIMO SAR using STFC is not available, in this subsection, the proposed correction method is assessed with an X-band airborne SAR using a single aperture and two STFCs which are transmitted in two consecutive PRIs. In this SAR, both the subband bandwidth and the frequency step are 30 MHz, the original PRF is 1600 Hz, and the sensor velocity is 215 m/s. The distribution of the original EPCs is illustrated by the first row in Figure 5.

To validate the proposed correction method on the real raw data, the echo data for the MIMO system have to be firstly constructed. As discussed before, in the MIMO system using STFCs, the echo for each subband can be regarded from a DPCA system [1]. Further, in the DPCA system, the data of each channel is equivalent to the counterpart single channel data processed by an azimuth time delay function and then N times subsampling [2]. Herein, the counterpart single channel data is the original subband data, and the delay function in Doppler domain for the m th subband received by the n th subaperture is set to

$$H_{m,n}(f_\eta) = \exp \{-j2\pi f_\eta \cdot t_{m,n}\}, \quad (16)$$

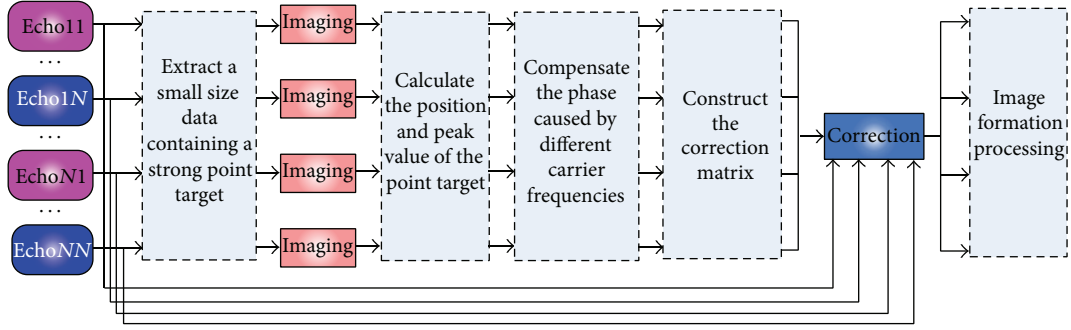


FIGURE 6: Block diagram of the channel imbalance correction.

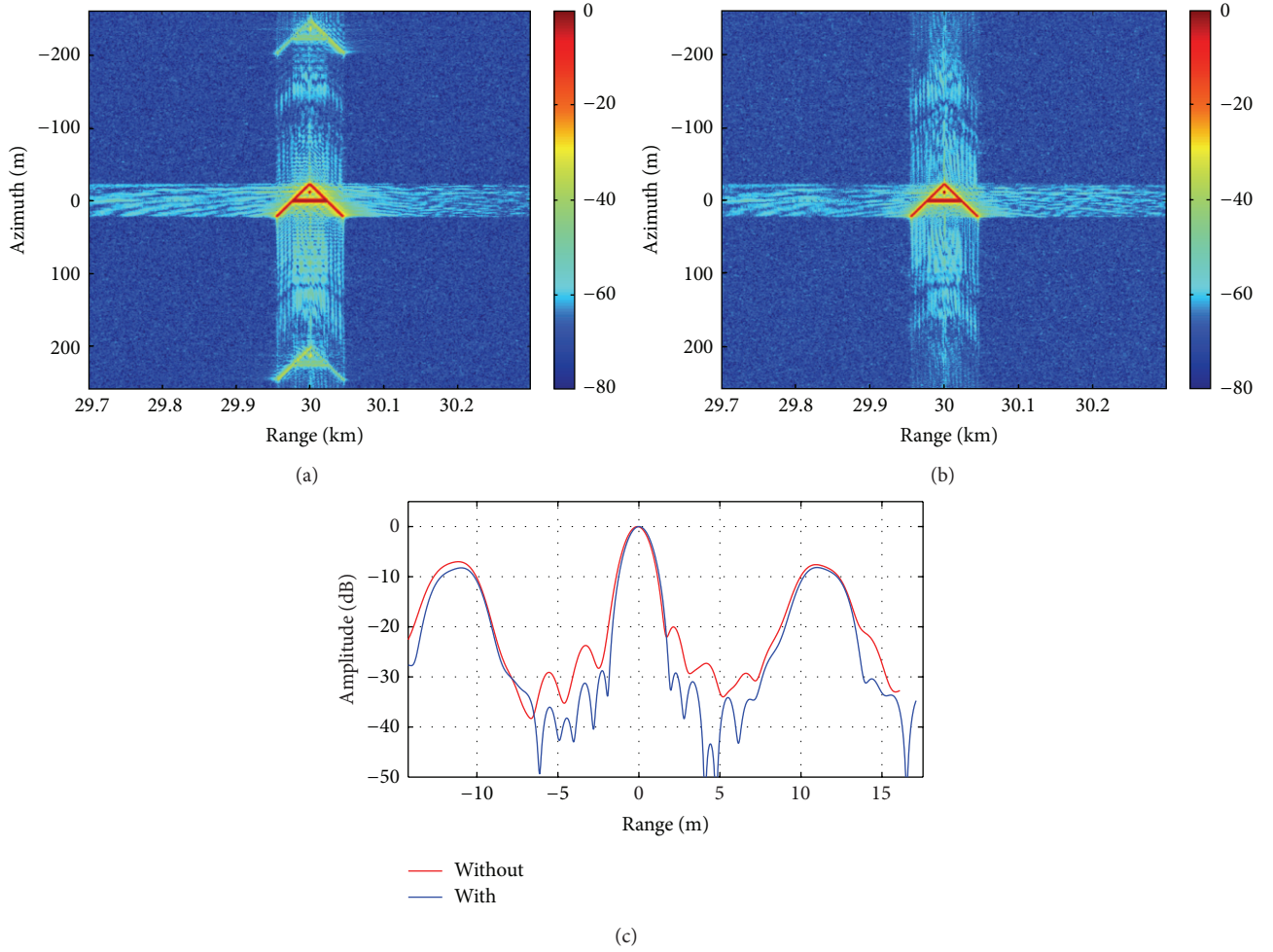


FIGURE 7: Simulation results for OFDM-MIMO SAR. (a) Imaging result without correction of channel imbalance. (b) Imaging result with correction of channel imbalance. (c) Range comparison of the amplification of the point target in (a) and (b).

TABLE 2: Channel errors (CE).

Channel (m, n)	Exact CE		Estimated CE for simulated data		Estimated CE for constructed raw data	
	A_k	φ_k ($^\circ$)	\bar{A}_k	$\bar{\varphi}_k$ ($^\circ$)	\bar{A}_k	$\bar{\varphi}_k$ ($^\circ$)
1, 1	1	0	1	0	1	0
1, 2	1.3	25	1.296	24.308	1.253	28.201
2, 1	1.5	30	1.500	29.649	1.468	33.325
2, 2	1.4	45	1.401	44.426	1.352	42.720

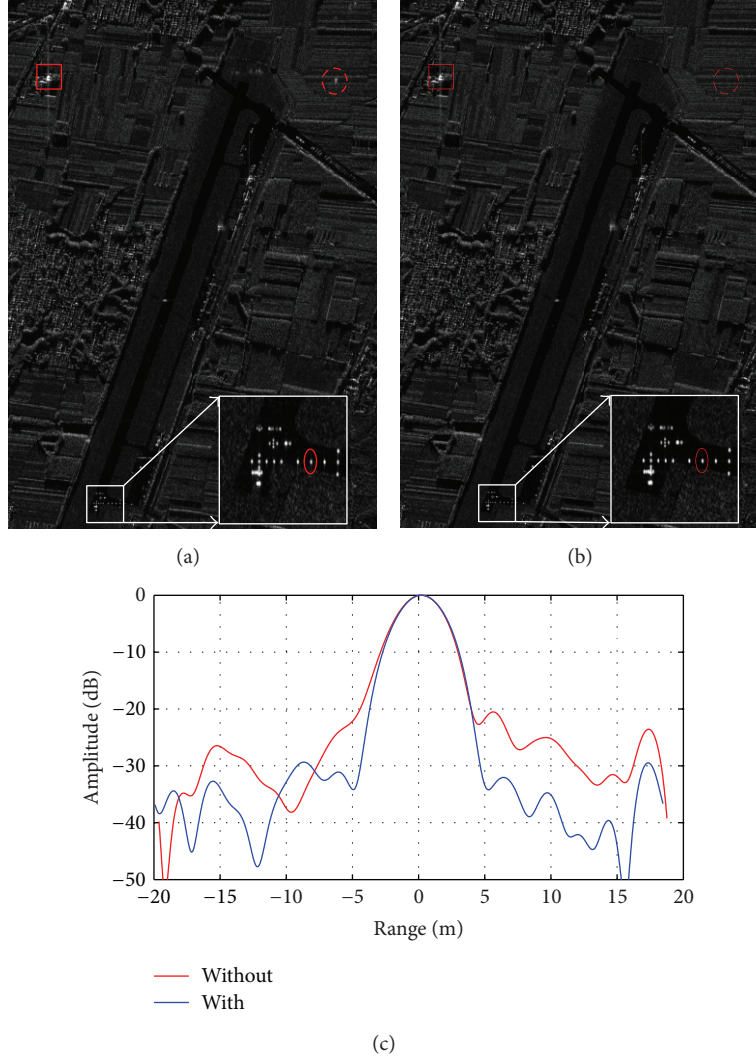


FIGURE 8: Real raw data results for OFDM-MIMO SAR. (a) Without correction. (b) With correction. (c) Range comparison of the amplification of the corner reflector.

with f_η the Doppler frequency, $t_{1,1} = 0$, $t_{1,2} = l_{az}/2v_s = (3/4) \cdot (1/2\text{PRF})$, $t_{2,1} = t_{1,2} - (1/4\text{PRF})$, and $t_{2,2} = t_{1,2} + t_{2,1}$. Then, the distribution of the EPCs for the four channels can be illustrated by the 2nd, 3rd, 4th, and 5th rows in Figure 5 where the dashed circles represent the discarded pulses to realize a two-time subsampling. With consideration of the channel errors specified in the 2nd and 3rd columns of Table 2, the four echo data of the MIMO system using STFCs are well constructed.

According to the error estimation process presented in Figure 6, the measured channel errors are listed in the 6th and 7th columns of Table 2. The final imaging results without and with correction of the channel imbalance are shown in Figures 8(a) and 8(b), respectively. The corner reflector used for external calibration is marked by ellipse in the two figures. After interpolation and amplification, the range comparison of the corner reflector in Figures 8(a) and 8(b) is shown in Figure 8(c), where one can see that the raising of the side lobes is eliminated by the compensation. Additionally, in

Figure 8(a) the peak amplitude of the ambiguity marked by dashed circle is -15.89 dB while in Figure 8(b) the ambiguity is not distinguishable from the background.

Therefore, for the constructed MIMO raw data, the presented correction method is also effective in removing the channel imbalance.

5. Conclusion

MIMO SAR using stepped frequency chirps is of great potential for future high-resolution wide-swath SAR missions. Channel imbalance is a key problem for this novel SAR mode, as it relates to the imaging performance. This paper proposed a simple and effective method to correct this channel imbalance, which was validated by simulation and real raw data experiments. Other problems, such as the system design and the orbit model, are not discussed in this paper. Nevertheless, they are also indispensable, especially when this novel mode is applied to spaceborne missions.

Conflict of Interests

The authors declare that there is no conflict of interests regarding the publication of this paper.

References

- [1] N. Gebert, G. Krieger, and M. A. Moreira, "Digital beamforming on receive: techniques and optimization strategies for high-resolution wide-swath SAR imaging," *IEEE Transactions on Aerospace and Electronic Systems*, vol. 45, no. 2, pp. 564–592, 2009.
- [2] W. Jing, M. Xing, C.-W. Qiu, Z. Bao, and T.-S. Yeo, "Unambiguous reconstruction and high-resolution imaging for multiple-channel SAR and Airborne experiment results," *IEEE Geoscience and Remote Sensing Letters*, vol. 6, no. 1, pp. 102–106, 2009.
- [3] A. Currie and M. A. Brown, "Wide-swath SAR," *IEE Proceedings, Part F: Radar and Signal Processing*, vol. 139, no. 2, pp. 122–135, 1992.
- [4] W.-Q. Wang, "Space-time coding MIMO-OFDM SAR for high-resolution imaging," *IEEE Transactions on Geoscience and Remote Sensing*, vol. 49, no. 8, pp. 3094–3104, 2011.
- [5] Y. Song and R. Yang, "High resolution, wide swath SAR using sub-aperture sub-band technique," in *Proceedings of the CIE International Conference on Radar (ICR '06)*, Shanghai, China, October 2006.
- [6] G. Krieger, "MIMO-SAR: opportunities and pitfalls," *IEEE Transactions on Geoscience and Remote Sensing*, no. 99, pp. 1–18, 2013.
- [7] J. H. G. Ender and J. Klare, "System architectures and algorithms for radar imaging by MIMO-SAR," in *Proceedings of the IEEE Radar Conference (RADAR '09)*, Pasadena, Calif, USA, May 2009.
- [8] A. W. Doerry, *SAR Processing with Stepped Chirps and Phased Array Antennas*, Sandia Nat. Lab., Albuquerque, NM, USA, 2006.
- [9] P. Berens, "SAR with ultra-high range resolution using synthetic bandwidth," in *Proceedings of the IEEE International Geoscience and Remote Sensing Symposium (IGARSS '99)*, pp. 1752–1754, Hamburg, Germany, July 1999.
- [10] W. Nel, J. Tait, R. Lord, and A. Wilkinson, "The use of a frequency domain stepped frequency technique to obtain high range resolution on the CSIR X-Band SAR system," in *Proceedings of the 6th IEEE AFRICON Conference in Africa*, pp. 327–332, October 2002.
- [11] J. H. G. Ender and A. R. Brenner, "PAMIR—a wideband phased array SAR/MTI system," *IEE Proceedings: Radar, Sonar and Navigation*, vol. 150, no. 3, pp. 165–172, 2003.
- [12] C.-G. Gao, Y.-K. Deng, and J. Feng, "Theoretical analysis on the mismatch influence of displaced phase center multiple-beam SAR systems," *Journal of Electronics & Information Technology*, vol. 33, no. 8, pp. 1828–1832, 2011.
- [13] X. Luo, R. Wang, Y. Deng, and W. Xu, "Influences of channel errors and interference on the OFDM-MIMO SAR," in *Proceedings of the IEEE Radar Conference*, pp. 1–5, Ottawa, Canada, 2013.
- [14] Y. Deng, H. Zheng, R. Wang, J. Feng, and Y. Liu, "Internal calibration for stepped-frequency chirp SAR imaging," *IEEE Geoscience and Remote Sensing Letters*, vol. 8, no. 6, pp. 1105–1109, 2011.
- [15] J. Feng, C. Gao, Y. Zhang, and R. Wang, "Phase mismatch calibration of the multichannel SAR based on azimuth cross-correlation," *IEEE Geoscience and Remote Sensing Letters*, vol. 10, no. 4, pp. 903–907, 2013.
- [16] L. Zhang, M.-D. Xing, C.-W. Qiu, and Z. Bao, "Adaptive two-step calibration for high-resolution and wide-swath SAR imaging," *IET Radar, Sonar and Navigation*, vol. 4, no. 4, pp. 548–559, 2010.
- [17] J. C. Curlander and R. N. McDonough, *Synthetic Aperture Radar: Systems and Signal Processing*, John Wiley & Sons, New York, NY, USA, 1991.
- [18] I. G. Cumming and F. H. Wong, *Digital Processing of Synthetic Aperture Radar Data: Algorithms and Implementation*, Artech House, Norwood, Mass, USA, 2005.

Research Article

Special MISO-SAR and MIMO-SAR Modes for Bidirectional Imaging

Hai Jiang,^{1,2} Hongjun Song,¹ Lei Guo,^{1,2} and Wei Wang^{1,2}

¹ Institute of Electronics, Chinese Academy of Sciences, Beijing 100190, China

² University of Chinese Academy of Sciences, Beijing 100190, China

Correspondence should be addressed to Hai Jiang; bradley0226@163.com

Received 15 January 2014; Accepted 27 February 2014; Published 31 March 2014

Academic Editor: Wei Xu

Copyright © 2014 Hai Jiang et al. This is an open access article distributed under the Creative Commons Attribution License, which permits unrestricted use, distribution, and reproduction in any medium, provided the original work is properly cited.

The paper proposes special multiple-input single-output synthetic aperture radar (MISO-SAR) and multiple-input multiple-output SAR (MIMO-SAR) for bidirectional imaging, which can simultaneously illuminate two areas from different directions in azimuth. For the proposed MISO-SAR, two subpulses with the same carrier frequency and phase coding are transmitted with different azimuth directions by switching the phase coefficients in the transmit modules, and echoes corresponding to the subpulses are received by the main lobe and the first grating lobe of the whole antenna. To suppress mutual interference, the two subpulses are transmitted with different range-frequency bands, and their echoes are demodulated and recorded in different channels in the proposed MIMO-SAR. This paper presents the system design of these modes and analyzes their azimuth ambiguity to signal ratio (AASR). Besides, simulation results on points are carried out to validate the proposed bidirectional imaging modes.

1. Introduction

The repeated acquisition of synthetic aperture radar (SAR) images is very useful for multiple observation applications, such as moving targets detection, terrain change detection, and velocity measurements by along-track interferometry [1–3]. For a SAR satellite, the time lag between two acquisitions must be more than several hours. However, for iceberg drifts or ship velocity measurements [4, 5], the time lag should be less than several minutes. The single channel bidirectional SAR imaging mode is proposed in [1] and implemented via a phased planner antenna to generate both main lobe and grating lobes to illuminate different areas. This imaging mode was first achieved by TerraSAR-X satellite [6–10]. TerraSAR-X and TanDEM-X have several new modes and finished some commissions in [7, 11–14]. Another advantage for bidirectional SAR mode is that the simultaneous imaging into two directions can obtain two widely separated Doppler subbands, which can offer many different interferometry or GMTI applications [15–19].

The major drawback of the single channel bidirectional SAR imaging mode is the high azimuth ambiguity to signal

ratio (AASR) level caused by the grating lobes. To suppress the high AASR level, a pulse repetition frequency (PRF) value higher than the one in the conventional stripmap mode with the same antenna length is required or the azimuth processed bandwidth is reduced. Therefore, the bidirectional imaging mode is balanced by the limited swath width due to the higher PRF and/or by the impaired azimuth resolution due to the reduced azimuth processed bandwidth.

In this paper, two special imaging modes for bidirectional imaging based on the phased planner antenna are proposed. In the first mode, two subpulses are transmitted in turn with different azimuth antenna beams by switching the phase coefficients in the transmit modules, and echoes of the two subpulses are simultaneously received by the main lobe and the first grating lobe of the whole antenna and recorded in a single channel. This imaging scheme with two transmitted subpulses and a single receive channel is named as multiple-input single-output SAR (MISO-SAR) for bidirectional imaging. To further distinguish the echoes, two subpulses are transmitted with different frequency bands, and then their echoes are demodulated and recorded in two channels. As

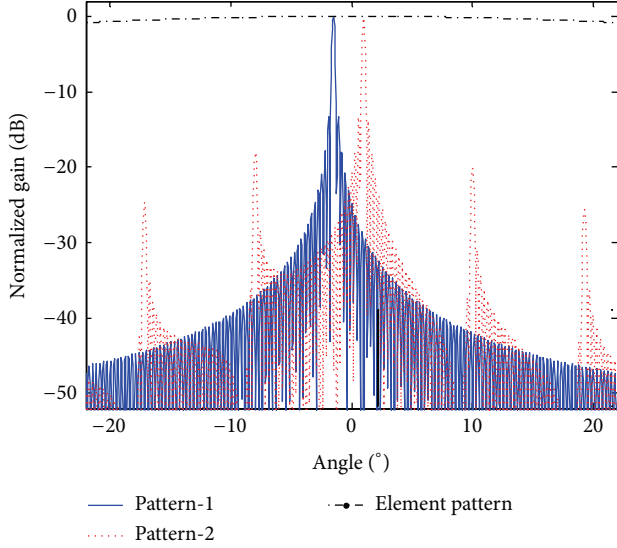


FIGURE 1: Antenna patterns of the phased array antenna.

a result, the second imaging mode is named as multiple-input multiple-output SAR (MIMO-SAR) for bidirectional imaging. Compared with the bidirectional imaging mode in [1], the two proposed imaging modes are with the lower AASR level. The system design and signal processing of the proposed modes are given in detail. Furthermore, simulation experiments on point targets are carried out to validate the proposed bidirectional imaging modes.

The paper has five sections. Section 2 focuses on presenting two proposed imaging modes for bidirectional imaging. The system design and AASR analysis of the two modes are given in Section 3. The imaging approach of two modes and simulation experiments on point targets are presented in Section 4. The paper is concluded in Section 5.

2. Special MISO-SAR and MIMO-SAR Modes

2.1. Antenna Pattern of the Phased Array Antenna. To implement antenna beam scanning in both azimuth and elevation, a phased two-dimension (2D) planar antenna is usually adopted in the future spaceborne SAR missions. According to the working principle of the phased array antenna, the one-way antenna pattern of the phased array antenna can be written as follows [4]:

$$G(\theta) = G_e(\theta) \cdot \left| \frac{1}{K} \sum_{k=0}^{K-1} C_{k,T} \cdot \exp\left(j \frac{2\pi k}{\lambda} L_{ae} \sin \theta\right) \right|, \quad (1)$$

with

$$G_e(\theta) = G_0 \cdot \left| \sin c\left(\frac{L_{ae}}{\lambda} \sin \theta\right) \right|, \quad (2)$$

where $G_e(\theta)$ indicates the antenna pattern of the element antenna, K is the number of the transmit/receive (T/R) modules, λ is the wavelength, and L_{ae} is the length of the

element antenna. To avoid the grating lobes during antenna beam steering, the length L_{ae} should be

$$L_{ae} \leq \frac{\lambda}{1 + |\sin \theta_{s,\max}|}, \quad (3)$$

where $\theta_{s,\max}$ is the maximal steering angle. To implement the desired antenna beam pointing direction, the phase coefficients of the T/R modules are expressed as

$$C_{k,T} = a_{k,T} \cdot \exp\left(j \frac{2\pi k}{\lambda} L_{ae} \sin \theta_s\right), \quad (4)$$

$$C_{k,T,g} = a_{k,T} \cdot \exp\left(j \frac{2\pi}{\lambda} \cdot \left\lfloor \frac{k}{M} \right\rfloor \cdot L_{ae} \sin \theta_s\right), \quad (5)$$

where $a_{k,T}$ is constant, θ_s indicates the desired antenna beam pointing direction, and M is the number of the T/R modules with the same phase coefficient. With the phase coefficient of (2), the distance between the main lobe and the first grating lobe is

$$\Delta\theta = \frac{\lambda}{M \cdot L_{ae}}. \quad (6)$$

Figure 1 shows antenna patterns of the phased array antenna with phase coefficient coding of (4) and (5), where the element antenna L_{ae} is 0.02 m, the wavelength is 0.03125 m, the number of elements is 320, and M is 20. Furthermore, the antenna beam pointing direction θ_s in (4) is -1.5° , while θ_s in (5) is 1° .

2.2. Acquisition Geometry. Figure 2 shows the proposed modified bidirectional SAR acquisition geometry with simultaneous fore and aft acquisitions. In the bidirectional SAR imaging mode in [1], each pulse is transmitted to two different areas in azimuth and its corresponding echoes are received by the main lobe and the first grating lobe of the same azimuth antenna pattern. However, the large transmitted radar pulse is divided into two subpulses to be transmitted into different azimuth areas in the proposed modified bidirectional SAR, and the subpulses are transmitted by different azimuth antenna patterns by steering the azimuth antenna beam as shown in Figure 2(a). The echoes of two subpulses from two azimuth areas are received by the main lobe and the first grating lobe of the whole azimuth antenna, respectively.

In the first case, two subpulses are with the same carrier frequency and phase coding, while their corresponding echoes are simultaneously received and sampled in a single channel. Therefore, this imaging scheme is named MISO-SAR. To suppress the interference between echoes, two transmitted subpulses could be with different carrier frequencies, and their corresponding echoes are received and sampled with different channels. As a result, the second imaging scheme is named MIMO-SAR.

Figure 3 shows azimuth antenna patterns of the proposed modified bidirectional SAR acquisition. It demonstrates that the well-behavior transmitting antenna pattern may suppress the power of grating lobes and side lobes of the azimuth receiving antenna pattern. In Figure 3, M is 10 and the

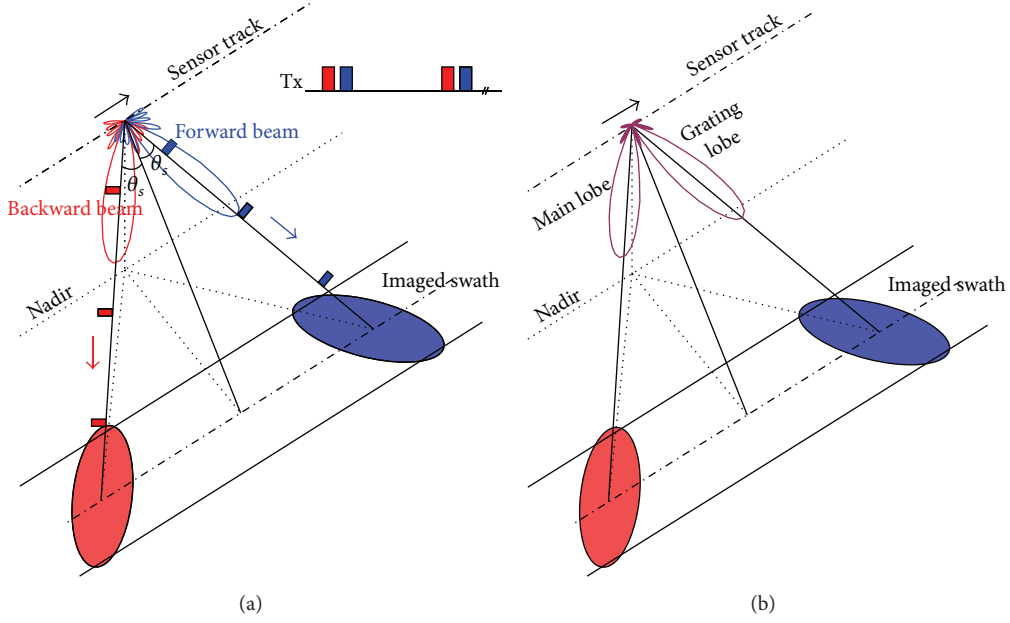


FIGURE 2: Modified bidirectional SAR acquisition geometry with simultaneous fore and aft acquisitions: (a) radar pulses transmitting and (b) radar echoes receiving.

angular interval between the main lobe and the first grating lobe is 8.952° . Therefore, the azimuth backward and forward beam pointing direction is -4.476° and 4.476° , respectively. Furthermore, the main lobe and the first grating lobe share the same antenna gain and are with 4 dB gain reduction compared with the main lobe of the azimuth transmitting beam pattern.

3. AASR Analysis and System Design

3.1. AASR Analysis. For the proposed MISO-SAR system, the AASR for the backward area and the forward area are computed as follows:

$$\begin{aligned} \text{AASR}_b = & \left(\sum_{k \neq 0} \int_{-B_a/2+f_{dc,b}}^{B_a/2+f_{dc,b}} \left[G_{t,b}(f_a + k \cdot \text{PRF}) \right. \right. \\ & \left. \left. + G_{t,f}(f_a + k \cdot \text{PRF}) \right] \right. \\ & \left. \cdot G_r(f_a + k \cdot \text{PRF}) df_a \right) \\ & \times \left(\int_{-B_a/2+f_{dc,b}}^{B_a/2+f_{dc,b}} \left[G_{t,b}(f_a) + G_{t,f}(f_a) \right] \right. \\ & \left. \cdot G_r(f_a) df_a \right)^{-1}, \end{aligned}$$

$$\begin{aligned} \text{AASR}_f = & \left(\sum_{k \neq 0} \int_{-B_a/2+f_{dc,f}}^{B_a/2+f_{dc,f}} \left[G_{t,b}(f_a + k \cdot \text{PRF}) \right. \right. \\ & \left. \left. + G_{t,f}(f_a + k \cdot \text{PRF}) \right] \right. \\ & \left. \cdot G_r(f_a + k \cdot \text{PRF}) df_a \right) \\ & \times \left(\int_{-B_a/2+f_{dc,f}}^{B_a/2+f_{dc,f}} \left[G_{t,b}(f_a) + G_{t,f}(f_a) \right] \right. \\ & \left. \cdot G_r(f_a) df_a \right)^{-1}, \end{aligned} \quad (7)$$

where $f_a = 2v \sin \theta / \lambda$ is the Doppler frequency, v is the speed of the radar, θ is the squint angle, B_a is the processed Doppler bandwidth, G_r is the azimuth receiving antenna pattern, k is an integer, $G_{t,b}$ and $G_{t,f}$ indicate the azimuth transmitting antenna patterns for the aft and fore directions, respectively, and $f_{dc,b}$ and $f_{dc,f}$ are the Doppler centroids for backward and forward imaging. For well-symmetric fore and aft azimuth directions, the AASR is connected to the spectral separation as the grating lobe is the strongest contribution of the ambiguous signal energy to the main lobe as shown in Figure 3.

Similar to the single channel bidirectional SAR system, the cyclic behavior of divergent and coincident folding also becomes visible by plotting the AASR versus the selected PRF as shown in Figure 4. The simulation parameters are listed in Table 1. As the grating lobe moves relative to the main lobe,

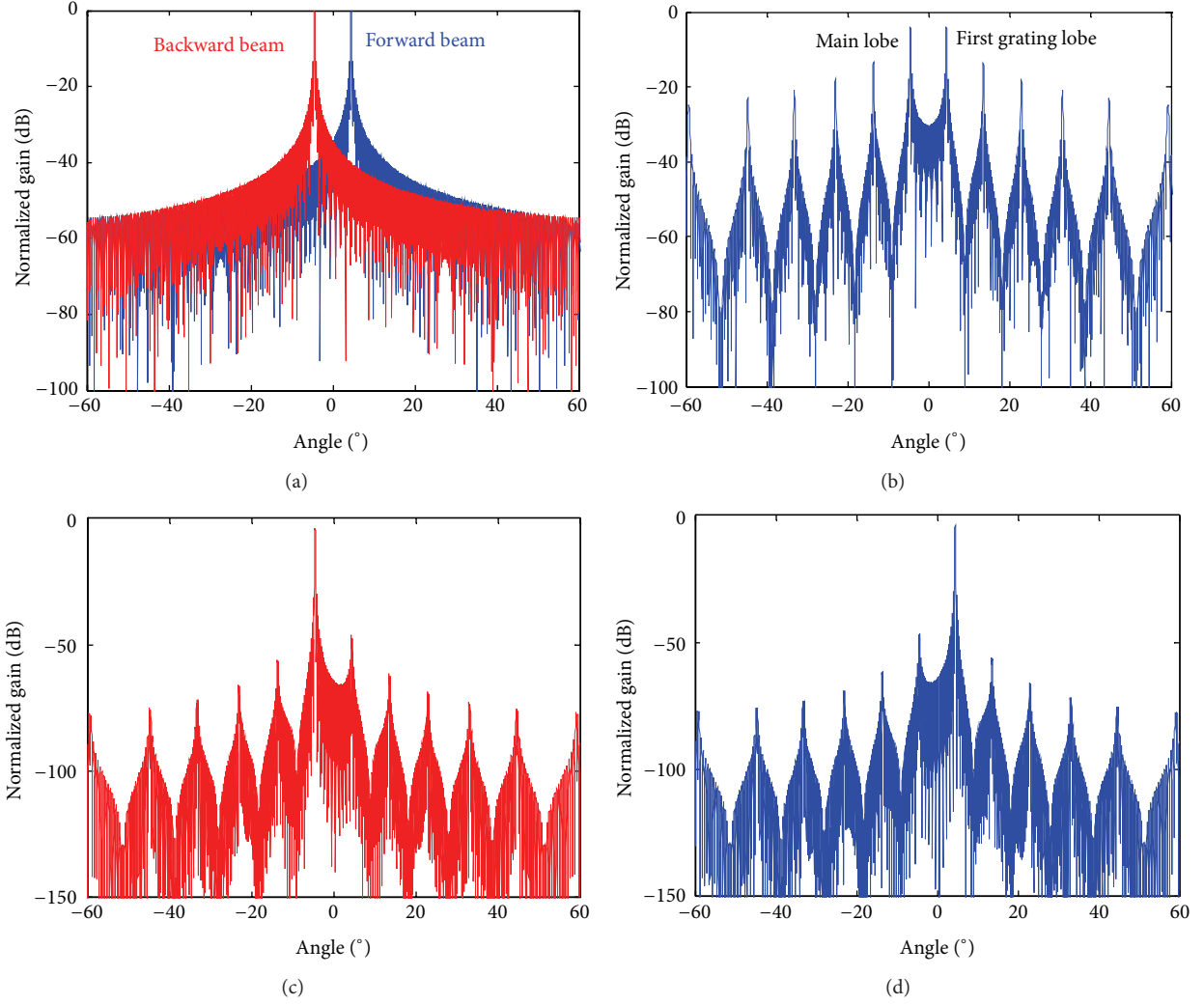


FIGURE 3: Azimuth antenna patterns of the phased antenna. (a) Transmitting antenna pattern. (b) Receiving antenna pattern. (c) Two-way antenna pattern for backward imaging. (d) Two-way antenna pattern for forward imaging.

TABLE 1: Simulation parameters.

Parameters	Value
Antennal length (m)	6.4
Azimuth element antenna length (m)	0.02
Number of T/R in azimuth	320
Number of T/R modules with the same phase on receive	20
Carrier frequency in MISO-SAR (GHz)	9.6
Carrier frequencies in MIMO-SAR (GHz)	9.4, 9.8
Transmitted pulse duration (μ s)	10
Pulse bandwidth (MHz)	150
Sampled frequency (MHz)	180
Sensor velocity (m/s)	7500
Slant range (km)	700
Squint angles for bidirectional imaging (°)	± 4.476

the AASR oscillates between high and low values. The high value of the AASR is about 0 dB and keeps constant, since it

reflects the coincident folding in the two-way antenna pattern for backward imaging and forward imaging. The low value becomes lower with increasing PRF, since Doppler spectra of backward imaging and forward imaging areas can be better separated by band-pass Doppler filtering. As the gain of the main lobe and the first grating lobe is the same in Figure 3(b), the AASR in the aft and fore images are equivalent. Compared with the AASR of the single channel bidirectional SAR system in [1], the AASR of the proposed MISO-SAR system is better than the conventional bidirectional SAR system, since the power of the grating lobes and side lobes of the azimuth receiving antenna pattern is suppressed by the azimuth transmitting antenna pattern as shown in Figure 2. In other words, for the desired AASR level (e.g., about -18 dB) as shown in Figure 4, the selected PRF should be more than 6500 Hz in the single channel bidirectional SAR system, while the selected PRF only should be more than 5100 Hz in the proposed MISO-SAR system. In this simulation, the processed Doppler bandwidth is related to the 6 dB beam

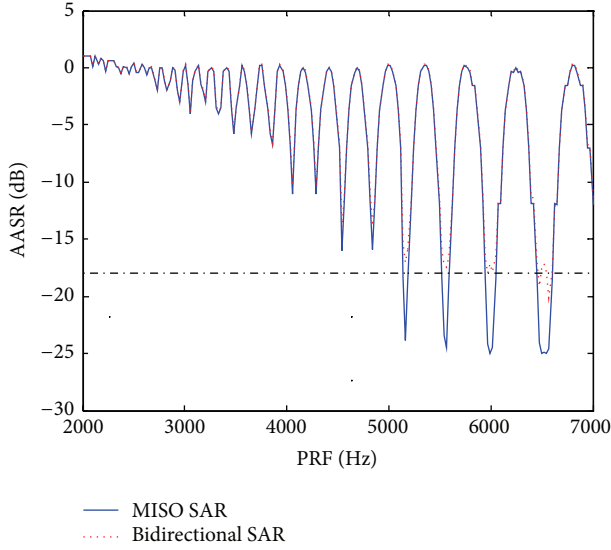


FIGURE 4: AASR of the proposed MISO-SAR and bidirectional SAR versus acquisition PRF.

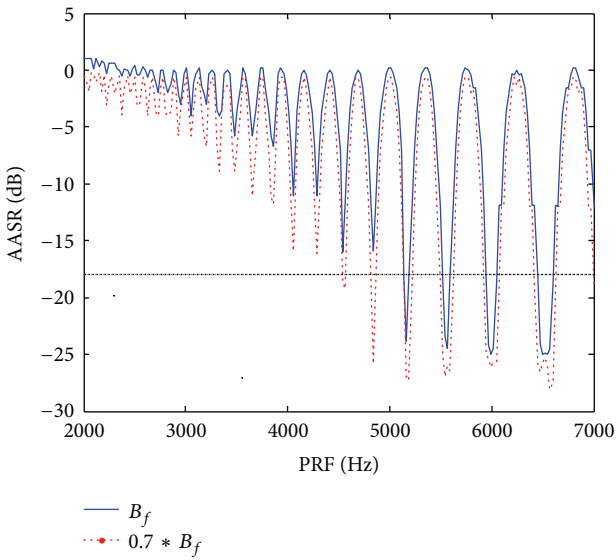


FIGURE 5: AASR of the proposed MISO-SAR versus acquisition PRF for different processed Doppler bandwidths.

width of the two-way azimuth antenna pattern and about 1454 Hz.

Similar to conventional SAR imaging modes, the AASR level can be improved after reducing the processed Doppler bandwidth under the same condition as shown in Figure 5 but with the impaired azimuth resolution.

From (7), the high AASR level is caused by the interference between echoes of two transmitted subpulses in a single pulse repetition interval (PRI). To suppress the interference in the proposed MIMO-SAR for bidirectional imaging, two subpulses are transmitted with different range-frequency bands and their echoes can be easily separated by range-frequency band-pass filtering. As two subpulses have

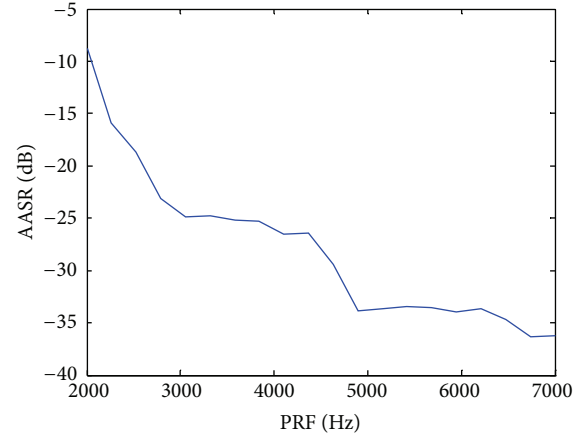


FIGURE 6: AASR of the proposed MIMO-SAR versus acquisition PRF.

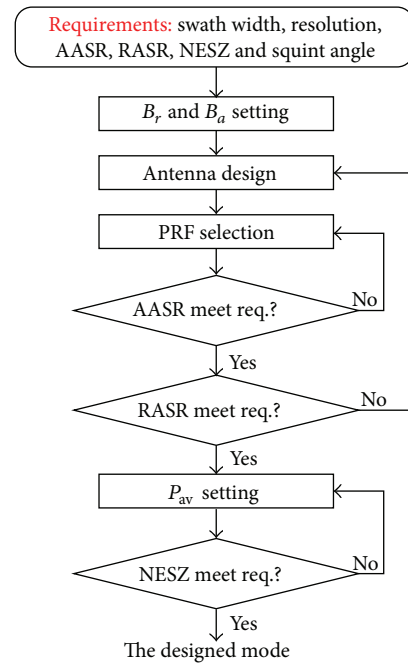


FIGURE 7: Block diagram of the system design of two proposed bidirectional SAR imaging modes.

different carrier frequencies, the AASR for the backward area and the forward area in the proposed MIMO-SAR system is computed as follows:

$$\begin{aligned}
 \text{AASR}_b = & \left(\sum_{k \neq 0} \int_{-B_a/2 + f_{dc,b}}^{B_a/2 + f_{dc,b}} G_{t,b}(f_a + k \cdot \text{PRF}) \right. \\
 & \left. \cdot G_r(f_a + k \cdot \text{PRF}) df_a \right) \\
 & \times \left(\int_{-B_a/2 + f_{dc,b}}^{B_a/2 + f_{dc,b}} G_{t,b}(f_a) \cdot G_r(f_a) df_a \right)^{-1},
 \end{aligned}$$

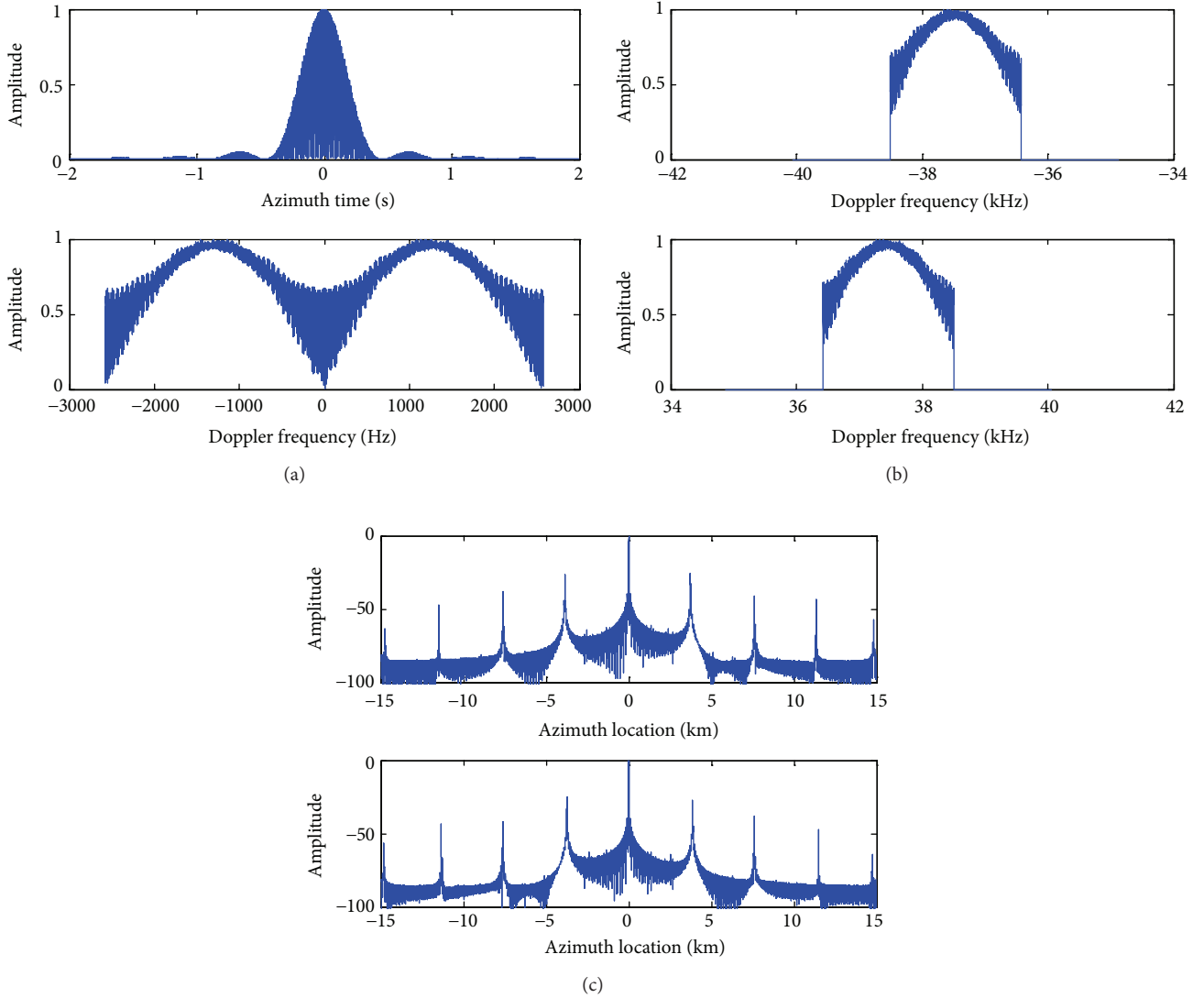


FIGURE 8: Simulation results of the proposed MISO-SAR with the PRF of 5170 Hz. (a) Azimuth raw data in the time and Doppler frequency domains. (b) Doppler spectra after separation. (c) Imaging results from different azimuth directions.

$$\begin{aligned}
 \text{AASR}_f = & \left(\sum_{k \neq 0} \int_{-B_a/2+f_{dc,f}}^{B_a/2+f_{dc,f}} G_{t,f}(f_a + k \cdot \text{PRF}) \right. \\
 & \left. \cdot G_r(f_a + k \cdot \text{PRF}) df_a \right) \\
 & \times \left(\int_{-B_a/2+f_{dc,f}}^{B_a/2+f_{dc,f}} G_{t,f}(f_a) \cdot G_r(f_a) df_a \right)^{-1}.
 \end{aligned} \quad (8)$$

As a result, the AASR level of the proposed MIMO-SAR system is much better than that of the MISO-SAR system. Figure 6 shows the AASR versus the selected PRF in the proposed MIMO-SAR system under the same condition.

3.2. The System Design. The block diagram in Figure 7 shows major system design steps of the two proposed bidirectional SAR imaging modes. The starting point is the desired system parameters of fore and aft images such as swath width, geometric resolution, AASR, range ambiguity to signal ratio (RASR), and noise equivalent sigma zero (NESZ), while fore and aft images are with the squint angles θ_s and $-\theta_s$, respectively. First, the transmitted pulse bandwidth B_r and the processed Doppler bandwidth B_a related to the azimuth antenna length are determined by the desired geometric ground resolution and azimuth resolution, respectively. According to the squint angle θ_s for bidirectional imaging, the number of T/R modules and the azimuth beam steering raw controlled by the phase coefficients in (4) and (5) can be set. The PRF selection is looking for the satisfied AASR level. Furthermore, in addition to reducing the selected PRF, we can

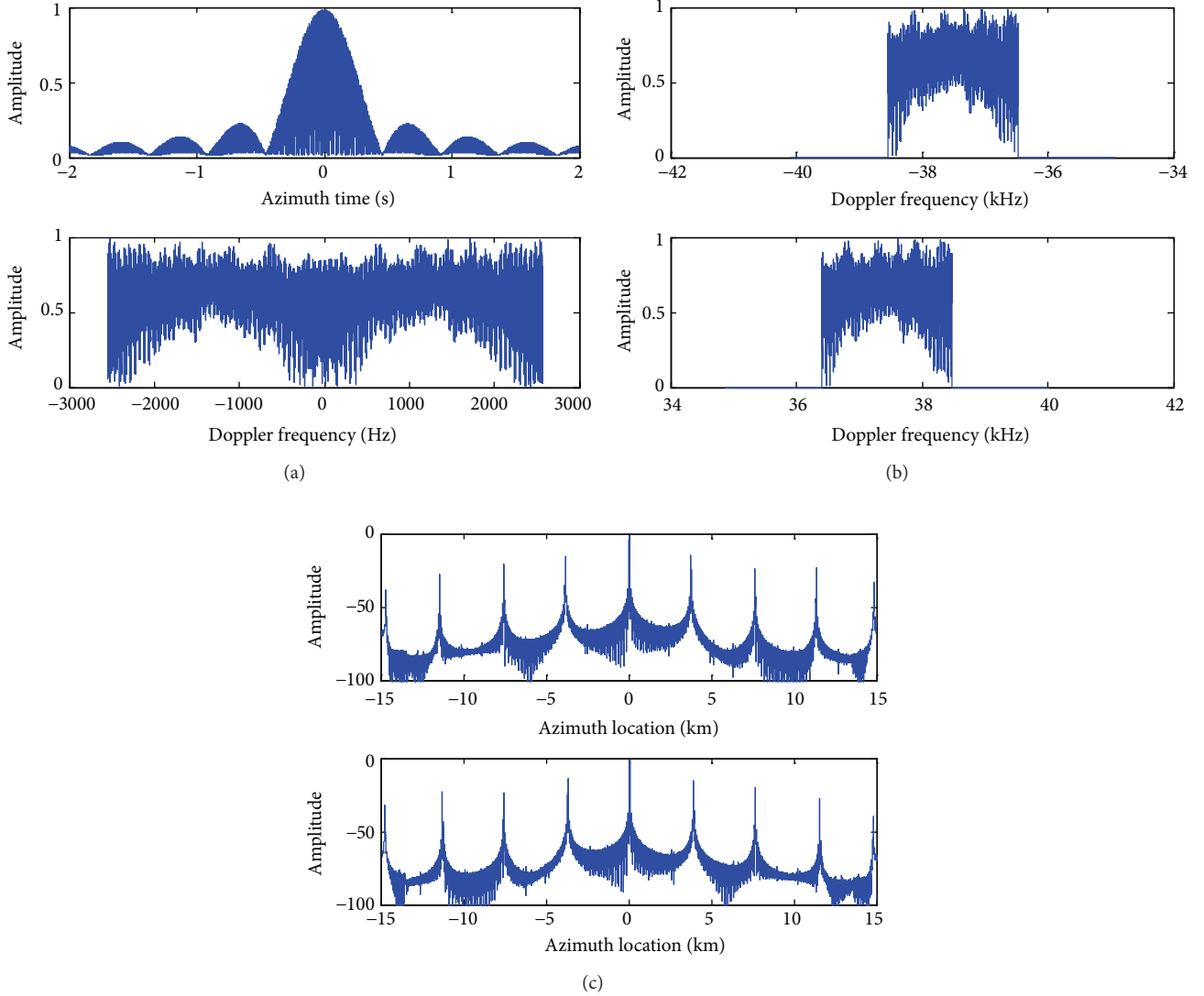


FIGURE 9: Simulation results of the original bidirectional SAR with the PRF of 5170 Hz. (a) Azimuth raw data in the time and Doppler frequency domains. (b) Doppler spectra after separation. (c) Imaging results from different azimuth directions.

enlarge the antenna height to improve the RASR level. Finally, the average power P_{av} is set to obtain the desired NESZ.

The major difference between the proposed MISO-SAR and MIMO-SAR for bidirectional imaging is that two subpulses are transmitted with different range-frequency bands to avoid mutual interference. As a result, a lower selected PRF is required for the desired AASR level in the MIMO-SAR system than in the MISO-SAR system under the same condition as shown in Figures 5 and 6. However, since the AASR oscillates between high and low values in the MISO-SAR system, a small PRF range should be selected for a better AASR level.

4. Raw Data Processing and Simulation

To validate the proposed MISO-SAR and MIMO-SAR for bidirectional imaging, simulation experiments on point

targets are carried out. Simulation parameters are listed in Table 1.

In the proposed MISO-SAR for bidirectional imaging, a much higher PRF than in the conventional stripmap case with the same antenna length is required according to Figures 8 and 10 which show raw data and imaging results of two targets from different azimuth locations by MISO-SAR mode. Figures 9 and 11 show the results by original bidirectional SAR mode with the same parameters.

Furthermore, with the PRF of 5170 Hz, spectra of two targets with the Doppler centroids -3746 Hz and 3746 Hz can be better separated via Doppler band-pass filtering and compressed, but the two spectra cannot be well separated and this phenomenon would introduce high azimuth ambiguities with the PRF of 5490 Hz. The weaker targets are azimuth ambiguities as shown in Figures 8(c) and

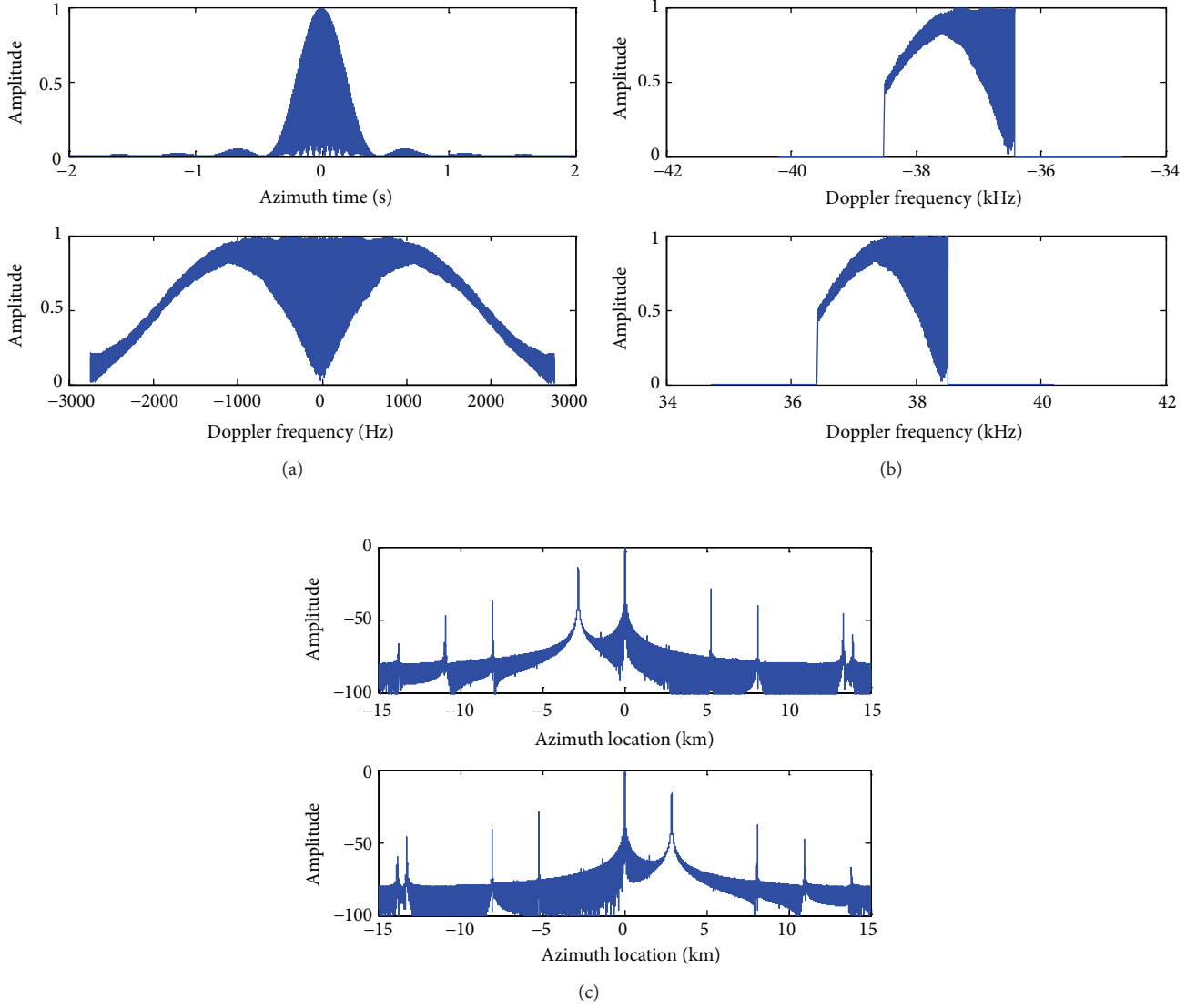


FIGURE 10: Simulation results of the proposed MISO-SAR with the PRF of 5490 Hz. (a) Azimuth raw data in the time and Doppler frequency domains. (b) Doppler spectra after separation. (c) Imaging results from different azimuth directions.

10(c). Results of Figures 8 and 10 also validate that the AASR oscillates between high and low values versus the PRF as shown in Figure 4. By comparing with Figures 8 and 9, it can be seen that the separation and imaging performances by the proposed MISO-SAR are obviously better than those in original bidirectional mode. With the PRF of 5490 Hz, it can lead to the same conclusion by comparing with Figures 10 and 11. Therefore, the superiority of the new MISO-SAR mode has been validated. With the same antenna length and the number of T/R modules, Figure 12 shows simulation results of azimuth raw data and spectra from two azimuth directions in the proposed MIMO-SAR for bidirectional imaging. The operated PRF is 3000 Hz.

5. Conclusion

The paper has put forward two novel imaging modes named MISO-SAR and MIMO-SAR for bidirectional imaging, and both modes allow for single-satellite short-term repeated SAR acquisitions in the range of seconds. In the two imaging modes, two subpulses are transmitted to different azimuth locations and the raw data from two directions simultaneously arrive at the sensor and are superimposed into the same receiving window. In the proposed MISO-SAR, echoes from different azimuth directions are separated by Doppler band-pass filtering. Echoes from different azimuth directions in MIMO-SAR are separated in the range-frequency domain due to different carrier frequencies. Compared with the bidirectional imaging mode in [1], the proposed MISO-SAR

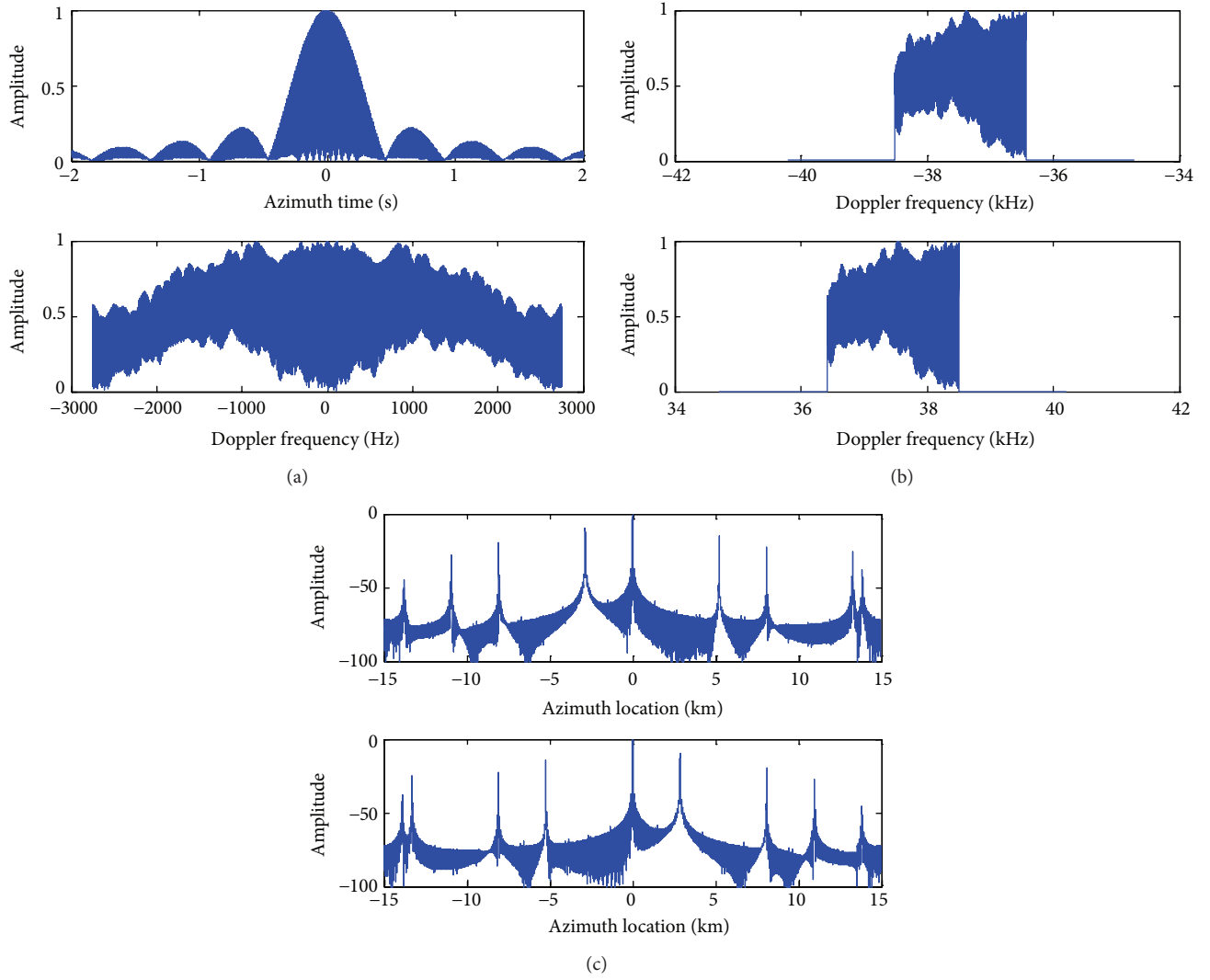


FIGURE 11: Simulation results of the original bidirectional SAR with the PRF of 5490 Hz. (a) Azimuth raw data in the time and Doppler frequency domains. (b) Doppler spectra after separation. (c) Imaging results from different azimuth directions.

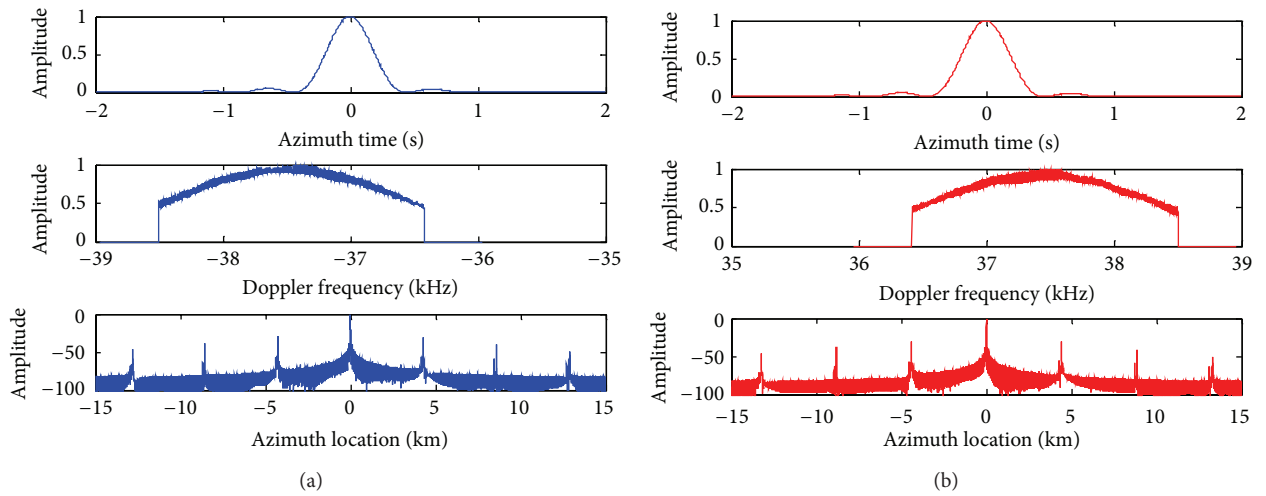


FIGURE 12: Simulation results of the proposed MIMO-SAR with the PRF of 3000 Hz. (a) Azimuth data of the point target for aft imaging. (b) Azimuth data of the point target for fore imaging.

and MIMO-SAR modes are with the better AASR under the same condition, especially the proposed MIMO-SAR.

Conflict of Interests

The authors declare that there is no conflict of interests regarding the publication of this paper.

References

- [1] S. J. Frasier and A. J. Camps, "Dual-beam interferometry for ocean surface current vector mapping," *IEEE Transactions on Geoscience and Remote Sensing*, vol. 39, no. 2, pp. 401–414, 2001.
- [2] D. d'Aria, F. de Zan, D. Giudici, A. M. Guarnieri, and F. Rocca, "Burst-mode SARs for wide-swath surveys," *Canadian Journal of Remote Sensing*, vol. 33, no. 1, pp. 27–38, 2007.
- [3] W. Xu and Y. K. Deng, "Investigation on electronic azimuth beam steering in the spaceborne sar imaging modes," *Journal of Electromagnetic Waves and Applications*, vol. 25, no. 14–15, pp. 2076–2088, 2011.
- [4] S. V. Baumgartner and G. Krieger, "Large along-track baseline SAR-GMTI: first results with the TerraSAR-X/TanDEM-X satellite constellation," in *Proceedings of the IEEE International Geoscience and Remote Sensing Symposium (IGARSS '11)*, S. V. Baumgartner and G. Krieger, Eds., pp. 1319–1322, Vancouver, Canada, July 2011.
- [5] J. Mittermayer, S. Wollstadt, S. Baumgartner et al., "Approach to velocity and acceleration measurement in the bi-directional SAR imaging mode," in *Proceedings of the IEEE International Geoscience and Remote Sensing Symposium (IGARSS '12)*, pp. 5618–5621, Munich, Germany, July 2012.
- [6] J. Mittermayer, S. Wollstadt, P. Prats-Iraola, P. López-Dekker, G. Krieger, and A. Moreira, "Bidirectional SAR imaging mode," *IEEE Transactions on Geoscience and Remote Sensing*, vol. 51, no. 1, pp. 601–614, 2013.
- [7] J. Mittermayer and S. Wollstadt, "Simultaneous bi-directional SAR acquisition with TerraSAR-X," in *Proceedings of the 8th European Conference on Synthetic Aperture Radar (EUSAR '10)*, J. Mittermayer and S. Wollstadt, Eds., pp. 1–4, Aachen, Germany, 2010.
- [8] J. Mittermayer, B. Schattler, and M. Younis, "TerraSAR-X commissioning phase execution summary," *IEEE Transactions on Geoscience and Remote Sensing*, vol. 48, no. 2, pp. 649–659, 2010.
- [9] S. Suchandt, H. Runge, H. Breit, U. Steinbrecher, A. Kotenkov, and U. Balss, "Automatic extraction of traffic flows using TerraSAR-X along-track interferometry," *IEEE Transactions on Geoscience and Remote Sensing*, vol. 48, no. 2, pp. 807–819, 2010.
- [10] J. Mittermayer, S. Wollstadt, P. Prats, P. Lopez-Dekker, G. Krieger, and A. Moreira, "Bi-directional SAR and interferometric SAR short term time series," in *Proceedings of the 9th European Conference on Synthetic Aperture Radar (EUSAR '12)*, pp. 308–311, Nuremberg, Germany, April 2012.
- [11] J. H. Gonzalez, M. Bachmann, and H. Hofmann, "TanDEM-X commissioning phase status," in *Proceedings of the 30th IEEE International Geoscience and Remote Sensing Symposium (IGARSS '10)*, pp. 2633–2635, Honolulu, Hawaii, USA, July 2010.
- [12] J. Mittermayer, M. Younis, R. Metzger, S. Wollstadt, J. M. Martinez, and A. Meta, "TerraSAR-X system performance characterization and verification," *IEEE Transactions on Geoscience and Remote Sensing*, vol. 48, no. 2, pp. 660–676, 2010.
- [13] J. Mittermayer and H. Runge, "Conceptual studies for exploiting the TerraSAR-X dual receive antenna," in *Proceedings of the IEEE International Geoscience and Remote Sensing Symposium (IGARSS '03)*, pp. 2140–2142, Toulouse, France, July 2003.
- [14] P. López-Dekker, P. Prats, F. de Zan et al., "Demonstration of SAR interferometry under crossing orbits using TerraSAR-X and TanDEM-X," in *Proceedings of the IEEE International Geoscience and Remote Sensing Symposium (IGARSS '11)*, pp. 3472–3475, Vancouver, Canada, July 2011.
- [15] R. Romeiser, S. Suchandt, H. Runge, U. Steinbrecher, and S. Grünler, "First analysis of TerraSAR-X along-track InSAR-derived current fields," *IEEE Transactions on Geoscience and Remote Sensing*, vol. 48, no. 2, pp. 820–829, 2010.
- [16] R. Scheiber and A. Moreira, "Coregistration of interferometric SAR images using spectral diversity," *IEEE Transactions on Geoscience and Remote Sensing*, vol. 38, no. 5, pp. 2179–2191, 2000.
- [17] G. Krieger, A. Moreira, H. Fiedler et al., "TanDEM-X: a satellite formation for high-resolution SAR interferometry," *IEEE Transactions on Geoscience and Remote Sensing*, vol. 45, no. 11, pp. 3317–3340, 2007.
- [18] R. Bamler and M. Eineder, "Accuracy of differential shift estimation by correlation and split-bandwidth interferometry for wideband and delta-k SAR systems," *IEEE Geoscience and Remote Sensing Letters*, vol. 2, no. 2, pp. 151–155, 2005.
- [19] K. Ouchi, "On the multilook images of moving targets by synthetic aperture radars," *IEEE Transactions on Antennas and Propagation*, vol. 33, no. 8, pp. 823–827, 1985.